Towards a hybrid electrostatic/atomic accelerometer for future space missions : study of rotation impact on a cold atom interferometer and mitigation strategy

Noémie Marquet

To cite this version:

Noémie Marquet. Towards a hybrid electrostatic/atomic accelerometer for future space missions : study of rotation impact on a cold atom interferometer and mitigation strategy. Atomic Physics [physics.atom-ph]. Université Paris-Saclay, 2024. English. NNT : 2024UPASP169 . tel-04890953

HAL Id: tel-04890953
https://theses.hal.science/tel-04890953v1

Submitted on 16 Jan 2025

Towards a hybrid electrostatic/atomic accelerometer for future space missions : Study of rotation impact on a cold atom interferometer and mitigation strategy

Vers un accéléromètre hybride électrostatique/atomique pour les futures missions spatiales :
Étude de l'impact de la rotation sur l'interféromètre à atomes froids et réduction de cet impact

Thèse de doctorat de l'université Paris-Saclay

École doctorale n° 572, Ondes et Matière (EDOM)
Spécialité de doctorat : Physique
Graduate School : Physique. Référent : Faculté des sciences d'Orsay

Thèse préparée dans l'unité de recherche **Physique, Instrumentation, Environnement, Espace** (Université Paris-Saclay, ONERA),
sous la direction de **Antoine GODARD**, Directeur de recherche
et le co-encadrement de **Nassim ZAHZAM**, Chargé de recherche.

Thèse soutenue à Paris-Saclay, le 9 décembre 2024, par

Noémie MARQUET

Composition du jury

Membres du jury avec voix délibérative

Eric CHARRON Professeur des Universités, ISMO - Université Paris-Saclay	Président
Jean-François CLEMENT Maître de conférence (HDR), IEMN - Université de Lille	Rapporteur et examinateur
Anne LOUCHET-CHAUVET Chargée de recherche (HDR), Institut Langevin - Université Paris Sciences et Lettres	Rapportrice et examinatrice
Franck PEREIRA DOS SANTOS Directeur de recherche, SYRTE - Université Paris Sciences et Lettres	Examinateur

THESE DE DOCTORAT

NNT : 2024UPASP169

université
PARIS-SACLAY

ÉCOLE DOCTORALE
Ondes et matière
(EDOM)

Titre : Vers un accéléromètre hybride électrostatique/atomique pour les futures missions spatiales : Étude de l'impact de la rotation sur l'interféromètre à atomes froids et réduction de cet impact

Mots clés : Atomes froids, Gravimétrie spatiale, Capteurs inertiels, Interférométrie atomique, Accéléromètre, Capteurs quantiques

Résumé : Le but des missions spatiales de gravimétrie est de mesurer le champ de gravité avec une grande précision. Les données récoltées sont utilisées en sciences du climat, en hydrologie, en géophysique et pour mieux comprendre le réchauffement climatique. Ces missions embarquent actuellement des accéléromètres électrostatiques avec une grande sensibilité mais dérivant à long terme. Cette dérive peut être corrigée en recalibrant l'accéléromètre électrostatique avec un accéléromètre à atomes froids ayant une plus importante stabilité. De tels accéléromètres utilisent l'interférométrie atomique pour mesurer l'accélération et une des difficultés de la mesure spatiale est la chute de contraste de l'interféromètre à cause de la rotation du satellite autour de la Terre.

Dans cette étude, nous avons mis en place expérimentalement une méthode pour limiter l'impact de la rotation sur l'interféromètre. Le dispositif expérimental est la combinaison d'un accéléromètre électrostatique et d'un interféromètre à atomes froids. La masse d'épreuve de l'électrostatique est employée comme miroir de rétro-réflexion pour l'interféromètre et est très bien contrôlée selon les six dégrées de liberté de l'espace. La méthode utilisée pour limiter l'impact de la rotation consiste à tourner le miroir pour garder la direction de mesure constante pendant l'interféromètre. Avec cette méthode de compensation de la rotation, 99% du contraste a été récupéré. De plus, la phase de l'interféromètre causée par la rotation a été mesuré et modélisée. Avec un modèle fiable, cette phase supplémentaire peut être corrigée de la mesure. Finalement, les performances attendues d'un accéléromètre atomique compensé de la rotation à bord d'un satellite ont été étudiées. Avec les hypothèses choisies, la rotation serait à l'origine d'une incertitude de $7 \times 10^{-10}\,\mathrm{m\,s^{-2}}$ sur la mesure de l'accélération pour un temps d'interrogation de $1\,\mathrm{s}$.

Title : Towards a hybrid electrostatic/atomic accelerometer for future space missions : Study of rotation impact on a cold atom interferometer and mitigation strategy

Keywords : Cold Atoms, Space Gravimetry, Inertial Sensor, Atom interferometry, Accelerometer, Quantum Sensor

Abstract : Space gravimetry missions aim to determine the Earth gravity field with great accuracy. The data gathered are very useful in the sciences of climatology, hydrology or geophysics and to understand global climate change. These missions board state-of-the-art space electrostatic accelerometers displaying a very good sensitivity but also a long-term drift. By combining an electrostatic accelerometer with a very stable cold atom accelerometer, the correction of this drift is possible. Such accelerometers principle relies on atomic interferometry and one of the difficulties of space measurements is the interferometer contrast loss due the satellite rotation around the Earth.

In this work, we experimentally implemented a method to limit the impact of rotation of the interferometer with an original setup. The hybrid lab prototype is the combination of an electrostatic accelerometer and a cold atom interferometer. The proof-mass of the electrostatic accelerometer, very well controlled in angle and position, is employed as an actuated retro-reflection mirror for the interferometer. The method tested to limit the rotation impact, consists in the rotation of the retro-reflection mirror to keep the direction of measurement constant during the interferometer. With the rotation compensation method, a contrast recovery up to 99% was demonstrated. Moreover, the impact of such a method on the phase shift bias was also measured and confronted to models. With an accurate model, the phase shift bias can be corrected from the measurement. Lastly, a study of the expected performances of a rotation compensated atom accelerometer boarded on a satellite was conducted. Under the considered hypothesis, the rotation should lead to an acceleration uncertainty of $7 \times 10^{-10}\,\mathrm{m\,s^{-2}}$ for a $1\,\mathrm{s}$ interrogation time.

This thesis has been prepared at

Office Nationale d'Etude et de Recherche Aérospatiale
6 Chemin de la Vauve aux Granges
91120 Palaiseau
France

Remerciements

Une thèse c'est pas toujours facile et ça nécessite le soutien de nombreuses personnes pour réussir. Voici donc une liste non exhaustive de personnes que j'ai pu côtoyer pendant ma thèse et que je tiens à remercier. Si cette thèse existe c'est grâce à vous.

Ma thèse a été financée par l'ONERA et l'ESA et je remercie Olivier Le Traon, Alexandre Bresson et Myriam Raybaut de m'avoir accueilli dans le département DPHY et l'unité SLM de l'ONERA à Palaiseau.

Je souhaite remercier les membres du jury d'avoir accepté d'évaluer ma thèse. Merci à Anne Louchet-Chauvet et Jean-François Clément d'avoir rapporté ma thèse. Merci à Eric Charron d'avoir accepté de présider le jury quelques années après m'avoir eu comme étudiante de master. Merci à Franck Pereira Dos Santos d'avoir accepté d'être examinateur et d'avoir lu si attentivement le manuscrit. Merci à tous les quatre pour votre gentillesse pendant ma soutenance.

Cette thèse n'aurait pas été possible sans mes encadrants Nassim Zahzam, Antoine Godard et Olivier Carraz.
Je voudrais particulièrement remercier Nassim de m'avoir accepté en stage début 2021, me permettant de découvrir l'interférométrie atomique et de travailler dans l'équipe CIAF. Dès le début du stage tu m'as laissé beaucoup d'autonomie sur la manip, me laissant exercer ma passion pour l'expérimentale. Néanmoins, ton bureau m'était toujours ouvert quelque soit la question ou le problème. Nos discussions scientifiques ou sur des sujets plus divers vont me manquer. J'ai beaucoup apprécié de travailler avec toi et j'ai appris pleins de choses grâce à toi pendant ces plus de 3 ans à l'ONERA. Mais je crois que j'ai eu une mauvaise influence sur toi: tu as fini par te mettre au café ;)
Merci aussi à Antoine d'avoir accepté de diriger ma thèse même si au début, tu n'étais pas un expert en interférométrie atomique. Malgré mes explications pas toujours très claires pendant nos réunions au bâtiment N, tu as su nous apporter un regard neuf sur mon travail de thèse avec tes remarques et conseils toujours pertinents.
Enfin, merci à Olivier d'avoir suivi mon travail pendant ces trois ans. D'abord à distance depuis les Pays-Bas puis d'un peu plus près quand je suis venue te rendre visite à l'ESTEC. Merci beaucoup de m'avoir accueilli à l'ESTEC et même chez toi lors d'un séjour un peu rocambolesque. Ce séjour m'a permis de prendre de recul sur mon travail expérimental et de découvrir un peu le fonctionnement de l'ESA.

Un grand merci à tous les membres de l'unité SLM que j'ai pu croiser pendant mon stage et ma thèse que vous soyez encore là ou parti vers de nouvelles aventures. Vous avez

tous contribué à la bonne ambiance de l'unité à travers des discussions scientifiques toujours bienvenues, des repas partagés à la cantine, des pauses café, des pots ou des discussions dans le couloir. Attention la liste va être longue. Merci à:
Yannick, Malo, Alexis et Sylvain les permanents atomes froids pour les discussions scientifiques, les débats le midi et les nombreux conseils. Vos bureaux sont toujours ouverts aux doctorants en plein doute. Merci beaucoup !
Merci aussi à Alex, toujours prêt à m'aider à résoudre mes difficultés administratives ou à parler info malgré ton emploi du temps chargé.
Myriam toujours prête à améliorer les conditions de travail de l'unité, à aider une doctorante en perdition en lui donnant du chocolat, et oui tu avais raison il fallait nettoyer notre bureau. Au bout de 30 ans il était temps.
Marie-Hélène pour les longues discussions et le remontage de moral pendant les derniers mois.
Quentin aussi pour le remontage de moral pendant la rédaction. J'espère que ça va aux Pays-Bas fait attention aux sectes ;)
Christophe pour son soutien sans faille.
Rosa a bientôt sur les chemins du Sancy :)
Jean-Pierre merci d'être sorti de ta retraite pour venir à ma soutenance. On est quitte maintenant un pot de retraite pour un pot de thèse.
Clément P. l'unité à maintenant une plante en pot pour mascotte.
Nelly pour m'avoir fait visiter l'ONERA Palaiseau il y a longtemps.
Maxime si tu fais une forêt noir je repasse au bâtiment S.
Et aussi Jean-Michel, Michaël, Jean-Baptiste, Gauthier, Laila, Alexandre M, Cédric et Christophe.

Merci aussi aux doctorants vous êtes responsables de la bonne ambiance de l'unité !
Une mention spéciale pour Clément S. jumeau de thèse. On a partagé beaucoup de choses ces trois dernière année, un bureau, une salle de manip, des conférences et aussi un peu un sujet de thèse (rotation ou accélération tu préfères quoi ?). Reviens entier de ton voyage en Nouvelle-Zélande.
Romain D., on a aussi partagé un bureau et beaucoup de conversations mais désolé j'ai peur de ne pas avoir retenu grand chose sur l'histoire du 20ème et les tueurs en série.
Romain G., Sarah et Mal avec vous je sais que la relève est assurée ! J'attendais avec impatience votre arrivée dans l'équipe et je ai pas été déçu.
Antoine, nos discussions décousues vont me manquer, on aura bien rigolé et bon courage pour la rédaction ça va le faire !
Claire, après t'avoir croisé au sympho ça a été super de te connaître plus à l'ONERA. On se revoit aux OPS ;)
et les nouveaux Léa et Tancrède.
Léa triste de pas t'avoir côtoyé plus longtemps, je suis sûre que tu vas faire une super thèse !
Petit coucou aux anciens doctorants: Élodie, Jeanne, Eve-line et Jonas.
Jeanne, c'était très cool de faire une partie de ma thèse en ta compagnie et d'avoir la chance d'enseigner à Supop avec toi. Tu m'as beaucoup manqué quand tu es partie de l'ONERA.
Élodie j'ai ramené les assiettes de la cantine comme promis ;)
Eve-line, n'oublie pas que tu es géniale toi aussi :)
et les nombreux stagiaires qui sont passés dans l'unité.
Anthony merci d'être venu à ma soutenance et au concert des OPS !

Merci aussi à l'unité IEA de l'ONERA dont j'ai pu rencontrer quelques membres pendant ma thèse. En particulier, Phuong-Anh Huynh pour avoir répondu à mes questions sur l'électrostatique même de dernière minute et à Hugo Lévy pour avoir partagé cette expérience de thèse à l'ONERA.

Merci aussi au secrétariat du DPHY, Eugénie et Marina de m'avoir aidé avec tous mes problèmes administratifs. A Nadia Chapiteau de l'école doctorale pour la même raison. Et à Marianne Daniel de l'École Polytechnique qui a été d'une aide précieuse pour organiser ma soutenance.

Merci aussi à l'équipe d'enseignement de l'IOGS Thierry Avignon, Cédric Lejeune et Fabienne Bernard, Julien Villemejane et Jeanne Bernard (encore toi). J'ai énormément appris en enseignant à vos côtés.

Les doctorants que j'ai pu rencontrer lors de conférences. C'était important pour moi de rencontrer des personnes avec des expériences similaires à la mienne.

Merci à tous les musiciens des OPS et en particulier du sympho que j'ai pu croiser ces dernières années. Vous êtes trop nombreux pour que je puisse tous vous citer ! Merci pour la pause musicale du lundi soir et les nombreux concerts du plateau de Saclay jusqu'en Allemagne en passant par l'opéra de Massy.

Merci à mes amis de l'orchestre et notre quatuor non-conventionnel Selma, Arsène et Jean-François pour les moments de musique, de rigolade et les goûters à n'importe quelle heure.

Merci à l'équipe d'aventuriers de Supop que l'on peut croiser sur les vélo-routes de France ou dans un labo au Danemark: Cécile, Léa, Raphaël, Hippolyte, Thomas, Arthur et Juliette. Toujours présents dans pour faire des rando vélo, des soirées jeux , des ciné et se remonter le moral mutuellement. On va être obligé de faire du bivouac maintenant qu'on est suréquipé ;)

Merci à mes amies de Clermont, Focéane et Leïla, d'être là après toutes ces années. On se revoit en Auvergne :)

Merci à Nathalie Piasi. Même si vous ne vous souvenez probablement pas de moi, sans vous les études ça aurait pas été aussi facile.

Merci à ma famille de m'avoir toujours soutenu de mille façons différentes, encouragé et aidé à faire des études. A Papou, Nana, Papi et Mamie, je sais que vous êtes fières de moi. Nana merci d'être venue à ma soutenance ça m'a fait très plaisir. Merci à Héloïse, Papa et Maman, vous savez pourquoi.

Votre petite physicienne

Résumé du travail de thèse

Introduction

Les missions de gravimétrie spatiales telles que les missions GRACE ou GOGE, permettent de mesurer le champ de gravité terrestre avec une grande précision. Les données ainsi obtenues sont utilisées dans les domaines des sciences de la Terre tels que la climatologie, l'hydrologie, la géophysique et pour mieux comprendre le réchauffement climatique. Ces missions embarquent actuellement des accéléromètres électrostatiques avec une grande sensibilité mais dérivant à long terme. Cette dérive peut être corrigée en recalibrant l'accéléromètre électrostatique avec un accéléromètre à atomes froids ayant une plus importante stabilité. De tels accéléromètres utilisent l'interférométrie atomique pour mesurer l'accélération. Une des difficultés de la mesure spatiale est la chute de contraste de l'interféromètre à cause de la rotation du satellite autour de la Terre. Nous avons donc étudié expérimentalement une méthode permettant de mesurer l'accélération dans un environnement en rotation avec un capteur atomique.

Résultats expérimentaux

Dans cette étude, nous avons mis en place expérimentalement une méthode pour limiter l'impact de la rotation sur l'interféromètre.

Le prototype de laboratoire est la combinaison d'un accéléromètre électrostatique et d'un accéléromètre à atomes froids. L'accéléromètre à atome froids considéré est basé sur le principe de l'interférométrie atomique. Un nuage d'atomes est placé dans une superposition d'état à l'aide d'un laser contra-propageant. Pour augmenter le temps d'interrogation des atomes, les atomes sont refroidis à 1 µK à l'aide d'un piège magnéto-optique. Le dispositif expérimental est constitué d'une enceinte ultra-vide contenant le nuage d'atomes froids, d'un laser interrogeant les atomes et d'un miroir sur lequel se réfléchit le laser. L'originalité de notre dispositif est le remplacement du miroir de rétro-réflexion du laser de l'interféromètre par la masse d'épreuve d'un accéléromètre électrostatique. Cette masse est très bien contrôlée selon les six degrés de liberté: il est possible de piloter sa vitesse de rotation. L'ensemble du dispositif peut être mis en rotation grâce à des cales piézo-électriques placées sous le capteur. La rotation du capteur est mesurée à l'aide d'un gyromètre.

Lorsque l'instrument est soumis à une rotation, le référentiel de mesure devient non Galiléen et les accélérations inertielles (accélération de Coriolis, accélération centrifuge, accélération angulaire) interviennent dans l'expression de l'accélération mesurée. L'impact des accélérations inertielles sur la phase dépend des paramètres cinétiques du nuage d'atomes froids tels que sa vitesse moyenne et sa position moyenne: une phase de biais du à la rotation apparaît.

L'impact des accélérations inertielles sur le contraste dépend de la distribution en position et en vitesse des atomes formant le nuage: la rotation entraîne une baisse de contraste. Un effet similaire apparaît lorsque le miroir de rétro-réflexion est en rotation. En tournant à la fois l'instrument et le miroir, certains de ces effets se compensent. La méthode utilisée pour limiter l'impact de la rotation consiste à tourner le miroir d'un mouvement angulaire opposé à celui de l'instrument pour garder la direction de mesure constante pendant la mesure.

Cette méthode de compensation de la rotation a été mise en place sur le dispositif expérimental et 99% du contraste a pu être récupéré. De plus, la phase de l'interféromètre causée par la rotation a elle-aussi été mesuré et modélisée pendant la compensation. Avec un modèle fiable, cette phase supplémentaire peut être corrigée de la mesure finale. C'est pourquoi, un calcul de la phase d'un interféromètre en rotation est présenté dans ce manuscrit. Pour se rapprocher d'applications spatiales, les performances attendues d'un accéléromètre atomique compensé de la rotation à bord d'un satellite ont été étudiées. Avec les hypothèses choisies, la rotation serait à l'origine d'une incertitude de $7 \times 10^{-10}\,\mathrm{m\,s^{-2}}$ sur la mesure de l'accélération pour un temps d'interrogation de 1 s. De plus, le dispositif expérimental et en particulier l'utilisation d'un miroir piloté électrostatiquement peut avoir une autre application: la rotation du miroir seul a permis de mesurer expérimentalement différents paramètres cinétiques du miroir tels que sa température, sa taille, sa position ou sa vitesse moyenne. En effet, la mesure du contraste et de la phase de l'interféromètre ainsi que le mouvement angulaire du miroir par détection capacitive permet de remonter à ces différents paramètres.

Conclusion

La mesure de l'accélération dans un environnement en rotation est difficile quelque soit la méthode de mesure. Cependant, l'impact de la rotation est particulièrement fort sur les accéléromètre a atomes froids en raison de la baisse de contraste engendrée. Lors de cette étude, nous démontré expérimentalement l'efficacité d'une méthode de compensation de la rotation sur un prototype de laboratoire. Cette méthode permet d'obtenir un contraste suffisant pour mesurer la phase de l'interféromètre en présence de rotation. Néanmoins, cette phase et donc la mesure d'accélération restent impactées par la rotation en raison de termes du à la rotation non compensés: des termes correspondant à l'accélération Centrifuge principalement. Un effort a été fait concernant la modélisation de la phase de l'interféromètre en rotation pour dans le future la retrancher de la mesure finalement. L'étude des performances d'un accéléromètre à atomes froids compensé de la rotation a montré que plusieurs architectures de capteurs sont possibles pour réduire l'impact résiduel de la rotation.

Acronyms

AOM	Acousto Optical Modulator - Modulateur Acousto-Optique
ASD	Amplitude Spectral Density- Densité Spectrale d'Amplitude
BEC	Bose Einstein Condensate - Condensat de Bose-Einstein
CHAMP	CHallenging Mini-satellite Payload
CoM	Center of mass - Centre d'inertie
DDS	Direct Digital Synthesis - Synthétiseur Digitale Direct
EA	Electrostatic Accelerometer - Accéléromètre Électrostatique
ECDL	External-Cavity Diode Laser - Diode Laser à Cavité Externe
EDFA	Erbium Doped Fiber Amplifier - Amplificateur Fibré Dopé à l'Erbium
ESA	European Space Agency - Agence Spatiale Européenne
ESTEC	European Space Research and Technology Centre - Centre Européen de Recherche et Technologies Spatiales
GOCE	Gravity field and steady-state Ocean Circulation Explorer
GRACE	Gravity Recovery and Climate Experiment
GRACE-C	Gravity Recovery and Climate Experiment Continuity
GRACE-FO	Gravity Recovery and Climate Experiment Follow On
LRI	Laser Ranging Instrument - Télémètre laser
MAGIC	Mass Change and Geoscience International Constellation
MOT	Magneto-Optical Trap - Piège Magnéto-Optique
NGGM	Next Generation Gravity Mission
PID	Proportional integral derivative lock-in system - asservissement Proportionnel Intégral Dérivé
PM	Phase Modulator - Modulateur de Phase
PPLN	Periodically Poled Lithium Niobate - Niobate de Lithium Périodiquement Orienté
VCO	Voltage Controlled Oscillator - Oscillateur contrôlé en tension

Table of Contents

Introduction

Outline of the current chapter

This work has been conducted at ONERA (Office National d'Etude et de Recherche Aérospatiales) in the SLM (Sources Laser et Métrologie) unit of the DPHY department (Département Physique, Instrumentation, Environnement, Espace) in collaboration with the European Space Agency (ESA) and the IEA (Instruments et Equipements Aérospatiaux) unit of the DPHY department. The CIAF (Capteurs Inertiels à Atomes Froids) team have developed onboard inertial sensors such as gravimeter, accelerometer or gyroscope based on atom interferometry for more than twenty years. The first marine [1] and airborne [2] gravimetric measurements with an atomic sensor were performed with the ONERA gravimeter GIRAFE 2 in 2015 and 2017. The CIAF team now works among other topics, on the potential of atomic sensors in spatial environments. The European Space Agency is a major actor of Earth observation space missions and among them gravimetry missions such as GOCE and NGGM. Until now, electrostatic accelerometers (EA) developed by the IEA unit at ONERA, were boarded on gravimetry satellites. EA display an important sensitivity but are limited by a slow drift. A collaboration was initiated to assert the feasibility of a merger between electrostatic and atomic sensors to limit this slow drift. The hybrid lab prototype was built from an EA designed by the IEA unit and an atomic gravimeter based on the GIRAFE gravimeter. This instrument has an original design as the combination of the two technologies have never been implemented before.

Spatial gravimetry aims to measure the Earth gravity field from space allowing the study of the geoid and the evolution of the mass distribution. Gathered data are useful in the fields of geophysics and Earth sciences. Currently, gravimetry satellites board electrostatic accelerometers which are the most sensitive accelerometers in micro-gravity environments. However, these accelerometers are not absolute sensors and display a drift at low frequencies. To overcome this limitation, atomic sensors could provide a drift-free absolute measurement. Nevertheless, atomic inertial sensors have yet to be operated in a spatial environment. Besides the weight and energy consumption limitations, an orbiting satellite has a rotation rate so important that atomic inertial sensors have trouble operating. The design of the hybrid lab instrument is interesting to tackle the rotation detrimental effect with the help of the EA: this is the object of this work. This work aims to implement experimentally on the hybrid setup the method used in [3] to limit the Earth rotation impact. The development of a rotation-proof atomic accelerometer could ease the use of atomic sensors in space but also for land-based applications in dynamical environments.

Firstly, the interest of space gravimetry missions will be detailed and some particular missions presented. Secondly, a short history of cold atoms inertial sensors and their interest for space gravimetry missions will be displayed. Then, a state of the art of atomic inertial sensors will give an overview of the field. Lastly, a presentation of this research work will be given.

Space gravimetry

Interest of space gravimetry missions

At the beginning of the 21st century, space missions have started to be launched to measure the Earth gravity field from space. These missions provided and still provide data of interest for Earth sciences. Here are a few examples of studies enabled by space gravimetry missions.

Geoid

The geoid is an equipotential surface of the Earth gravity field: it can be seen as the shape the ocean would take under the action of Earth gravity only. It is usually expressed as a height above or below a reference ellipsoid. The geoid is not smooth and its height varies due to the density variations inside the Earth. Despite the important altitude variations on Earth, the geoid height stays between ±100 m. The geoid is a reference for precise altitude measurements, ocean circulation, sea-level, ... and also for the study of water movements in drainage basins. The space missions CHAMP and GOCE goals was to improve the knowledge of the geoid by increasing the accuracy of the measurement and the spatial resolution. CHAMP aimed to measure the geoid at a centimetric level with a resolution of about 1000 km [4]. Previously, the geoid was known at a metric level with a spatial resolution about 1200 km. Later, the GOCE mission improved even further the geoid measurement with a comparable accuracy but a better spatial resolution of about 100 km (Figure 1) [5].

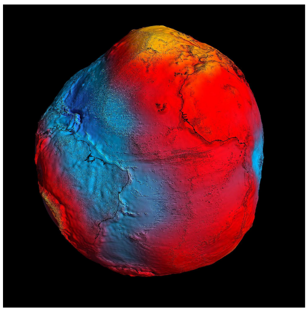

Figure 1: Earth's geoid measured by the GOCE mission from [6]. The blue values represent low height deviations from and ideal geoid and the reds and yellows the high deviations.

Water distribution

If the geoid study is the study of the constant component of the gravity field, the measurement of the temporal gravity variations enables the study of the water cycle. Gravimetry missions provide a measurement of the global water cycle and give information about subsurface and sub-glacial water movements which are difficult to measure otherwise. GOCE mission focused on slow variations of the gravity field and was able to measure ocean currents at the planet level (Figure 5b). GRACE missions were designed to detect small variations in the gravity field allowing the study of inland water distribution and its temporal evolution. In a context of climate change, the study of ground water, surface water or polar ice sheets is crucial. GRACE resolution is about 300 km and monthly data are furnished. In the context of global warming, the study of water storage is critical as 80% of the world population faces threats to water security as flood and drought episodes increase. For example, GRACE data helped measure the decreasing water storage in California during an important drought (Figure 7a). The mass loss in the Greenland and Antarctic ice sheets were also measured during more than a decade (Figure 2). From 2002 to 2017, Greenland showed a quite homogeneous mass loss of 281 Gt year^{-1} inducing a global mean sea-level rise of 1 cm. The Antarctic mass loss is concentrated in the region of the Amundsen Sea Embayment in red on Figure 2 for a global mass loss of 125 Gt year^{-1} [7–9].

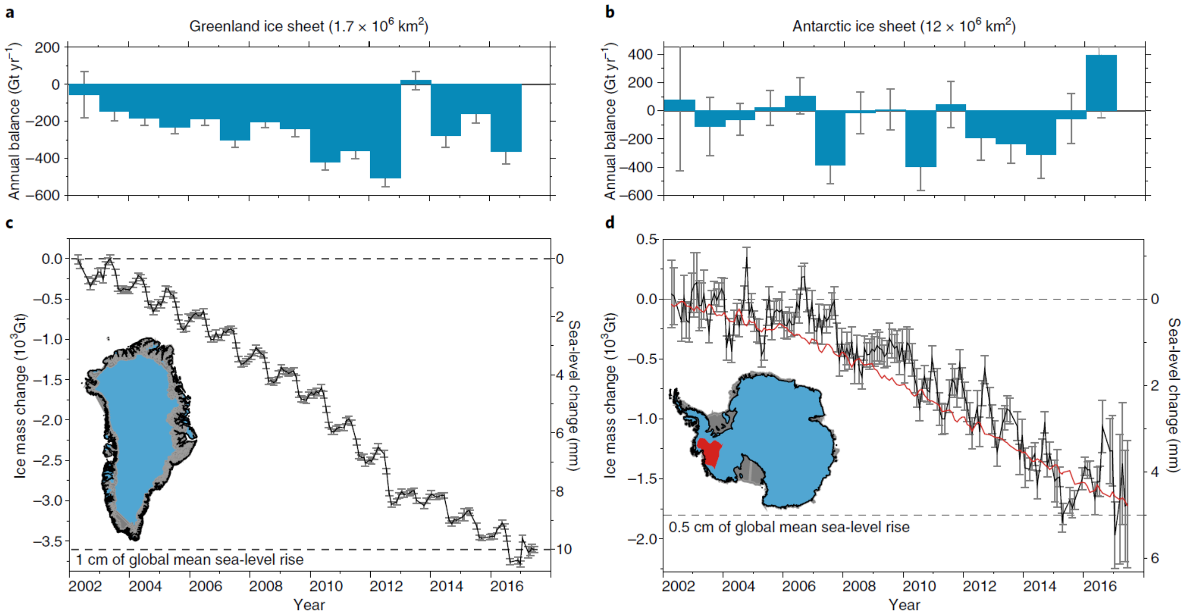

Figure 2: GRACE observations of mass changes of the polar ice sheets between 2002 and 2017. Annual mass balance of the Greenland Ice Sheet (a) and the Antarctic Ice Sheet (b). Time series of mass change of the Greenland Ice Sheet (c) and the Antarctic Ice Sheet (d) from [7].

Solid Earth mass

Gravimetry spatial data also carry the signature of deep Earth mass distribution. For example, the response movements inside the Earth to the last deglaciation have been measured by GRACE. Movements in the Earth mantle were measured by GOCE leading to a map of material rising in the mantle from more than 2000 km deep (Figure 3). GRACE data can also be used to study inner Earth movements. For example, [10] proposes to study the mass flows at the boundary between the outer core and lower mantle by correlating GRACE data with magnetic data. [11] have been able to constrain the value of the Earth's inner core differential rotation using GRACE data again. Seismic waves observations suggested that the inner core was not rotating with the same angle as the mantle. According to GRACE data, this angle is smaller than 0.4°.

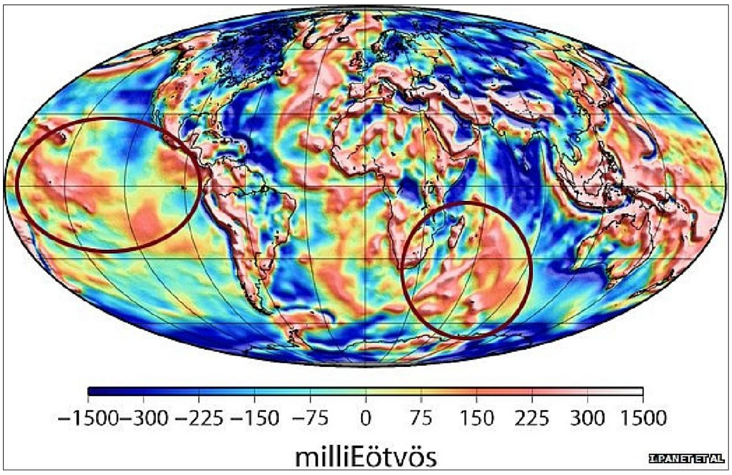

Figure 3: Deep plumes of the mantle material rising from more than 2000 km down measured by the GOCE mission from [6].

Past and future gravimetry missions

Since the beginning of the century, several gravimetry missions have been launched by DLR, ESA and NASA. These past and current missions supplied interesting data to Earth scientists. Thus, future missions are planned to keep providing data.

CHAMP (CHAllenging Mini-satellite Payload)

One of the first gravimetry mission was the German mission (DLR) CHAMP launched in 2000. CHAMP aimed to measure both the gravity and magnetic field. The magnetic field measurement was performed by several magnetometers while the gravity field was deduced from the satellite orbit. The satellite orbit was known thanks to GPS tracking and the non-gravitational forces (drag and radiation pressure) were measured thanks to an accelerometer at the satellite centre of mass. The boarded accelerometer STAR was an electrostatic accelerometer developed by ONERA. Its measurement principle is based on the electrostatic suspension of a metallic proof mass between electrodes [4, 12].

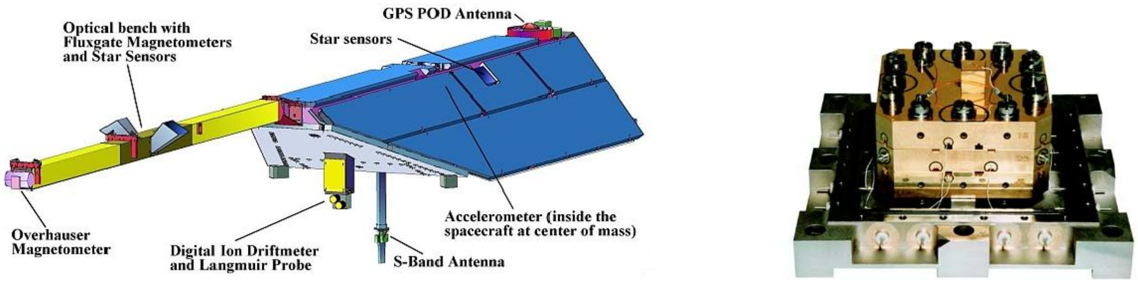

(a) CHAMP spacecraft.

(b) STAR electrostatic accelerometer of the CHAMP mission .

Figure 4: The DLR CHAMP mission technical details from [12].

GOCE (Gravity field and steady-state Ocean Circulation Explorer)

The ESA mission GOCE launched in 2009 aimed to measure the Earth geoid height at a centimetric level and the gravity anomalies at level $1 \times 10^{-5}\,\mathrm{m\,s^{-2}}$ with a spatial resolution of 100 km. The payload consisted in three gradiometers at the centre of mass of the satellite. Each gradiometers contains two electrostatic accelerometers distant of 50 cm, has a noise of about 10 mE/Hz$^{1/2}$ with the eotvos unit E=$1 \times 10^{-9}\,\mathrm{s}^{-2}$ and a measurement bandwidth between 5 and 100 mHz. The knowledge of the geoid and the measurement of the mean ocean surface by satellite radar altimetry allow the deduction of the ocean global dynamics (Figure 5b). The GOCE mission ended in 2013 when the satellite ran out of fuel [5, 6, 13].

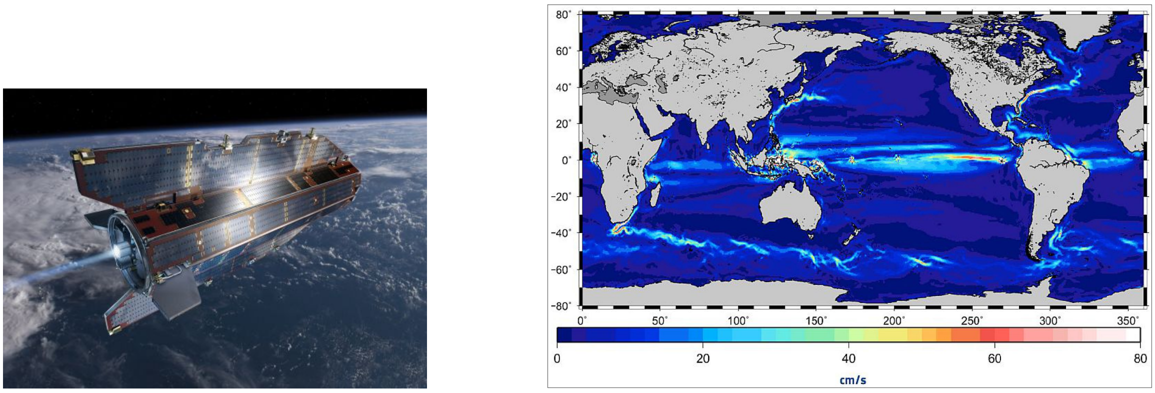

(a) Artist's view of the GOCE satellite.

(b) Ocean currents measured by GOCE.

Figure 5: GOCE mission design and results from [6].

GRACE (Gravity Recovery and Climate Experiment) and GRACE-FO (Follow-On)

The GRACE and GRACE-FO missions are DLR/NASA operated missions aiming to measure the variations of the Earth gravity field. The focus of these missions is on the fast variations of the gravity field. Thus, a good sensitivity is required. The measurement principle is depicted in Figure 6. A pair of satellites orbiting around the Earth follow each other at a distance measured by a telemeter. A mass on Earth creates a gravity field accelerating or decelerating the satellite as it gets closer to the mass. The Earth mass distribution impacts directly the inter-satellite distance. The knowledge of this distance thanks to the telemeter enables the measurement of the gravity field. Nevertheless, the gravity is not the only force applied to the satellites: the residual atmosphere creates a drag force and the Earth and solar radiations exerts a radiative pressure. The non-gravitational forces are measured by two electrostatic accelerometers at the centre of mass of each satellite and corrected from the gravity measurement. GRACE missions focus on the study of the water distribution and its evolution over time ranging from the water storage on land to the study of ice sheets. Moreover, the movements of the solid Earth can also be detected (Figures 2 and 7).

The GRACE mission was launched in 2002, largely exceeded the expected mission duration of 5 years and ended in 2017. The inter-satellite distance was measured with a K-band micro-wave telemeter [14]. The GRACE-FO mission was launched in 2018 to continue the GRACE mission and provide continuous data. The two missions are almost identical. Nevertheless, GRACE-FO boards a laser ranging instrument (LRI) in addition to the micro-wave telemeter. The LRI was tested during the mission and showed better performances than the micro-wave telemeter [15].

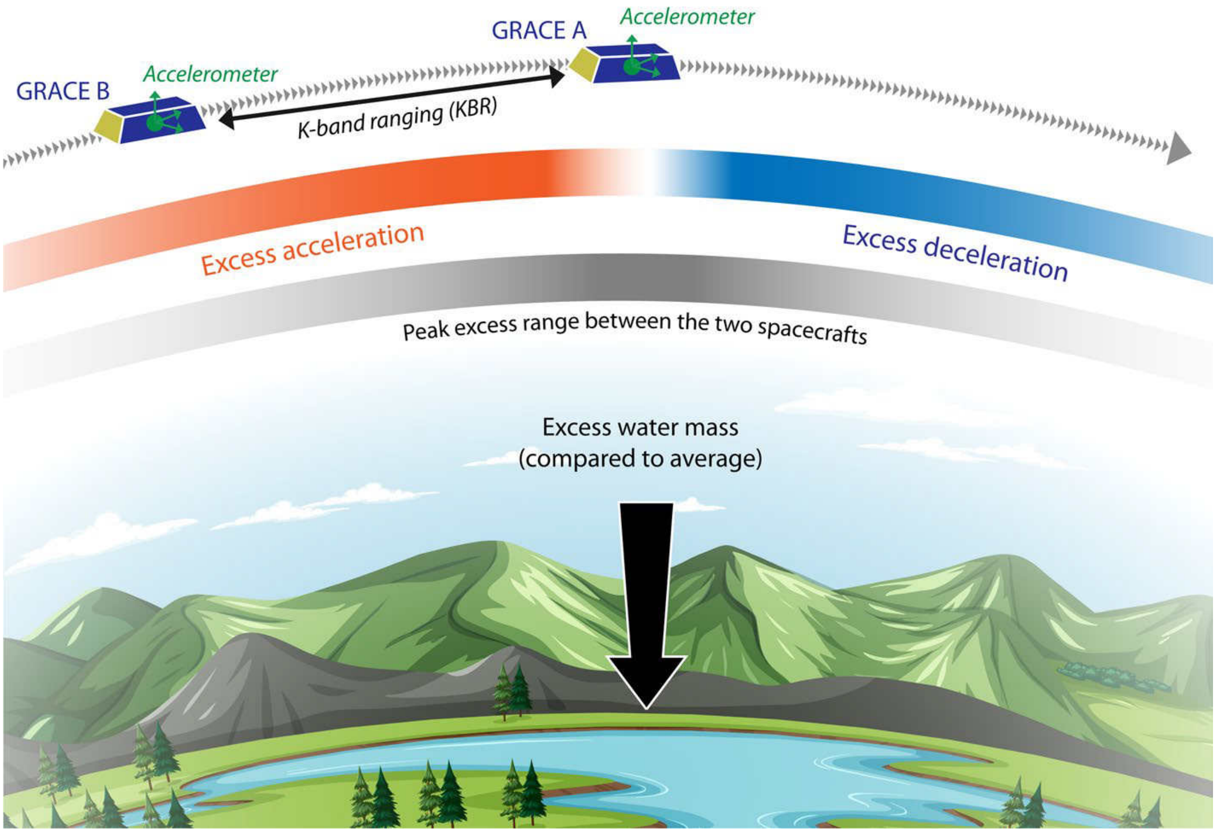

Figure 6: Measurement principle of GRACE mission. The distance between the satellites is about 220 km and their altitude about 500 km from [8].

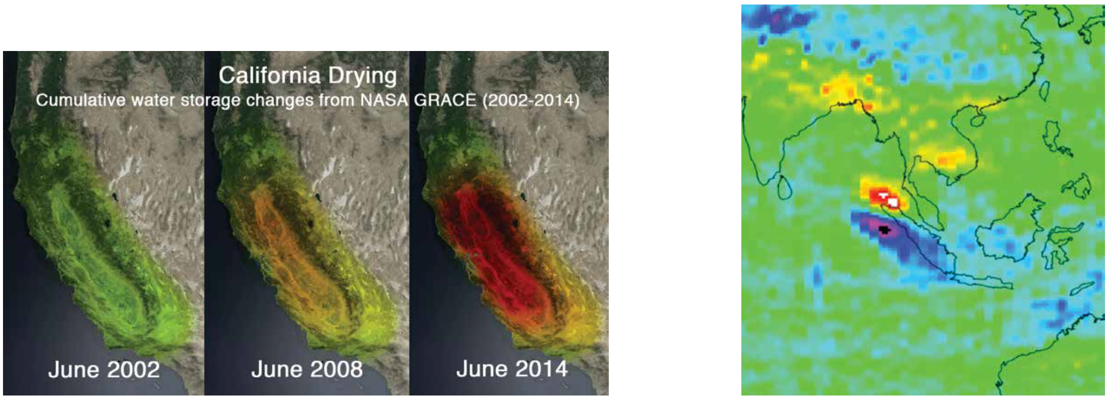

(a) Mass loss in California Central Valley due to groundwater extraction (GRACE Data). Water height anomaly in cm: 0 in green -12 in red.

(b) Gravity changes caused by the 2004 Sumatra earthquake. Acceleration anomaly: $0\,\mathrm{nm\,s^{-2}}$ in green, $-10\,\mathrm{nm\,s^{-2}}$ in purple and $10\,\mathrm{nm\,s^{-2}}$ in red.

Figure 7: Results from GRACE mission extracted from [16].

GRACE-C (Gravity Recovery and Climate Experiment Continuity) and NGGM (Next Generation Gravity Mission) toward MAGIC (Mass Change and Geoscience International Constellation)

As the data provided by GRACE-FO are useful to Earth sciences, the continuity of the data acquisition has to be granted after the end of the mission. To replace GRACE-FO, the NASA mission GRACE-C should be launched in 2028. While being close to the previous missions, the future mission will only use a LRI to measure the inter-satellite distance as its performances and reliability were demonstrated during the GRACE-FO mission. To improve the spatial and temporal resolutions of the gravity mission, a second pair of satellites, the NGGM mission, is planned to be launch by ESA in 2030. The two missions will operate in a Bender constellation (Figure 8). The GRACE-C satellites have a polar orbit in red and the NGGM satellites have tilted orbit at 70° in pink. Space gravimetry missions with a GRACE-like configuration are currently limited by aliasing effects linked to limitations in the modelling of high-frequency oceanic and atmospheric mass variations. This problem would be overcome by using a satellite constellation: several pairs of satellites would measure at the same time from different orbits [17]. Such constellation would measure a mass source from different points of view thus limiting the effect of quick atmospheric and oceanic mass variations [18].

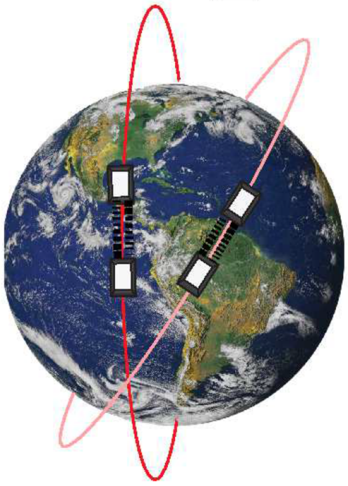

Figure 8: The MAGIC configuration is a Bender constellation with GRACE-C one of the satellite pair at a polar orbit (in red) and NGGM the other pair at a tilted orbit (in pink) from [19].

Cold atoms inertial sensors

The field of atomic based sensors ranging from atomic clocks to magnetometers by way of inertial sensors, have known an important growth in the past decades. Such sensors start to go out of the lab and to be tested in applicative conditions. As explained in [20], most atomic sensors are based on the following principle: the evolution in an external field of a two-levels atomic system. The principle of measurement is summed up on Figure 9. Firstly, the atom is prepared in a given state: a spin, an hyperfine internal state, ... Secondly, the state evolves in the external field to be measured: a magnetic field, gravity field, an electric field, ... The evolution time is generally limited by the relaxation of the system. Thirdly, the atomic state is measured. The field can be measured thought its effects on the atomic state.

Atomic sensors have several advantages among them the absolute feature of the measurement. Atomic sensors do not need to be calibrated as their scale factor depends of the atom characteristics. Such sensors also display good repeatability: the atoms properties do not change over time contrary to mechanical moving parts which can deteriorate. The evolving time is a key parameter of an atomic sensor: the longer the evolving time is, the more sensitive is the sensor. The evolving time can be limited by relaxation processes or mechanical limits (the free-falling distance in an atomic gravimeter). One of the limits of atomic sensors is the quantum projection noise. This noise comes from the quantum fluctuations of the atomic state at the end of the evolution [21]. The quantum noise limit can be overcome by squeezing the atomic states [22].

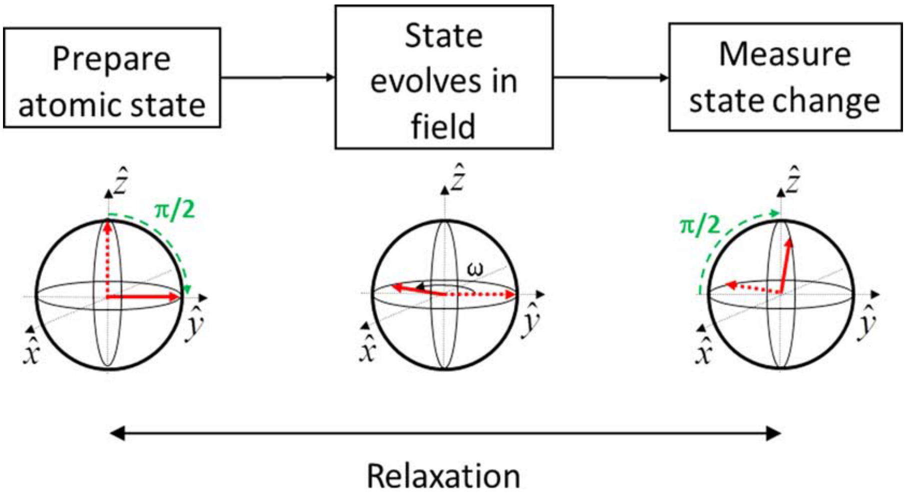

Figure 9: Measurement principle of atomic sensors represented in three steps on the Bloch sphere. First, the atoms are prepared in a well-known state. Then, the state evolves in the field. Finally, the atomic state is measured and the field properties deduced. Figure from [20].

Cold atoms inertial sensors such as accelerometers and gyroscopes are most of the time using atomic interferometry. Atomic interferometers take advantages of the wave-like property of matter to put an atom in a superposition of states. Atomic and optical interferometers are based on the same principle but the roles of matter and light are reversed (Figure 10). In an optical interferometer, a light-wave is manipulated by matter optics (glass beamsplitters and mirror). In an atomic interferometer, a matter-wave is shaped by laser pulses used as atom optics. Contrary to optical interferometers, atomic interferometers are sensitive to inertial forces thanks to the finite mass of the atoms.

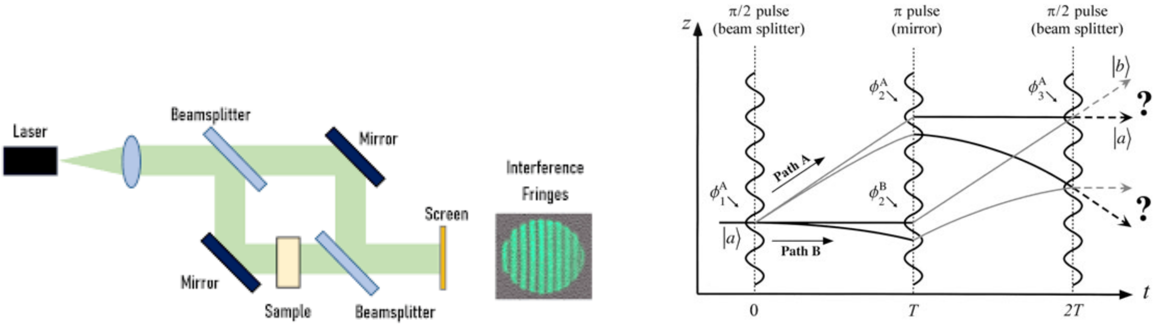

(a) Optical Mach-Zehnder interferometer from [23].

(b) Atomic Mach-Zehnder interferometer from [24].

Figure 10: Comparison between atomic and optical interferometers.

Interest of cold atoms inertial sensors for space gravimetry

The electrostatic accelerometers currently boarded on gravimetry missions are limited by a thermal long-term drift. The use of cold atom accelerometers could help reduce this drift as they display good long-term stability (Figure 11a). Several studies have been conducted to assess the feasibility and the performances of a space cold atom accelerometer or gradiometer as the same limitation arises for electrostatic gradiometers.

Some studies conceive a GOCE-like mission using a cold atom gradiometer to overcome the low frequency noise of the electrostatic gradiometer of GOCE and improve the gravity field retrieval [25–28]. These studies consider several configurations (Nadir-pointing or inertial mode satellites) and simulate the expected performances of the instrument. [27] expects a sensitivity of $5\,\mathrm{mE/Hz^{1/2}}$ with an atomic gradiometer using a BEC source similar to the one proposed by [25].

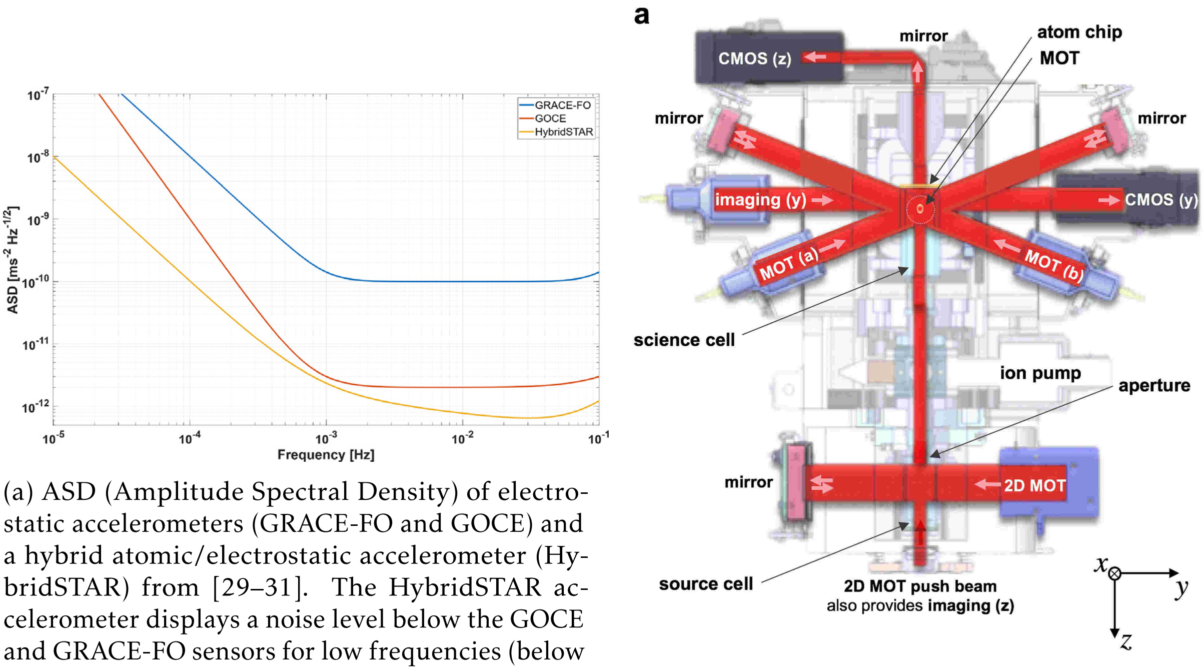

(a) ASD (Amplitude Spectral Density) of electrostatic accelerometers (GRACE-FO and GOCE) and a hybrid atomic/electrostatic accelerometer (HybridSTAR) from [29–31]. The HybridSTAR accelerometer displays a noise level below the GOCE and GRACE-FO sensors for low frequencies (below 1×10^{-1} Hz).

(b) Science module of CAL on the ISS from [32].

Figure 11: Toward space operated inertial atomic sensors.

Other studies focus on a GRACE-like configuration involving a pair of satellites. Thus, [33] proposes a general configuration of a long baseline gradiometer useful to measure the gravity gradient or to detect gravitational waves. In this configuration, two satellites boarding an atom interferometer are linked with a laser telemeter. [34] considers a similar configuration and expects a sensitivity of $6 \times 10^{-10}\,\mathrm{m/s^2/Hz^{1/2}}$. A last group of studies envision a combination of an electrostatic accelerometer and an atomic sensor to combine the stability of the atomic and the high frequency performances of the EA [29, 30, 35]. [30] studied the feasibility of a hybrid instrument in a GRACE-like configuration with the implementation of the rotation compensation with the EA acting as a mirror. A lab prototype of the hybrid instrument was built and a preliminary experimental study of the rotation compensation was conducted. [29] modelized a GRACE-like mission with an EA at the centre of mass of each satellite and cold atom accelerometer beside. Thanks to this approach, the achievable stability is expected to be at the level of $5 \times 10^{-10}\,\mathrm{m/s^2/Hz^{1/2}}$.

The operation of cold atom interferometers in space either on board a satellite or a space station is still an experimental challenge. Nevertheless, several experiments paved the way to space atomic sensors. Since 2013, interferometers using a BEC source have been operated in micro gravity in the Bremen drop tower [36]. Bose-Einstein Condensates have also been prepared on board of the sounding-rocket mission MAIUS [37]. The preparation of the BEC source is the first step toward the implementation of an atom interferometer. The first cold atoms at a temperature of 100 µK in space were prepared in the Chinese space laboratory Tiangong-2 for the implementation of the atomic clock CACES [38]. In 2018, the Bose-Einstein condensation was achieved in the International Space Station (ISS) with the Cold Atom Lab (CAL) [32] (Figure 11b).

A short history of atom interferometry and cold atom inertial sensors

The implementation of atomic interferometry was enabled by the introduction of the wave-particle duality concept at the beginning of the 20th century by Albert Einstein. The wave-like property of the light was proposed by Huygens and confirmed by Young's interference experiment. Nevertheless, the photo-electric effect challenges this approach. If Max Planck proposed the energy quantification in 1900 to explain the black-body radiation [39], Einstein used this theory to explain the photo-electric effect in 1905 with the help of light quanta later called "photons" [40]. Niels Bohr adapted Planck's idea into a model of the hydrogen atom to explain its discreet spectra lines. In 1917, Albert Einstein expanded the energy quantification to explain the absorption and emission of energy by atoms [41] laying the foundations of laser theory and atom interferometry theory.

Matter-wave interferometry

The first matter-wave experiments were the observations of diffraction patterns of electrons (Figure 12a) through a nickel crystal in 1927 by Davisson and Germer [42]. Similar experiments were performed with heavier particles in the following years. In 1930, Estermann and Stern realised the diffraction of hydrogen H and dihydrogen H_2 by a lithium fluorure crystal LiF [43]. The diffraction of neutrons was also observed in 1936 by Halban and Preiswerk [44] and Mitchell and Powers [45] the same year. In the last experiment, the neutrons were diffracted by a magnesium oxide crystal.

After the wave-like properties of particle was observed, the first two-wave interferometers using matter-waves were built. An experiment using electrons and three crystals to build a Mach-Zehnder-like interferometer was conducted by Marton in 1952 [46]. Later, neutron interferometers (Figure 12b) were built by Maier-Leibnitz and Springer using "neutron mirrors" [47]. It is worth mentioning the development of the Ramsey interferometry which happened at the same period [48]. Ramsey interferometry or spectroscopy uses an oscillating magnetic field to measure the transition frequency of a particle leading to the creation of atomic clocks.

Matter-wave interferometry is sensitive to inertial forces thanks to the mass of the involved particles. The first experimental implementations of interferometers sensitive to inertial forces were in the 70's with neutrons and were able to measure the Earth rotation [49] and the Earth gravity [50]. These experiments were proofs of principle and paved the way to inertial sensors. If neutrons are sensitive to inertial forces, their masses are not as important as the masses of atoms. But how to manipulate the atomic wave function ? Several methods were studied with the use of splits [51], mechanical gratings [52] and matter-light interactions. One photon transitions were considered by Riehle [53] and two photons transitions by Kasevich and Chu [54]. Such transitions modify the internal atomic state as well as its external state easing the state detection [55]. Later, atomic beamsplitters were created with Bragg scattering from standing light waves but Bragg transitions do not modify the external atomic state. The development of such methods led to the creation of inertial sensors based on atom interferometry

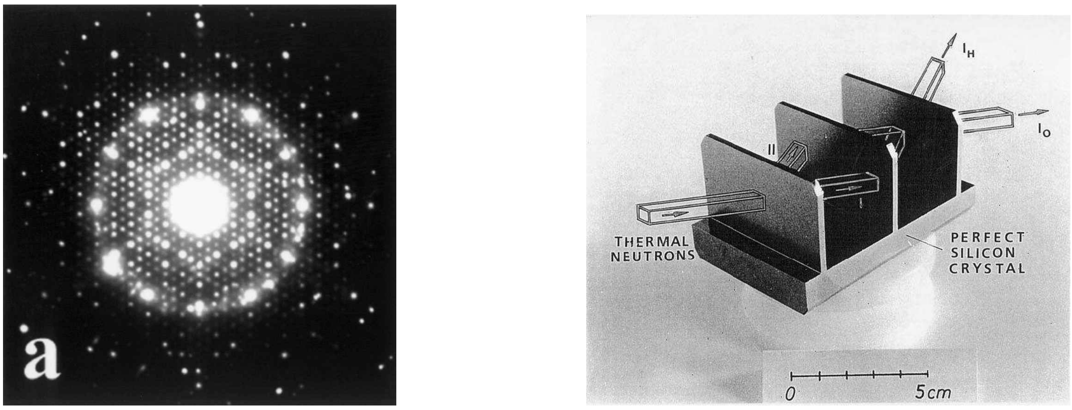

(a) Electron diffraction figure from [56]. (b) Neutron interferometer from [57].

Figure 12: Example of wave-like properties of particles.

Inertial sensors

Atom interferometry based inertial sensors were developed since the 80's. The first atomic gravimeter was built by Kasevich and Chu using sodium [54] and cesium [58] atomic fountains. The development of atomic inertial sensors was supported by the progress of atomic cooling techniques below µK of alkali atoms [59–64]. Cold atoms have larger wave packet and a smaller velocity distribution limiting the expansion of the atoms. This enables longer interrogation times and better sensitivity of the interferometer. At the beginning of the 21^{st} century, the sensitivity of the Stanford gravimeter [24] was 2×10^{-7} m/s^2/Hz$^{1/2}$ and displayed performances similar to classical gravimeters based on free-falling corners [65]. At the same time, atomic gradiometers using two atomic clouds aiming to measure the gravity gradient were implemented [66]. Cold atom gyroscopes were also developed [67]. Moreover, atomic interferometry can also be useful to determine fundamental constants such as the fine structure constant α [68, 69] or the gravity constant G [70]. Some tests of the Weak Equivalence Principle (WEP) were also performed with atom interferometry using two different atomic species [71].

State of the art of atomic inertial sensors

Cold atom inertial sensors have known an exponential growth in the last two decades thanks to their interesting long term stability and absolute measurement. In this state of the art, the focus is on atomic accelerometers/gravimeters.

Static cold atom accelerometers

In this section, a non-exhaustive list of sensors operating in static environment will be presented. A static environment is most of the time the Earth surface and the sensor aims to measure the Earth gravity field. Such sensors operate in regular laboratories or low-vibration environments such as underground laboratories but also in less protected environments for mobile sensors.

Laboratory instruments

Laboratory sensors were the first cold atom sensors developed and aim for important stability and low uncertainty. Thus, the interrogation time have to be as large as possible. This can be achieved by launching the atoms in a fountain configuration [24] or by increasing the height of the interferometer up to 10 m [72, 73]. Table 1 sums up the characteristics and performances of a few lab accelerometers. The Stanford gravimeter was one of the first cold atom sensor to display interesting performances. The vast majority of sensors implements a Mach-Zehnder interferometer for its sensitivity to inertial forces.

Reference	Characteristics	Sensitivity ($m/s^2/Hz^{1/2}$)	Stability ($m\,s^{-2}$)	Uncertainty ($m\,s^{-2}$)
Stanford University (Stanford) [24, 74]	MZ-Raman Fountain (T=160 ms) molasses source	1.7×10^{-7}	1×10^{-8} (2000 s)	3.4×10^{-8}
Huazhong (Wuhan) [75]	MZ-Raman Fountain (T=300 ms) molasses source	4.2×10^{-8}	3×10^{-9} (300 s)	X
SYRTE (Paris) [76]	MZ-Raman Free fall (T=80 ms) BEC-like evaporative source	5.6×10^{-8}	1×10^{-9}	1.3×10^{-8}
Australian National University (Canberra) [77]	MZ-Bragg Free fall (T=60 ms) molasses source	6×10^{-7}	2.7×10^{-8} (1000 s)	X

Table 1: Performances of static laboratory cold atom accelerometers (non-exhaustive list).

Mobile instruments

Once the proof was made of the performances of cold atom accelerometers, mobile sensors started to be developed. Such sensors aim to measure out of the lab either for comparison campaigns in low noise environments [78] or in less protected environments on a volcano side for example [79] for geosciences applications. Mobile sensors can be transported from one measure site to another but cannot be operate in a dynamical environment. They are usually more compact than lab sensors with the use of fibre laser system and free fall configurations. Field operated sensors like [80] also have shorter interrogation times. Table 2 presents some mobile gravimeters developed around the world.

Reference	Characteristics	Sensitivity ($m/s^2/Hz^{1/2}$)	Stability ($m\,s^{-2}$)	Uncertainty ($m\,s^{-2}$)
SYRTE (Paris) [78, 81]	MZ-Raman Free fall (T=80 ms) Molasses source	5.7×10^{-8}	2×10^{-9} (2000 s)	4.3×10^{-8}
National Institute of Metrology (Beijing) [82]	MZ-Raman Free fall (T=70 ms) Molasses source	4.4×10^{-7}	2×10^{-9} (30 000 s)	5.2×10^{-8}
University of California (Berkeley) [83]	MZ-Raman Free fall (T=130 ms) Molasses source	3.7×10^{-7}	2×10^{-8} (1800 s)	4×10^{-7}
Humboldt University (Berlin) [84]	MZ-Raman Fountain (T=260 ms) Molasses source	9.6×10^{-8}	5×10^{-10} (1×10^{5} s)	3.9×10^{-8}
Exail (Bordeaux) [80, 85]	MZ-Raman Free fall (T=60 ms) Molasses source	7.5×10^{-7}	1×10^{-8} (1×10^{4} s)	X
Huazhong University (Wuhan) [86]	MZ-Raman Free fall (T=200 ms) Molasses source	2.4×10^{-7}	5×10^{-9} (2000 s)	3×10^{-8}

Table 2: Performances of static transportable cold atom accelerometers (non-exhaustive list).

Static sensors currently compete with state-of-the-art absolute classical gravimeters such as free fall cube corner gravimeters. Such gravimeters take advantage of the free fall of a cube corner to measure the gravity with an optical Mach-Zehnder interferometer [65]. In [78], an atomic gravimeter and a commercial cube corner gravimeter FG5 were compared. The atomic sensor has a higher repetition rate than the FG5: its average signal reaches a lower level more quickly. The $1 \times 10^{-8}\,m\,s^{-2}$ level was reached in 36 s for the atomic gravimeter and 86 s for the FG5. Moreover, using atoms as a test mass avoids any deterioration of mechanical parts and atomic gravimeters do not need to be calibrated. The level of vibration can limit the stability of gravimeter which is why comparison campaigns are performed in underground labs. Currently, the uncertainty of atomic sensors are limited either by the Earth rotation induced Coriolis acceleration or by wave-front aberrations of the Raman laser.

Onboard cold atoms accelerometers

A last type of atomic accelerometers was developed in the last decade aiming to be boarded on moving platforms for marine or airborne measurements. A sensor able to operate in dynamical environments have many applications such as Earth gravity maps or ground correlation navigation. Nevertheless, onboard sensors have to sustain important rotation rates and horizontal accelerations. Until now, gyro-stabilised platform have been used to protect the gravimeter from the carrier movement [1, 87, 88]. This type of instruments were able to perform marine measurements as displayed on Figure 13. Shorter interrogation times also have to be performed in dynamically operated sensors as can be seen in Table 3. The case of [89] is a bit different as the sensor was operated in micro-gravity paving the way for spatial applications. If no atomic interferometers have been operated in space either on a satellite or space stations, many theoretical [29] or preliminary experimental [36, 37] studies have been performed. This work belongs to this research topic.

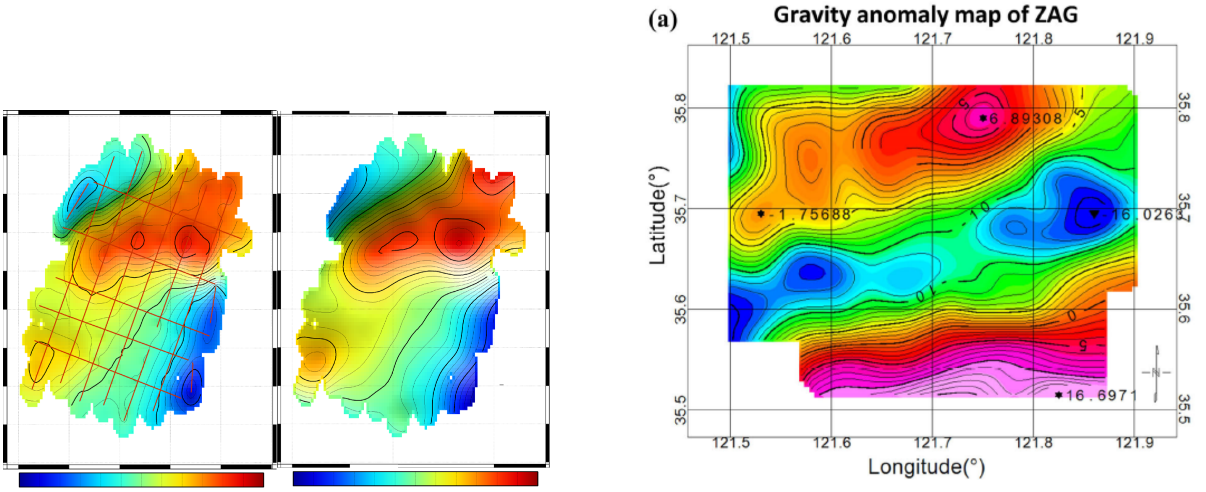

(a) Gravity anomaly off the coast of Bretagne in France measured by the GIRAFE 2 gravimeter from [1]. The red lines correspond to the atomic measurements. Right: model obtained from shipborne atom gravimeter measurements. The red lines are the profiles on which the gravity was measured. Left: model obtained from satellite measurements.

(b) Gravity anomaly in the Yellow Sea of China measured by an atomic gravimeter aboard a marine geological ship from [88].

Figure 13: Marine measurements of atomic gravimeters.

Reference	Characteristics	Sensitivity ($m/s^2/Hz^{1/2}$)	Stability ($m\,s^{-2}$)	Uncertainty ($m\,s^{-2}$)
ONERA (Palaiseau) [1, 87]	MZ-Raman Free fall (T=20 ms) Molasses source marine and airborne measurements	8×10^{-6}	X	1.7×10^{-6}
Zhejiang University (Hangzhou) [88]	MZ-Raman Free fall (T=20 ms) Molasses source marine measurements	2×10^{-6}	X	7×10^{-6}
LP2N (Bordeaux) [89]	MZ and 4 pulses interferometer-Raman Free fall (T=10 ms for MZ) velocity selected molasses source (300 nK) 0g plane measurements with an horizontal accelerometer	2×10^{-4}	X	X

Table 3: Static performances of onboard cold atom accelerometers (non-exhaustive list).

Cold atoms sensors and the impact of rotation

The cross-talk between acceleration and rotation is well known and can be explained by the presence of inertial forces which create a pseudo acceleration due to the rotation. Let's consider an inertial frame $\mathfrak{R}$ and a rotating frame $\mathfrak{R}'$ both centred in O . The acceleration of a body M in the rotating frame is:

$$\vec{a}(M)_{(\mathfrak{R}')} = \vec{a}(M)_{(\mathfrak{R})} - 2\vec{\Omega} \wedge \vec{v}(M)_{(\mathfrak{R}')} - \vec{\Omega} \wedge \vec{\Omega} \wedge \overrightarrow{OM} - \dot{\vec{\Omega}} \wedge \overrightarrow{OM} \tag{1}$$

with $\vec{a}(M)_{(\mathfrak{R})}$ the acceleration in the inertial frame resulting from the forces applied to the body, $\vec{v}(M)_{(\mathfrak{R}')}$ the velocity in the rotating frame and $\vec{\Omega}$ the rotation vector of $\mathfrak{R}'$ around $\mathfrak{R}$. The pseudo accelerations are usually labelled as Coriolis acceleration $-2\vec{\Omega} \wedge \vec{v}(M)_{(\mathfrak{R}')}$, Centrifugal acceleration $-\vec{\Omega} \wedge \vec{\Omega} \wedge \overrightarrow{OM}$ and Angular acceleration $-\dot{\vec{\Omega}} \wedge \overrightarrow{OM}$. Hence, any accelerometers measuring the acceleration of a rotating body will also measure the pseudo accelerations in addition to the acceleration resultant of the forces acting on the body. The case of atomic accelerometer is slightly different as the action of rotation will also result in a loss of sensitivity. The contrast of a rotating interferometer will indeed diminish due to the velocity and position dispersion of the atomic cloud used as proof-mass.

The effect of the Earth rotation was noticed in the first atomic gravimeters and can be a limiting parameter of the uncertainty due to the Coriolis systematic effect [24]. Then, the focus was on the reduction of the Coriolis systematic effect and several methods were tested. In [90], the laser retro-reflection mirror was mounted on tip-tilt piezo actuator to compensate the Earth rotation by rotating the mirror enabling the reduction of the uncertainty on the gravimeter measurement. The same approach was implemented on a large space-time area interferometer in [3]. Due to the important momentum transfer allowed by the Bragg transitions and the long interrogation time, the Earth rotation induced an important contrast loss. The mirror rotation improved the contrast up to 350% and the removal of the Coriolis systematic effect. The mirror was also rotated thanks to a tip-tilt mount for the Weak Equivalence Principle interferometric test in [91] to reduce the Coriolis error term and improve the contrast in a double diffraction scheme. This method can even be implemented in point source interferometers [92]. A slightly different approach is considered for long baseline interferometry dedicated to gravitational waves detection. [93] proposed to rotate the laser beam around a tunable point to prevent an important separation between the incoming and the reflected laser beams. In [94], a different approach was chosen to evaluate the Coriolis effect on the gravimeter measurement. As the sensor was mobile, its orientation could be rotated of 180°. This manipulation changes the sign of the Coriolis induced phase shift allowing its measurement. The Coriolis bias can then be removed from the acceleration measurement.

The effect of the carrier rotation is also a problem for onboard sensors. Moreover the rotation rates encountered are larger than the Earth rotation rate. For onboard gravimeters, the problem was solved with the use of gyrostabilised platforms [1, 88]. Prospective studies have been conducted to use a tip-tilt mirror to compensate the carrier rotation either for terrestrial applications [42] or space applications [95]. The last study even proposes to rotate the incoming laser beam to further diminish the Centrifugal acceleration. The rotation problem is quite similar in atomic gyroscope even if the rotation rate is the parameter to be measured. [96] used the tip-tilt compensation method to recover the contrast and extend the gyroscope measurement range. An interesting method was implemented in [97] by generating a pseudo rotation with the two-photon Raman detuning to compensate the sensor rotation. The contrast was recovered while measuring the rotation rate and expanding the dynamic range of the sensor. Nevertheless, this method can only be implemented in thermal beam sensors.

Present work

Organisation of the research work

This PhD manuscript presents the research study performed on the hybrid lab prototype in order to study and mitigate the impact of rotation. The work conducted was mostly experimental associated with theoretical modelling of the rotating sensor in the lab. Some simulations of a space sensor were also conducted to assess the performances onboard a satellite.

The experimental setup used in this work was originally built to study the hybridisation of the electrostatic and atomic accelerometer [30]. For this study, the electrostatic and atomic sensors were closely linked as the laser interrogating the atoms was reflected on the EA proof-mass. Here, this property was used to compensate the sensor rotation. The EA was designed by the IEA unit in Châtillon and is close to space EA design. Some differences reside in the design to sustain the Earth gravity and to allow the laser to be reflected on the proof-mass. The atomic sensor head was reused from the first ONERA gravimeter GIRAFE 1 [98] while the laser system was designed and built during the PhD of Clément Diboune. The laser system is completely fibered and can manipulate three atomic species: ^{87}Rb, ^{85}Rb and ^{133}Cs [99]. In this work, only the laser dedicated to the manipulation of ^{87}Rb was used.

The first step of this work consisted in the improvement of the laser system. Some temporal variations of the laser intensity and spectral power distribution had been observed and induced a variation of the interferometer contrast. To solve this issue, closed-loop lock systems were added to the laser system. Afterwards, the first experiments of the mirror rotation were performed. At the beginning, only the contrast of the interferometer could be measured, as the electrostatic levitation of the proof-mass and the use of the passive vibration isolation platform was difficult to achieve. After several steps of alignment and calibration of the EA capacitive detection both contrast and phase shift were measured. These measurements were important to the understanding of the mirror rotation impact on the interferometer. They also led to improve the knowledge of the atomic cloud kinetic parameters. Then, the whole sensor was rotated. This step was also challenging as the different parts of the setup: the table supporting the sensor, the isolation platform and the EA had to be parallel and perpendicular to the gravity direction. Moreover, the sensor rotation and the isolation platform made the EA levitation difficult. The contrast and phase shift were studied only in the presence of the sensor rotation then the compensation was implemented. Lastly, during a two month stay at ESTEC (European Space Research and Technology Centre), the ESA research centre in the Netherlands, a theoretical study of space performances of the rotation compensated atomic accelerometer was carried out.

Layout of the present manuscript

In this manuscript, the work carried out in this PhD work is presented as follows:
Chapter 1 is a theoretical Chapter presenting the information necessary to understand the atomic interferometer principle of operation for measure acceleration. The impact of the rotation on the interferometer is also analysed.
Chapter 2 contains the description of the experimental setup: the atomic interferometer and the electrostatic accelerometer are described as well as the improvements made to the atomic interferometer during the PhD work. The experimental methods implemented to collect and process the experimental data are also described.
In **Chapter 3**, the impact of the rotation of the EA accelerometer acting as an actuated retro-reflection mirror is experimentally studied. In particular, this study enables us to gain a better understanding of the effects induced by the mirror rotation. Moreover, the excellent control of the mirror rotation provides a way to characterize the kinetic parameters of the atomic cloud.
In **Chapter 4**, the impact of the sensor rotation and its compensation were studied for constant and time-dependent rotation rates. The results of the rotation compensation implementation are presented for several case studies.
Chapter 5 aims to give a preliminary budget performance of a rotation compensated atomic accelerometer boarded on a satellite. A nadir-pointing gravimetry satellite boarding an atomic accelerometer is considered.
Lastly, the conclusion will give an overview of the PhD work as well as some perspectives to this work.

CHAPTER 1

Theory of atomic interferometry for inertial sensing

Outline of the current chapter

Introduction

The principle of atomic interferometry is based upon the wave-particle duality: an atom can be described as a wave function expressing the presence probability amplitude [100]. In an atomic interferometer, the atom is in a coherent state superposition between the two arms of the interferometer: the amplitude probability of the atom is divided between the two arms. At the end of the interferometer, the two arms are recombined and an interference phenomenon appears: an atomic interferometer is an interferometer of amplitude division [101]. As the state superposition is created by a light-driven transition, the momentum of the atom varies during the interferometer. Thereby, phase shift between the two arms of the interferometer can be sensitive to inertial forces in some configurations. Atomic interferometry can be a tool to implement an accelerometer [24, 54]. Nevertheless, the rotation of such a sensor can lead to a deterioration of the acceleration measurement [3, 95].

In this Chapter, the building blocks of a Mach-Zehnder atomic interferometer are presented such as the dynamics of two-photon transitions used as optics for atoms. Then, the interferometer is described globally and its phase shift is computed from the point of view of an atomic accelerometer. Finally, the detrimental impacts of the sensor rotation on the interferometer is examined. A method to reduce those detrimental effects is studied theoretically by rotating the mirror in the opposite way of the sensor. A numerical method to compute the phase shift and contrast of the rotating interferometer is also introduced.

1.1 Two photons Raman transitions

To implement the atomic interferometer, two-photon Raman transitions are used to put the atom in a coherent superposition between two atomic states. The two photons Raman transition changes the momentum and the internal state of the atoms thus implementing "state labelling" presented in [55]. This technique eases the detection as detecting the internal states is easier than detecting the external states. Indeed, to detect an external state, it is necessary to wait for a spatial separation. The state labelling is an advantage of Raman transitions and is not possible with Bragg transitions [102] for example as Bragg transitions do not change the atom internal state.

Two-photon Raman transition give a large recoil momentum greater than the associated microwave transition. This important recoil increases the space-time area of the interferometer and thus its sensitivity to inertial effects such as acceleration, gravity, rotation and gravity gradient. The alkali atoms are particularly well adapted to implement such transitions as they only have one electron on the external energy level. Moreover, their ground states have a long live-time. In this work, the energy levels of the D_2 line of the Rubidium 87 are coupled with a laser at 780 nm.

1.1.1 Three level atom

Let's consider a three level atom of mass m in interaction with an electro-magnetic field. Two stable states $|e\rangle$ and $|f\rangle$ and an intermediate state $|c\rangle$ are coupled with an electro-magnetic field. The electro-magnetic field results in two counter-propagating laser beams with two different frequencies. Their wave vectors and pulsations are $(\overrightarrow{k_l}, \omega_l)$ with $l \in \{1, 2\}$. The two corresponding electric fields can be written as a plane wave (Equation 1.1).

$$\overrightarrow{\hat{E_l}}\left(\overrightarrow{\hat{r}}, t\right) = E_l \exp\left(i(\omega_l t - \overrightarrow{k_l}.\overrightarrow{\hat{r}} + \phi_l(t))\right)\overrightarrow{\hat{\epsilon_l}} + c.c. \tag{1.1}$$

with $\hat{\overrightarrow{\epsilon_l}}$ the polarisation, $\hat{\overrightarrow{r}}$ the position operator and $\phi_l(t)$ the laser beam phase.

The two stable atomic states $|e\rangle$ and $|f\rangle$ are coupled with an intermediate state $|c\rangle$ of natural width Γ through the electromagnetic field. The laser frequency difference $\omega_1 - \omega_2$ is close to the frequency difference between the two stable states $|e\rangle$ and $|f\rangle$. The one-photon transition is detuned by a frequency Δ from the intermediate level $|c\rangle$ (Equation 1.2). This Raman detuning is larger than the natural width $\hbar\Delta \gg \hbar\Gamma$ to limit the spontaneous emission from the intermediate state $|c\rangle$ [103].

$$\Delta = \omega_1 - (\omega_c - \omega_f) \tag{1.2}$$

Momentum transfer

As represented on Figure 1.1a, the Raman transition transfers the atom from a state $\left|f, \overrightarrow{p}\right\rangle$ to a state $\left|e, \overrightarrow{p} + \hbar\overrightarrow{k_{\mathrm{eff}}}\right\rangle$. The momentum $\hbar\overrightarrow{k_{\mathrm{eff}}}$ is transferred to the atom with $\overrightarrow{k_{\mathrm{eff}}}$ the effective wave vector of the two-photon transition:

$$\overrightarrow{k_{\mathrm{eff}}} = \overrightarrow{k_1} - \overrightarrow{k_2} \tag{1.3}$$

As described on Figure 1.1b, the photon of pulsation ω_1 is absorbed: a momentum $\overrightarrow{k_1}$ is transferred to the atom. The photon at ω_2 generates a stimulated emission at the same frequency: a momentum $-\overrightarrow{k_2}$ is transferred to the atom. The total transferred momentum is now $\overrightarrow{k_{\mathrm{eff}}}$. A change in the external state is now associated with a change of the internal state of the atom.

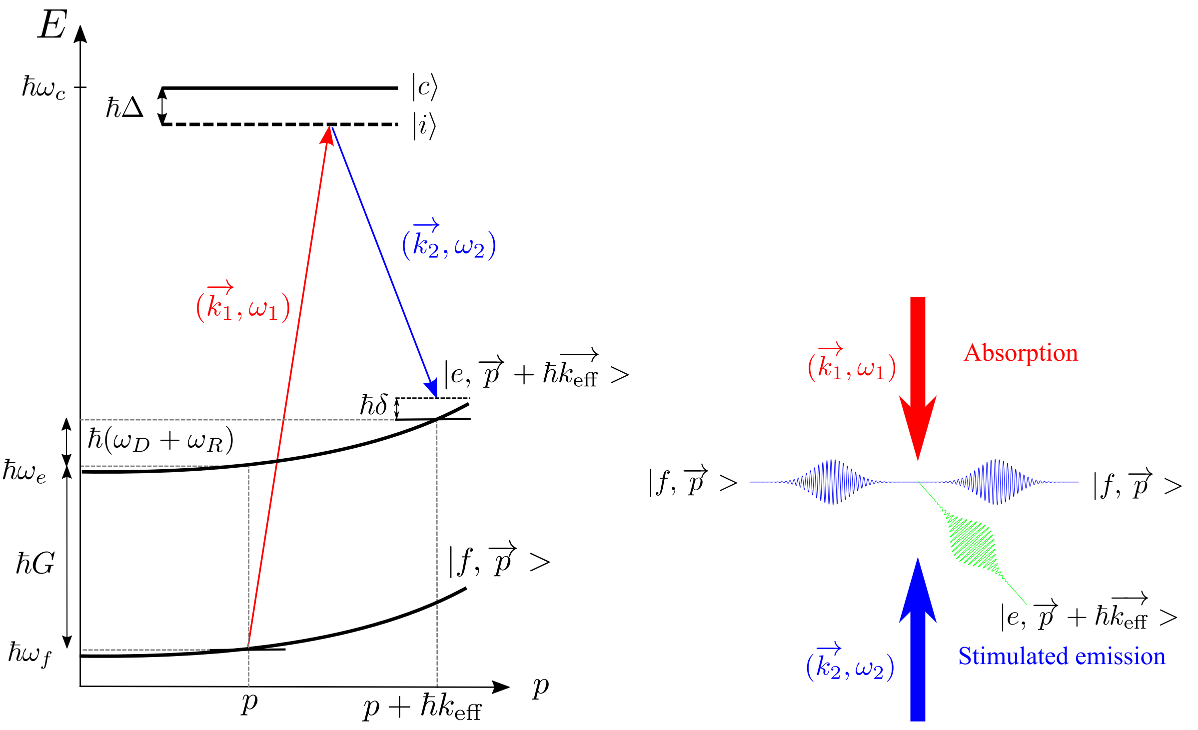

(a) Energy diagram of a three levels atom. The photons at a frequency ω_1 and ω_2 address a transition between the stable states $\left|f, \overrightarrow{p}\right\rangle$ and $\left|e, \overrightarrow{p} + \hbar\overrightarrow{k_{\mathrm{eff}}}\right\rangle$ through an intermediate state $|c\rangle$.

(b) Momentum transfer from the photons to the atom during a two-photon transition.

Figure 1.1: Description of the two-photon Raman transition.

Resonance condition

According to the energy conservation for the transition $\left|f,\vec{p}\right\rangle \rightarrow \left|e,\vec{p}+\hbar\overrightarrow{k_{\text{eff}}}\right\rangle$ and neglecting the light-shifts and the Zeeman effect, Equation 1.4 has to be respected for the transition to be efficient.

$$\hbar\omega_1 + \hbar\omega_f + \frac{\vec{p}^{\,2}}{2m} = \hbar\omega_2 + \hbar\omega_e + \frac{(\vec{p}+\hbar\overrightarrow{k_{\text{eff}}})^2}{2m} \tag{1.4}$$

The detuning δ of the two-photon transition can be written has:

$$\delta = (\omega_1 - \omega_2) - G - \omega_R - \omega_D \tag{1.5}$$

with $G = \omega_e - \omega_f$ the frequency of the transition between the two stable states, $\omega_R = \frac{\hbar k_{\text{eff}}^2}{2m}$ the recoil frequency associated to the Raman transition and $\omega_D = \frac{\vec{p}.\overrightarrow{k_{\text{eff}}}}{m}$ the Doppler detuning. The resonance condition is verified if $\delta = 0$. Experimentally, the frequency difference between the two lasers $(\omega_1 - \omega_2)$ is tuned to compensate the Doppler and recoil frequency.

1.1.2 Dynamics of a Raman transition

The system temporal evolution during the interaction between the atom and the electromagnetic fields, can be studied by solving the Schrödinger equation:

$$i\hbar\frac{\partial|\Psi(t)\rangle}{\partial t} = \left(\hat{H}_A + \hat{H}_{int}\right)|\Psi(t)\rangle \tag{1.6}$$

with $|\Psi(t)\rangle$ the state vector of the system. The system Hamiltonian is the sum of the atomic Hamiltonian and the interaction Hamiltonian. The atomic Hamiltonian (Equation 1.7) involves the three atomic states and the movement of the atom centre-of-mass.

$$\hat{H}_A = \frac{\hat{\vec{P}}^2}{2m} + \hbar\omega_f|f\rangle\langle f| + \hbar\omega_e|e\rangle\langle e| + \hbar\omega_c|c\rangle\langle c| \tag{1.7}$$

The interaction Hamiltonian characterises the interaction between the atom and the electric fields:

$$\hat{H}_{int} = -\hat{\vec{d}}.\left(\hat{\overrightarrow{E_1}}\left(\hat{\vec{r}},t\right) + \hat{\overrightarrow{E_2}}\left(\hat{\vec{r}},t\right)\right) \tag{1.8}$$

with $\hat{\vec{d}}$ the operator electrical dipolar moment.

To express the coupling between the stable states $|e\rangle$ or $|f\rangle$ and the intermediate state $|c\rangle$ through the laser, the Rabi pulsations can be defined:

$$\Omega_{j,l} = -\frac{2E_l}{\hbar}\langle c|\,\hat{\vec{d}}.\hat{\vec{\epsilon_l}}\,|j\rangle \tag{1.9}$$

with $j \in \{e,f\}$ and c the atomic states and $l \in \{1,2\}$ the electric field.

As the Raman detuning Δ is very large compared to the Rabi pulsations and the natural linewidth Γ of the transition, the intermediate state $|c\rangle$ is almost not populated and the spontaneous emission can be neglected. Moreover, as the stable states have a very long lifetime, the coherence of the state superposition is not limited by the linewidth Γ. Thus, the intermediate state $|c\rangle$ can be eliminated adiabatically as demonstrated in [101]. The system can then be reduced to a two-level system: $\left\{\left|f,\vec{p}\right\rangle, \left|e,\vec{p}+\hbar\overrightarrow{k_{\text{eff}}}\right\rangle\right\}$ coupled by the Raman transition. Therefore, an effective Rabi pulsation characterising the coupling between $|f\rangle$ and $|e\rangle$, can be defined:

$$\Omega_{\text{eff}} = \frac{\Omega_{f,1}\Omega_{e,2^*}}{2\Delta} \tag{1.10}$$

The wave function $|\Psi(t)\rangle$ can be expressed in the basis $\{\left|f,\overrightarrow{p}\right\rangle,\left|e,\overrightarrow{p}+\hbar\overrightarrow{k_{\text{eff}}}\right\rangle\}$:

$$|\Psi(t)\rangle = C_f(t)\left|f,\overrightarrow{p}\right\rangle + C_e(t)\left|e,\overrightarrow{p}+\hbar\overrightarrow{k_{\text{eff}}}\right\rangle \tag{1.11}$$

with C_f and C_e complex numbers associated to the presence probability of each state. The resolution of Equation 1.6 gives the temporal evolution of the system and can be found in [101]. The temporal evolution from an initial state $|\Psi(t)\rangle$ can be written as an evolution matrix $M(t,\tau,\varphi)$.

$$\begin{pmatrix} C_f(t+\tau) \\ C_e(t+\tau) \end{pmatrix} = M(t,\tau,\varphi)\begin{pmatrix} C_f(t) \\ C_e(t) \end{pmatrix} \tag{1.12}$$

The evolution matrix for an interaction of duration τ is the following:

$$M(t,\tau,\varphi) = \begin{pmatrix} \left[\cos\left(\frac{\Omega_R\tau}{2}\right) - i\cos\theta\sin\left(\frac{\Omega_R\tau}{2}\right)\right]e^{-i\bar{\omega}_f\tau} & -ie^{i[(\omega_1-\omega_2)t+\varphi]}\sin\theta\sin\left(\frac{\Omega_R\tau}{2}\right)e^{-i\bar{\omega}_f\tau} \\ -ie^{-i[(\omega_1-\omega_2)t+\varphi]}\sin\theta\sin\left(\frac{\Omega_R\tau}{2}\right)e^{-i\bar{\omega}_e\tau} & \left[\cos\left(\frac{\Omega_R\tau}{2}\right) + i\cos\theta\sin\left(\frac{\Omega_R\tau}{2}\right)\right]e^{-i\bar{\omega}_e\tau} \end{pmatrix} \tag{1.13}$$

In the resolution of Equation 1.6, the one-photon light-shifts induced by the two electric fields have to be computed:

$$\begin{aligned} \delta\omega_f &= \frac{|\Omega_{f,1}|^2}{4\Delta} + \frac{|\Omega_{f,2}|^2}{4(\Delta - G)} \\ \delta\omega_e &= \frac{|\Omega_{e,1}|^2}{4(\Delta + G)} + \frac{|\Omega_{e,2}|^2}{4\Delta} \end{aligned} \tag{1.14}$$

The differential δ^{LS1} and mean μ^{LS1} one-photon light shift can also be defined.

$$\begin{aligned} \delta^{LS1} &= \delta\omega_e - \delta\omega_f \\ \mu^{LS1} &= \delta\omega_e + \delta\omega_f \end{aligned} \tag{1.15}$$

The generalised Rabi frequency taking into account the one-photon light-shifts can be determined.

$$\Omega_R = \sqrt{\Omega_{\text{eff}}^2 + \left(\delta - \delta^{LS1}\right)^2} \tag{1.16}$$

To simplify the expression of the evolution matrix, the following expressions were introduced.

$$\begin{aligned} \cos\theta &= \frac{\delta - \delta^{LS1}}{\Omega_R} \\ \sin\theta &= \frac{|\Omega_{\text{eff}}|}{\Omega_R} \end{aligned} \tag{1.17}$$

$$\begin{aligned} \bar{\omega}_f &= \omega_f + \frac{\overrightarrow{p}^2}{2m\hbar} + \frac{\left(\mu^{LS1} - \delta\right)}{2} \\ \bar{\omega}_e &= \omega_e + \frac{\left(\overrightarrow{p} + \hbar\overrightarrow{k_{\text{eff}}}\right)^2}{2m\hbar} + \frac{\left(\mu^{LS1} + \delta\right)}{2} \end{aligned} \tag{1.18}$$

The laser phases are considered constant during the interaction of duration τ between the atom and the electromagnetic field. The Raman laser phase φ is defined as the difference between the phase of the two lasers: $\varphi = \phi_1 - \phi_2$.

For an initial system in a state $\left|f, \vec{p}\right\rangle$ interacting for a duration τ, the presence probabilities in each state can be computed thanks to the evolution matrix:

$$\begin{aligned} P_f(\tau) = |C_f(\tau)|^2 &= 1 - \frac{\Omega_{\text{eff}}^2}{\Omega_R^2} \sin^2\left(\frac{\Omega_R \tau}{2}\right) \\ P_e(\tau) = |C_e(\tau)|^2 &= \frac{\Omega_{\text{eff}}^2}{\Omega_R^2} \sin^2\left(\frac{\Omega_R \tau}{2}\right) \end{aligned} \tag{1.19}$$

Generalised resonance condition

The resonance condition presented in Section 1.1.1 can be improved by taking into account the one and two-photon light-shifts and the Zeeman effect. These effects shift the atomic levels due to the atom/laser interaction for the light-shifts and due to the atom/magnetic field interaction for the Zeeman effect. The differential shift between the levels considering these effects can be written as:

$$\delta^{\text{diff}} = \delta^{LS1} + \delta^{LS2} + \delta^{Z} \tag{1.20}$$

with δ^{LS1} the one-photon light-shift, δ^{LS2} the two-photon light-shift and δ^{Z} the shift due to the Zeeman effect. Due to the light shifts and the Zeeman effect, the resonance condition of Equation 1.5 can be corrected and the generalised resonance condition is now:

$$\delta = \delta^{\text{diff}} = (\omega_1 - \omega_2) - G - \omega_R - \omega_D \tag{1.21}$$

The shift of the atomic level due to the Zeeman effect can be limited by choosing a hyperfine sub-level $m_F = 0$ which is insensitive to the first order Zeeman effect [100, 104]. The one-photon light shift can be cancelled experimentally by carefully tuning the Raman laser spectrum (see Section 1.1.3 and [103]). Moreover, the residual Zeeman and one-photon light shifts can be cancelled at the end of the interferometer by alternately changing the direction of the effective wave vector $\overrightarrow{k_{\text{eff}}}$: the sign of these two light-shifts depends on the sign of $\overrightarrow{k_{\text{eff}}}$. The two-photon light shift cannot be cancelled and impacts the phase shift of the interferometer. For a more exhaustive treatment see [105, 106].

One photon light-shift

The photon light shift is provoked by the atom/light interaction and thus depends on the laser spectrum power distribution. The hyperfine levels $|f\rangle$ and $|e\rangle$ are shifted from a mean light-shift $\overline{\Omega_f}$ and respectively $\overline{\Omega_e}$ as can be seen on Figure 1.2. As both levels are shifted, the relevant value for the resonance condition is the mean differential light-shift $\delta^{LS1} = \overline{\Omega_e} - \overline{\Omega_f}$. As the light-shift depends on the laser power distribution, a well-chosen spectrum can cancel the differential light shift. Figure 1.2 represents the hyperfine structure of the D_2 line of the Rubidium 87 and the laser frequencies accounted for during the Raman transition. The frequencies ω_1 and ω_2 realise the two-photon transition. The frequency $\omega_2 = \omega_0$ is the carrier frequency of the modulated laser. As the laser is phase modulated at ω_m several side-bands are present in the laser spectrum. The first order modulated frequency $\omega_1 = \omega_0 + \omega_m$ is used to perform the Raman transition. The modulation also creates many frequencies which are not used in the Raman transition in the considered case. In this work, only the first order modulated frequencies are considered and the other first order modulated frequency $\omega_p = \omega_0 - \omega_m$ is called the parasite frequency. For more information on the laser system see Chapter 2. The different frequency differences are defined as algebraic numbers ($\Delta < 0$, $\Delta_2 > 0$, $G > 0$ et $\Delta_3 > 0$) and the reference level is F'=1 ($\Delta_1 = 0$). Δ the Raman detuning, is a parameter of the experiment and the energy splittings between the atomic levels can be found in [107].

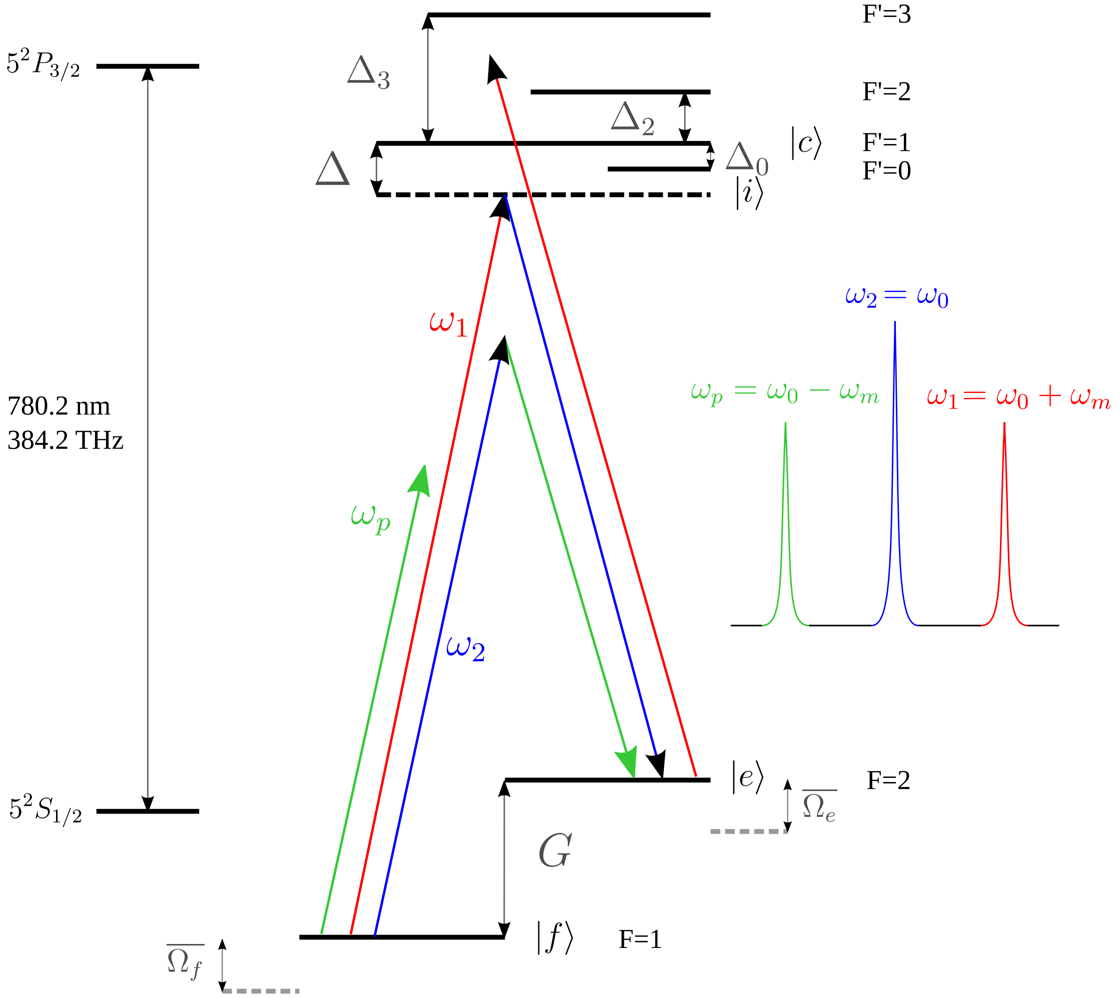

Figure 1.2: Rubidium 87 D2 line structure and frequencies of a Raman pulse. ω_1 and ω_2 are the frequencies of the two-photon Raman transition. ω_p is a parasite frequency due to the laser modulation. The energy diagram is not to scale.

The one photon light-shift can be expressed as a function of the Rabi frequency and the detuning for each laser frequency ω, each atomic sub-level k of $5^2P_{3/2}$ and each polarisation σ [103,108].

$$\begin{aligned} \overline{\Omega_f} &= \sum_k \sum_\omega \sum_{\sigma=\pm1} \frac{|\Omega_{kf\omega\sigma}|^2}{4\delta_{fk\omega}} \\ \overline{\Omega_e} &= \sum_k \sum_\omega \sum_{\sigma=\pm1} \frac{|\Omega_{kf\omega\sigma}|^2}{4\delta_{ek\omega}} \end{aligned} \tag{1.22}$$

The Rabi frequency is expressed as:

$$\begin{aligned}\Omega_{mk\omega\sigma} &= -\frac{1}{\hbar}\left\langle 5^2P_{3/2}F' = k\middle|d.\hat{e}.E_{\omega\sigma}\middle|m\right\rangle \\ &= \Omega_{\omega\sigma}\left\langle k|m\right\rangle\end{aligned} \tag{1.23}$$

with m=e or f, $\Omega_{\omega\sigma} = \frac{2DE_{\omega\sigma}}{\hbar}$ the simplified Rabi frequency, $E_{\omega\sigma}$ the amplitude of the electric field at a frequency ω and polarisation σ and $\langle k|m\rangle$ the Clebsch-Gordan coefficient of the transition. As the Raman laser has a $lin \perp lin$ polarisation, each linear polarisation have to be decomposed on the σ^+ and σ^- circular polarisations. The values of the detunings $\delta_{fk\omega}$ of Equation 1.22 are the following:

- $\delta_{fk1} = \Delta - \Delta_k$
- $\delta_{fk2} = -G + \Delta - \Delta_k$
- $\delta_{fkp} = -2G + \Delta - \Delta_k$
- $\delta_{ek1} = G + \Delta - \Delta_k$
- $\delta_{ek2} = \Delta - \Delta_k$
- $\delta_{ekp} = -G + \Delta - \Delta_k$

Considering a three laser frequencies interacting with the D_2 line of the Rubidium, the one photon light-shifts can be expressed as a function of the different detunings:

$$\begin{aligned}\overline{\Omega_f} &= \frac{\Omega_1^2}{4}\left[\frac{5}{24(\Delta)} + \frac{1}{8(\Delta-\Delta_2)}\right] + \frac{\Omega_2^2}{4}\left[\frac{5}{24(\Delta-G)} + \frac{1}{8(\Delta-G-\Delta_2)}\right] \\ &+ \frac{\Omega_p^2}{4}\left[\frac{5}{24(\Delta-2G)} + \frac{1}{8(\Delta-\Delta_2-2G)}\right] \\ \overline{\Omega_e} &= \frac{\Omega_1^2}{4}\left[\frac{1}{120(\Delta+G)} + \frac{1}{8(\Delta-\Delta_2)} + \frac{1}{5(G+\Delta-\Delta_3)}\right] + \frac{\Omega_2^2}{4}\left[\frac{1}{120(\Delta)} + \frac{1}{8(\Delta-\Delta_2)} + \frac{1}{5(\Delta-\Delta_3)}\right] \\ &+ \frac{\Omega_p^2}{4}\left[\frac{1}{120(\Delta-G)} + \frac{1}{8(\Delta-\Delta_2-G)} + \frac{1}{5(\Delta-G-\Delta_3)}\right]\end{aligned} \tag{1.24}$$

For clarity's sake, the one photon light-shifts can be written in a simplified form with the coefficients $\alpha_{m\omega}$.

$$\begin{aligned}\overline{\Omega_f} &= \alpha_{f1}\frac{\Omega_1^2}{4} + \alpha_{f2}\frac{\Omega_2^2}{4} + \alpha_{fp}\frac{\Omega_p^2}{4} \\ \overline{\Omega_e} &= \alpha_{e1}\frac{\Omega_1^2}{4} + \alpha_{e2}\frac{\Omega_2^2}{4} + \alpha_{ep}\frac{\Omega_p^2}{4}\end{aligned} \tag{1.25}$$

To cancel the differential one photon light-shift, the light shifts of the level f and e have to be equal: $\overline{\Omega_f} = \overline{\Omega_e}$. Moreover, the Rabi frequencies depend on the electric field of each frequency component: $\Omega_1 = \frac{2DE_1}{\hbar}$, $\Omega_2 = \frac{2DE_2}{\hbar}$ and $\Omega_p = \frac{2DE_p}{\hbar}$. The electrical fields of the components ω_1 and ω_p, are expected to have the same amplitude and intensity: $E_1 = E_p$ and $I_1 = I_p$. An intensity ratio R cancelling the differential one-photon light shift can be found:

$$R = \frac{I_1}{I_2} = \frac{\alpha_{f2} - \alpha_{e2}}{\alpha_{e1} + \alpha_{ep} - \alpha_{f1} - \alpha_{fp}} \tag{1.26}$$

This intensity ratio R depends on the Raman detuning Δ as can be seen on Figure 1.3. The choice of the detuning Δ is a trade-off between an important Rabi frequency and a small spontaneous emission. In this work, the detuning was fixed to -1 GHz. The optimal ratio is slightly different considering the parasite frequency or not as shown by Equation 1.26. For $\Delta = -1\,\mathrm{GHz}$, in the absence of the a parasite frequency ω_p, the optimal ratio is $R = 0.57$. Considering the parasite frequency, the optimal ratio becomes 0.6.

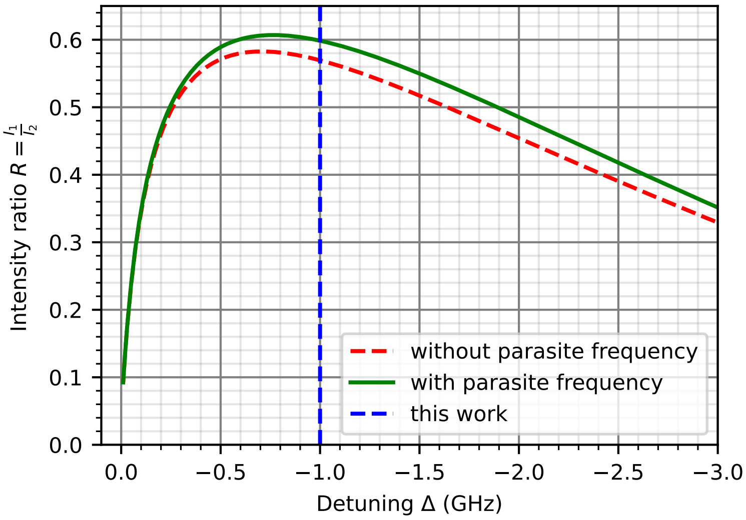

Figure 1.3: Intensity ratio R cancelling the one photon light-shift as a function of the Raman detuning Δ.

1.1.3 Atomic mirror and beamsplitter

To implement an atomic Mach-Zehnder interferometer, atomic beamsplitters and mirrors are needed to manipulate the wave packet. By tuning the laser pulse duration, the laser/atom interaction can put the wave packet in a state superposition or redirecting the wave packet creating an atomic beamsplitter or an atomic mirror. Let's consider the resonance condition true: the evolution matrix of Equation 1.13 can be simplified as $\delta = \delta^{\mathrm{diff}}$ and $\Omega_R = |\Omega_{\mathrm{eff}}|$.

$$M(t,\tau,\varphi) = \begin{pmatrix} \cos\left(\frac{\Omega_{\mathrm{eff}}\tau}{2}\right) e^{-i\bar{\omega}_f\tau} & -ie^{i[(\omega_1-\omega_2)t+\varphi]}\sin\left(\frac{\Omega_{\mathrm{eff}}\tau}{2}\right) e^{-i\bar{\omega}_f\tau} \\ -ie^{-i[(\omega_1-\omega_2)t+\varphi]}\sin\left(\frac{\Omega_{\mathrm{eff}}\tau}{2}\right) e^{-i\bar{\omega}_e\tau} & \cos\left(\frac{\Omega_{\mathrm{eff}}\tau}{2}\right) e^{-i\bar{\omega}_e\tau} \end{pmatrix} \tag{1.27}$$

Atomic beamsplitter

To create an atomic beamsplitter, the duration τ of the atom/light interaction has to be chosen to have an equiprobability between the states $\left|e, \overrightarrow{p} + \hbar\overrightarrow{k_{\mathrm{eff}}}\right\rangle$ and $\left|f, \overrightarrow{p}\right\rangle$. The duration of a beamsplitter $\tau_{\frac{\pi}{2}}$ can be chosen as a quarter of a Rabi oscillation (Figure 1.4a): $\tau_{\frac{\pi}{2}} = \frac{\pi}{2\Omega_{\mathrm{eff}}}$. In these conditions, the evolution matrix becomes:

$$M_{\frac{\pi}{2}}(t,\tau_{\frac{\pi}{2}},\varphi) = \frac{1}{\sqrt{2}}\begin{pmatrix} e^{-i\bar{\omega}_f\tau_{\frac{\pi}{2}}} & -ie^{i[(\omega_1-\omega_2)t+\varphi]-i\bar{\omega}_f\tau_{\frac{\pi}{2}}} \\ -ie^{-i[(\omega_1-\omega_2)t+\varphi]-i\bar{\omega}_e\tau_{\frac{\pi}{2}}} & e^{-i\bar{\omega}_e\tau_{\frac{\pi}{2}}} \end{pmatrix} \tag{1.28}$$

After a beamsplitter pulse, for an initial state $\left|f, \overrightarrow{p}\right\rangle$, the atom ends in a coherent superposition $\frac{1}{\sqrt{2}}\left(\left|f, \overrightarrow{p}\right\rangle + \left|e, \overrightarrow{p} + \hbar\overrightarrow{k_{\mathrm{eff}}}\right\rangle\right)$ (Figure 1.4b). The beamsplitter pulse is used to divide the wave packet at the beginning of the interferometer and to recombine the wave packet at the end.

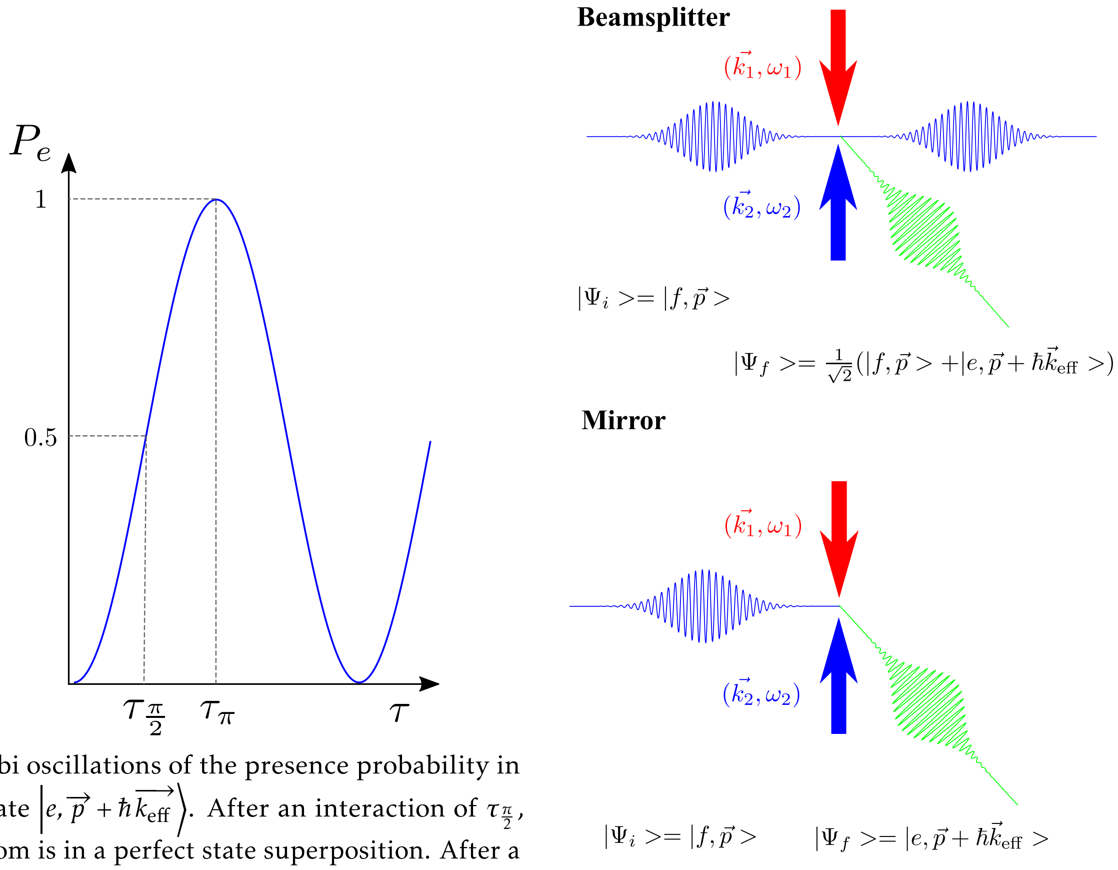

(a) Rabi oscillations of the presence probability in the state $\left|e, \vec{p} + \hbar\overrightarrow{k_{\text{eff}}}\right\rangle$. After an interaction of $\tau_{\frac{\pi}{2}}$, the atom is in a perfect state superposition. After a duration, τ_π, the state of the atom has completely changed.

(b) Atomic beamplitter and mirror using two-photon transitions.

Figure 1.4: Building blocks of atom optics

Atomic mirror

To create a mirror, the atomic states have to be inverted between $\left|f, \vec{p}\right\rangle$ and $\left|e, \vec{p} + \hbar\overrightarrow{k_{\text{eff}}}\right\rangle$ or vice-versa. The duration of a mirror pulse τ_π can be chosen as half a period of a Rabi oscillation (Figure 1.4a): $\tau_\pi = \frac{\pi}{\Omega_{\text{eff}}}$. The evolution matrix is now:

$$M_\pi(t, \tau_\pi, \varphi) = -i \begin{pmatrix} 0 & e^{i[(\omega_1-\omega_2)t+\varphi]-i\bar{\omega}_f\tau_\pi} \\ e^{-i[(\omega_1-\omega_2)t+\varphi]-i\bar{\omega}_e\tau_\pi} & 0 \end{pmatrix} \tag{1.29}$$

The mirror pulse allows to reflect the wave packet and is used to redirect the wave packet in the middle of the interferometer.

Raman induced phase

During each Raman pulse, the phase of the wave function is modified under the influence of the Raman laser. The wave function now depends on the laser phase φ at the interaction time. The phase term depends on the momentum (mirror or beamsplitter) and on the state modification. Table 1.1 sums up the phase accumulated during the laser pulse in the different cases.

For the interferometer, the relevant phase is $(\omega_1 - \omega_2)t$ and φ. According to Table 1.1, the atom is sensitive to this phase only if its state is modified and the sign of the gained phase

Transition	Phase for a mirror	Phase for a beamsplitter
$\lvert f\rangle \rightarrow \lvert f\rangle$	0	$-\bar{\omega}_f \tau_{\frac{\pi}{2}}$
$\lvert f\rangle \rightarrow \lvert e\rangle$	$-(\omega_1-\omega_2)t-\varphi-\bar{\omega}_e\tau_\pi-\frac{\pi}{2}$	$-(\omega_1-\omega_2)t-\varphi-\bar{\omega}_e\tau_{\frac{\pi}{2}}-\frac{\pi}{2}$
$\lvert e\rangle \rightarrow \lvert f\rangle$	$(\omega_1-\omega_2)t+\varphi-i\bar{\omega}_f\tau_\pi-\frac{\pi}{2}$	$(\omega_1-\omega_2)t+\varphi-\bar{\omega}_f\tau_{\frac{\pi}{2}}-\frac{\pi}{2}$
$\lvert e\rangle \rightarrow \lvert e\rangle$	0	$-\bar{\omega}_e \tau_{\frac{\pi}{2}}$

Table 1.1: Phase shift gained during a Raman transition for different initial states and pulse duration (beamsplitter or mirror).

depends on the initial state.

1.2 Mach-Zehnder interferometer

In the previous section, the building blocks of the interferometer were presented. Now, the Mach-Zehnder interferometer used in this work can be implemented. The Mach-Zehnder interferometer was chosen among other interferometers for its sensitivity to inertial effects such as the acceleration.

1.2.1 Description of a Mach-Zehnder interferometer

The Mach-Zehnder interferometer consists in a succession of three Raman pulses as described on Figure 1.5. The input state of the interferometer is $\left|f,\overrightarrow{p}\right\rangle$, then a first beamsplitter pulse creates a coherent superposition of states. After a propagation lasting a time T, a mirror pulse redirects the two components of the wave packet allowing them to cross after a time T. A last beamsplitter recombines the two components and makes them interfere. The total duration of the interferometer is $2T+4\tau$. The repartition of amplitude probability between the states $\left|f,\overrightarrow{p}\right\rangle$ and $\left|e,\overrightarrow{p}+\hbar\overrightarrow{k_{\text{eff}}}\right\rangle$ expresses the interference fringes and thus the phase shift between the two arms of the interferometer. For example, this interferometer can be used to measure the Earth gravity acceleration [24, 58] when the Raman laser is vertically aligned.

To compute the atomic state after the interferometer, the formalism of the evolution matrix is useful. In the previous section, the effect of the Raman interaction was written as a matrix. With the same formalism, the effect of the free propagation between the laser pulses can also be written as a propagation matrix:

$$M_P(t)=\begin{pmatrix} e^{-i\omega_f t} & 0 \\ 0 & e^{-i\omega_e t} \end{pmatrix} \tag{1.30}$$

The total evolution matrix of the interferometer can be computed as a product of the interaction matrices and the free propagation matrices.

$$M_{interfero}=M_{\frac{\pi}{2}}(t_0+2T+3\tau,\tau,\varphi(t_0+2T)).M_P(T).M_\pi(t_0+T+\tau,2\tau,\varphi(t_0+T)).M_P(T).M_{\frac{\pi}{2}}(t_0,\tau,\varphi(t_0)) \tag{1.31}$$

with τ the duration of a beamsplitter pulse and 2τ the duration of a mirror pulse. This expression is valid under the hypothesis of a constant laser phase during each pulse.

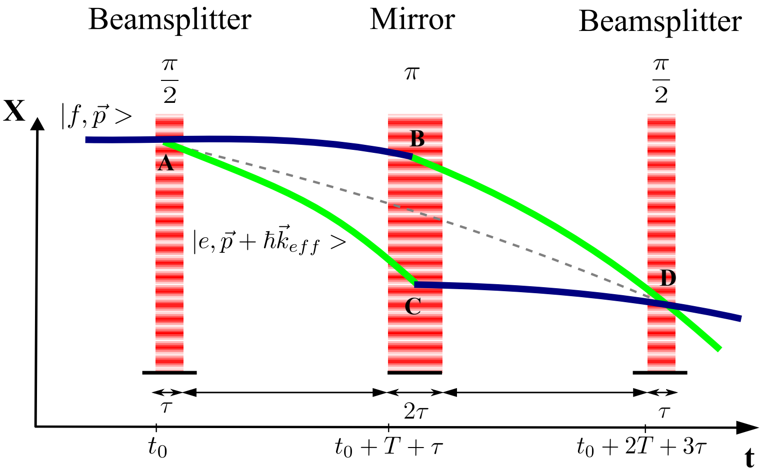

Figure 1.5: Space-time diagram of a Mach-Zehnder atomic accelerometer with a direction of measurement along the X axis. The three long red rectangles represents the laser pulses $\frac{\pi}{2} - \pi - \frac{\pi}{2}$ driving the atomic transitions between the ground state $\left|f, \overrightarrow{p}\right\rangle$ and the excited state $\left|e, \overrightarrow{p} + \hbar\overrightarrow{k_{\text{eff}}}\right\rangle$. The atoms free fall for a time t_0 before the beginning of the interferometer. The first and third laser pulses put the atoms in a superposition of states and have a duration τ. The second pulse redirects the atomic cloud and lasts 2τ.

1.2.2 Phase shift calculation

The knowledge of the interferometer phase shift is essential as it enables the acceleration measurements. The probability to detect the atom in the state $\left|e, \overrightarrow{p} + \hbar\overrightarrow{k_{\text{eff}}}\right\rangle$ can be expressed with the help of the interferometer matrix.

$$\begin{aligned} P_e &= |\left\langle e, \overrightarrow{p} + \hbar\overrightarrow{k_{\text{eff}}}\right| M_{interfero} \left|f, \overrightarrow{p}\right\rangle|^2 \\ &= \frac{1 - \cos(\Delta\Phi)}{2} \end{aligned} \tag{1.32}$$

with $\Delta\Phi$ the phase shift between the two arms of the interferometer. The phase difference between the two arms of the interferometer is only impacted by the phase φ accumulated during the Raman transitions.

$$\Delta\Phi = \varphi(t_0) - 2\varphi(t_0 + T) + \varphi(t_0 + 2T) \tag{1.33}$$

Thanks to the symmetry of the interferometer, each arm spends the same amount of time in each state: the phase due to the difference between the laser frequency is cancelled. The terms due to the propagation between the pulses are also cancelled for the same reason. Therefore, the phase shift of the interferometer only depends on the laser phase during each pulse.

Phase shift induced by a constant acceleration

All the previous calculations were conducted for a motionless atom. One can consider an atom in free fall with a constant acceleration $\vec{a}_0$. In the free falling atom frame, the momentum of the atom is constant: the atom hamiltonian interacting with the Raman laser is given by Equations 1.7 and 1.8. Experimentally, the Raman laser is reflected on a mirror used as the laser phase reference. Thus, the laser phase depends on the position between the mirror and the atom. The position operator $\hat{\vec{R}}$ in the electric field expression needs to be expressed in the atom frame: supplementary terms appear in the laser phase expression. For plane waves, the laser phase φ in the atom frame depends on the effective wave vector of the Raman transition $\vec{k}_{\text{eff}}$, the position of the atom with respect to the mirror $\vec{r}$ and the initial laser phase ϕ_i:

$$\varphi(t) = \vec{k}_{\text{eff}}(t).\vec{r}(t) + (\phi_1(t) - \phi_2(t)) \tag{1.34}$$

The laser phase variations during the pulse are neglected: $(\phi_1(t) - \phi_2(t)) \approx 0$ and the laser pulses are considered infinitely short $\tau \ll T$. The position of the atom with respect to the mirror $\vec{r}(t) = \vec{MA}$ is the mean position of the atom between the two arms of the interferometer represented as the dotted grey line on Figure 1.5.

Under a constant acceleration $\vec{a}_0$, the atom trajectory can be written as $\vec{r}(t) = \vec{a}_0 \frac{t^2}{2} + \vec{v}_0 t + \vec{r}_0$ with $\vec{v}_0$ and $\vec{r}_0$ the initial position and velocity at $t = 0$. In these conditions, the phase shift is proportional to projection of the acceleration along the direction of the effective wave vector.

$$\Delta\Phi \approx T^2 \vec{k}_{\text{eff}}.\vec{a}_0 \tag{1.35}$$

The interferometer allows to measure the acceleration along the effective wave vector which gives the direction of the measurement. The measured acceleration is the acceleration of the free falling atom with respect to the mirror. The sensitivity of the accelerometer created by the interferometer is given by the scale factor $S = k_{\text{eff}} T^2$. A longer interrogation time will lead to an increased sensitivity.

Another method to calculate the phase shift

The phase shift of an atomic interferometer can also be calculated using the path integral method. This method allows to obtain a more accurate value of the phase shift and to take into account other inertial effects such as the gravity gradient. This method can be used to compute the phase shift of many interferometry based setups from accelerometers to gyroscopes and atomic clocks [109].

In this method, the total phase shift of the interferometer is divided in three contributions:

$$\Delta\Phi_{\text{total}} = \Delta\Phi_{\text{prop}} + \Delta\Phi_{\text{laser}} + \Delta\Phi_{\text{sep}} \tag{1.36}$$

Propagation: $\Delta\Phi_{\text{prop}}$ is the phase shift associated with the wave packet propagation between the laser pulses. This term is calculated using the Feynman path integral. The classical actions of the wave packet trajectories are computed by integrating the Lagrangian over the classical trajectories of the mean position of the wave packets.

Laser: $\Delta\Phi_{\text{laser}}$ is the phase shift due to the atom-laser interactions used to manipulate the wave packets. This phase shift can be written as:

$$\Delta\Phi_{\text{laser}} = \overrightarrow{k_{\text{eff}}}.(\overrightarrow{r_A} - \overrightarrow{r_B} - \overrightarrow{r_C} + \overrightarrow{r_D}) \tag{1.37}$$

with k_{eff} the effective wave vector and $\overrightarrow{r_i}$ the mean position of the atomic wave packet. The letter $i \in \{A, B, C, D\}$ refers to Figure 1.5.

Separation: $\Delta\Phi_{\text{sep}}$ appears if the interferometer is not closed in position: at the last pulse of the interferometer, the positions of the wave packets do not coincide. This phase shift can be approximated as:

$$\Delta\Phi_{\text{sep}} = \overrightarrow{p}.\frac{\Delta\overrightarrow{r}}{\hbar} \tag{1.38}$$

with $\overrightarrow{p}$ the momentum of the wave packet and $\Delta\overrightarrow{r}$ the spatial separation between the centres of the two wave packets at the last beamsplitter.

1.2.3 Contrast calculation

The contrast of the interferometer expresses the amplitude of the interference fringes. In Equation 1.32 the contrast is considered ideal and equal to 1 but several phenomena can induce a lower contrast. Here is a non-exhaustive list of phenomena causing a loss of contrast.

- the velocity and position distributions of the atomic cloud [110]
- the gaussian intensity profile of the laser beam
- the rotation of the interferometer
- the spontaneous emission
- the inhomogeneity of the magnetic field ...

In this Section, only the effect of a variation of the laser intensity on the contrast will be studied. As regards the contrast loss due to a rotation, it will be detailed in Section 1.3.

Impact of the laser intensity on the contrast

To account for the reduction of the contrast, the probability to detect the atom in the state $\left|e, \overrightarrow{p} + \hbar\overrightarrow{k_{\text{eff}}}\right\rangle$ can be expressed as:

$$P_e = P_0 - \frac{C}{2}\cos(\Delta\Phi) \tag{1.39}$$

with P_0 the mean probability and C the contrast of the interference fringes. The laser intensity has an impact on the interferometer contrast through the quality of the atomic optics (beamsplitters and mirrors). A laser pulse with a duration τ used as an atomic optic can be characterised by their reflection and transmission coefficients:

$$R(\tau) = \frac{\Omega_{eff}^2}{\Omega_R^2}\sin^2\left(\frac{\Omega_R\tau}{2}\right) \tag{1.40}$$

$$T(\tau) = 1 - \frac{\Omega_{eff}^2}{\Omega_R^2}\sin^2\left(\frac{\Omega_R\tau}{2}\right) \tag{1.41}$$

with Ω_{eff} the effective Rabi pulsation and $\Omega_R = \sqrt{\Omega_{eff}^2 + \delta^2}$ the generalised Rabi pulsation. If the resonance condition is verified: $\delta = 0$, and then $\Omega_{eff} = \Omega_R$. Under these conditions, for a beamsplitter of a pulse duration $\tau_{\frac{\pi}{2}}$, the reflection and transmission coefficients have to be $R(\tau_{\frac{\pi}{2}}) = T(\tau_{\frac{\pi}{2}}) = 0.5$ so $\tau_{\frac{\pi}{2}} = \frac{\pi}{2\Omega_{eff}}$. For a mirror of a pulse duration τ_π, the coefficients are $R(\tau_\pi) = 1$ and $T(\tau_\pi) = 0$, then $\tau_\pi = \frac{\pi}{\Omega_{eff}}$. Therefore, the pulse durations of the atomic optics are determined by the Rabi pulsation.

As the effective Rabi pulsation depends on the laser intensity, the pulse duration also depends on the laser intensity. The effective Rabi pulsation can be written as $\Omega_{eff} = \frac{\Omega_{f,1}\Omega_{e,2}^*}{2\Delta}$ with $\Omega_{f,1} = \frac{2DE_1}{\hbar}$ and $\Omega_{e,2} = \frac{2DE_2}{\hbar}$. The amplitude of the electric fields E_1 and E_2 are proportional due to the conception of the laser system. The intensity ratio $R = \frac{I_1}{I_2}$ of the two laser components are tunable experimentally. Experimentally, the intensity I_2 is the intensity of the carrier of the modulated laser. This is the reason why I_2 is chosen as a reference in the rest of the calculation. The effective Rabi pulsation is then proportional to the laser intensity $I_2 \propto |E_2|^2$:

$$\Omega_{eff} = \frac{2D^2 E_1 E_2}{\Delta\hbar^2} \propto \frac{2D^2\sqrt{R}E_2^2}{\Delta\hbar^2} \tag{1.42}$$

A variation of the laser intensity will lead to a variation of the Rabi pulsation and a deterioration of the atomic optics quality. If the pulses duration is set for a given laser intensity and this intensity varies, the atom optic quality will be deteriorated. Here considered the intensity variations are slower than the duration of the atomic interferometer. Thus, the variation is the same for the three pulses of the interferometer. If the resonance condition is verified, the reflection coefficient of a laser pulse becomes:

$$R(\tau) = \sin^2\left(\frac{\Omega_{\mathrm{eff}}\tau}{2}\right) \tag{1.43}$$

Let's consider an initial intensity I_2^0, an initial Rabi pulsation Ω_{eff}^0 and an initial pulse duration for a mirror $\tau_{\pi 0} = \frac{\pi}{\Omega_{\mathrm{eff}}^0}$ and for a beamsplitter $\tau_{\frac{\pi}{2}0} = \frac{\pi}{2\Omega_{\mathrm{eff}}^0}$. Temporal variations can occur in the experiment leading to an intensity variation. Let δI be the relative intensity variation, the laser intensity is then expressed as $I_2(t) = (1+\delta I)I_2^0$. The reflection coefficient can now be written as:

$$\begin{aligned} R_{mirror} &= \sin^2\left(\frac{\pi\Omega_{\mathrm{eff}}}{2\Omega_{\mathrm{eff}}^0}\right) \\ R_{beamsplitter} &= \sin^2\left(\frac{\pi\Omega_{\mathrm{eff}}}{4\Omega_{\mathrm{eff}}^0}\right) \end{aligned} \tag{1.44}$$

The evolution of the reflection coefficients were computed as a function of the variation of the laser intensity δI (Figure 1.6a). For a variation of 10% of the laser intensity, the mirror reflection decreases from 1 to 0.98 and the beamsplitter reflection increases from 0.5 to 0.58.

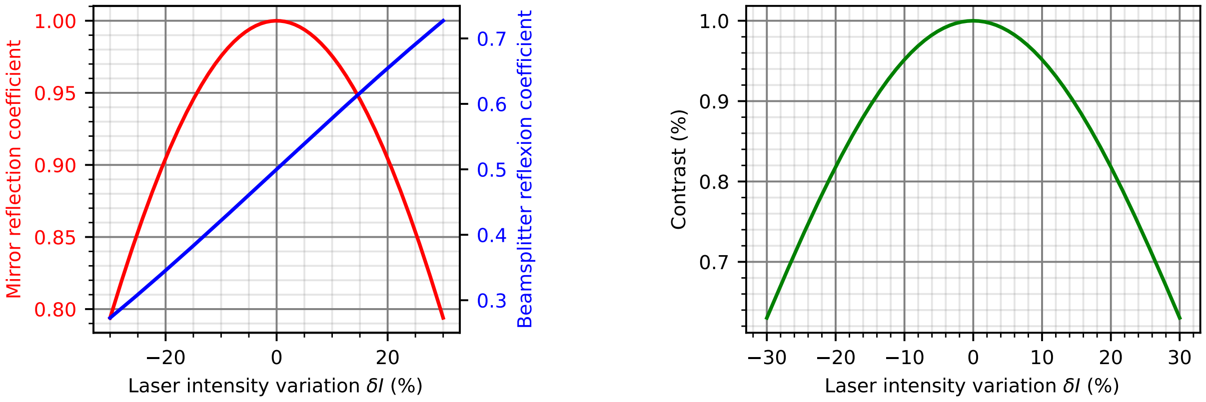

(a) Reflection coefficients of the atomic mirror in red and beamsplitter in blue as a function of the laser intensity.

(b) Contrast loss due to the laser intensity variations

Figure 1.6: Impact of the laser intensity variations on the interferometer contrast.

The contrast of the interferometer can be expressed as a function of the reflection and transmission coefficients [111]:

$$C = 4R_{mirror}R_{beamsplitter}T_{beamsplitter} \tag{1.45}$$

The contrast as a function of the laser intensity variation is a parabola and can be seen on Figure 1.6b. For a intensity variation of 10% , the contrast is expected to decrease from 1 to 0.95. The laser intensity variations below 10% have a limited impact on the contrast as the contrast loss is parabolic and will not deteriorate the interferometer performances significantly.

1.3 Rotating Mach-Zehnder interferometer

The rotation of the interferometric setup impacts the phase shift and contrast of the interferometer negatively [3, 29, 95]. Due to the influence of inertial accelerations: Coriolis acceleration, Centrifugal acceleration and Angular acceleration, additional phase shifts appear at the output of the interferometer [91, 112]. These additional phase shifts depend on the velocity and position of each atom. As the detected quantity is the probability averaged over the atomic cloud, these additional phase shifts depend on the mean velocity and the mean position of the detected atomic cloud and will engender a bias in the acceleration measurement. Moreover, due to the size and temperature of the cloud, the rotation induces a loss of contrast [3]. The interferometer contrast has to be high enough to avoid any deterioration of the phase measurement. In this section, the calculation of the phase shift and contrast of a rotating interferometer is presented.

1.3.1 Description of the rotation

In this section, the movements of the different moving parts of the setup are defined to anticipate the contrast and the phase shift computation in the next sections.

Definition of the different frames

To ease the calculation, each moving part will be associated with a frame pictured in Figure 1.7. The first frame is the laboratory frame $\aleph_L = \{O, \vec{x_L}, \vec{y_L}, \vec{z_L}\}$ considered inertial in this work. $\vec{x_L}$ is the unitary vector in the direction of the Earth gravity $\vec{g}$ and O is the sensor centre of rotation. The Earth rotation has an angular velocity of $73\,\mu\mathrm{rad\,s^{-1}}$ and is considered constant during the experiment. Thus, its effect on the interferometer is constant and will not be studied in this work. The table supporting the sensor (in blue on Figure 1.7) is associated with the sensor frame $\aleph_S = \{O, \vec{x_S}, \vec{y_S}, \vec{z_S}\}$. $\vec{x_S}$ is in the direction of the wave vector $\vec{k}_1$ as the incoming laser is fixed in the sensor frame. $\vec{x_S}$ is also the normal vector to the table supporting the sensor head. A last frame is the mirror frame $\aleph_M = \{M, \vec{x_M}, \vec{y_M}, \vec{z_M}\}$. M is the center of rotation of the mirror and $\vec{x_M}$ the normal vector to the mirror.

The vector $\vec{x_r}$ is defined as the unitary vector in the direction of the reflected laser of wave vector $\vec{k}_2$. If the mirror is not rotating in the sensor frame: $\aleph_M = \aleph_S$ then $\vec{x_r} = \vec{x_S}$. The centres of rotation are O the centre of rotation of the sensor and M the centre of rotation of the mirror. The centre of the atomic cloud is represented as A.

Definition of the sensor rotation

In the following sections 1.3.3 and 1.3.5, the sensor rotates around the axis $\vec{z_S} = \vec{z_L} = \vec{z_M}$. The rotation will be characterised by the angle θ_S between $\vec{x_S}$ and $\vec{x_L}$. The interferometer is only sensitive to the sensor angle at the Raman pulses instant: $\theta_S(t_0)$ at the first pulse, $\theta_S(t_0+T)$ at the second and $\theta_S(t_0+2T)$ at the third. Thus, a polynomial expression of the second order is

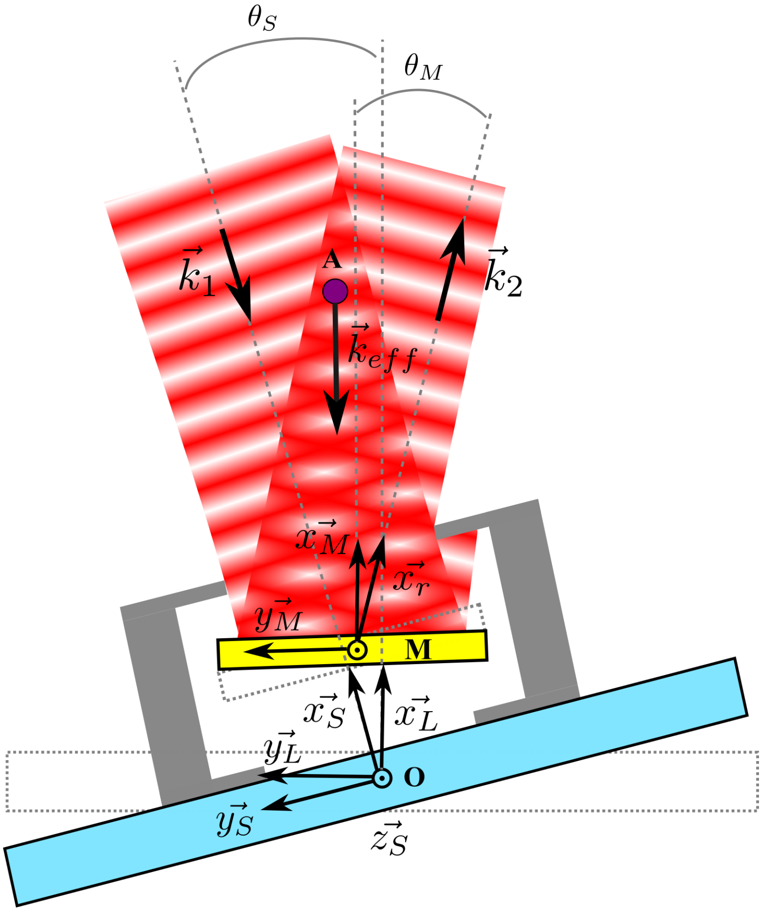

Figure 1.7: Diagram of the interferometric setup and definition of the different frames. The blue rectangle is the table supporting the sensor and O its rotation centre. The yellow rectangle is the retro-reflection mirror with M its centre of rotation. The atomic cloud A is depicted as the purple disc. $\mathfrak{R}_L = \{O, \vec{x_L}, \vec{y_L}, \vec{z_L}\}$ is the laboratory frame. $\mathfrak{R}_S = \{O, \vec{x_S}, \vec{y_S}, \vec{z_S}\}$ is the sensor frame and $\mathfrak{R}_M = \{M, \vec{x_M}, \vec{y_M}, \vec{z_M}\}$ the mirror frame. $\vec{k_1}$ is the wave vector of the incoming laser and $\vec{k_2}$ is the wave vector of the reflected laser. $\vec{x_r}$ is the unitary vector in the direction of the reflected laser.

sufficient to describe the sensor angular movement θ_S:

$$\theta_S(t) = \theta_S^0 + \Omega_S.(t - t_0 - T) + \frac{1}{2}\dot{\Omega}_S.(t - t_0 - T)^2 \tag{1.46}$$

In this expression of the sensor angle, the temporal reference is chosen at the centre of the interferometer i.e. the second pulse because the angle at the second pulse $\theta_S(t_0+T) = \theta_S^0$ impacts the most the interferometer. Ω_S is the mean angular velocity seen by the interferometer and can be expressed as:

$$\Omega_S = \frac{\theta_S(t_0 + 2T) - \theta_S(t_0)}{2T} \tag{1.47}$$

$\dot{\Omega}_S$ is the mean angular acceleration seen by the interferometer and can be computed as:

$$\dot{\Omega}_S = \frac{\theta_S(t_0) - 2\theta_S(t_0 + T) + \theta_S(t_0 + 2T)}{T^2} \tag{1.48}$$

Definition of the mirror rotation

The mirror rotation is also considered around the axis $\vec{z_M}$ axis in the Sections 1.3.4 and 1.3.5. The angle θ_M between $\vec{x_M}$ and $S\vec{x_S}$ can also be expressed as a second order polynomial as the interferometer is only sensitive to the mirror angle during the three Raman pulses.

$$\theta_M(t) = \theta_M^0 + \Omega_M.(t - t_0 - T) + \frac{1}{2}\dot{\Omega}_M.(t - t_0 - T)^2 \tag{1.49}$$

The temporal reference is once again chosen at the centre of the interferometer. $\theta_M^0 = \theta_M(t_0 + T)$ is the angle at the second Raman pulse. Ω_M is the mean angular velocity seen by the interferometer and can be expressed as:

$$\Omega_M = \frac{\theta_M(t_0 + 2T) - \theta_M(t_0)}{2T} \tag{1.50}$$

$\dot{\Omega}_M$ is the mean angular acceleration seen by the interferometer and can be computed as:

$$\dot{\Omega}_M = \frac{\theta_M(t_0) - 2\theta_M(t_0 + T) + \theta_M(t_0 + 2T)}{T^2} \tag{1.51}$$

1.3.2 Description of the atoms trajectory

Experimentally, an atomic cloud of roughly one million atoms is used to implement the interferometer. Each atom is put in a superposition of states and interferes with itself at the end of the interferometer but all the atoms are detected at the same time. The probability P_e for the atoms to be in the state $\left|e, \overrightarrow{p} + \hbar\overrightarrow{k_{\text{eff}}}\right\rangle$ is estimated by measuring the number of atoms N_e in $\left|e, \overrightarrow{p} + \hbar\overrightarrow{k_{\text{eff}}}\right\rangle$ and the number of atoms N_f in $\left|f, \overrightarrow{p}\right\rangle$. The probability averaged over the atomic cloud can be written as the proportion of atoms in $\left|e, \overrightarrow{p} + \hbar\overrightarrow{k_{\text{eff}}}\right\rangle$:

$$\overline{P_e} = \frac{N_e}{N_e + N_f} = \overline{P_0} - \frac{\overline{C}}{2}\cos\left(\overline{\Delta\Phi}\right) \tag{1.52}$$

with $\overline{\Delta\Phi}$ the mean phase shift, $\overline{C}$ the mean contrast and $\overline{P_0}$ the mean offset of the cloud. As the whole cloud contributes to the detected phase shift, the mean trajectory of the cloud will be used to compute the phase shift of the interferometer:

$$\vec{r}(t) = \begin{pmatrix} a_{x_L}\frac{t^2}{2} + v_{x_0}t + x_{MA} \\ v_{y_0}t + y_{MA} \\ v_{z_0}t + z_{MA} \end{pmatrix} \tag{1.53}$$

The time origin is chosen at the end of the cooling step so all the kinetic parameters are defined at this moment. With this definition, the kinetic parameters can be compared to value given in the literature. At $t = 0$, an initial position (x_{MA}, y_{MA}, z_{MA}) and an initial velocity $(v_{x_0}, v_{y_0}, v_{z_0})$ along the three space directions are considered. The different coordinates (v_{x_0},v_{y_0},v_{z_0},x_{MA},y_{MA} and z_{MA}) used to compute the trajectory are given in the laboratory frame. In this work, the impact of the sensor rotation on the MOT position at the release time of the atoms is not considered. This rotation induced displacement is below 0.1 mm for an angular amplitude of 100 µrad.

The only acceleration considered is the acceleration resulting from the gravity: a_{x_L} expressed in the laboratory frame. In the absence of rotation, the direction of measurement is aligned with the gravity acceleration. The average transition probability $\overline{P_e}$ defined in Equation 1.52 can also be written as a function of $D_{\vec{v}}$ the velocity distribution and $D_{\vec{r}}$ the position distribution of the atomic cloud:

$$\overline{P_e} = \iint P_e(\vec{v},\vec{r}) D_{\vec{v}}(\vec{v}) D_{\vec{r}}(\vec{r}) d\vec{v} d\vec{r} \tag{1.54}$$

Thus, the normalised contrast (Equation 1.55) can be expressed as a function of the velocity and position distributions:

$$\frac{\overline{C}}{C} = \frac{1}{\cos\left(\overline{\Delta\Phi}\right)} \iint \cos(\Delta\Phi(\vec{r},\vec{v})) D_{\vec{v}}(\vec{v}) D_{\vec{r}}(\vec{r}) d\vec{v} d\vec{r} \tag{1.55}$$

Equation 1.55 is valid only under the hypothesis that C does not depend on the velocity and position of the atom. A most rigorous method would consider the contrast dependency on the velocity and position due to several phenomena such as the detection system or the transverse Gaussian intensity of the laser beam. In first approximation, Gaussian velocity and position distributions will be considered to describe the atomic cloud after 3D molasses. The Gaussian velocity and position distributions along the three space axes will be written as:

$$D_k(k) = \frac{1}{\sqrt{2\pi}\sigma_k} \exp\left[-\frac{1}{2}\left(\frac{k-\mu_k}{\sigma_k}\right)^2\right] \tag{1.56}$$

with $k \in \{x_{MA}, y_{MA}, z_{MA}, v_{x_0}, v_{y_0}, v_{z_0}\}$, μ_k the position of the centre of the Gaussian distribution and σ_k^2 the variance of the distribution. σ_k also expresses the half width of the distribution at the height of $\frac{1}{\sqrt{e}}$. The phase shift of the interferometer in the presence of rotation can be written as a function of the mean positions and velocities of the cloud.

$$\overline{\Delta\Phi} = A_0 + A_x x_{MA} + A_y y_{MA} + A_z z_{MA} + A_{v_x} v_{x_0} + A_{v_y} v_{y_0} + A_{v_z} v_{z_0} \tag{1.57}$$

with $x_{MA}, y_{MA}, z_{MA}, v_{x_0}, v_{y_0}, v_{z_0}$ the mean kinetic parameters of the cloud, $A_x, A_y, A_z, A_{v_x}, A_{v_y}, A_{v_z}$ some constants associated with each parameters and A_0 a constant. Thanks to Equation 1.55, the normalised contrast can be expressed as a function of the previously defined constants and the width of the velocity and position distributions σ_k.

$$\frac{\bar{C}}{C_0} = \exp\left[-\frac{1}{2}\left(A_x^2\sigma_x^2 + A_y^2\sigma_y^2 + A_z^2\sigma_z^2 + A_{vx}^2\sigma_{vx}^2 + A_{vy}^2\sigma_{vy}^2 + A_{vz}^2\sigma_{vz}^2\right)\right] \tag{1.58}$$

Once the phase shift in the presence of rotation is known, the constants A_k can be determined. Then, the contrast loss due to the sensor rotation or the mirror rotation can be easily computed thanks to Equation 1.58.

1.3.3 Impact of the sensor rotation on the interferometer

In this Section, the impact of the sensor rotation around the axis $\vec{z_S}$ (see 1.7) on the interferometer will be computed. The sensor refers to the whole atom interferometer including the retro-reflection mirror and the mount of the downward laser which are both fixed on a supporting table. The sensor angular positions are given for each of the three laser pulses by Equation 1.46.

Phase shift

Firstly, the phase shift is calculated using Equation 1.33. To compute the laser phase at each pulse, the effective wave vector of the laser has to be expressed as a function of the rotation parameters. The effective wave vector is the difference between the wave vector of the incoming laser $\vec{k_1} = -k_1\vec{x_S}$ and of the reflected laser $\vec{k_2} = k_2\vec{x_S}$. The unitary vector $\vec{x_S}$ can be written as $\vec{x_S} = R_S(\theta_S)\vec{x_L}$ with R_S the rotation matrix around $\vec{z_S}$ (see Equation 1.59).

$$R_S = \begin{pmatrix} \cos\theta_S & -\sin\theta_S & 0 \\ \sin\theta_S & \cos\theta_S & 0 \\ 0 & 0 & 1 \end{pmatrix} \tag{1.59}$$

As θ_S is small, the expression of $\vec{x_S}$ will be simplified by the approximation of small angles: $\cos\theta_S \approx 1 - \frac{\theta_S^2}{2}$ and $\sin\theta_S \approx \theta_S$. The mean trajectory of the atomic cloud is expressed through Equation 1.53. Using Equation 1.33, the phase shift of the rotating interferometer is:

$$\overline{\Delta\Phi_S} = k_{\text{eff}}T^2[-a_{x_L}-2\Omega_S v_{y_0}-\dot{\Omega}_S(v_{y_0}(t_0+T)+y_{OA})+\Omega_S^2(a_{x_L}(\frac{t_0^2}{2}+t_0T+T^2)+v_{x_0}(t_0+T)+x_{OA})] \tag{1.60}$$

This is the phase shift is the detected phase shift. Hence, it is the phase shift integrated over the atomic cloud. This Equation is an approximation as terms in Ω_S^n and $\dot{\Omega}_S^n$ are neglected for $n \geq 2$ for $\dot{\Omega}_S$ and for $n > 2$ for Ω_S. The terms scaling in $\dot{\Omega}_S\Omega_S$ are also neglected same as the terms in θ_S^0.

Equation 1.60 can be rearranged to show the dependence of the phase shift on the three following inertial accelerations:

- Coriolis acceleration: $-2\Omega_S v_{y_0}$
- Centrifugal acceleration: $\Omega_S^2(a_{x_L}(\frac{t_0^2}{2} + t_0T + T^2) + v_{x_0}(t_0 + T) + x_{OA})$
- Angular acceleration: $-\dot{\Omega}_S(v_{y_0}(t_0 + T) + y_{OA})$

The rotation induced phase shift terms can be explained the inertial accelerations which appear in a rotating frame. As both the mirror and the input laser are rotated, only the direction of measurement i.e. the direction of the effective wave vector, is rotated. The magnitude of the effective vector does not change during the interferometer $\| \vec{k_{\text{eff}}} \| = k_{\text{eff}}$. The rotating interferometer detects the same acceleration as a perfect accelerometer in rotation.

$$\vec{k_{\text{eff}}} = -k_{\text{eff}} \begin{pmatrix} 1 - \frac{\theta_S^2}{2} \\ \theta_S \\ 0 \end{pmatrix} \tag{1.61}$$

The rotation induces a dependence of the phase shift on the mean velocity and mean position of the cloud. A null initial velocity would reduce the rotation induced phase shift as would a perfect transverse alignment ($y_{OA} = 0$). Nevertheless, the rotation induced phase shift cannot be cancelled as the Centrifugal acceleration depends on the acceleration a_{x_L} and the vertical distance x_{OA}.

The recoil velocity $v_{rec} = \frac{\hbar k_{\text{keff}}}{m} \approx 12\,\text{mm}\,\text{s}^{-1}$ due to the absorption and emission of photons changes the atom/mirror distance. Thus, a supplementary term depending of the recoil velocity appears in the Centrifugal acceleration: $-\frac{3T}{4m}\hbar k_{\text{eff}}\Omega_S^2$. As $\frac{3T}{4m}\hbar k_{\text{eff}} \approx 0.4\,\text{mm} \ll x_{OA} \approx 50\,\text{cm}$, the recoil velocity term can be neglected.

Contrast

Secondly, the contrast is computed using the previous paragraph 1.3.2 and Equation 1.58 considering gaussian velocity and position distributions.

$$\frac{\overline{C}_S}{C_0} = \exp\left[-\frac{k_{\text{eff}}^2 T^4}{2}\left(\Omega_S^4\sigma_x^2 + \dot{\Omega}_S^2\sigma_y^2 + (t_0+T)^2\Omega_S^4\sigma_{v_x}^2 + ((t_0+T)\dot{\Omega}_S + 2\Omega_S)^2\sigma_{v_y}^2\right)\right] \tag{1.62}$$

As inertial accelerations depends on the velocity and position of the atom, the dispersion of velocities and positions in the cloud will induce different phase shifts leading to a loss of contrast. If all the inertial accelerations can lead to contrast loss, it can be noted that the Coriolis and Angular contributions due to the velocity distributions can compensate each other. In the following term $((t_0+T)\dot{\Omega}_S + 2\Omega_S)^2\sigma_{v_y}^2$, a negative angular acceleration and a positive angular velocity would reduce the contrast loss. The contrast loss due to the rotation induces a lower sensitivity of the cold atom accelerometer and is a major difference with a perfect accelerometer.

1.3.4 Impact of the mirror rotation on the interferometer

In this work, the mirror rotation was also considered and its effect on the interferometer computed. The rotation of the mirror is only around the axis $\vec{z_M}$. The mirror angular movement is given by Equation 1.49. The phase shift and contrast calculation is based on the same principle as the calculation of Section 1.3.3.

Phase shift

The phase shift is computed using Equation 1.33. To calculate the laser phase at each pulse, the effective wave vector of the laser is expressed as a function of the mirror rotation parameters (see Section 1.3.1). As the sensor is not rotating: $\vec{x_S} = \vec{x_L}$ and the incoming wave vector is $\vec{k_1} = -k_1\vec{x_S}$. The reflected wave vector is $\vec{k_2} = k_2\vec{x_r}$ due to the mirror rotation. The unitary vector $\vec{x_r}$ in the direction of the reflected laser can be expressed with the unitary vectors of the mirror and sensor frame as $\vec{x_r}$ is the symmetric of $\vec{x_S}$ with respect to the axis defined by $\vec{x_M}$.

$$\vec{x_r} = -\vec{x_S} + 2(\vec{x_M}.\vec{x_S})\vec{x_M} \tag{1.63}$$

The unitary vector $\vec{x_M}$ can be expressed with the help of the mirror rotation matrix: $\vec{x_M} = R_M(\theta_M)\vec{x_S}$ with R_M the rotation matrix for a rotation around $\vec{z_M}$.

$$R_M = \begin{pmatrix} \cos\theta_M & -\sin\theta_M & 0 \\ \sin\theta_M & \cos\theta_M & 0 \\ 0 & 0 & 1 \end{pmatrix} \tag{1.64}$$

As θ_M is small, the expression of $\vec{x_M}$ will be simplified by the approximation of small angles: $\cos\theta_M \approx 1-\frac{\theta_M^2}{2}$ and $\sin\theta_M \approx \theta_M$. Then $\vec{x}_r$ can be expressed and the phase shift computed:

$$\overline{\Delta\Phi}_M = k_{\text{eff}}T^2[-a_{x_L}-2\Omega_M v_{y_0}-\dot{\Omega}_M((t_0+T)v_{y_0}+y_{MA})+2\Omega_M^2(a_{x_L}(\frac{t_0^2}{2}+t_0T+T^2)+(t_0+T)v_{x_0}+x_{MA})] \tag{1.65}$$

This Equation is an approximation as Ω_M^n and $\dot{\Omega}_M^n$ are neglected for $n \geq 2$ for $\dot{\Omega}_M$ and $n > 2$ for Ω_M. The terms scaling in $\dot{\Omega}_M\Omega_M$ are also neglected same as the terms in θ_M^0. The contributions of each inertial accelerations are the following:

- Coriolis acceleration: $-2\Omega_M v_{y_0}$
- Centrifugal acceleration: $2\Omega_M^2(a_{x_L}(\frac{t_0^2}{2}+t_0T+T^2)+v_{x_0}(t_0+T)+x_{MA})$
- Angular acceleration: $-\dot{\Omega}_M(v_{y_0}(t_0+T)+y_{MA})$

The Equation 4.13 is similar to Equation 1.60 except for the contribution of the Centrifugal acceleration. Now, the relevant distance for the Centrifugal and Angular acceleration is the atom/mirror distance and differs from the case of the sensor rotation. Moreover, the Centrifugal contribution is multiplied by 2 when the mirror is rotated. When the mirror is rotated, the direction of the effective wave vector $\overrightarrow{k_{\text{eff}}}$ is modified but also its magnitude as the incoming and reflected lasers are not aligned anymore: $\| \overrightarrow{k_{\text{eff}}} \| \approx k_{\text{eff}}\left(1-\frac{\theta_M^2}{2}\right)$. As the mirror is rotated but not the input laser, the direction of the effective wave vector is:

$$\overrightarrow{k_{\text{eff}}} = -k_{\text{eff}}\begin{pmatrix} 1-\theta_M^2 \\ \theta_M \\ 0 \end{pmatrix} \tag{1.66}$$

When the retro-reflection mirror is rotated, the rotation induced phase shift cannot be fully explained by the inertial accelerations as a phenomenon peculiar to the atom interferometer appears.

Contrast

The contrast loss due to the mirror rotation (Equation 1.67) computed using Equations 1.58 and 4.13, is similar to the contrast loss due to the sensor rotation (Equation 1.62). The only difference is the contribution of the Centrifugal acceleration which is multiplied by 2 due to a variation of $\overrightarrow{k_{\text{eff}}}$ magnitude. The similarities between the sensor and the mirror rotations impacts allows the implementation of the rotation compensation method.

$$\frac{\overline{C}_M}{C_0} = \exp\left(-\frac{k_{\text{eff}}^2T^4}{2}(\,4\Omega_M^4\sigma_x^2+\dot{\Omega}_M^2\sigma_y^2+4(t_0+T)^2\Omega_M^4\sigma_{v_x}^2+((t_0+T)\dot{\Omega}_M+2\Omega_M)^2\sigma_{v_y}^2\,)\right) \tag{1.67}$$

1.3.5 Impact of the rotation compensation on the interferometer

In order to limit the impact of the sensor rotation on the interferometer computed in section 1.3.3, a rotation compensation method can be implemented by rotating the retro-reflection mirror. Such a method has already been implemented to correct the Earth rotation [3, 90, 91] or the carrier rotation [42, 95, 96] This method consists in rotating the retro-reflection mirror with an opposite angle leaving the mirror immobile during the interferometer. Firstly, a more general case can be considered with a sensor angular movement given by Equation 1.46 and a mirror angular movement given by Equation 1.49.

Phase shift

The phase shift is once again computed using Equation 1.33. The effective wave vector of the laser is expressed as a function of the mirror rotation matrix R_M and the sensor rotation matrix R_S. The incoming wave vector is $\vec{k_1} = -k_1\vec{x_S}$ with $\vec{x_S} = R_S(\theta_S)\vec{x_L}$. The reflected wave vector is $\vec{k_2} = k_2\vec{x_r}$. $\vec{x_r}$ can be calculated with Equation 1.79 and the unitary vector in the mirror frame with the mirror rotation matrix: $\vec{x_M} = R_M(\theta_M)\vec{x_S}$. For a general case, the phase shift of the interferometer is:

$$\begin{aligned}\overline{\Delta\Phi}_{M+S} = k_{\text{eff}}T^2[&-a_{x_L} - 2(\Omega_M+\Omega_S)v_{y_0} - (\dot{\Omega}_S+\dot{\Omega}_M)((t_0+T)v_{y_0}+y_{OA}) - \dot{\Omega}_M y_{MO}) \\ &+ (2\Omega_M^2+\Omega_S^2+2\Omega_M\Omega_S)(a_{x_L}(\frac{t_0^2}{2}+t_0T+T^2)+(t_0+T)v_{x_0}+x_{OA})+2\Omega_M^2 x_{MO}]\end{aligned} \tag{1.68}$$

This Equation is an approximation as Ω_i^n and $\dot{\Omega}_i^n$ are neglected for $n \geq 2$ for $\dot{\Omega}_i$ and $n > 2$ for Ω_i. The terms scaling in $\dot{\Omega}_i\Omega_i$ and θ_i^0 are also neglected with i=M or S. The cross terms between the sensor and the mirror rotations are also neglected such as $\Omega_M\Omega_S$ or $\dot{\Omega}_S\dot{\Omega}_M$. The contributions of each inertial accelerations are the following:

- Coriolis acceleration: $-2(\Omega_M+\Omega_S)v_{y_0}$
- Centrifugal acceleration: $(2\Omega_M^2+\Omega_S^2+2\Omega_M\Omega_S)(a_{x_L}(\frac{t_0^2}{2}+t_0T+T^2)+(t_0+T)v_{x_0}+x_{OA})+2\Omega_M^2 x_{MO}$
- Angular acceleration: $-(\dot{\Omega}_S+\dot{\Omega}_M)((t_0+T)v_{y_0}+y_{OA}) - \dot{\Omega}_M y_{MO})$

As shown by Equation 4.15, the Coriolis acceleration can by cancelled by the compensation method when $\Omega_M = -\Omega_S$. Nevertheless, the contributions of the Angular and Centrifugal accelerations depend on both the positions of the center of rotation. This will have an impact on the rotation compensation method as it is not possible to cancel their contributions to the phase shift.

Contrast

The contrast can also be computed for a general sensor and mirror rotations:

$$\begin{aligned}\frac{\overline{C}_{M+S}}{C_0} = \exp\Bigg(&-\frac{k_{\text{eff}}^2T^4}{2}(\,(2\Omega_M^2+\Omega_S^2+2\Omega_M\Omega_S)^2\sigma_x^2+(\dot{\Omega}_S+\dot{\Omega}_M)^2\sigma_y^2 \\ &+((t_0+T)(2\Omega_M^2+\Omega_S^2+2\Omega_M\Omega_S))^2\sigma_{v_x}^2+((t_0+T)(\dot{\Omega}_S+\dot{\Omega}_M)+2(\Omega_M+\Omega_S))^2\sigma_{v_y}^2\,)\Bigg)\end{aligned} \tag{1.69}$$

As shown by Equation 1.69, the contrast loss due to the Coriolis and Angular accelerations can be cancelled. The corresponding terms are $((t_0+T)(\dot{\Omega}_S+\dot{\Omega}_M)+2(\Omega_M+\Omega_S))^2\sigma_{v_y}^2$ and $(\dot{\Omega}_S+\dot{\Omega}_M)^2\sigma_y^2$. Nevertheless, the contrast loss due to the Centrifugal acceleration cannot be cancelled as the corresponding terms are $(2\Omega_M^2+\Omega_S^2+2\Omega_M\Omega_S)^2\sigma_x^2$ and $((t_0+T)(2\Omega_M^2+\Omega_S^2+2\Omega_M\Omega_S))^2\sigma_{v_x}^2$.

Perfect rotation compensation

In the perfect rotation compensation case, the sensor and the mirror rotate in the exact opposite way each around their own center of rotation. Their angular positions are exactly opposite:

$$\theta_S(t) = -\theta_M(t) \tag{1.70}$$

Thus, $\Omega_S = -\Omega_M$ and $\dot{\Omega}_S = -\dot{\Omega}_M$. In this configuration, some terms in the phase shift are cancelled by the rotation compensation. The remaining phase shift is:

$$\overline{\Delta\Phi}_{S=M} = k_{\text{eff}}T^2[-a_{x_L} + \dot{\Omega}_S y_{MO} + \Omega_S^2(a_{x_L}(\frac{t^2}{2} + t_0T + T^2) + (t_0+T)v_{x_0} + x_{OA} + 2x_{MO})] \tag{1.71}$$

As the mirror is rotated as well as the input laser, the magnitude of the effective vector does changes during the interferometer $\| \vec{k_{\text{eff}}} \| = k_{\text{eff}}\left(1 - \frac{\theta_S^2}{2}\right)$ explaining the Centrifugal term. Thanks to the compensation, the direction of the wave vector does not change during the interferometer:

$$\vec{k_{\text{eff}}} = -k_{\text{eff}}\begin{pmatrix} 1 - \frac{\theta_S^2}{2} \\ 0 \\ 0 \end{pmatrix} \tag{1.72}$$

The phase shift is not impacted anymore by the Coriolis acceleration as shown by Equation 1.71. Nevertheless, the Centrifugal acceleration is increased by the mirror rotation leading to the term in $\Omega_S^2(a_{x_L}(\frac{t^2}{2} + t_0T + T^2) + (t_0+T)v_{x_0} + x_{OA} + 2x_{MO})$. The Angular acceleration is not perfectly compensated due to the transverse distance between the centres of rotation of the mirror and the sensor leading to a term in $\dot{\Omega}_S y_{MO}$.

In the same conditions, the contrast can also be computed:

$$\frac{\overline{C}_{S=M}}{C_0} = \exp\left(-\frac{k_{\text{eff}}^2T^4}{2}\left(\Omega_S^4\sigma_x^2 + (t_0+T)^2\Omega_S^4\sigma_{v_x}^2\right)\right) \tag{1.73}$$

As the contrast is not impacted by the relative position of the centres of rotation, the contrast is not impacted anymore by the Coriolis and Angular accelerations. For a perfectly compensated rotation, the only source of contrast loss left is the Centrifugal acceleration.

The main goal of the rotation compensation is to recover the contrast loss, this can be achieved as the Coriolis and Angular contributions to the contrast loss are cancelled. Nevertheless, the contrast cannot be completely recovered as the Centrifugal contribution is not cancelled. If the Centrifugal induced contrast loss is not cancelled by this method, it is not increased either. The reduction of the rotation induced phase shift is a side effect of the rotation compensation method. To further reduce the phase shift, the position and velocity of the atomic cloud has to be controlled to impose a null initial velocity and a perfect transverse alignment of the centres of rotation ($y_{MO} = 0$). Lastly, the term scaling in $x_{OA} + 2x_{MO}$ could be cancelled by placing the mirror in the middle of the atomic cloud and the sensor centre of rotation.

1.3.6 Numerical model

A numerical code of the phase shift and contrast was developed to have a more accurate model and to take into account a more realistic movement of the sensor and mirror. With this numerical calculation, the terms in T^3 and higher are not neglected anymore. Moreover, the sensor and the mirror rotations are not perfectly around the Z axis and a component along the Y axis is present. The mirror also has a vertical movement. These two last effects are included in the numerical model.

The input data of the numerical model are the angles of the sensor and mirror and the vertical position of the mirror position at each pulse. The sensor angular positions around $\overrightarrow{z_S}$ and $\overrightarrow{y_S}$ are θ^z_{Si} and θ^y_{Si} with $i \in \{1,2,3\}$ the pulse number. $i = 1$ is the first pulse (beamsplitter) at $t = t_0$. $i = 2$ is the second pulse (mirror) at $t = t_0 + T$. $i = 3$ is the third pulse (beamsplitter) at $t = t_0 + 2T$. The mirror angular positions around the axes $\overrightarrow{z_M}$ and $\overrightarrow{y_M}$ are Ψ_{Mi} and Θ_{Mi} (see Chapter 2 for more details about the actuated mirror). A last input is the mirror movement supplied by the EA capacitive detection. This movement is given by the distance between the centre of the mirror M and the centre of the mirror at rest M_0. The vector $\overrightarrow{M_0M}$ is expressed in the sensor frame.

$$\overrightarrow{M_0M} = \begin{pmatrix} \delta x_M \\ \delta y_M \\ \delta z_M \end{pmatrix} = \begin{pmatrix} x_M - x_{M0} \\ y_M - y_{M0} \\ z_M - z_{M0} \end{pmatrix} \tag{1.74}$$

Phase shift

As previously, the phase shift is calculated thanks to the following equation with $\varphi(t) = \overrightarrow{k_{\text{eff}}} . \overrightarrow{r(t)}$.

$$\Delta\Phi = \varphi(t_0) - 2\varphi(t_0 + T) + \varphi(t_0 + 2T) \tag{1.75}$$

A first step is the calculation of the effective wave vector $\overrightarrow{k_{\text{eff}}} = \overrightarrow{k_1} - \overrightarrow{k_2}$. As $\overrightarrow{k_1} = -k_1 \overrightarrow{x_S}$, $\overrightarrow{x_S}$ needs to be calculated. Let's define the rotation matrices along an axis Z and an axis Y:

$$R_Z(\theta) = \begin{pmatrix} \cos\theta & -\sin\theta & 0 \\ \sin\theta & \cos\theta & 0 \\ 0 & 0 & 1 \end{pmatrix} \tag{1.76}$$

$$R_Y(\theta) = \begin{pmatrix} \cos\theta & 0 & \sin\theta \\ 0 & 1 & 0 \\ -\sin\theta & 0 & \cos\theta \end{pmatrix} \tag{1.77}$$

The vector $\overrightarrow{x_S}$ is calculated at the instant of each pulse thanks to the rotation matrices:

$$\overrightarrow{x_{Si}} = R_Y(\theta^y_{Si}) R_Z(\theta^z_{Si}) \overrightarrow{x_L} \tag{1.78}$$

This calculation is an approximation as the sensor angles are considered small to use the multiplication of rotation matrices. The reflected unitary vector $\overrightarrow{x_r}$ needs to be computed to have access to the reflected wave vector $\overrightarrow{k_2} = k_2 \overrightarrow{x_r}$:

$$\overrightarrow{x}_{ri} = -\overrightarrow{x_{Si}} + 2(\overrightarrow{x_{Mi}} . \overrightarrow{x_{Si}}) \overrightarrow{x_{Mi}} \tag{1.79}$$

$\overrightarrow{x_{Mi}}$ is calculated with the use of rotation matrices:

$$\overrightarrow{x_{Mi}} = R_Y(\Theta_{Mi}) R_Z(\Psi_{Mi}) \overrightarrow{x_S} \tag{1.80}$$

The effective wave vector at the pulse i is:

$$\overrightarrow{k_{\text{eff}\,i}} = -k_1 \overrightarrow{x_{Si}} - k_2 \overrightarrow{x_{ri}} \tag{1.81}$$

A second step is the calculation of the distance atom/mirror $\overrightarrow{r_i}$ at each pulse.

$$\overrightarrow{r_i} = \overrightarrow{AO} + R_Y(\theta^y_{Si}) R_Z(\theta^z_{Si}) (\overrightarrow{OM_0} + \overrightarrow{M_0 M_i}) \tag{1.82}$$

with $\overrightarrow{AO}$ the vector atom/centre of rotation of the sensor. This distance is expressed in the laboratory frame and does not depend on the rotation. $\overrightarrow{OM_0}$ is the vector between the sensor centre of rotation and the mirror centre of rotation at rest. This vector rotates with the sensor. The last vector $\overrightarrow{M_0 M}$ is the vector mirror centre of rotation at rest and mirror centre of rotation. This vector also rotates with the sensor. At the pulse number i, the laser phase is:

$$\varphi_i = \overrightarrow{k_{\text{eff}\,i}}.\overrightarrow{r_i} \tag{1.83}$$

The phase shift of the interferometer can be computed as:

$$\Delta\Phi_{num} = \varphi_1 - 2\varphi_2 + \varphi_3 \tag{1.84}$$

Contrast

From the phase shift calculation, the contrast loss due to the sensor rotation and the mirror rotation can be computed by taking into account the atomic cloud velocity and position distributions. The contrast calculation is based on Equation 1.55.

$$\frac{\overline{C}}{C} = \frac{1}{\cos\left(\overline{\Delta\Phi}\right)} \iint \cos(\Delta\Phi(\vec{r},\vec{v})) D_{\vec{v}} D_{\vec{r}} d\vec{v} d\vec{r} \tag{1.85}$$

The velocity and position distributions are considered Gaussian:

$$D_k(k) = \frac{1}{\sqrt{2\pi}\sigma_k} \exp\left[-\frac{1}{2}\left(\frac{k-\mu_k}{\sigma_k}\right)^2\right] \tag{1.86}$$

with $\mu_k \in \{x_{MA}, y_{MA}, z_{MA}, v_{x_0}, v_{y_0}, v_{z_0}\}$, μ_k the position of the centre of the Gaussian distribution and σ_k^2 the variance of the distribution with $\sigma_k \in \left\{\sigma_x, \sigma_y, \sigma_z, \sigma_{v_x}, \sigma_{v_y}, \sigma_{v_z}, \right\}$. The distributions are then discretized from $-N_s\sigma_k + \mu_k$ to $N_s\sigma_k + \mu_k$ as depicted on Figure 1.8 with N_S the number of standard deviations considered. For $N_S = 3$ standard deviations considered, 99% of the cloud is modelled.

Then, the phase shift corresponding to the mean trajectory of the cloud $\overline{\Delta\Phi}$ is computed using the method described in the previous paragraph. The probability of each element of the six dimensions distribution $D((i,j,k,l,m,n)) = D_x(i) D_y(j) D_z(k) D_{v_x}(l) D_{v_y}(m) D_{v_z}(n)$ is computed with i,j,k,l,m,n the index associated to each discretised dimension. The phase shift for each element of the discretised cloud is computed using the previous method $\Delta\Phi(i,j,k,l,m,n)$ and the integrals along the six dimensions are computed using the trapezoidal rule.

This numerical method is a point of comparison for the theoretical model presented in the previous Sections of this Chapter. A more realistic movement of the moving parts of the experimental setup is taken into account and its effect on the interferometer studied thanks to this numerical model.

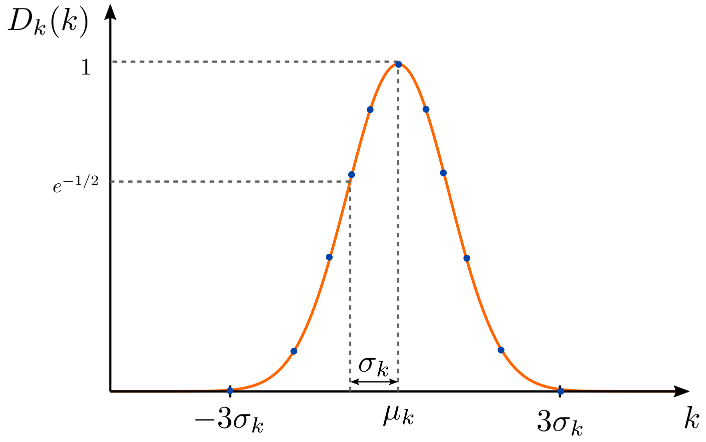

Figure 1.8: Example of a Gaussian velocity or position distribution D_k and its discretisation between $-3\sigma_k$ and $3\sigma_k$ with μ_k its mean and σ_k its standard deviation.

Conclusion

In this Chapter, the fundamental theoretical tools needed to implement an atomic interferometer were presented. Thanks to the two-photon Raman transitions, the wave packets can be manipulated to form the interferometer from atomic beamsplitters and mirror. As the Raman transitions address both the internal and external states of the atoms, the detection of the atomic state at the output of the interferometer is simplified. A simple calculation of the interferometer phase shift was presented using evolution matrices.

The influence of the sensor rotation on the interferometer was studied from a theoretical point of view and explained by the presence of inertial accelerations in a rotating frame: Coriolis, Centrifugal and Angular accelerations. The rotation of the sensor creates a phase shift bias due to these accelerations as expected. Nevertheless, a loss of contrast depending on the kinetic parameters of the cloud also appears. Similarities were observed between the effect of the retro-reflection mirror rotation and the effect of the sensor rotation. A well-chosen mirror rotation could limit the effect of the sensor rotation as described in [3, 42, 95]. By rotating the mirror in the opposite way of the sensor, the phase shift bias and the loss of contrast can be reduced as depicted in previous studies. The main goal of the rotation compensation method is to recover the contrast loss due to Coriolis acceleration. This recovery is predicted in the theory presented in this Chapter and was also demonstrated in [3] where the Earth rotation was compensated. The Angular acceleration induced contrast loss can also be compensated as shown theoretically in this Chapter. Nevertheless, the Centrifugal acceleration induced contrast loss cannot be compensated. The mirror rotation induces variations of the effective wave vector magnitude: a Centrifugal-like term appears and cannot be compensated. With this method, it would be the only source of contrast loss left.

The rotation compensation also happens to reduce the rotation induced phase shift. The Coriolis induced phase shift is cancelled as depicted in [3, 95]. However, when the mirror does not coincide with with the sensor centre of rotation, the Angular induced phase shift cannot be fully compensated due to the distance between the centres of rotation. Lastly, the Centrifugal induced phase shift is not compensated as shown in [95]. A term depending on the atoms/mirror distance and on the sensor and mirror centres of rotation distance is not cancelled. If [95] proposes to rotate the incoming laser to cancel this term, it could also be reduced by placing the mirror at an equal distance of the atomic cloud and the sensor centre of rotation.

This rotation compensation method was already implemented or described in diverse setups to compensate the Earth rotation [3, 91] or to compensate the rotation of a carrier [42, 95].

CHAPTER 2

Experimental setup and methods

Outline of the current chapter

Introduction

The experimental study was performed on the hybrid lab prototype. This lab experiment was developed to study the hybridisation of the atomic sensor with the electrostatic accelerometer (EA) [30]. Thanks to its original design using the EA proof-mass as an actuated mirror, the rotation compensation method can be implemented on this setup.

The experimental setup described in this Chapter and used during the experimental study is close to the atomic gravimeter GIRAFE [98] and the electrostatic accelerometer MicroSTAR [113] both developed at ONERA. The atomic gravimeter uses an 87 Rubidium atomic source to implement an atomic interferometer and measure the Earth gravity. The laser system used to manipulate the atoms, was built by the previous student Clément Diboune during his PhD thesis [99]. The atomic sensor head including the glass vacuum cell containing the Rubidium atoms, was developed for the GIRAFE gravimeter in the SLM unit. The electrostatic sensor head was developed for the hybrid atomic/electrostatic study by the IEA unit. In this chapter, the experimental setup and the improvements added to the laser system during this work are described. Firstly, the organisation of the different elements of the setup is depicted. Secondly, the atomic interferometer and its laser system are described. Thirdly, the operation of the electrostatic accelerometer is explained. Finally, the methods implemented to realise the experimental study are depicted.

2.1 Architecture of the experiment

In this Section, an overview of the experiment and the layout of the different elements are given. The original architecture of the experiment allows the Raman laser interrogating the atoms to be reflected on the EA proof-mass. In this prototype, the proof-mass acts as the Raman mirror and its angular position is controlled and measured thanks to the EA setup. The architecture of the sensor head is particularly important as the actuation of the mirror and sensor head will impact the rest of the study.

2.1.1 Description of the experiment

The experimental setup used to perform the rotation study, is composed of a cold atom accelerometer, an electrostatic accelerometer, a two axis gyroscope, a passive isolation platform and piezo-electric actuators. The experiment at ONERA is visible in Figure 2.1.

The architecture of the setup is the following: the ultra-high vacuum glass cell containing a hot Rubidium vapor stands above the electrostatic accelerometer. This configuration allows the electrostatic proof-mass to be employed as a retro-reflection mirror for the atomic interferometer Raman laser. The proof-mass is in electrostatic levitation between electrodes and its angular position can be driven and detected by the EA control system. The whole experiment, including the vacuum glass cell, its magnetic shield, the electrostatic accelerometer and a two-axis gyroscope, is installed on a passive vibration isolation platform. This platform is necessary to reduce the impact of ground vibrations on the interferometer. Without the platform, an acceleration noise due to vibrations would be detected by the interferometer preventing any measurement. The isolation platform itself stands on a table reposing on piezo-electric actuators. This configuration allows the rotation of the sensor head around the Z axis (see Figure 2.2) by driving the height of the piezo-electric actuator B. The rotation of the sensor is measured by a two-axis gyroscope. The architecture of the whole sensor head is depicted on Figure 2.2.

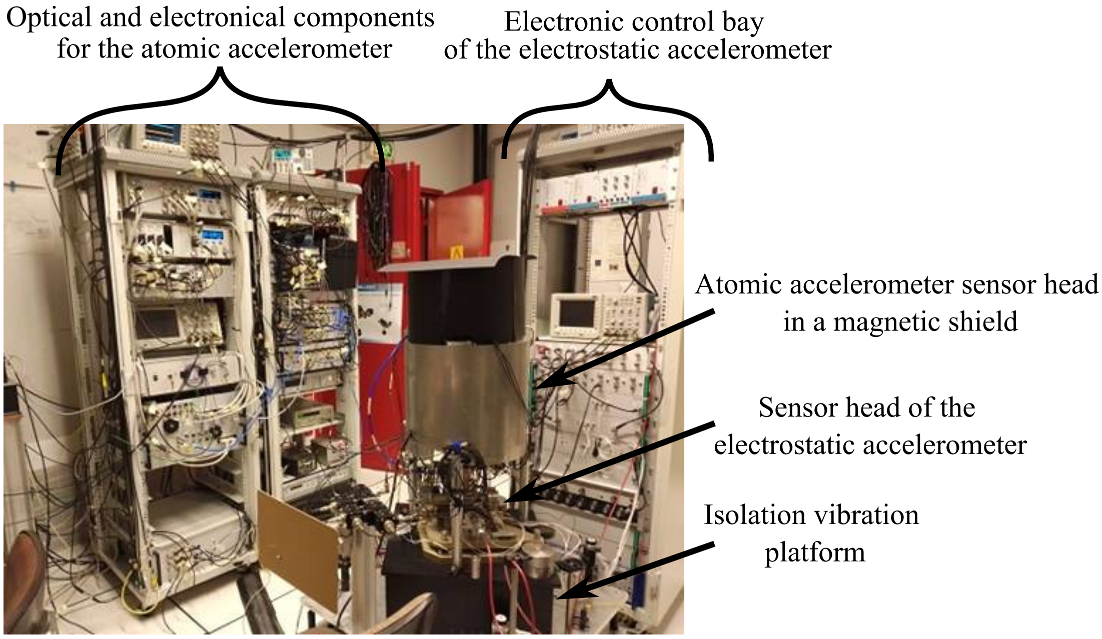

Figure 2.1: Picture of the experimental setup at ONERA. The sensor head of the atomic accelerometer including the vacuum cell, MOT coils, optical fibres inside a magnetic shield, stands above the EA sensor head. The latter is a vacuum cell containing the proof-mass surrounded by electrodes. Both sensor heads rest on a vibration platform.

2.1.2 Vibration isolation platform

The vibration isolation platform is necessary to limit the impact of vibrations on the atomic interferometer. The vibrations create a rapidly varying phase shift. This phase shift noise prevents the measurement of the interferometer phase shift. To limit this effect, the sensor head: the ultra-high vacuum glass cell, the gyroscope and the EA sensor head, repose on a passive isolation platform MinusK Technology 100BM4 visible in black on Figure 2.2. The passive isolation platform MinusK has a vertical natural frequency tunable around 0.5 Hz and rejects vibrations at a higher frequency [114] with a slope of roughly 40 dB/decade. This characteristic will be used to excite in rotation the sensor head. This passive vibration isolation system is based on the principle of a spring placed between the device to be isolated and the vibrating surface. As the spring deforms, the vibrations energy is absorbed.

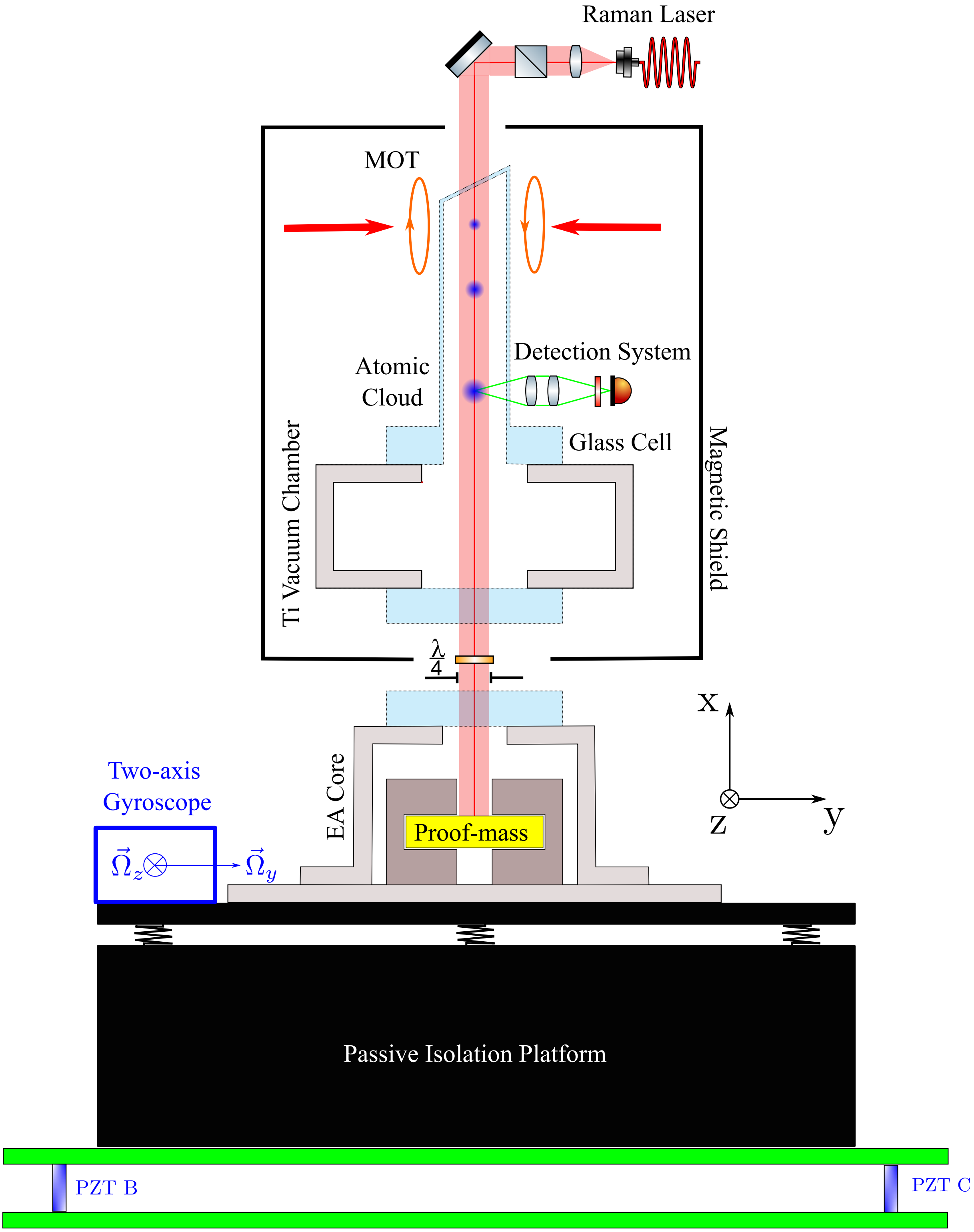

Figure 2.2: Architecture of the sensor head of the hybrid prototype. The whole sensor head can be rotated thanks to piezo-electric actuators under the sensor (PZT B and C). The atomic and electrostatic sensor heads as well as the gyroscope, rest on a vibration isolation platform. The atoms are cooled by a MOT setup at the top of the glass vacuum cell. The atoms are released and the interferometer implemented thanks to the Raman laser coming from the top of the cell. The laser goes through the cell and is reflected on the EA proof-mass. Once the interferometer is performed, the fluorescence light of the atom is collected on a photodiode.

2.1.3 Excitation platform

To study the impact of rotation on the atomic interferometer, it was necessary to impose a controlled rotation on the sensor head. That's why the vibration isolation platform supporting the sensor head lays on a metallic table called the excitation platform. The metallic table is held by three piezo vertical actuators (PZT A, B and C) as depicted on Figure 2.2 and 2.3. The piezo actuators PI P-212 80 associated with a controller PI E-500 are high-resolution linear piezo translators for static and dynamic applications. They display sub-millisecond response, sub-nanometre resolution for a travel range of 120 µm and a linearity of 0.2% [115]. They can apply a force up to 2000 N for an input voltage up to 1 kV.

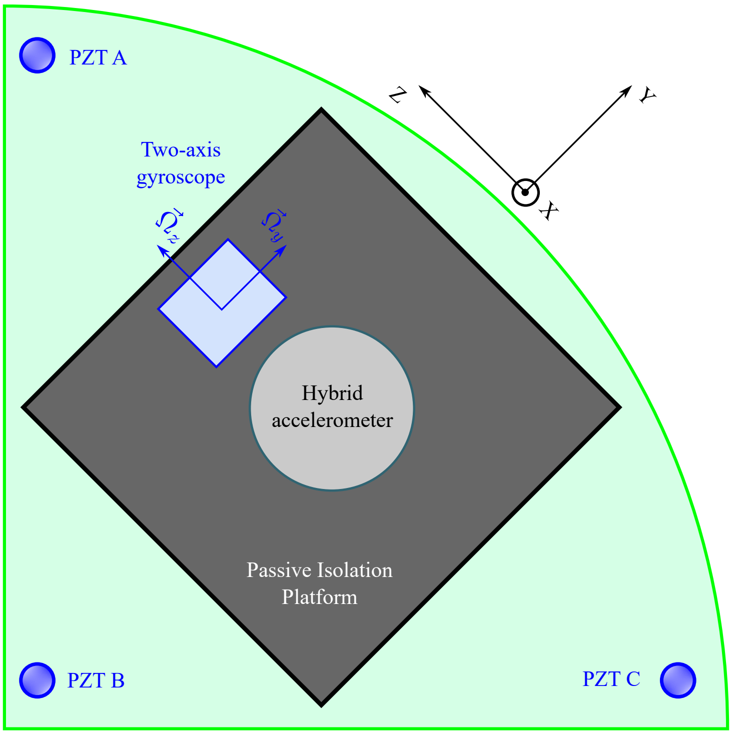

Figure 2.3: Architecture of the excitation platform. The table in green is rotated around the Z axis by driving the height of the piezo-electric actuator PZT B. The rotation of the table induces the rotation of the passive isolation platform as well as the sensor head of the hybrid accelerometer resting on the platform.

To generate an angular motion of the sensor head, a time-dependant voltage is applied to the piezo actuator B to change its height. A rotation is created along the Z axis. The angular velocity of the sensor head is measured with a two-axis gyroscope. The two-axis Innalabs gyroscope has a measurement range of $\pm 110\,^\circ\,\mathrm{s}^{-1}$ and an analogue output with a scale factor of $1.83\,\mathrm{V\,s\,rad}^{-1}$. The scale factor is known with an error of 3%. The gyroscope bandwidth is up to 300 Hz which is sufficient for the experiments performed in this study. The rotation rate frequencies won't exceed a few Hz. The output noise is below $0.01\,^\circ\,\mathrm{s}^{-1}$ or $0.2\,\mathrm{mrad\,s}^{-1}$ [116].

2.2 Atomic interferometer

The atomic interferometer has a cyclic operation at a frequency of 4 Hz. The atomic cycle begins with the cooling of the atoms and preparation of the atomic state. Then, the interferometer sequence takes place. Finally, the states of the atoms are detected and the phase shift of the interferometer extracted. The different steps of the atomic interferometer cycle are depicted on Figure 2.4. The operation of the atomic sequence is fully automated and controlled by a real-time computer. The control of the different components and data acquisition by the real-time computer will not be detailed in this manuscript.

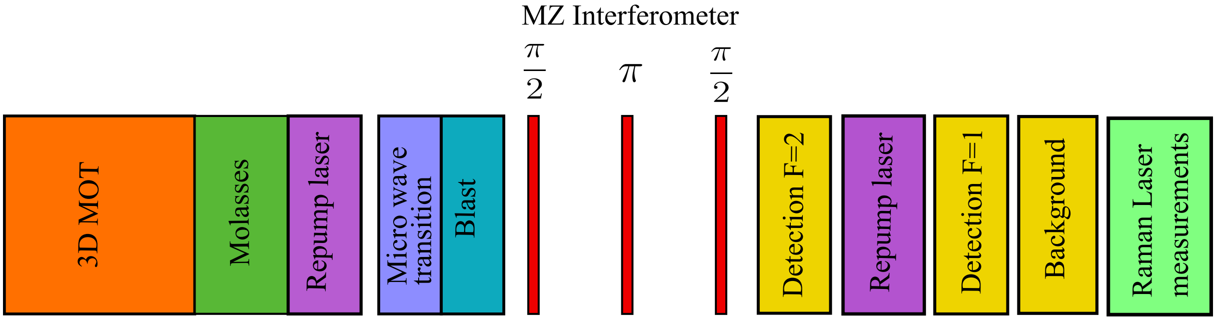

Figure 2.4: Atomic interferometer cycle. The cycle begins with the cooling of the atoms with a 3D MOT. After a stage of molasses, the atoms are prepared in the input state of the interferometer $|F=1, m_F=0\rangle$ thanks to a repump laser pulse, a micro wave pulse and a blast laser pule. Only then, the interferometer can be realised with three Raman laser pulses. Finally, the atomic states are detected by fluorescence. The atoms in the state F=2 are detected first. A repump laser transfers the atoms in F=1 to F=2. These atoms are then detected. After a detection of the background, a long Raman pulse is used to measure the Raman laser characteristics such as its intensity.

2.2.1 Cold atom source

In this paragraph, the preparation of the cold atom source of Rubidium 87 prior to the interferometer is described. This source is obtained after a stage of cooling prior to a stage of preparation of the atomic state. The different characteristics of the atomic source are also given in this paragraph.

Atomic cooling

The first step of the atomic sequence is the cooling of the Rubidium 87 from a hot atomic vapour. In the glass cell, dispensers of Rubidium are heated by a current between 2 and 3 A releasing a hot vapor of Rubidium. Then a Magneto-Optical Trap (MOT) made of two magnetic coils in anti-Helmholtz configuration and six contra-propagating laser beams in each space direction, is loaded from the background vapour for 77 ms. The physics phenomena taking place in a MOT are described in [117]. The characteristics of the MOT elements are the following. The three contra-propagating laser beams have a polarisation $\sigma^+ - \sigma^-$ and a waist 13.5 mm [111]. The total maximal optical power available for the MOT is 600 mW [99]. During this first cooling stage, the two laser frequencies needed are generated by phase modulation. The cooling laser frequency is detuned by -3Γ from the cooling transition $\left|5S_{1/2}, F=2\right\rangle \rightarrow \left|5P_{3/2}, F'=3\right\rangle$ (see Figure 2.5) with Γ the natural width of the transition. The repumping laser frequency is at resonance with the transition $\left|5S_{1/2}, F=1\right\rangle \rightarrow \left|5P_{3/2}, F'=2\right\rangle$. The magnetic field gradient generated by the coils in anti-Helmholtz configuration is null at the centre of the trap and has a magnetic field of 20 G cm^{-1} [111]. After this cooling stage, an atomic cloud of a few 10^8 atoms of Rubidium 87 is captured.

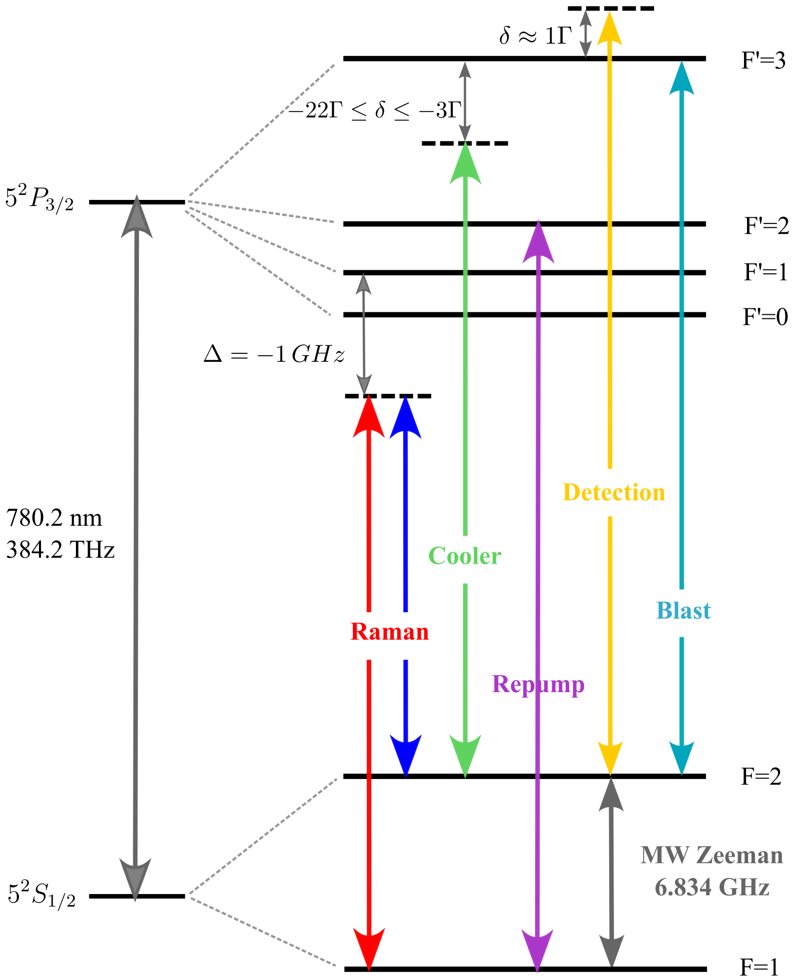

Figure 2.5: Rubidium 87 D_2 structure and laser frequencies used during the cooling, preparation of the atoms and the interferometer. During the MOT, the cooler and repump frequencies are shined. For the molasses step, the repump laser is switched off and the cooler frequency and intensity ramped. The blast and MW Zeeman frequencies are useful to prepare the atoms in $|5S_{1/2}, F = 1, m_F = 0\rangle$. The detection frequency induces the fluorescence of the atoms in F=2 allowing their detection.

Then, a second cooling stage is set up called optical red-detuned molasses. The magnetic field and the repumping laser are switched off and the laser frequency and intensity are ramped to boost sub-Doppler cooling mechanism [60, 64]. The cooling laser frequency is ramped from -3Γ to -22Γ in 3 ms. After 15 ms, the laser intensity is extinguished in 6 ms. A last repumper pulse of 0.5 ms put some remaining atoms in $|5S_{1/2}, F = 1\rangle$ to $|5P_{3/2}, F' = 2\rangle$. The cloud contains $\approx 10^8$ atoms and has now a temperature of $\approx$1 µK, a size of $\approx$1 mm [98]. At this stage, the atoms are in $|5S_{1/2}, F = 2\rangle$.

Atomic state preparation

The atoms have now to be prepared in the initial state of the interferometer $\left|5S_{1/2}, F=1, m_F=0\right\rangle$ which is less sensitive to magnetic field. After the cooling stage, the atoms are distributed into the different sub-levels of $\left|5S_{1/2}, F=2\right\rangle$ (See Figure 2.6a). A linear magnetic field along the X axis of 0.5 G is generated by two horizontal coils in Helmholtz configuration to remove the degeneracy of the Zeeman sub-levels. This field creates a frequency splitting of 700 kHz between the Zeeman levels. The different hyperfine transitions are described on Figure 2.6a and can be addressed with a micro-wave pulse. By scanning the micro-wave frequency, the different possible transitions and the splitting can be observed (Figure 2.6b).

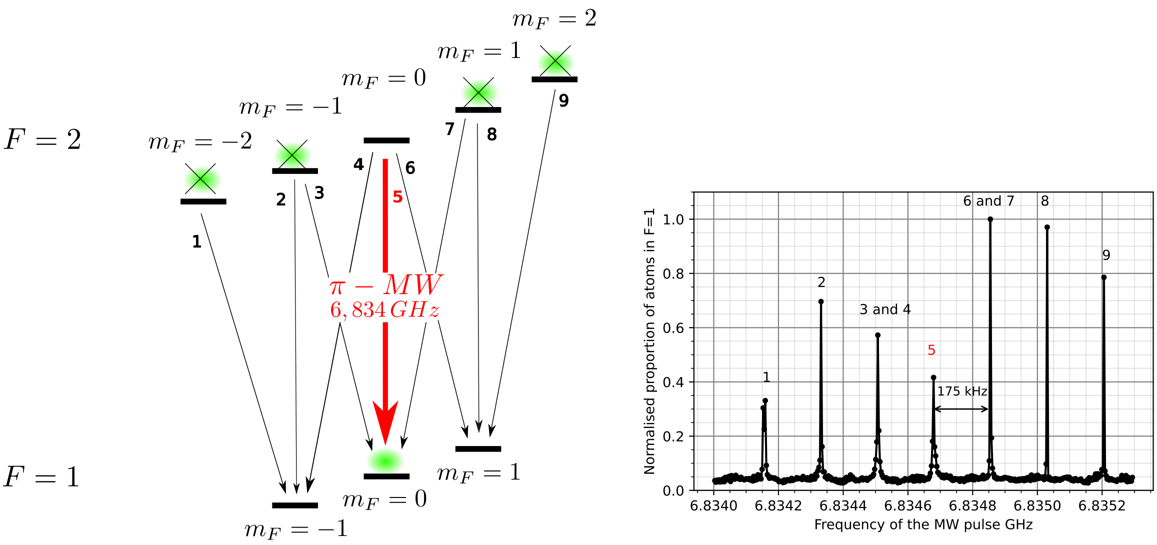

(a) Selection of the hyperfine sub-level. To prepare the atoms in the input state of the interferometer, the atoms in $\left|5S_{1/2}, F=2, m_F=0\right\rangle$ are transferred in $\left|5S_{1/2}, F=1, m_F=0\right\rangle$ with a micro-wave pulse (in red). The remaining atoms in $\left|5S_{1/2}, F=2\right\rangle$ are ejected from the cloud by transferring them an important momentum.

(b) Spectrum of the transition $\left|5S_{1/2}, F=2\right\rangle \rightarrow \left|5S_{1/2}, F=1\right\rangle$ addressed with a micro-wave pulse. To realise this spectrum, the micro-wave frequency was scanned. During the experimental sequence, only the transition 5 is addressed.

Figure 2.6: Selection of the input atomic state with a micro-wave transition.

To obtain atoms in the input state insensitive to magnetic field, the transition $\left|5S_{1/2}, F=2, m_F=0\right\rangle \rightarrow \left|5S_{1/2}, F=1, m_F=0\right\rangle$ is addressed with a micro-wave pulse of 280 µs. The pulse duration is chosen to have the maximum efficiency (see the Rabi oscillations on Figure 2.7). After, a blast laser pulse of 1 ms at resonance between $\left|5S_{1/2}, F=2\right\rangle$ and $\left|5P_{3/2}, F'=3\right\rangle$, pushes the remaining atoms in $\left|5S_{1/2}, F=2\right\rangle$. The number of atoms is roughly divided by five but the atoms are now in the initial state of the interferometer.

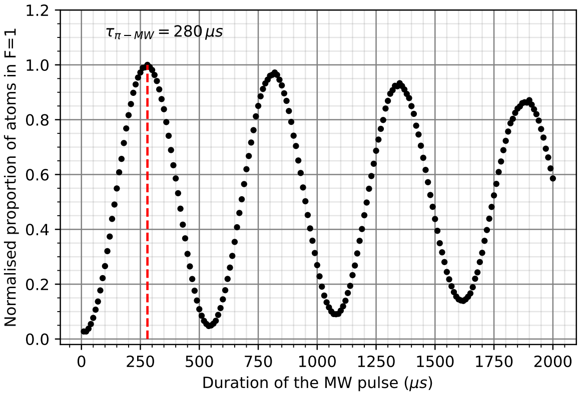

Figure 2.7: Rabi oscillations between $\left|5S_{1/2}, F = 2, m_F = 0\right\rangle$ and $\left|5S_{1/2}, F = 1, m_F = 0\right\rangle$ with a micro-wave pulse. The duration of the micro-wave pulse was scanned in order to determine the duration of a π pulse. For a pulse with a duration $\tau_{\pi-MW}$, a maximum of atoms are transferred in $\left|5S_{1/2}, F = 1, m_F = 0\right\rangle$.

2.2.2 The atomic interferometer

After the cooling stage, the atoms are free falling during 10 ms to let their vertical velocity increases. Then the Mach-Zehnder atomic interferometer is completed as the atoms are free falling. The interferometer takes place in the same glass cell as the atomic cooling. The maximal falling height is 6 cm [111] and limits the interrogation time of the interferometer. A Mach-Zehnder interferometer consists of three equally spaced laser pulses addressing two-photon Raman transitions between the hyperfine states $|f\rangle = \left|5S_{1/2}, F = 1, m_F = 0\right\rangle$ and $|e\rangle = \left|5S_{1/2}, F = 2, m_F = 0\right\rangle$. The first and third laser pulses last a duration τ. The second laser pulse last 2τ. The time delay between the three laser pulses is T the interrogation time. During this work, the time delay was set to 46 ms close to its maximum.

Characteristics of the Raman beam

The Raman laser addressing the atomic transition has the following optical path (its generation will be explained in section 2.2.4). A fibre brings the Raman laser to the sensor head with a fibre mount with an adjustable orientation. The position and angle of the Raman beam can be tuned to a certain extent allowing some alignment. Then, the beam is collimated with a lens of focal distance 96 mm. The waist of the beam after the lens is 10 mm. The polarisation after the fibre is linear. After the lens, the beam goes through a polarisation cube (see Figure 2.2). Then, the beam is sent downward with a mirror, goes through the glass cell, the atomic cloud and a $\lambda/4$ plate. The polarisation is now circular. The laser is reflected on the EA proof-mass acting as a mirror. The retro-reflected beam goes through the $\lambda/4$ plate again. When the upward laser meets the atoms, its polarisation is now linear but perpendicular to the polarisation of the downward laser as can be seen on Figure 2.8a. This choice of polarisations allows the Raman transition between the ground state and the excited state. Moreover, in this configuration called $lin \perp lin$, only the contra-propagating pair of photons can address the transition [108]. This can be seen on Figure 2.8b. The Raman photons have to be contra-propagating for the interferometer to be sensitive to the acceleration. If the contra-propagating transitions are the most probable transitions, the co-propagating transition still has a small probability due to imperfections in the laser polarisation. During the interferometer, a uniform magnetic field of 30 mG is generated along the vertical axis of the atomic free fall to lift the degeneracy of the Zeeman sub-levels [111]. The vertical axis is then the quantification axis.

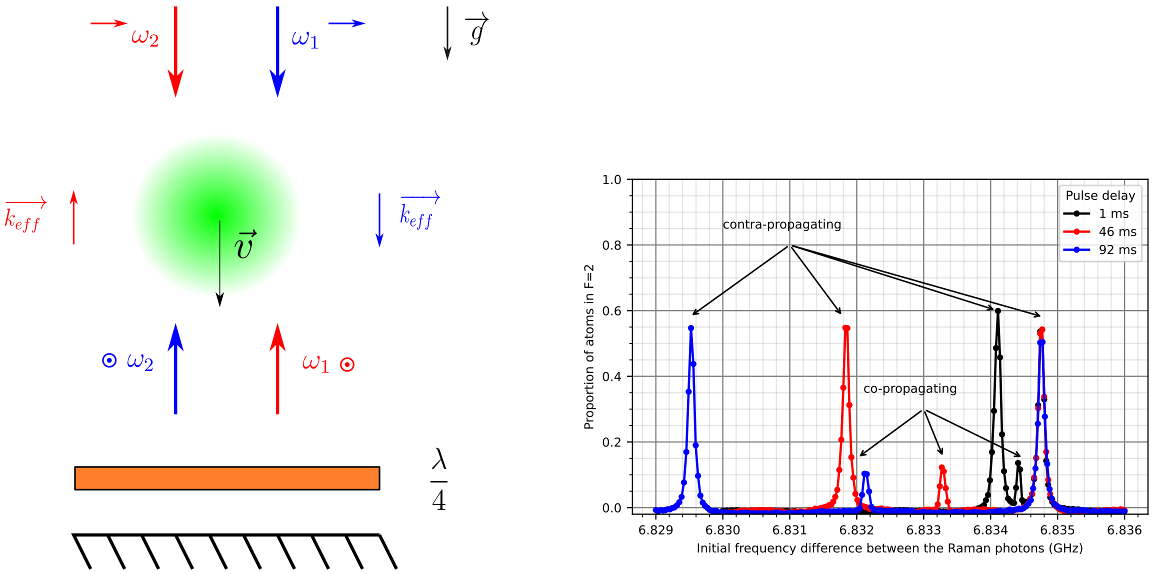

(a) Polarisation of the Raman laser. The incoming laser has a linear polarisation. The direction of the polarisation is modified by $\frac{\lambda}{4}$and the reflection on a mirror. Two different Raman transitions are then possible: the Doppler effect allows to choose between the two contra-propagating transition. Thus, the direction of the effective wave vector $\overrightarrow{k_{\text{eff}}}$ is tunable.

(b) Raman spectroscopy of the contra-propagating transitions for different Raman pulse delay after the end of the cooling stage (1 ms, 46 ms or 92 ms) corresponding to different vertical atomic velocities. As the laser frequency was chirped during the atoms free fall to compensate for the Doppler effect, one of the contra-propagating transition is addressed by the same initial frequency. The other is not corrected from the Doppler effect: its position varies on the spectrum during the fall. The pulse duration was set to τ=8 µs.

Figure 2.8: Description of the Raman transitions.

During the interferometer, the atoms are falling under gravity. Their vertical velocity increases and the Doppler effect becomes non-negligible. To compensate the Doppler effect, one of the laser frequencies has to be chirped with a rate α. At rest, the frequency difference between the two hyperfine states is 6.834 GHz. The choice of this rate allows to select the pair of the Raman photons (in red or in blue on Figure 2.8a) addressing the transition: the direction of the effective wave vector can be chosen. The red pair corresponds to an upward effective wave vector and the blue pair to a downward wave vector. On Figure 2.8b, the right contra-propagating peak corresponds to the transition at resonance at all times thanks to the chirp. The left contra-propagating peaks are not at resonance: their position is shifted as the pulse delay changes. For this experience, a rate of α =25.143 MHz s^{-1} is applied, corresponding to a downward wave vector.

Duration of the laser pulses

The duration of the pulse allows to choose between a mirror and a beamsplitter pulse as explained in Chapter 1. The duration of the second pulse τ_π has to be twice the duration of the first and third pulses $\tau_{\frac{\pi}{2}}$. To determine experimentally the optimal pulse duration, the pulse duration was scanned at different time of the fall to observe Rabi oscillations. On Figure 2.9, the transition efficiency is more than 70% and the optimal pulse duration for an atomic mirror is between 7.4 µs and 8.7 µs. To optimize the interferometer, the laser beam has to be aligned with the atomic fall. Thus, the laser beam was aligned such as Rabi oscillations are the most similar during the fall but imperfections remains due to misalignment and the cloud expansions. The intensity of the laser beam also has an impact on the optimal duration of the laser pulses. During this work, the durations of the pulses were τ_π=8 µs and $\tau_{\frac{\pi}{2}}$=4 µs.

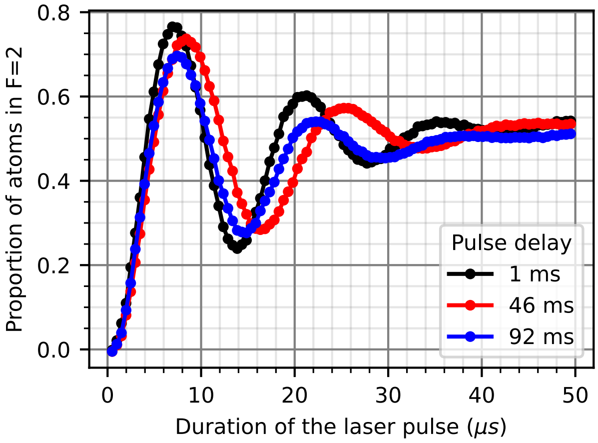

Figure 2.9: Rabi oscillations driven by a Raman pulse. The duration of the laser pulse is scanned for different pulse delays corresponding to different moments of the fall. The addressed transition is a contra-propagating transition.

On Figure 2.9, the Rabi oscillations are damped due to decoherence phenomena over the atomic cloud. Several phenomena cause the spatial inhomogeneity of the Rabi pulsation over the atomic cloud [111].

Firstly, the Rabi pulsation depends on the atoms velocity due to the Doppler effect. As the atomic cloud has a velocity distribution which can be modelled by a Gaussian distribution, the Rabi pulsation is not homogeneous over the cloud. At a time t after the release of the cloud, the cloud velocity distribution along the X axis can be written as:

$$D_{v_x}(v_x, t) = \frac{1}{\sqrt{2\pi}\sigma_{v_x}} \exp\left(-\frac{(v_x - gt)^2}{2\sigma_{v_x}^2}\right) \tag{2.1}$$

with σ_{v_x} the standard deviation of the Gaussian distribution and g the Earth gravity constant. The initial velocity along X is assumed to be null.

Secondly, the cloud also expands in position along the perpendicular plan of the beam due to the velocity distribution in this plan. Moreover, the beam has a Gaussian intensity profile and the Rabi pulsation depends on the beam intensity. Thus, the Rabi pulsation depends on the radial position of the atom r:

$$\Omega_{\text{eff}}(r) = \Omega_0 e^{-\frac{(r-r_0)^2}{\omega_0^2}} \tag{2.2}$$

with r_0 the position of the centre of the beam, ω_0 its waist and Ω_0 the Rabi pulsation for an atom at the centre of the beam. As t increases, the position distribution of the cloud broadens due to the non-zero temperature of the cloud. Assuming Gaussian position distribution, the standard deviation at t is $\sigma_r(t) = \sigma_r(0) + t\sigma_{v_r}$ with $\sigma_r(0)$ the initial standard deviation after the cooling and σ_{v_r} the deviation of the velocity distribution. During their fall, the atoms explore more and more spatial areas of the beam with a lower intensity, leading to more Rabi pulsation inhomogeneities.

A cold atom source is an advantage to limit the spatial inhomogeneities as its velocity distribution is narrow.

2.2.3 Atomic states detection by fluorescence

After the interferometer, the atomic state is detected by fluorescence. The light emitted by the atoms is collected by two lenses of focal length 26 mm and a diameter of 30 mm. The light collected is sent on a photodiode of surface ≈1 cm^2 as can be seen on Figure 2.2. When the falling atoms pass in front of the detection system, a first vertical beam addressing the transition $\left|5S_{1/2}, F = 2\right\rangle \rightarrow \left|5P_{3/2}, F' = 3\right\rangle$ detuned from resonance by 1Γ is shined to detected the atoms in the excited state $|e\rangle$. The detuning allows to push the atoms away from the detection area. Then a repump laser is shined to put the atoms from the ground state $|f\rangle$ to the excited state $|f\rangle$. A second detection laser pulse allows the detection of the atoms previously in the ground state. A last detection pulse is sent to measure the background light due to the background hot vapour for example. Thanks to the signals given by the photodiode, the number of atoms is each state can be evaluated: $N_e = S_e - S_b$ and $N_g = S_g - S_b$. The useful signal for the interferometer is the probability for an atom to be in the excited state:

$$P_e = \frac{N_e}{N_e + N_g} \tag{2.3}$$

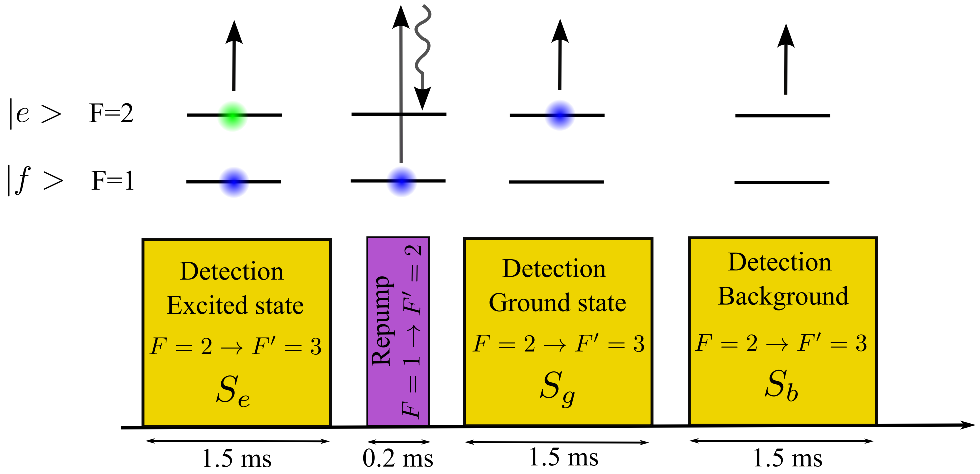

Figure 2.10: Detection by fluorescence scheme. A laser slightly detuned from $\left|5P_{3/2}, F' = 3\right\rangle$ is shinned to make the atoms in $\left|5S_{1/2}, F = 2\right\rangle$ fluoresce. Then, a repump laser transfers the atoms in F=1 to F=2. These atoms are then detected by fluorescence. Lastly, the background signal is measured.

2.2.4 Laser architecture

Several laser frequencies are needed during the cooling, interferometric and detection stages. To generate all these frequencies, a tunable laser system with a frequency close to the D_2 transition of the Rubidium 87 was built by Clément Diboune during his PhD [99]. This laser system was developed to manipulate Rubidium 87 but also Rubidium 85 and Caesium 133. In this work, only the laser system dedicated to Rubidium 87 was operated. Thus, only this part of the laser system will be detailed.

Laser system

The generation of the laser frequencies is based on the principle of a frequency-doubled Telecom laser. A primary laser diode DL1 is used as a frequency reference. Its frequency is locked on a hyperfine transition of the Rubidium 85. A secondary laser diode is used to generated the laser beam manipulating the atoms. Its frequency is locked through beat-note on the frequency of the primary diode. The design of the laser system can be seen on Figure 2.11.

The primary laser diode DL1 is an ECDL laser diode of model RIO ORION diode with a power of $\approx 15\,\mathrm{mW}$. The laser width specified is 4.9 kHz at 1560.4 nm. Its frequency is tunable with a current sensitivity of $-55\,\mathrm{MHz\,mA^{-1}}$ within a range of 14 GHz. The output of the primary diode is amplified by a 500 mW fibered EDFA laser amplifier from Keopsys at 1560 nm. Then, the laser frequency is doubled with a fibered non-linear PPLN crystal from NTT. The frequency doubling is necessary to obtain a frequency close to the D_2 transition of the Rubidium. Afterwards, the laser is sent in a glass cell containing Rubidium hot vapour to perform saturated absorption. The frequency locking of the primary diode will be explained in the next paragraph.

The secondary diode DL2 is a DFB laser diode from JDS Uniphase (CQF935) with a specified spectral width of 100 kHz at 1560.61 nm. The diode is tunable with a current sensitivity of $-130\,\mathrm{MHz\,mA^{-1}}$. Its frequency is locked on the frequency of the primary diode. The output of the laser diode is then modulated with a fibered phase modulator (Photline) to create sidebands. The frequency and amplitude of the sidebands are determined by the frequency ν_{mw} and amplitude A_{mw} of the micro wave sent in the phase modulator. Afterwards, the laser is amplified by a fibre EDFA amplifier at 1560 nm from Manlight of maximal power 2 W. The laser is then sent on a first fibred accousto-optical modulator (AOM) acting as a switch to turn ON or OFF the laser. The first order of the AOM is doubled in frequency with a PPLN crystal and used to create the MOT beams. The zero order of the AOM 1 is sent on a secondary AOM to allow the generation of the Raman pulses. Then the laser is doubled with another PPLN crystal and used to create the Raman, detection and blast laser beams. With this laser architecture, the extinctions of the two optical paths are controlled independently and without mechanical shutters. More information can be found in the thesis of Clément Diboune [99].

Frequency referencing and locking

The frequency of the primary diode has to be stable over time to be used as a reference. The frequency of the primary diode is locked on an atomic transition with saturated absorption spectroscopy and lock-in technique. With this technique, the laser can be used as a stable frequency reference. In this case, the frequency is locked on the saturated absorption peak of the cross-over between two hyperfine transitions of the Rubidium 85 $F = 3 \rightarrow F' = 3x4$ (see Figure 2.12). The saturated absorption spectrum is obtained with a counter-propagating laser inside a hot Rubidium vapor. The frequency of the primary diode is modulated at 6 kHz to obtain the error signal by lock-in detection. Then, a close-loop locking (PID) acts on the diode current to keep the frequency stable.

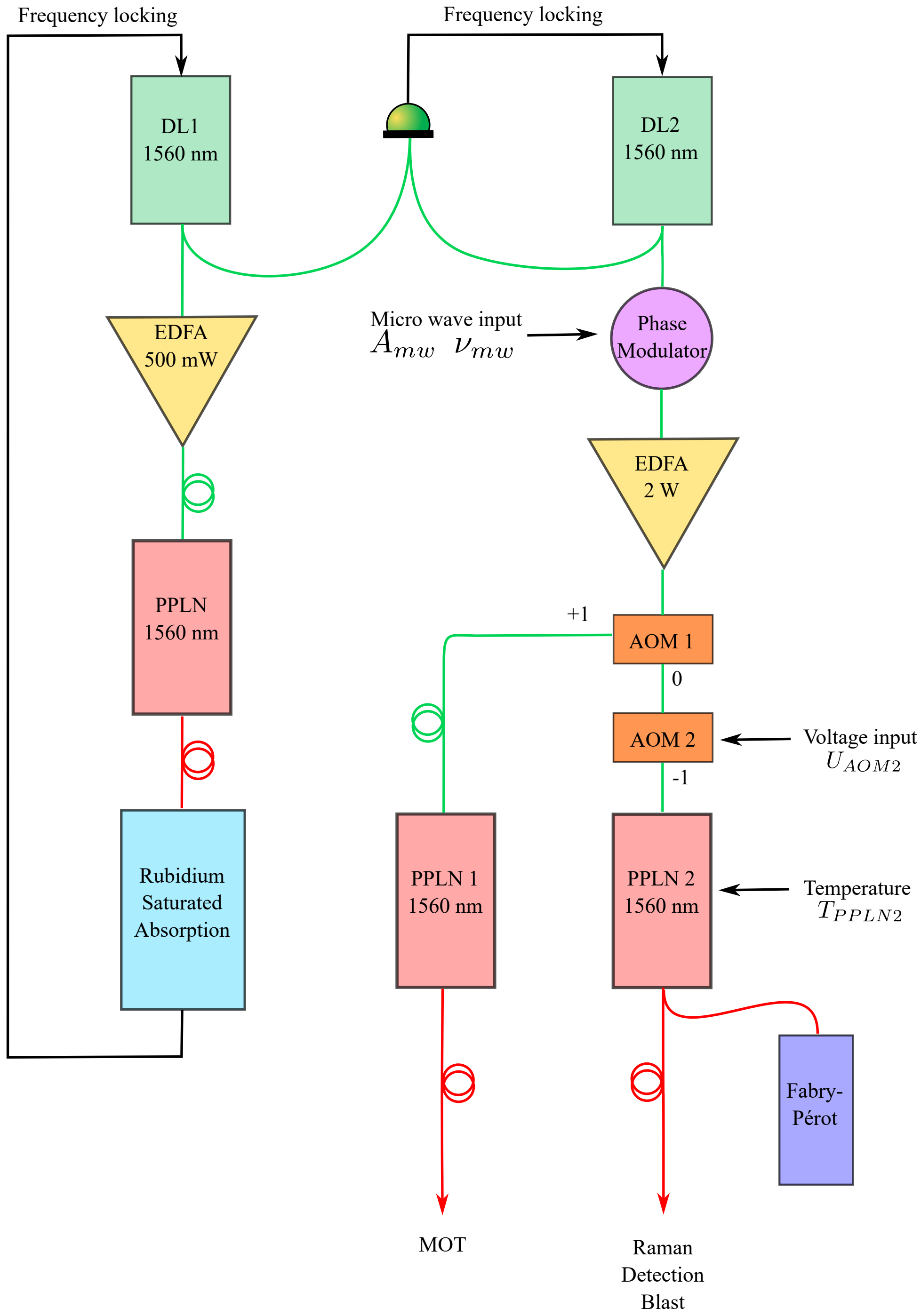

Figure 2.11: Fibred laser system for the manipulation of the Rubidium 87 based on frequency-doubled Telecom diodes. In green, fibred laser system at 1560 nm. In red, fibred laser system at 780 The diode DL1 is locked on a hyperfine absorption peak of Rubidium 85 and serves as a frequency reference. DL2 generates the light sent on the atoms. A phase modulator is used to generate the different frequencies needed.

The frequency of the secondary diode also has to be controlled with precision to address the different atomic transitions during the experiment. The beat-note between the frequency of the secondary diode and the frequency of the primary diode is locked. The difference of frequency between the two diodes is controlled and tunable. The output of the two diodes at 1560 nm are combined and sent on a fast photodiode (FPD 310 from Menlosystems) with a

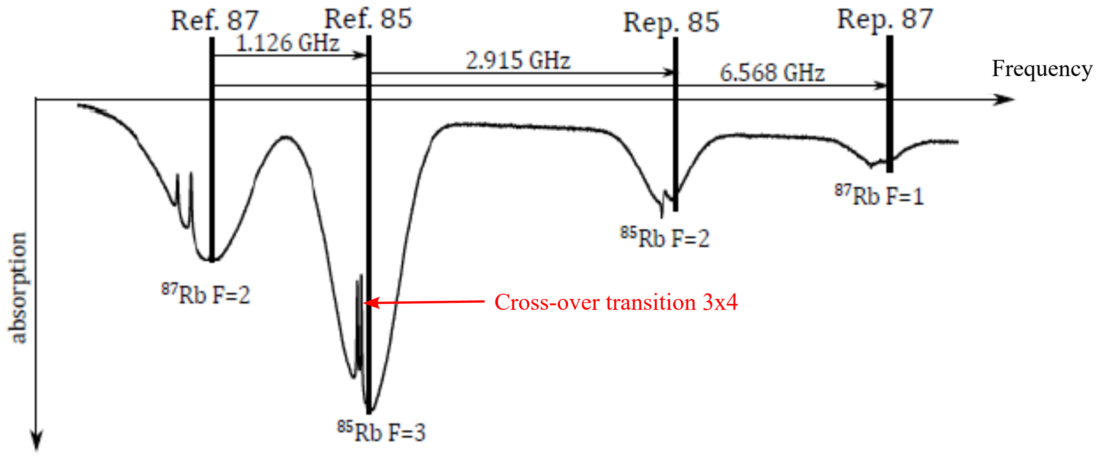

Figure 2.12: Saturated absorption spectrum of Rubidium 87 and 85 vapour. The frequency of the primary diode is locked on the cross-over transition F'=3x4 of the ^{85}Rb. This figure is extracted from [111].

bandwidth of 1 GHz. The beat note frequency is converted to a voltage to generate the error signal. Then a PID lock-in system drives the secondary diode intensity. The frequency difference between the two diodes can range from 423 MHz (cooling stage) to 914 MHz (interferometric stage). With this setup, the frequency of the secondary diode can be tuned during the experiment by changing the beat-note lock setpoint.

Generation of the different laser frequencies

During the experiment, several laser frequencies are necessary to prepare the atoms and implement the interferometer. The different frequencies necessary and the addressed transitions are visible in Figure 2.5.

- Cooling frequencies to address the transition $F = 2 \rightarrow F' = 3$ tunable between -22Γ and -3Γ (red detuned)
- Blast frequency at resonance with the transition $F = 2 \rightarrow F' = 3$
- Detection frequency detuned by +1Γ from the transition $F = 2 \rightarrow F' = 3$
- Repump frequency at resonance with the transition $F = 1 \rightarrow F' = 2$
- The two Raman frequencies detuned by -1 GHz from the transitions $F = 1 \rightarrow F' = 1$ and $F = 2 \rightarrow F' = 1$. One of the Raman frequency has to be tuneable to compensate the Doppler effect during the interferometer.

To generate the different needed laser frequencies, two mechanism are used. First, the beat note between the primary laser and the secondary laser can be tuned. Thus, changing the secondary laser frequency can be done by changing the input voltage of the close-loop locking system. The secondary laser is also modulated thanks to a phase modulator. The frequencies and amplitudes of side bands are controlled with the amplitude and frequency of the input micro-wave. Several micro-wave frequencies are needed during the experiment to generate the laser frequencies but also to address the atomic transition $F = 1 \rightarrow F = 2$ directly during the atomic state preparation (summary in Table 2.1).

Frequency	MW frequency	Agility	
Cooler/Detection/Blast	944 MHz	$-22\Gamma \rightarrow 1\Gamma$	Optical
Repump	6568 MHz		Optical
Raman	6834 MHz	Chirp $\alpha \approx 25MHz/s$	Optical
Zeeman	6834 MHZ		MW

Table 2.1: Micro-wave frequencies necessary to the experiment either to address directly an atomic transition (Zeeman micro-wave) or to generate an optical frequency.

The micro-waves needed are generated by a stable, tunable in frequency and spectrally pure hyper frequency micro wave system described in details in [99]. This system relies on a frequency comb between 6.8 and 9.1 GHz mixed with radio frequency sources. A band-pass filter selects the needed frequency.

During the cooling stage, the cooling frequency is the zero order of modulation and the repump frequency the first order of modulation. It is possible to cancel the zero order of modulation for a certain micro wave power thanks to the characteristics of phase modulation.

During the interferometric stage, the zero order is shifted by changing the set point of the secondary diode frequency lock. The first Raman laser corresponds to the zero order of modulation. The second Raman laser is the first order of modulation generated with a micro-wave at 6.834 GHz. The intensity of the micro wave allows to control the power distribution between the two Raman frequencies.

Thanks to the laser system depicted in this Section, all the frequencies of Figure 2.5 can be generated. The atoms can be cooled, prepared in the input state of the interferometer which can then be implemented and lastly, the state of the atoms can be detected.

2.2.5 Improvement of the laser system

In this section, some improvements of the laser system, done during this work, are described. The focus was on how to better control the Raman laser during the interferometer. Different locking systems were implemented to improve the stability of the Raman laser power and spectrum.

Laser power stabilisation

A stable laser intensity improves the atomic mirror and beamsplitters quality as the pulse durations are set for a given laser intensity. The stability of the contrast over time is improved. The experiment repeatability is also improved as the light-shifts become constants. The phase shift is also more stable over time.

Before the laser power stabilisation, the laser used to manipulate the atoms displayed power variations up to 7% over 64 hours. This measured was not performed when the interferometer was operated in order for the laser to operate continuously with the same parameters. This power instability could be due to the fibre amplifier and variations of the temperature as

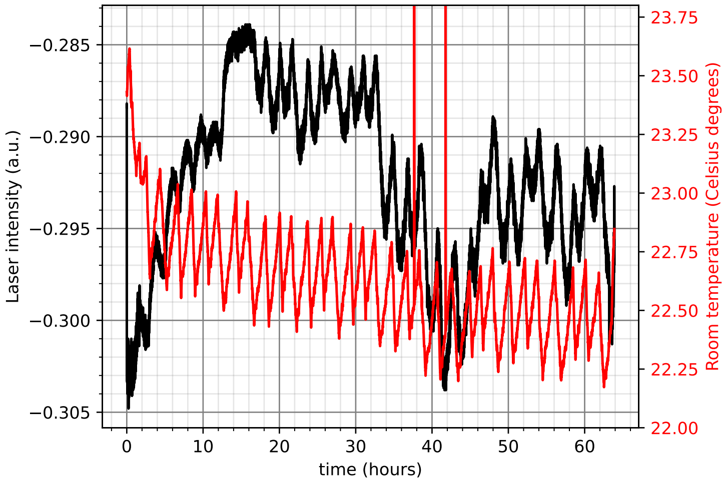

Figure 2.13: Temporal variation of the DL2 laser intensity and of the room temperature. For this measurement, the interferometer was not operated and the laser was shined continuously.

can be seen on Figure 2.13. Both laser intensity and room temperature display variations with a 2 hours period.

This instability impacted the contrast and phase shift of the interferometer. Figure 2.14a shows a variation of 6% of the contrast for a variation of 23% of the Raman laser intensity and a strong correlation between the intensity and contrast variations. This could be explained the impact of the intensity variations on the atomic beamsplitters and mirror. For this measurement, the interferometer was operated and the laser parameters were varying during the cycle. This could explain the more important variation of the laser intensity with respect to Figure 2.13. The phase shift also shows a variation of 65 mrad in the same conditions. This could be due to the evolution of the light-shifts under the intensity variations.

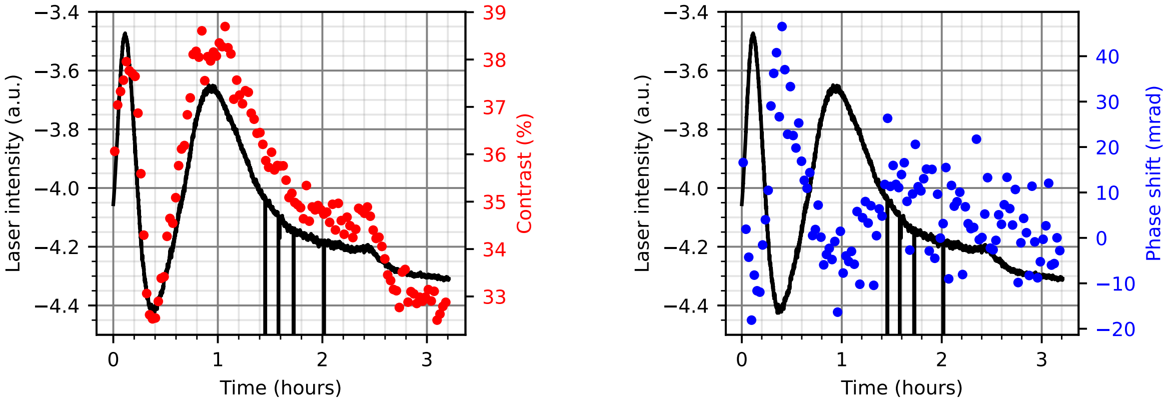

(a) Temporal variations of the contrast and laser intensity over time.

(b) Temporal variations of the phase shift and laser intensity

Figure 2.14: Influence of the unlocked laser intensity on the atomic interferometer. The interferometer was operated with an interrogation time of 46 ms and a constant mirror pulse duration $\tau_\pi = 8\,\mu s$. The Raman laser intensity was measured at the end of every cycle.

To have a stable laser intensity, a close-loop locking was implemented as described on Figure 2.15.

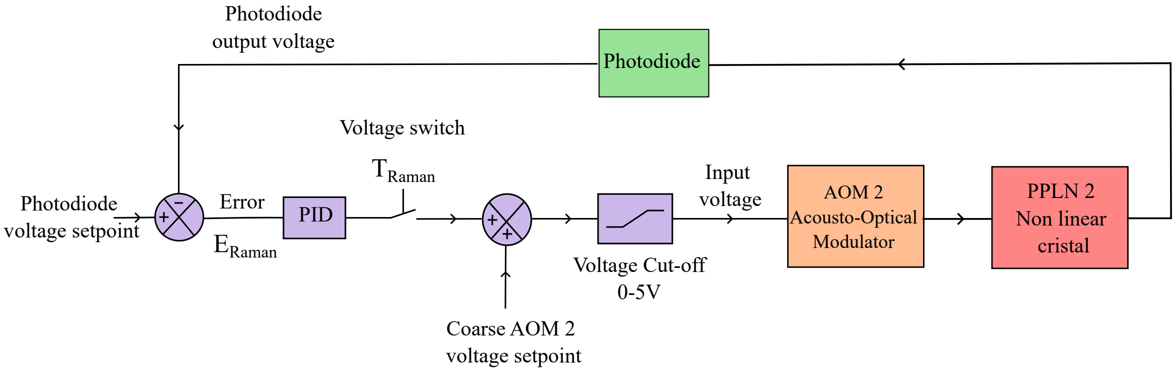

Figure 2.15: Description of the Raman laser intensity locking system. A photodiode measures the intensity of the Raman laser. Its signal is used to change the setpoint of the AOM 2. Thus, Raman laser intensity is stable over time. A switch allows the correction on the AOM 2 setpoint only during the interferometer: the other phases of the cycle are not impacted.

The intensity variations are corrected through the setpoint of AOM 2. The laser intensity is measured by a photodiode placed after the mirror redirecting the laser inside the glass cell (Figure 2.2). A new step was added in the experiment cycle (Figure 2.4) in order to measure the parameters of the Raman laser including its intensity. During this step, the configuration of the laser system is the same as the configuration for the interferometer laser pulses. During this last step, the Raman laser is shined for 21 ms. Then, the photodiode signal is compared to a setpoint and a PID is applied to the error. This error is added to a coarse voltage setpoint. A voltage cut-off system is used to limit the input voltage of the AOM 2 and avoid any damage. A system of electronical switch placed after the PID allows the retro-action only during the interferometric phase and the Raman laser measurements.

After the implementation of the laser intensity locking, the laser displays a variation of 0.8% of its intensity over 3.7 hours.

Laser spectrum control

Variations in the laser spectrum generated by phase modulation can also induce variations in the experiment. The light-shifts varies with the amplitude of the different laser frequencies affecting the phase shift of the interferometer. After the modulation, the laser spectrum consists in three main frequencies: the order 0 of modulation $\omega_0 = \omega_2$, the order 1 of modulation $\omega_1 = \omega_0 + \omega_m$ and the order -1 of modulation $\omega_p = \omega_0 - \omega_m$. The modulation frequency is ω_m (Figure 2.16a). Only ω_1 and ω_2 are used to address the Raman transitions. Higher orders of modulations are neglected. Two parameters will be considered to control the laser spectrum. First, the relative amplitude of the modulated peaks: $M = \frac{A_{-1}+A_1}{2A_0}$ and the asymmetry between the two modulated peaks $A = \frac{A_{-1}-A_1}{2A_0}$. Before the stabilisation, the mean amplitude M of the modulated peaks varied by 12% during 3 hours and the asymmetry A of the peaks varied by 6 % in the same conditions (Figure 2.16b).

To measure the laser spectrum at every experimental cycle, a Fabry-Perot interferometer was added to the fibered laser system after a fibered splitter 99/1% (Figure 2.11). The Fabry-Perot interferometer is a SA2012-5B from Thorlabs with a 10 GHz free spectral range. The acquisition of one spectrum lasts 11 ms. The laser spectrum is measured at the end of the experiment cycle during a laser pulse with the same laser parameters as the Raman laser during the interferometer. The laser spectrum can be seen on Figure 2.17b, the 0 order of modulation and the first orders of modulation are visible. Due to frequency folding, there are

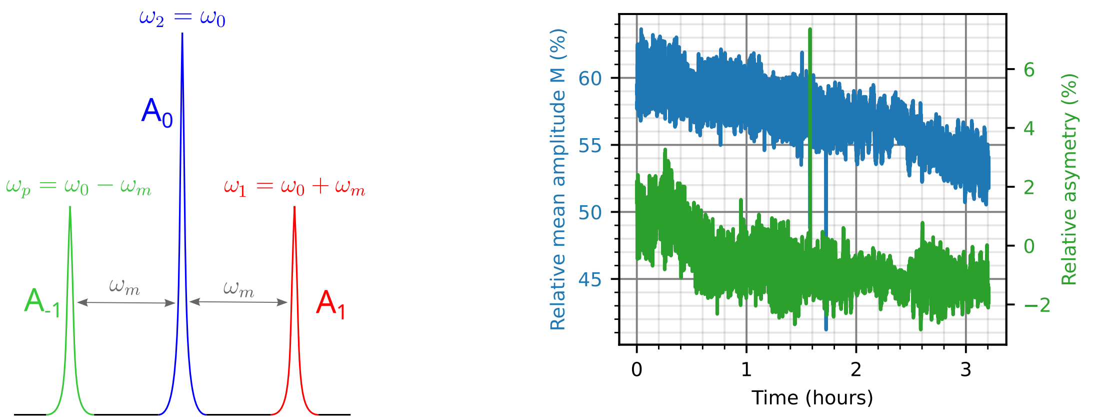

(a) Raman laser spectrum after phase modulation. ω_2 is the frequency of the carrier while Ω_1 and ω_p are the first orders of modulation. Higher orders of modulation are not represented. ω_1 and ω_2 are the frequencies used to perform the Raman transition.

(b) Temporal variations of the Raman laser spectrum. The spectrum was measured at the end of every interferometric cycle with a Fabry-Perot.

Figure 2.16: Raman laser spectrum before stabilisation.

two orders of modulation in a free spectral range. At each cycle, the amplitude of each order of modulation (0,1 and -1) is extracted numerically from the spectrum and the parameters M and A are computed.

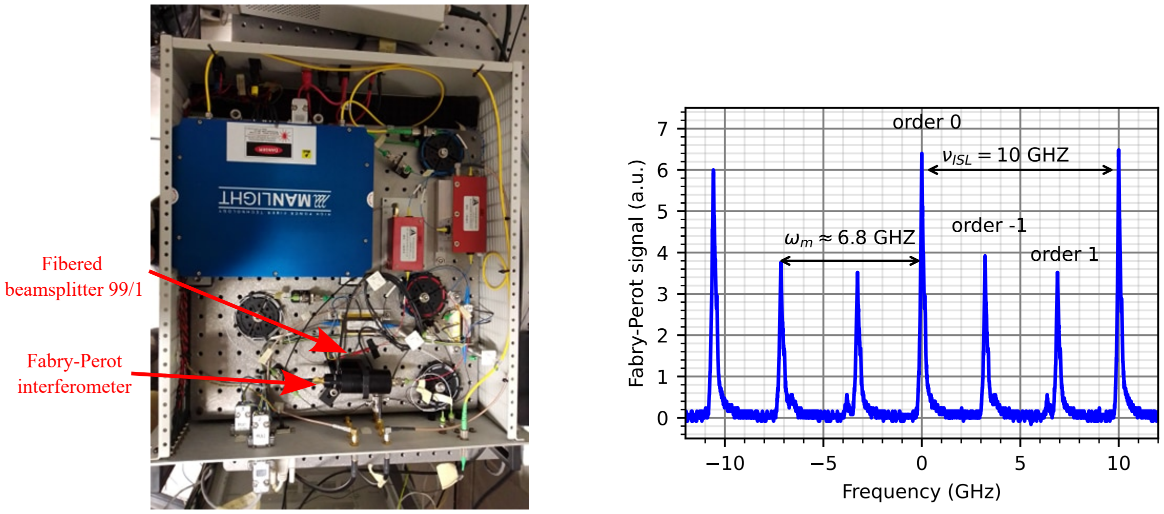

(a) Fibred laser rack for the generation of the Rubidium laser. After the AOM 2, a splitter derives a small part of the laser power on a Fabry-Perot interferometer to measure the laser spectrum.

(b) Spectrum of the Raman laser measured by the Fabry-Perot (FP) interferometer. The free spectral range of the FP is $\nu_{ISL} = 10\,\mathrm{GHz}$. The first orders of modulation at $\omega_M \approx 6.8\,\mathrm{GHz}$ are visible on the spectrum.

Figure 2.17: Raman laser spectrum measurement system.

Two locking systems are implemented to control the laser spectrum: one for the relative amplitude M and one for the asymmetry A. The mean amplitude of the modulated orders is controlled by retro-acting on the micro-wave amplitude at the input of the phase modulator. The asymmetry can be explained by imperfect phase matching in the PPLN crystal due to the crystal temperature control. The control of the asymmetry is performed by retro-acting on the temperature of the PPLN crystal. The Figure 2.18 sums up the two locking systems controlling the Raman laser spectrum.

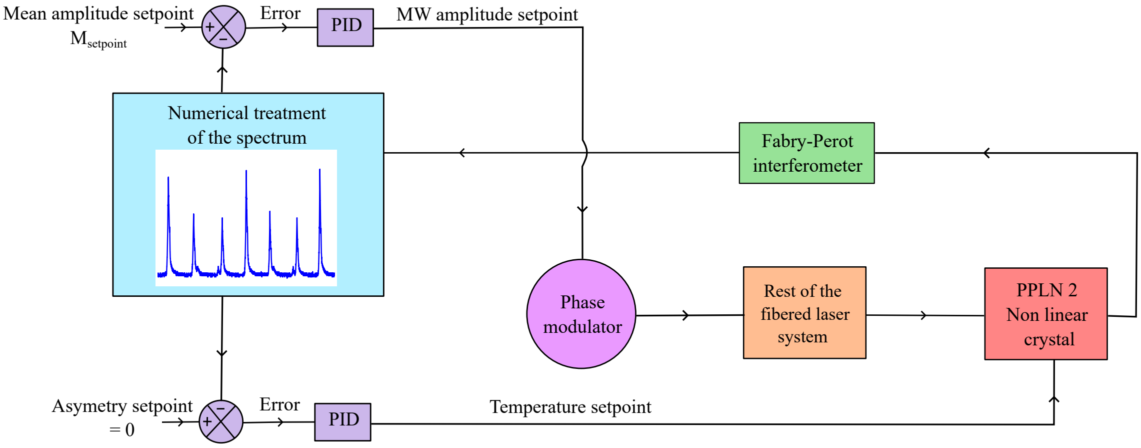

Figure 2.18: Description of the Raman laser spectrum locking system. The laser spectrum is measured by the Fabry-Perot interferometer and the mean amplitude M and asymmetry extracted numerically. The error on the mean amplitude M is used to modify the micro-wave amplitude of the phase modulator. The error on the asymmetry A allows to change the crystal temperature.

After the spectrum stabilisation, the mean amplitude M varies by 8% during 3.8 hours (12% without the stabilisation). To minimize the one photon light-shift, the M parameter is set at 57%. The variation of the asymmetry is reduced to 4% in the same conditions (6% before the stabilisation). If the laser spectrum is more stable with the locks, the stabilisation is not as effective as expected due to noise on the measurement of M and A.

Results of the laser stabilisation

The interferometer was performed with the stabilised laser with an interrogation time $T = 46\,\mathrm{ms}$ and its contrast and phase shift measured. The contrast displays a variation of 2% and the phase shift varies of 55 mrad in 3.7 hours (Figure 2.19). The effect of the stabilisation on the contrast is important as the contrast displayed a variation of 23% before the stabilisation of the laser. As the contrast was strongly impacted by the laser intensity, the stability of the contrast could be explained by the efficiency of the laser intensity lock-in system. The results on the phase shift variations are not as important. The phase shift displayed a variation of 65 mrad before the improvements and 55 mrad for $T = 46\,\mathrm{ms}$.

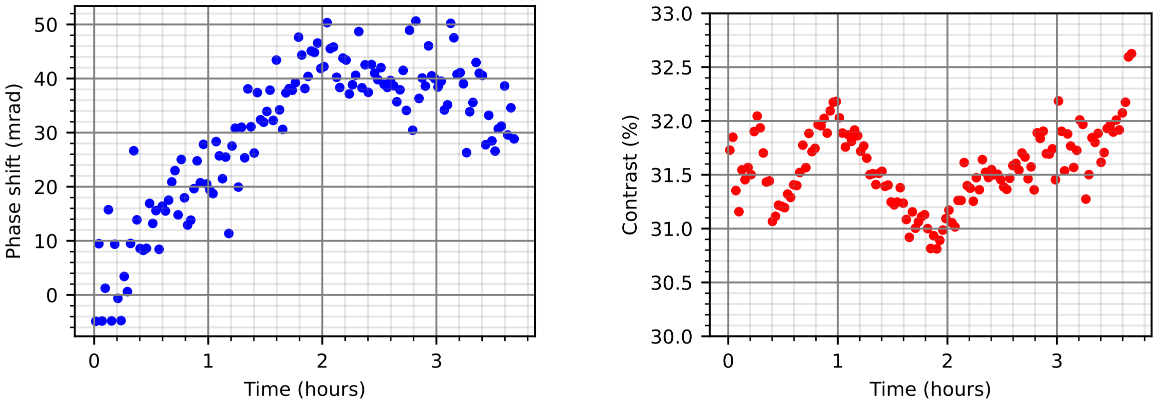

(a) Temporal variations of the interferometer phase shift after the stabilisation of the Raman laser intensity and spectrum.

(b) Temporal variations of the interferometer contrast after the stabilisation of the Raman laser intensity and spectrum.

Figure 2.19: Impact of the laser stabilisation on the interferometer. The interferometer was operated with an interrogation time of 46 ms and a constant mirror pulse duration $\tau_\pi = 8\,\mu\mathrm{s}$.

2.2.6 Performances

The performances of the atomic interferometer can be characterized by the output interference fringes as can be seen on Figure 2.20a. For this measurement, the vibrations isolation platform was ON in order to the fringes to be visible. The total interrogation time of the interferometer was $2T = 92\,\text{ms}$ which is the maximum interrogation time for this experimental setup ($T = 46\,\text{ms}$). The duration of the mirror pulse was $\tau_\pi = 8\,\mu\text{s}$ and the duration of a beam-splitter pulse was $\tau_{\frac{\pi}{2}} = 4\,\mu\text{s}$. After the improvements of the laser system presented in Section 2.2.5, the contrast C of the interferometer was 42% and the offset of the interference fringes 57%.

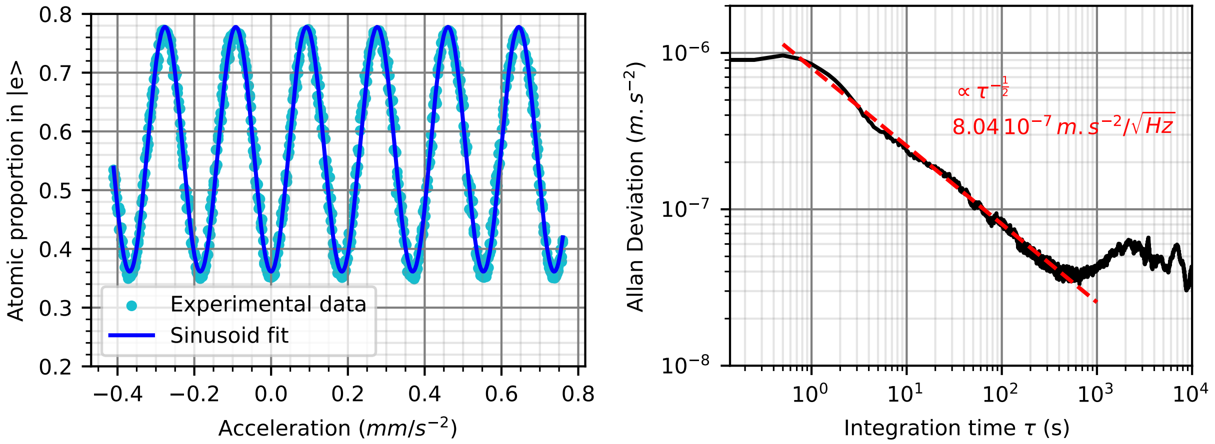

(a) Atomic interference fringes. A pseudo-acceleration is generated by scanning the laser frequency chirp α to access the fringes. The fringes display a 42% contrast.

(b) Allan deviation of the atomic accelerometer allowing to study its long term performances. For integration times below 300 s, the Allan deviation display a $\tau^{-1/2}$ decay signature of a white noise. The sensitivity (the slope of the decay) of the accelerometer is $8.04 \times 10^{-7}\,\text{m/s}^2/\text{Hz}^{1/2}$. The maximal stability reached for an integration time around 700 s and the smallest acceleration possible to detect is $4 \times 10^{-8}\,\text{m}\,\text{s}^{-2}$.

Figure 2.20: Performances of the atomic accelerometer for an interrogation time of 46 ms and the isolation vibrations platform ON.

The atomic accelerometer performances were studied with the help of the Allan deviation. The Allan deviation is a mathematical indicator useful to study the long-term stability of a sensor [118]. The Allan deviation presented on Figure 2.20b was recorded before the laser stabilisation with an interrogation time of 46 ms. Between 1 s and 300 s, the signal is dominated by white noise as the Allan variance decreases as $\tau^{-\frac{1}{2}}$ [118]. The atomic accelerometer has a sensitivity of $8 \times 10^{-7}\,\text{m/s}^2/\text{Hz}^{-1/2}$. The maximum resolution is $40\,\text{nm}\,\text{s}^{-2}$ and is reached after an integration of 16 minutes.

2.3 Electrostatic accelerometer

Electrostatic accelerometers (EA) were first developed at NASA in the 60' [119]. From the 70', numerous designs of EA were developed at ONERA such as CACTUS [120], GRADIO, STAR, CubeSTAR (still under development) [113] or more recently T-SAGE [121] for space missions dedicated to Earth observation (space gravimetry) or fundamental physics (test of the equivalence principle). Recently, some EA are being developed in China such as Taiji [122].

The electrostatic accelerometer used during this work was developed by the DPHY/IEA unit at ONERA for the hybrid experiment. The design of the EA was conceived to be operated on Earth: the electrostatic levitation is able to sustain the gravity on Earth. Thus, the design is slightly different from the EA operated in space and its performances are degraded. Moreover, a window was added to the EA vacuum cell to allow the Raman laser reflection on the proof-mass.

2.3.1 Principle of measurement

The operation of the EA resides in the electrostatic levitation of a centimetric proof mass. A detailed description of the EA operation can be found in [113, 122, 123]. The EA proof-mass is in levitation between two electrodes thanks to the electrostatic force applied between each electrode and the proof-mass. The EA architecture is displayed on Figure 2.21.

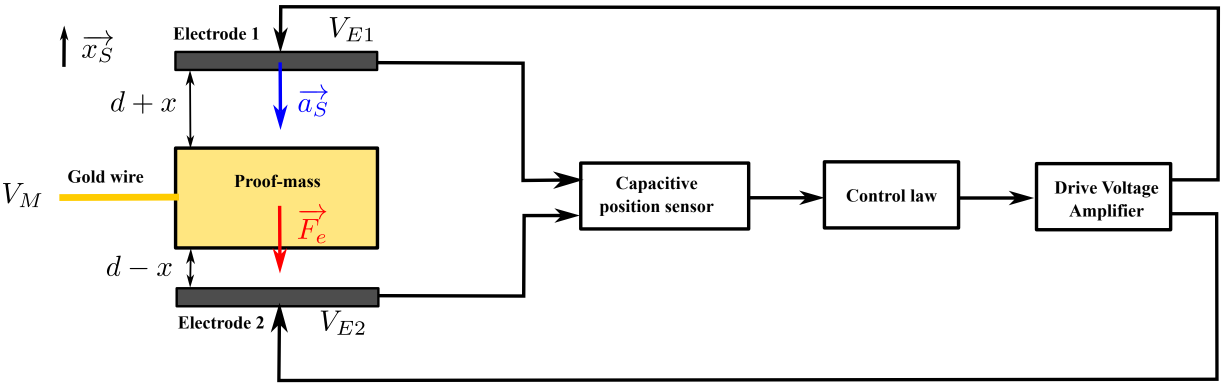

Figure 2.21: Principle of the electrostatic accelerometer. The proof-mass is in electrostatic levitation between electrodes. The electric potential of the proof-mass is controlled through a thin gold wire. The position of the proof-mass is locked at the centre of the electrodes.

Let's consider the upper electrode and the proof-mass to be two infinite charged plates. The force applied between the upper electrode and the proof-mass $\overrightarrow{F_{E2/M}}$ is then:

$$\overrightarrow{F_{E1/M}} = -\frac{\epsilon_0 A}{(d+x)^2}(V_{E1} - V_M)^2 \vec{U_x} \tag{2.4}$$

with V_{E1} the potential of the electrode, V_M the potential of the proof-mass, A the area of the electrode, ϵ_0 the electric permittivity of the vacuum, d the distance between the two plates and x the small displacement from the mean position. $\overrightarrow{x_S}$ is the unitary vector in the perpendicular direction of the electrodes surfaces. In this approximation, edge effects are neglected. The electrostatic force $\overrightarrow{F_{E2/M}}$ is the following for the lower electrode and the proof-mass:

$$\overrightarrow{F_{E2/M}} = -\frac{\epsilon_0 A}{(d-x)^2}(V_{E2} - V_M)^2 \overrightarrow{x_S} \tag{2.5}$$

In the EA setup, the electrodes potentials are opposites $V_{E1} = -V_{E2} = V_E$ for the proof-mass to be at the centre of the electrodes. In this case, the total force applied on the proof-mass is:

$$\overrightarrow{F_e} = -\frac{2\epsilon_0 A}{d^2}(V_M V_E - 2\frac{x}{d}(V_E^2 + V_M^2))\overrightarrow{x_S} \tag{2.6}$$

This force is used to maintained the proof-mass at the centre of the electrodes. To measure the position of the proof-mass with respect to the electrodes, a capacitive detection is used as the deviation x of the PM from the mean position is proportional to the differential capacitance ΔC due to the small displacement x from the centre.

$$\Delta C = \frac{2\epsilon_0 A x}{d^2} \tag{2.7}$$

To perform the capacitive detection, the electrical current has to vary in time. Thus, the voltage applied to the proof-mass V_M through the gold wire has to be modulated at a high frequency ω.

$$V_M = V_p + V_d \sin(\omega t) \tag{2.8}$$

The modulated voltage of amplitude V_d generates a small displacement of the proof-mass creating a non-zero intensity in the capacitive detection sensor (as $i(t) = C\frac{\mathrm{d}V(t)}{\mathrm{d}t}$). The output voltage of the position sensor depends on the modulated amplitude and the differential capacitance.

$$V_s \propto V_d \frac{\Delta C}{C} \tag{2.9}$$

Thanks to the capacitive detection, the proof-mass position is locked at the centre of the electrodes so $x = 0$, $x' = 0$ and $x'' = 0$.
The measurement of the acceleration undergone by the sensor can be perform as followed. The forces applied on the proof-mass are the electrostatic force $\overrightarrow{F_e}$ and the force applied to the whole sensor result in an acceleration $\overrightarrow{a_s}$. The forces compensate each other:

$$x'' = a_s - \frac{F_e}{m} \tag{2.10}$$

The position proof-mass is locked at the centre of the electrodes therefore, $x'' = 0$. Then, the acceleration of the sensor can be expressed as:

$$a_s = -\frac{F_e}{m} \tag{2.11}$$

When the proof-mass position is locked at the centre of the electrodes, the sensor acceleration is proportional to the electrostatic force applied to the proof-mass. The electrostatic force is known as the voltages applied to the electrodes and the proof-mass are controlled. The acceleration measurement can then be performed.

2.3.2 Design of the accelerometer

The electrostatic accelerometer used for this work was designed by the ONERA unit DPHY/IEA for the hybrid electrostatic/atomic accelerometer described in [30].

The design of this EA is closed to previously developed EA at ONERA such as the accelerometer boarded on GOCE mission [123]. The EA proof-mass of the lab prototype is a parallelepiped of ULE (Ultra Low Expansion glass) with a side of 4 cm and a mass of 35 g. The proof-mass is enclosed in a set of electrodes as depicted on Figure 2.22a. The six pairs of electrodes allow to control the EA movement along the six degrees of freedom: the position along each axis X, Y and Z and the three angles Φ, Θ and Ψ (Figure 2.22a). The gap between the proof-mass and the electrodes is 30 µm along the vertical axis and 300 µm along the horizontal axis. Both electrodes and proof-mass are in a vacuum chamber. A peculiarity of this EA is the addition of a glass window in the EA vacuum chamber allowing the interferometer laser to be reflected on the EA proof-mass. The hole between the electrodes allows the laser to be reflected on the proof-mass has a diameter of 7 mm (Figure 2.22b). The proof-mass is not a dedicated optical mirror but has a flatness below $\frac{\lambda}{4}$ ($\lambda \approx 600\,\mathrm{nm}$) due to the important constraints of the electrostatic control.

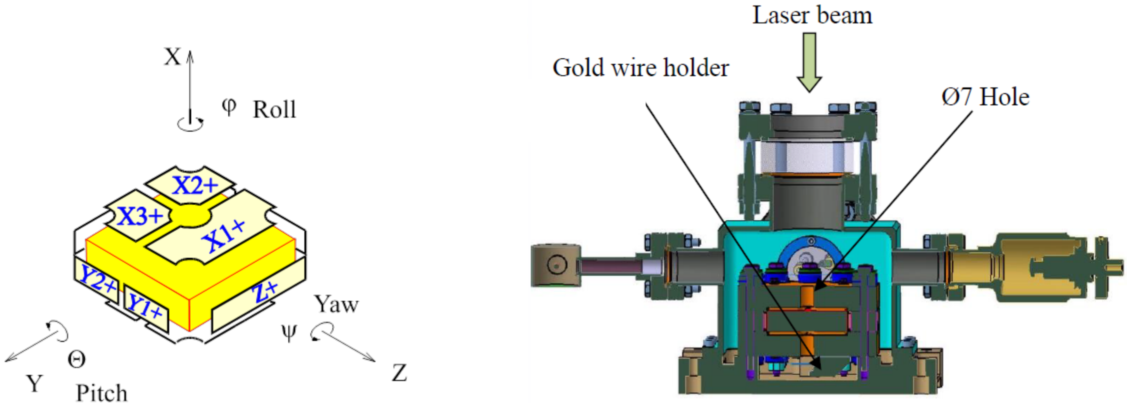

(a) Electrostatic accelerometer proof-mass and electrodes. The six pairs of electrodes allows the control of the X, Y and Z positions and the angles Φ, Θ and Ψ.

(b) Electrostatic accelerometer of the hybrid experiment. A glass window was added on the top of the vacuum cell to allow the reflection of the Raman laser on the proof-mass.

Figure 2.22: Electrostatic accelerometer design.

This EA is designed to operate on Earth and sustains gravity. The potential applied to the X electrodes $V_X = 144\,\mathrm{V}$ for the proof-mass to levitate is higher than the potential applied to the Y and Z electrodes $V_Y = V_Z = 0\,\mathrm{V}$ if the EA is vertically aligned. Nevertheless, in order to sustain misalignment and vibrations, the maximal potential for each electrode is ±300 V. The polarisation of the EA proof-mass is controlled by a gold wire of 5 µm diameter attached to the proof-mass. The proof-mass DC potential is $V_p = 100\,\mathrm{V}$. In a regular operating mode, the EA position is locked at the centre of the electrodes allowing the measurement of the acceleration undergone by the EA. Another peculiarity of the EA is the addition of a non-zero setpoint in the control law of the EA position. This non-zero setpoint allows to drive the proof-mass position along the six degrees of freedom in the limit of the displacement allowed by the gap between electrodes and proof-mass. The proof-mass can be rotated along the Θ and Ψ angles and its position is measured with the capacitive detection.

2.3.3 Calibration of the capacitive detection

Before to perform any measurements with the capacitive detection of the EA, several output channels were calibrated. The angular detections in the horizontal plan were calibrated using the deviation of the Raman laser. The vertical position detection was calibrated using the atomic interferometer signal.

Angular detections calibration

To calibrate the voltage output corresponding to the measurements of the angles Ψ and Θ on Figure 2.22a, a laser beam was reflected on the proof-mass and sent on a CCD camera. Then, a constant voltage setpoint was applied to the angular control of the proof-mass along Ψ or Θ. The position of the laser spot Δr on the CCD camera was measured for different angles of the proof-mass (Figure 2.23a). The angle θ of the proof-mass can be deduced from Δr and the total distance L between the mirror and the CCD as $\theta \approx \frac{\Delta r}{2L}$. The distance L was evaluated at 2860 ± 30 mm. The calibration factors for the Ψ and Θ channels were measured by fitting linearly the angle of the mirror as a function of the measurement voltage (Figure 2.23b). For the channel Ψ, the calibration factor is $C_\Psi = 97.5 \pm 0.4\,\mu\text{rad}\,\text{V}^{-1}$ and for the channel Θ at $C_\Theta = 108.8 \pm 0.4\,\mu\text{rad}\,\text{V}^{-1}$.

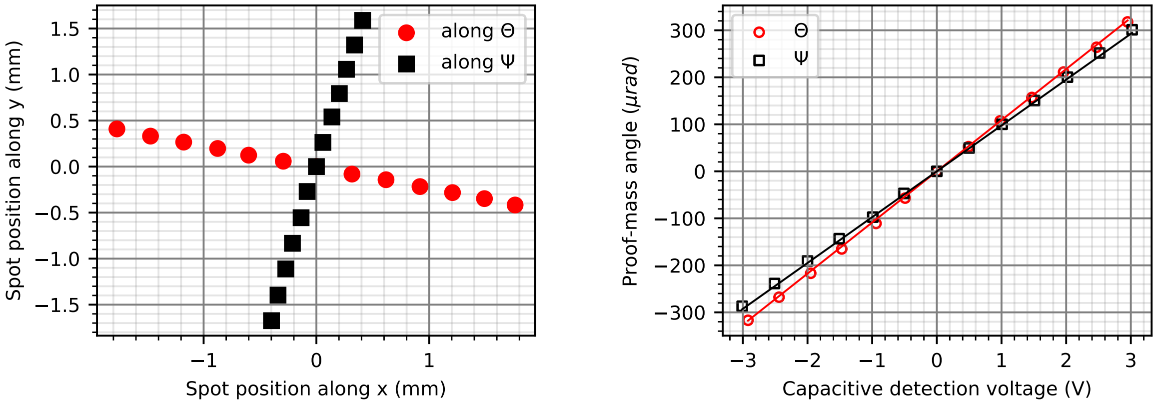

(a) Position of the laser beam on the CCD camera for different angles of the proof-mass. The angle of the proof-mass is deduced from the spot position

(b) Determination of the calibration factor. For each angle of the proof-mass deduced from the beam position, the capacitive detection voltage was measured. A calibration factor for the channels Ψ and Θ can be deduced.

Figure 2.23: Angular calibration of the EA capacitive detection.

Vertical position calibration

A calibration was also needed for the vertical position detection. The knowledge of the vertical position of the proof-mass is useful to evaluate its acceleration and the contribution of the latter to the interferometer phase shift. To calibrate the vertical detection, a time-dependent vertical movement was imposed on the proof-mass in order to generate an acceleration. This acceleration of the proof-mass is measured with the atomic interferometer. To maximise the acceleration of the proof-mass, a sinusoid movement with a frequency of $\frac{1}{2T}$ was chosen. Let's consider A_x the amplitude of the capacitive detection signal displayed on Figure 2.24a. For such a movement, the acceleration of the proof-mass is:

$$a_{proof-mass} = \frac{4K_xA_x}{T^2} \tag{2.12}$$

with K_x the calibration factor of the vertical capacitive detection. The phase shift of the interferometer is then:

$$\Delta\Phi = k_{\text{eff}} T^2 a_{proof-mass} = 4 k_{\text{eff}} K_x A_x \tag{2.13}$$

The phase shift of the interferometer was measured for different amplitude of the sinusoid vertical movement A_x. The calibration factor of the vertical capacitive detection was deduced from these measurement (Figure 2.24b). Finally, the calibration factor of the vertical detection was found to be $K_x = 1.088\,\mu\mathrm{m\,V^{-1}}$.

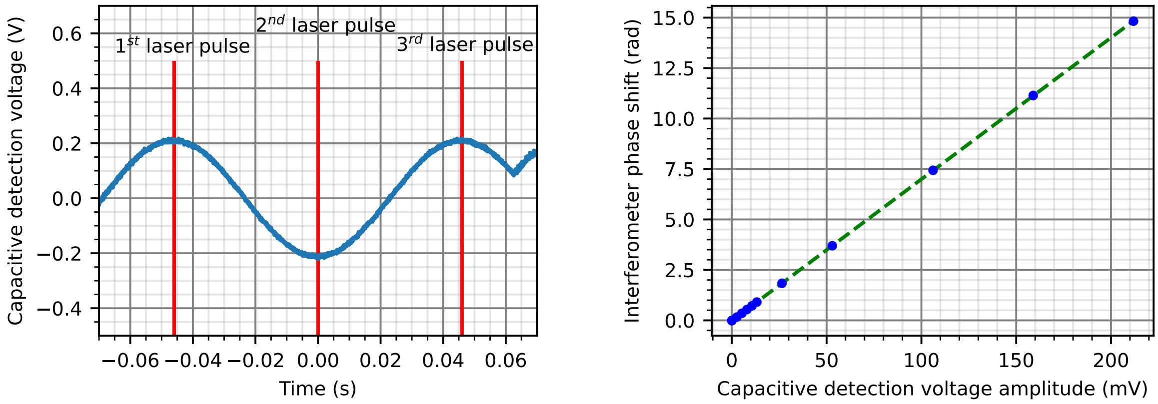

(a) Capacitive detection signal for a sinusoid vertical movement of the proof-mass at frequency $\frac{1}{2T}$. The acceleration of the proof-mass can be detected by the interferometer and the capacitive detection calibrated.

(b) Phase shift of the interferometer due to the EA sinusoid vertical movement. The amplitude of the EA movement is proportional to the phase shift allowing the measurement of the capacitive detection calibration factor.

Figure 2.24: Calibration of the EA vertical capacitive detection.

2.3.4 Performances

The electrostatic accelerometer displays an important sensitivity at high frequencies but drifts in the long term. The performances of the lab prototype were studied but its performances under the Earth gravity are deteriorate in comparison to the performances achieved in space by similar instrument. The lab prototype displays a maximal resolution of $6.5 \times 10^{-6}\,\mathrm{m\,s^{-2}}$ while GOCE instrument had a maximal resolution around $2 \times 10^{-12}\,\mathrm{m\,s^{-2}}$.

The performances of the lab prototype of the EA were studied with Allan deviation indicator (Figure 2.25a). The EA maximal resolution is $6.5 \times 10^{-6}\,\mathrm{m\,s^{-2}}$ and is achieved after an integration time of 2 s. The EA was characterised with the vibration isolation platform ON. Nevertheless, vibrations could still be detected by the EA. The maximal resolution achieved here could be limited by the vibration level and not by the EA instrument. For long interrogation times, the performances of the EA are deteriorated due to long term drift. The EA is more sensitive at high frequencies. The EA noise can also be studied with the power spectral density (Figure 2.25b). The EA acceleration noise increases for low frequencies which is characteristic of a long-term drift. [30]

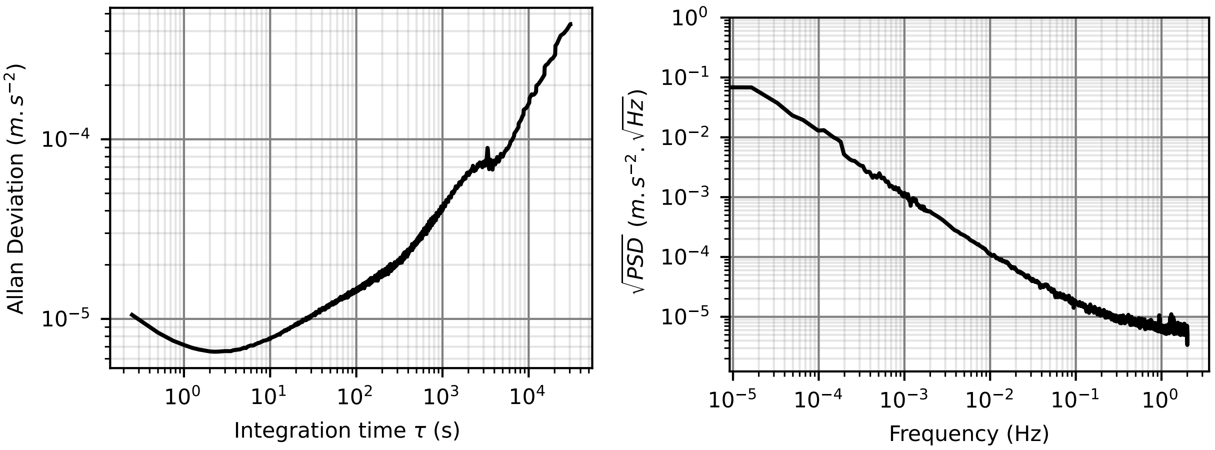

(a) Allan variance of the electrostatic accelerometer lab prototype.

(b) Acceleration noise of the electrostatic accelerometer lab prototype.

Figure 2.25: Performances of the EA accelerometer prototype on Earth. The measurements were performed on the vibration isolation platform.

2.4 Experimental methods

In this section, are presented the experimental methods used to perform, collect and explain the experimental results of Chapters 3 and 4.

2.4.1 EA alignment

To perform the experiment, the EA proof-mass had to be at the centre of the Raman laser beam and perpendicular to the Raman laser direction. Moreover, the direction of measurement of the atomic interferometer had to be aligned with the Earth gravity field $\vec{g}$. To be certain that the proof-mass was perpendicular to the Raman laser and that the direction of measurement was along $\vec{g}$, the proof-mass was rotated along the Z axis (channel Ψ) then the Y axis (channel Θ) of a constant angle. The measured acceleration is the projection of $\vec{g}$ on the measurement axis: the phase shit depends on the proof-mass angle θ. If the sensor is correctly aligned, the phase shift is a parabola centred around zero (Equation 2.14).

$$\Delta\Phi = -k_{\text{eff}} T^2 g \theta^2 \tag{2.14}$$

After several stages of alignment of the Raman laser beam direction and of the EA position, the Figures 2.26a and 2.26b were retrieved showing the correct alignment of the sensor with the vertical.

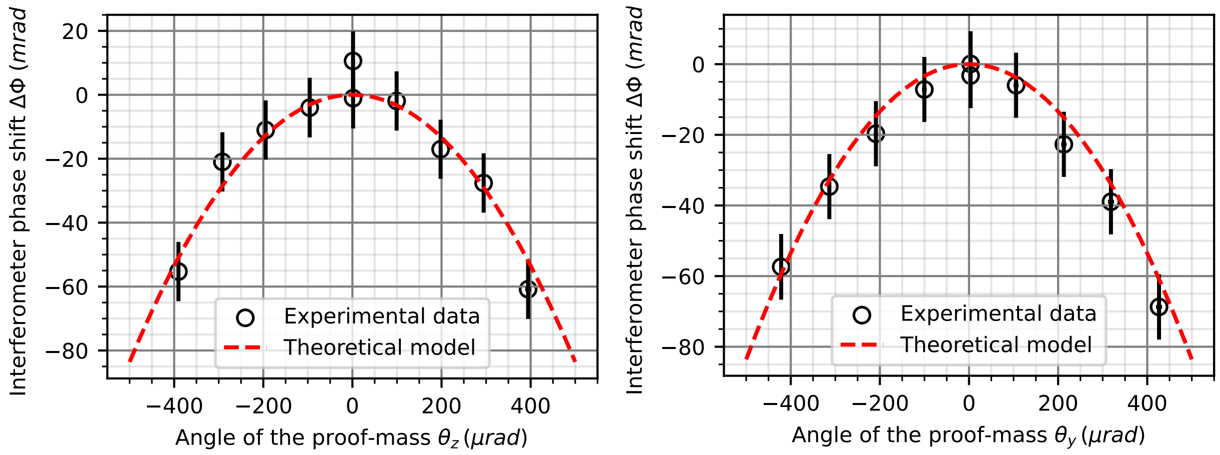

(a) Phase shift induced by a constant angle of the proof-mass around the Z axis.

(b) Phase shift induced by a constant angle of the proof-mass around the Y axis.

Figure 2.26: Alignment of the EA with the atomic interferometer. The parabolas are centred around a zero angle: the proof-mass and laser beam are correctly aligned with the Earth gravity.

2.4.2 Available rotations

The experimental setup allows the rotation of the mirror (the EA proof-mass) and of the whole sensor head. Here is a presentation of the achievable rotations on the setup and how they can be measured.

Rotation of the sensor

To rotate the whole sensor, a time-dependent voltage is applied to the piezo-electric actuator B on Figure 2.2. To benefit from a smooth dynamic of the sensor and thus not exciting some vibrations mode of the instrument mechanical structure, we choose to apply on the piezo actuator a sinusoidal input voltage at a 4 Hz frequency which is the repetition rate of the experimental cycle. This way, the rotation excitation is synchronised with the interferometer. The Minus-K platform helps isolating the setup from the ground vibrations but also from the high frequency vibrations generated by the piezo actuator. The rotation rate of the upper part of the isolation platform is measured with the two-axis gyroscope.

Two different cases of sensor rotation were studied. The first case corresponds to a sinusoidal angular movement at 4 Hz with a phase that maximised the angular velocity and minimises the angular acceleration (Equation 2.15). The angular movement of the sensor is the most linear possible during the interferometer. As the rotation rate is measured by the gyroscope, the amplitude and phase of the angular movement can be deduced by simple integration from the gyroscope signal (Figure 2.27a).

$$\theta_{S1}(t) = A\sin(\omega(t - t_0 - T)) \tag{2.15}$$

with A the amplitude of the angular movement, ω its frequency, t_0 the instant of the first pulse of the interferometer and T the interrogation time. For the second case, the phase chosen maximises the angular acceleration and minimises the angular velocity of the sensor (Equation 2.16). The angular movement can also be deduced from the gyroscope measurement (Figure 2.27b).

$$\theta_{S2}(t) = A\sin\left(\omega(t - t_0 - T) + \frac{\pi}{2}\right) \tag{2.16}$$

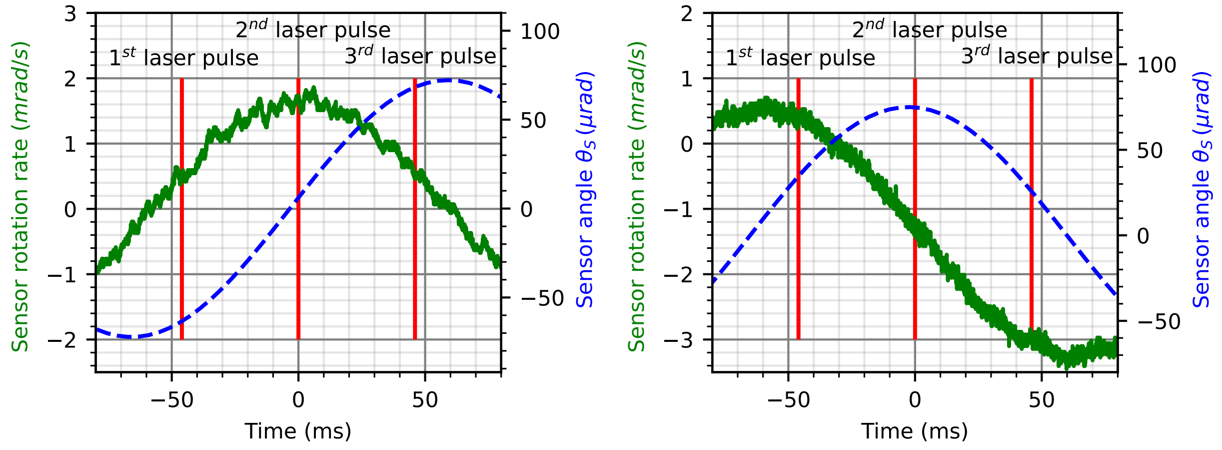

(a) First case: maximal angular velocity.

(b) Second case: maximal angular acceleration.

Figure 2.27: Rotation of the sensor. In red are represented the three laser pulses of the interferometer. In green, the gyroscope signal and in blue the sensor angular position deduced by integration of the gyroscope signal.

Rotation of the mirror

The retro-reflection mirror can be rotated by driving the electrostatic force applied between the electrodes and the proof-mass. The angle between the proof-mass and the electrodes is measured by the capacitive detection of the electrostatic accelerometer: the angular position of the mirror is directly measured. For this work, the mirror was rotated along the Z axis (the Ψ channel) and the Y axis (the Θ channel) (Figure 2.22a). During this study, several angular movements were experimented such as angular ramps to study the impact of a constant angular rate (Equation 2.17) in blue on Figure 2.28a.

$$\theta_{M1}(t) = \Omega.(t - t_0) \tag{2.17}$$

with Ω the angular velocity and t_0 the instant of the first pulse of the interferometer.

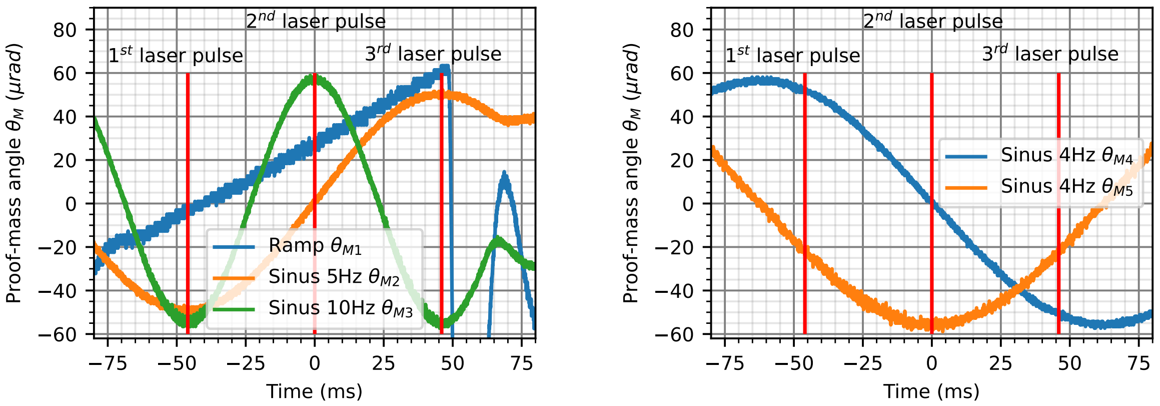

(a) Angular movements presented in Chapter 3 to study the impact of the mirror rotation on the interferometer.

(b) Angular movements presented in Chapter 4 to study the rotation compensation.

Figure 2.28: Different schemes of mirror rotation implemented in this study. In red are represented the three pulses of the interferometer. In blue, orange and green are represented the capacitive detection of the EA.

Another case minimising the impact of the angular acceleration was studied. A sinusoidal angular movement at a frequency $\frac{1}{4T} \approx 5\,\mathrm{Hz}$ was impose on the EA proof-mass (Equation 2.18) in orange on Figure 2.28a. This case advantage is the smooth movement imposed to the mirror limiting uncontrolled response of the proof-mass at the end of the angular ramp.

$$\theta_{M2}(t) = A\sin\left(\frac{\pi}{2T}(t - t_0 - T)\right) \tag{2.18}$$

with A the amplitude of the angular movement, ω its frequency and T the interrogation time of the interferometer. A case θ_{M3} maximising the angular acceleration compared to the two previous cases θ_{M1} and θ_{M2} was implemented to study its effect. A sinusoidal angular movement at a frequency $\frac{1}{2T} \approx 10\,\mathrm{Hz}$ was imposed on the EA proof-mass (Equation 2.19) in green on Figure 2.28a.

$$\theta_{M3}(t) = A\sin\left(\frac{\pi}{T}(t - t_0 - T) + \frac{\pi}{2}\right) \tag{2.19}$$

The two last cases are similar to the ones implemented for the sensor movement in order to study the rotation compensation method: the angular movement has to be opposite to the angular movement of the sensor. In the first case, the angular acceleration is minimised (Equation 2.20) in blue on Figure 2.28b. In the second case, the angular acceleration is maximised (Equation 2.21) in orange on Figure 2.28b.

$$\theta_{M4}(t) = A\sin(\omega(t - t_0 - T) - \pi) \tag{2.20}$$

$$\theta_{M5}(t) = A\sin\left(\omega(t - t_0 - T) - \frac{\pi}{2}\right) \tag{2.21}$$

2.4.3 Fringes acquisition

To study the impact of rotation on the interferometer, the contrast and phase shift have been measured. To access these parameters, interference fringes are acquired by scanning the frequency chirp rate α that allows to sweep artificially the acceleration seen by the atoms. This method allows to obtain atomic interference fringes from which the phase shift and contrast of the interferometer can be deduced with a sinusoidal fit. Interference fringes are visible on Figure 2.29 without rotation and in the presence of a sinusoidal angular movement of the EA proof-mass at $\approx 10\,\mathrm{Hz}$. To obtain this kind of atomic signal, the MinusK isolation platform has to be operating, otherwise the atomic signal is blurred. The phase shift cannot be retrieved as ground vibrations add noise to the interferometer signal. The contrast is deduced from the amplitude A of the sinusoid fit and the phase shift from its phase φ. The fit function is:

$$P_{\mathrm{fit}}(a) = P_0 - A\cos(-\omega a + \varphi) \tag{2.22}$$

with A, P_0 and φ free parameters adjusted by the fit. The fringes pulsation is set to $\omega = k_{\mathrm{eff}}T^2$ and the abscissa is the pseudo acceleration generated by the scan of the frequency chirp rate. The zero of acceleration is set when the chirp rate compensates exactly for the Doppler effect due to the Earth gravity. The phase reference is the phase shift in the absence of rotation.

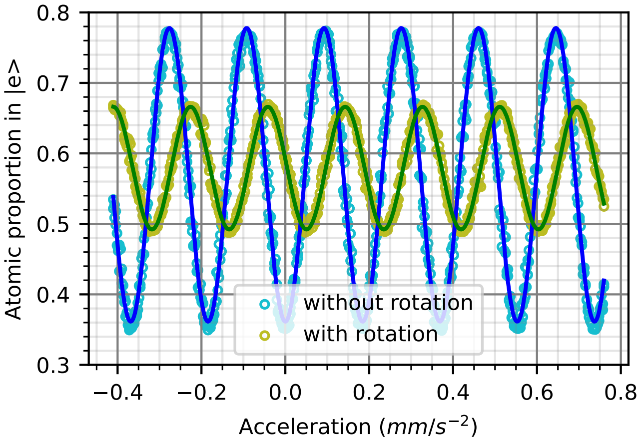

Figure 2.29: Interference fringes with the mirror at rest in blue and with a 10 Hz angular movement of the mirror in green. In the presence of a mirror rotation, the angular acceleration is $\dot{\Omega}_M = -52.4\,\mathrm{mrad\,s^{-2}}$ and the angular velocity is null.

2.4.4 Limitations of the experiment

To explain the experimental results, several side effects linked to the sensor rotation have to be considered. These side effects result in experimental limitations.

Sensor rotation

The sensor is set in motion mechanically and the rotation generated is not perfectly controlled as the transfer function of the isolation platform cannot be anticipated. Moreover, the position of the sensor centre of rotation is not known precisely. The sensor rotation setup was conceived to create a rotation around the $\overrightarrow{z_S}$ axis but a component of the rotation appears around the $\overrightarrow{y_S}$ axis. The rotation around the $\overrightarrow{y_S}$ axis has an amplitude of 8% of the main rotation around the $\overrightarrow{z_S}$ axis and has a phase shift of 0.5 rad with the main rotation. The rotation around the $\overrightarrow{y_S}$ axis was measured by the two axis gyroscope as can be seen on Figure 2.30.

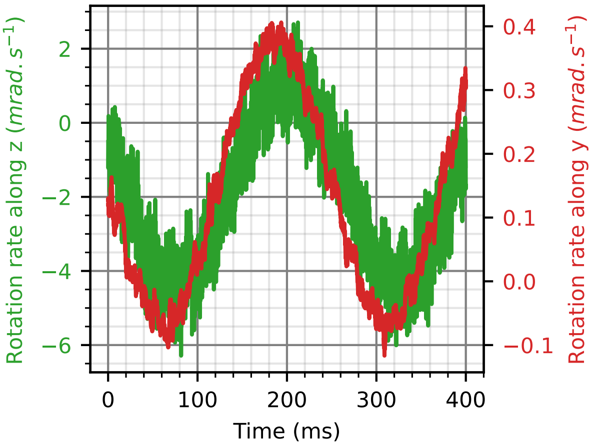

Figure 2.30: Rotation rates measured by the two-axis gyroscope. The main rotation in green is around the $\overrightarrow{z_S}$ axis. The secondary rotation is around the $\overrightarrow{y_S}$ axis.

The effect of the residual rotation around the $\overrightarrow{y_S}$ axis can be computed using 2.23. This expression is valid only if the cross-terms between the rotation around $\overrightarrow{y_S}$ and $\overrightarrow{z_S}$ are neglected.

$$\overline{\Delta\Phi}_{SY} = k_{\text{eff}}T^2\left[2\Omega_{Sy}v_{z_0} + \dot{\Omega}_{Sy}(v_{z_0}(t_0+T)+z_{OA}) + \Omega_{Sy}{}^2\left(a_{x_L}(\frac{t_0^2}{2}+t_0T+T^2)+v_{x_0}(t_0+T)+x_{OA}\right)\right] \tag{2.23}$$

with Ω_{Sy} the angular velocity and $\dot{\Omega}_{Sy}$ the angular acceleration around the $\vec{y_S}$ axis seen by the interferometer.

Mirror rotation

When the sensor is rotating and the electrostatic proof-mass levitates, a vertical acceleration of the proof-mass with respects to its electrodes is observed due to limitations in the servo loop controlling the proof-mass position. This vertical acceleration creates an additional phase shift on the interferometer. As the position of the proof-mass is measured by the capacitive detection, the vertical acceleration of the proof mass can be computed as well as the induced phase shift (Equation 2.24).

$$\Delta\Phi_{acc\,EA} = k_{\text{eff}}T^2(\delta x_{EA}(t_0) - 2\delta x_{EA}(t_0+T) + \delta x_{EA}(t_0+2T)) \tag{2.24}$$

with δx_{EA} the variation of the EA proof-mass position with respect to a rest position along the $\overrightarrow{x_S}$ axis. This position is measured during the interferometer thanks to the capacitive detection.

The impact of those two side phenomena on the phase shift can be computed and corrected from the experimental data.

2.4.5 Atomic cloud kinematic parameters

As explained in Chapter 1, the atomic cloud kinematic parameters play an important role in how the rotation affects the interferometer. The knowledge of these parameters supports the calculation of the rotation effects on the phase shift and contrast. Some of the cloud parameters such as its temperature, size, mean velocity, mean position relative to centre of rotation of the mirror were measured by rotating the retro-reflection mirror. These measurements are detailed in Chapter 3. Some distances such as the distance between the atomic cloud A and the mirror centre M along the X axis or the distance between the atomic cloud A and the sensor centre of rotation O depends on the setup building. Some kinematic parameters of the cloud along the x axis are measured by Raman spectroscopy. Nevertheless, the size of the cloud cannot be measured by spectroscopy and was expected to be the same as measured in [2]. The acceleration of the atoms is only due to the Earth gravity so its value is $a_{x_L} = 9.81\,\mathrm{m\,s^{-2}}$. The Table 2.2 sums up the parameters used to estimate the phase shift and contrast in the rest of this work.

2.4.6 Computation of the phase shift and contrast

To explain the experimental results presented in Chapters 3 and 4, the phase shift and contrast of the rotating interferometer were computed using two different methods.

Theoretical model

The theoretical model is based on the theoretical calculation of the phase shift and contrast presented in Chapter 1. For example, for a rotation of the sensor around the $\overrightarrow{z_S}$ and of the

Parameter	Value	Type of measurement
v_{x_0}	$-23.1\,\mathrm{mm\,s^{-1}}$	Raman spectroscopy
v_{y_0}	$-1.3\,\mathrm{mm\,s^{-1}}$	Mirror rotation
v_{z_0}	$0.31\,\mathrm{mm\,s^{-1}}$	Mirror rotation
σ_{v_x}	$11.3\,\mathrm{mm\,s^{-1}}$	Raman spectroscopy
σ_{v_y}	$10.8\,\mathrm{mm\,s^{-1}}$	Mirror rotation
σ_{v_z}	$11.1\,\mathrm{mm\,s^{-1}}$	Mirror rotation
x_{MA}	420 mm	Mechanical
y_{MA}	1.09 mm	Mirror rotation
z_{MA}	0.66 mm	Mirror rotation
σ_{x_0}	0.5 mm	from [2]
σ_{y_0}	0.42 mm	Mirror rotation
σ_{z_0}	0.66 mm	Mirror rotation
x_{OA}	550 mm	Mechanical
y_{OA}	$\in [-6\,\mathrm{mm}, -5\,\mathrm{mm}]$	Free parameter
z_{OA}	$\in [12.4\,\mathrm{mm}, 20\,\mathrm{mm}]$	Free parameter

Table 2.2: Kinematic parameters of the atomic cloud used to compute the phase shift and contrast of the rotating interferometer.

mirror around the $\overrightarrow{z_M}$, the phase shift of the interferometer is:

$$\begin{aligned}\overline{\Delta\Phi}_{M+S} = k_{\text{eff}}T^2[&-a_{x_L} - 2(\Omega_M+\Omega_S)v_{y_0} - (\dot{\Omega}_S+\dot{\Omega}_M)((t_0+T)v_{y_0}+y_{OA}) - \dot{\Omega}_M y_{MO})\\ &+ (2\Omega_M^2+\Omega_S^2+2\Omega_M\Omega_S)(a_{x_L}(\frac{t_0^2}{2}+t_0T+T^2)+(t_0+T)v_{x_0}+x_{OA})+2\Omega_M^2 x_{MO}]\end{aligned} \tag{2.25}$$

The contrast of the interferometer is the following according to the theoretical model:

$$\begin{aligned}\frac{\overline{C}_{M+S}}{C_0} = \exp\Bigg(&-\frac{k_{\text{eff}}^2T^4}{2}(\,(2\Omega_M^2+\Omega_S^2+2\Omega_M\Omega_S)^2\sigma_x^2+(\dot{\Omega}_S+\dot{\Omega}_M)^2\sigma_y^2\\ &+((t_0+T)(2\Omega_M^2+\Omega_S^2+2\Omega_M\Omega_S))^2\sigma_{v_x}^2+((t_0+T)(\dot{\Omega}_S+\dot{\Omega}_M)+2(\Omega_M+\Omega_S))^2\sigma_{v_y}^2\,)\Bigg)\end{aligned} \tag{2.26}$$

In order to compute the output parameters of the interferometer, the mean angular velocity of the mirror and of the sensor seen by the interferometer Ω_M and Ω_S have to be known. The mean angular accelerations $\dot{\Omega}_M$ and $\dot{\Omega}_S$ also have to be computed.

To characterise the mirror rotation, the capacitive detection measurement is used. The output of the detection is fitted with the expected function of the mirror angle $\theta_{Mi}(t)$ given by Equations 2.17 to 2.21 depending on the considered case. Once the parameters of the mirror angular movement are known, the mean angular velocity and acceleration are calculated:

$$\begin{aligned}\Omega_M &= \frac{\theta_{Mi}(t_0+2T)-\theta_{Mi}(t_0)}{2T}\\ \dot{\Omega}_M &= \frac{\theta_{Mi}(t_0)-2\theta_{Mi}(t_0+T)+\theta_{Mi}(t_0+2T)}{T^2}\end{aligned} \tag{2.27}$$

The procedure to extract the parameters of the sensor rotation is different as the sensor rotation is measured by the gyroscope. The gyroscope signal $\Omega_{gyro}(t)$ is fitted with the expected function of the rotation rate $\Omega_S^{\text{fit}}(t) = \Omega_0 + A_S\omega\cos(\omega(t-t_0-T)+\phi_S)$ for a sinusoid rotation excitation. Once the amplitude A_S and the phase ϕ_S of the rotation rate are known, the angular movement is known by integration $\theta_S^{\text{fit}} = A_S \sin(\omega(t - t_0 - T) + \phi_S)$. The two angular movements studied are depicted by Equations 2.15 and 2.16. The mean sensor angular velocity and acceleration can be deduced from the angular movement as previously:

$$\begin{aligned}\Omega_S &= \frac{\theta_S^{\text{fit}}(t_0 + 2T) - \theta_S^{\text{fit}}(t_0)}{2T} \\ \dot{\Omega}_S &= \frac{\theta_S^{\text{fit}}(t_0) - 2\theta_S^{\text{fit}}(t_0 + T) + \theta_S^{\text{fit}}(t_0 + 2T)}{T^2}\end{aligned} \tag{2.28}$$

The theoretical phase shift and contrast can now be calculated for each experimental rotation data.

In Chapters 3 and 4, the experimental phase shift and contrast are presented as a function of the previously defined angular velocities and accelerations Ω_S, Ω_M, $\dot{\Omega}_S$ and $\dot{\Omega}_M$. The uncertainties associated with these parameters take into account the uncertainties on the fitting and the uncertainty on the scale factor of the detection (either the capacitive detection or the gyroscope).

Numerical model

A numerical computation of the interferometer phase shift and contrast was developed to help understand the experimental data measured when the interferometer is rotated. This numerical model was described in Chapter 1 and takes into account more parameters of the rotation than the theoretical model: the sensor (respectively mirror) rotation around the $\overrightarrow{z_S}$ (resp. $\overrightarrow{z_M}$) axis and the $\overrightarrow{y_S}$ (resp. $\overrightarrow{y_M}$) is considered. Moreover, less approximations are made in the numerical model than in the theoretical model. For example, terms scaling in Ω^3 or $\dot{\Omega}^2$ are not neglected.

The input rotation data of the numerical model are the following. The rotation data of the mirror are the angular positions detected by the capacitive detection at each interferometric pulse. For the rotation around the $\overrightarrow{z_M}$ (respectively $\overrightarrow{y_M}$) axis, the angular position of the channel Ψ (resp. Θ) at each pulse are Ψ_{Mi} (resp. Θ_{Mi}) with $i = 1, 2, 3$ the interferometric pulse. For the sensor data, the rotation rates around each axis are measured by the two-axis gyroscope. The gyroscope signals for each axis is fitted with a sinusoid function $\Omega_S^k(t) = A\omega\cos(\omega(t - t_0 - T) + \varphi)$ as the excitation is a 4 Hz with k=y or z. The angular sensor positions are deduced by integration given by the function $\theta_S^k = A\sin(\omega(t - t_0 - T) + \varphi)$. The input data of the numerical model is the sensor angular positions along each axis θ_{Si}^y and θ_{Si}^z.

Conclusion

In this Chapter, the experimental setup used to study the impact of rotation is described. The lab experiment was developed to study the hybridisation of a cold atom accelerometer and electrostatic accelerometer (EA). The cold atom accelerometer uses a molasses source of Rubidium 87 to implement a Mach-Zehnder interferometer. Two-photon Raman transitions act as atomic mirrors and beamsplitters for the interferometer. To perform the two-photon transition, the Raman laser has to be reflected on a mirror which also acts as the laser phase reference. In this original setup, the proof-mass of an electrostatic accelerometer is the retro-reflection mirror. The proof-mass position is controlled and detected along the six degrees of freedom thanks to the EA. The electrostatic actuation of the mirror allows to rotate the mirror enabling the study of the mirror rotation impact on the interferometer and the compensation of the whole sensor rotation. The whole sensor head including the atomic accelerometer and the EA can be rotated thanks to piezo-electric actuators.

The methods developed during this study to obtain the experimental results of Chapters 3 and 4 are also presented. The alignment of the EA with the atomic interferometer was done carefully. The Raman laser has to be retro-reflected and parallel to the Earth gravity. Thus, the EA is perpendicular to the gravity. The angular movements of the sensor and mirror studied are presented. Sinusoidal angular movements are favoured as they limit the excitation of resonance. The experimental procedure to retrieve the phase shift and contrast of the interferometer are detailed as well as the different parameters used to compute the phase shift and contrast models.

CHAPTER 3

Impact of the mirror rotation: a way to characterise the atomic cloud

Outline of the current chapter

Introduction

The originality of our experimental setup enables to study the impact of the mirror rotation on the interferometer. A chosen rotation is imposed to the retro-reflection mirror and the angular position of the mirror is measured in real time thanks to the capacitive measurement. The experimental phase shift and contrast can then be compared to the theoretical and numerical models presented in Chapters 1 and 2. As the phase shift and contrast depend on the kinematic parameters of the cloud, several kinematic parameters of the atomic cloud were estimated such as its temperature, size, mean transverse velocity and mean transverse position.

The temperature of the cloud was also measured with two other methods for the sake of comparison. The first implemented method uses the velocity selection of the Raman transition. The second method is based on the imperfect closure of a temporal asymmetric interferometer.

This study enlightened some limitations of the rotation of the EA proof-mass. Some unexpected phase shifts were measured when the mirror was rotating. This phase shift could be linked to the reflection of the laser beam on the EA proof mass as they depend on the rotation magnitude. The unexplained phase shift could be explained by wave front aberrations introduced by the reflection on the proof-mass or by the effect of the mirror rotation during the detection step. As the proof-mass was rotated, some limitations in the proof-mass position control were observed such as a vertical acceleration and a residual rotation along the perpendicular axis.

3.1 Influence of the mirror rotation on the interferometer

Firstly, the impact of the sole mirror rotation was studied and compared to the theoretical and numerical models. An interpretation using the inertial accelerations is also proposed. In this work, the detection system is not taken into account even if the detection system has a spatial response. The contribution of one atom to the output signal depends on its position during the detection step and thus on its initial velocity and position. This effect was studied in [124] which has shown the influence of the detection on the detected velocity distribution and thus the detected Coriolis acceleration. The kinematic parameters used to compute the theoretical and numerical model are summed up in Section 2.4.5.

3.1.1 Impact of angular velocities

In order to study the impact of the angular velocity on the interferometer, an angular ramp around the axis $\overrightarrow{z_M}$ was imposed on the mirror. The interferometer is implemented <while the mirror rotates with an interrogation time of $T = 46\,\text{ms}$. As the angular acceleration of a ramp is null, only the Coriolis and Centrifugal accelerations are expected to impact the contrast and phase shift.

Contrast

The contrast loss due to the angular velocity is presented on Figure 3.2a. As the angular acceleration is null for an angular ramp, the contrast loss should only be due to the Coriolis and Centrifugal acceleration leading to Equation 3.1. Nevertheless, the experimental contrast loss can be explained by the Coriolis acceleration only which scales as $4\Omega_M^2\sigma_{v_y}^2$. In this experiment, the Centrifugal acceleration contribution to the contrast loss is negligible as it scales in Ω_M^4.

$$\frac{\overline{C}_M}{C_0} = \exp\left(-\frac{k_{\text{eff}}^2 T^4}{2} \left(4\Omega_M^4 \sigma_x^2 + 4(t_0+T)^2\Omega_M^4\sigma_{v_x}^2 + 4\Omega_M^2\sigma_{v_y}^2 \right) \right) \tag{3.1}$$

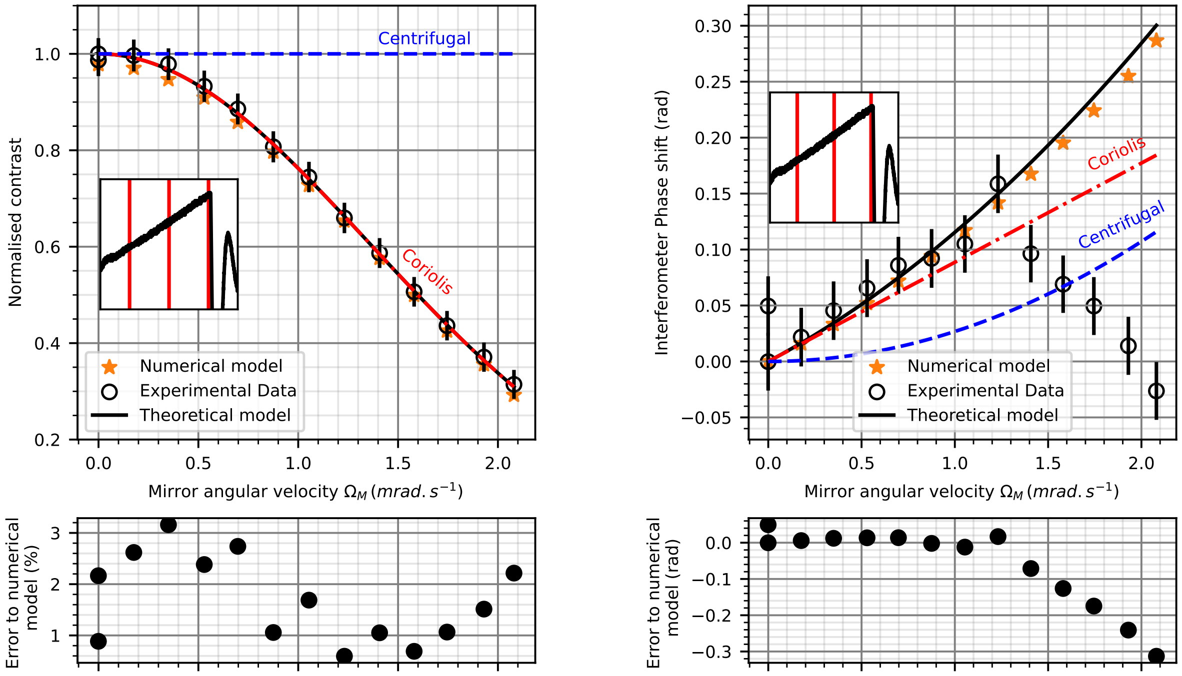

(a) Contrast loss due to an angular ramp around the axis $\overrightarrow{z_M}$. The impact of the Coriolis acceleration fully explains the observed contrast loss. The theoretical and numerical model explain the experimental data with an error below 3% for the numerical model.

(b) Phase shift induced by an angular ramp around the axis $\overrightarrow{z_M}$. The phase shift is impacted linearly by the Coriolis acceleration and quadratically by the Centrifugal acceleration. Both numerical and theoretical models agree with the experimental data for angular velocities below 1.3 rad s^{-1}. For higher angular velocities, a linear error up to -0.3 rad appears.

Figure 3.1: Influence of an angular velocity on the interferometer. The angular movement is depicted in black in the insets. The three red lines represent the laser pulses of the interferometer. For an angular ramp, only the Coriolis and Centrifugal accelerations impact the interferometer.

Phase shift

The measured phase shift is presented on Figure 3.2b and should also be explained by the Coriolis acceleration $-2\Omega_M v_{y_0}$ and the Centrifugal acceleration $2\Omega_M^2(a_{x_L}(\frac{t_0^2}{2}+t_0T+T^2)+(t_0+T)v_{x_0}+x_{MA})$. The factor 2 in the Centrifugal acceleration is explained by the magnitude variation of the effective wave vector when the mirror rotates. If the experimental data, the numerical and theoretical models agree for angular velocities below 1.3 rad s^{-1}, it is difficult to discriminate the Coriolis from the Centrifugal acceleration. For higher angular velocities, an error up to -0.3 rad appears. This error is a linear function of the angular velocity and is further investigated in Section 3.5.1.

$$\overline{\Delta\Phi}_M = k_{\text{eff}}T^2\left[-a_{x_L} - 2\Omega_M v_{y_0} + 2\Omega_M^2\left(a_{x_L}\left(\frac{t_0^2}{2}+t_0T+T^2\right)+(t_0+T)v_{x_0}+x_{MA}\right)\right] \tag{3.2}$$

3.1.2 Impact of angular accelerations

The control of the EA proof-mass allows to impose important angular accelerations on the mirror and to study their effect on the interferometer. A sinusoid angular movement at a frequency $\frac{1}{2T}$ (insets of Figure 3.2a) was chosen to maximise the angular acceleration and to avoid any discontinuity in the movement (which would deteriorate the EA control).

Contrast

The contrast loss induced by the angular acceleration (Figure 3.2a) is explained by the impact of the Angular acceleration as anticipated by Equation 3.3. As no angular velocity is imposed, the Coriolis and Centrifugal accelerations are null.

$$\frac{\overline{C}_M}{C_0} = \exp\left(-\frac{k_{\text{eff}}^2 T^4}{2} \left(\dot{\Omega}_M^2 \sigma_y^2 + ((t_0+T)\dot{\Omega}_M)^2 \sigma_{v_y}^2 \right) \right) \tag{3.3}$$

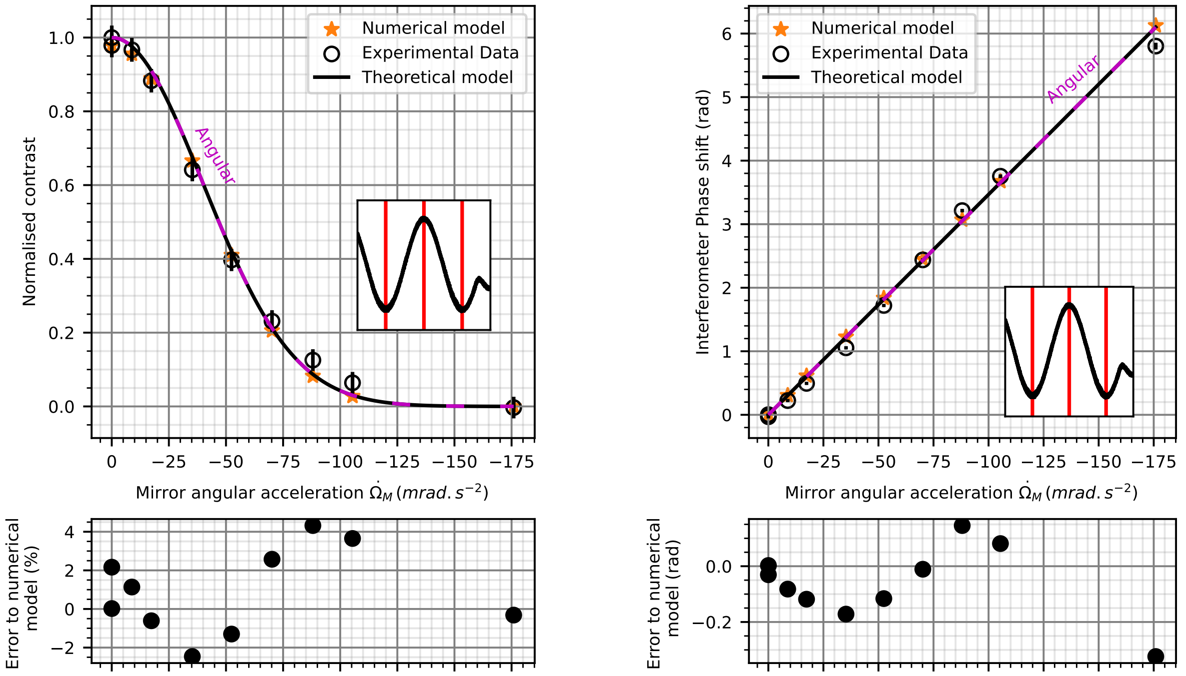

(a) Contrast loss due to a sinusoid movement around the axis $\overrightarrow{z_M}$. The impact of the Angular acceleration fully explains the observed contrast loss. The theoretical and numerical model explain the experimental data with an error below 6% for the numerical model.

(b) Phase shift induced by a sinusoid movement around the axis $\overrightarrow{z_M}$. The phase shift is only impacted linearly by the Angular acceleration.

Figure 3.2: Influence of an angular acceleration on the interferometer. The angular movement is depicted in black in the insets. The three red lines represent the laser pulses of the interferometer. For this angular movement, only the Angular acceleration impacts the interferometer.

Phase shift

The experimental phase shift induced by the angular acceleration is explained by the linear contribution of the Angular acceleration as anticipated by the theoretical model (Equation 3.4). This phase shift is very important(up to 6 rad) and the error between the experimental data is also relatively important (up to −0.3 rad). This error could be due to variations in the kinematic parameters of the cloud.

$$\overline{\Delta\Phi}_M = k_{\text{eff}}T^2[-a_{x_L} - \dot{\Omega}_M((t_0+T)v_{y_0} + y_{MA})] \tag{3.4}$$

3.2 Temperature measurements

In this Section, a method to measure the atomic cloud transverse temperature by rotating the retro-reflection mirror is presented. Here, the term "temperature" is be employed to name a pseudo-temperature deduced from the deviation of the velocity distribution. Two other temperature measurements were also implemented: a measurement by Raman spectroscopy and a temperature measurement through the contrast loss of an asymmetric interferometer. These two last methods were used to check the results of the rotation method. Nevertheless, the Raman spectroscopy and the asymmetric interferometer allow only to measure the vertical temperature and not the transverse temperature. The transverse and vertical temperature should be equal if the cloud is in a thermodynamic equilibrium. In addition, one should note that a time-of-flight measurement couldn't be performed due to experimental limitations: the detection of the atoms is achieved with a photodiode and there is no CCD camera inside the magnetic shied.

3.2.1 Mirror rotation

The atomic cloud temperature can be measured through the rotation induced contrast loss. A similar measurement was performed in [3]: a tip-tilt mounted mirror was rotated linearly up to 400 µrad s^{-1} and the size of the wave packet was deduced from the contrast loss. The measurement presented here is based on the same principle but uses a different range of angular velocities (up to 2 mrad s^{-1}) and a variety of angular movements. As described in Chapter 1, the contrast loss depends on the velocity and position distributions of the cloud. If the contrast is only impacted by the Coriolis acceleration, the contrast only depends on the velocity distribution. In this experimental setup, the impact of the Centrifugal acceleration on the contrast is null. Thus, for an angular movement with a null angular acceleration, the contrast loss would only depend on Coriolis acceleration. As presented in Chapter 1, to simplify the calculation, the hypothesis of a Gaussian velocity distribution was made. Nevertheless, the velocity distribution of a molasses cooled atomic cloud is predicted by theory [125] to be a Lorentzian distribution. This was verified experimentally in [124, 126–128].

Angular ramp

The simplest movement without an angular acceleration is an angular ramp. This first movement was imposed to the mirror during the interferometer (see insets in Figure 3.3). As there is no angular accelerations, only the Coriolis and Centrifugal accelerations impact the interferometer. The Centrifugal acceleration induces a negligible contrast loss for an angular velocity below 2 mrad s^{-1} and an atomic velocity distribution of roughly 13 mm s^{-1} deviation (1.8 µK). The temperature is extracted from a similar setup [98]. The Centrifugal acceleration is negligible due to its quadratic effect and the short interrogation time (46 ms). Thus, the contrast is considered only impacted by the Coriolis acceleration.

Thanks to the EA proof-mass, the mirror can be rotated along two perpendicular axes $\overrightarrow{y_M}$ and $\overrightarrow{z_M}$ (corresponding to the EA channels Ψ and Θ of Figure 2.22a). The layout of the different axes is displayed on Figure 1.7. The angular positions along these two axes are also measured thanks to the capacitive detection. The angular velocities Ω_Ψ and Ω_Θ are determined with the signal of the capacitive detection as explained in Section 2.4.6.

An angular ramp around the axis $\overrightarrow{z_M}$ allows the measurement of the atomic velocity distribution deviation σ_{v_y} along the axis $\overrightarrow{y_S}$. The contrast loss model is a decreasing exponential (Equation 3.5) depending only on the angular velocity Ω_Ψ and the velocity distribution of the atomic cloud. The angular velocity was scanned and the interferometer contrast measured (Figure 3.3a). To determine the cloud temperature, the normalised contrast was fitted with Equation 3.5 with the velocity distribution deviation σ_{v_y} as a free parameter.

$$\frac{\bar{C}}{C_0} = \exp\left(- 2k_{\text{eff}}^2 T^4 \Omega_\Psi^2 \sigma_{v_y}^2 \right) \tag{3.5}$$

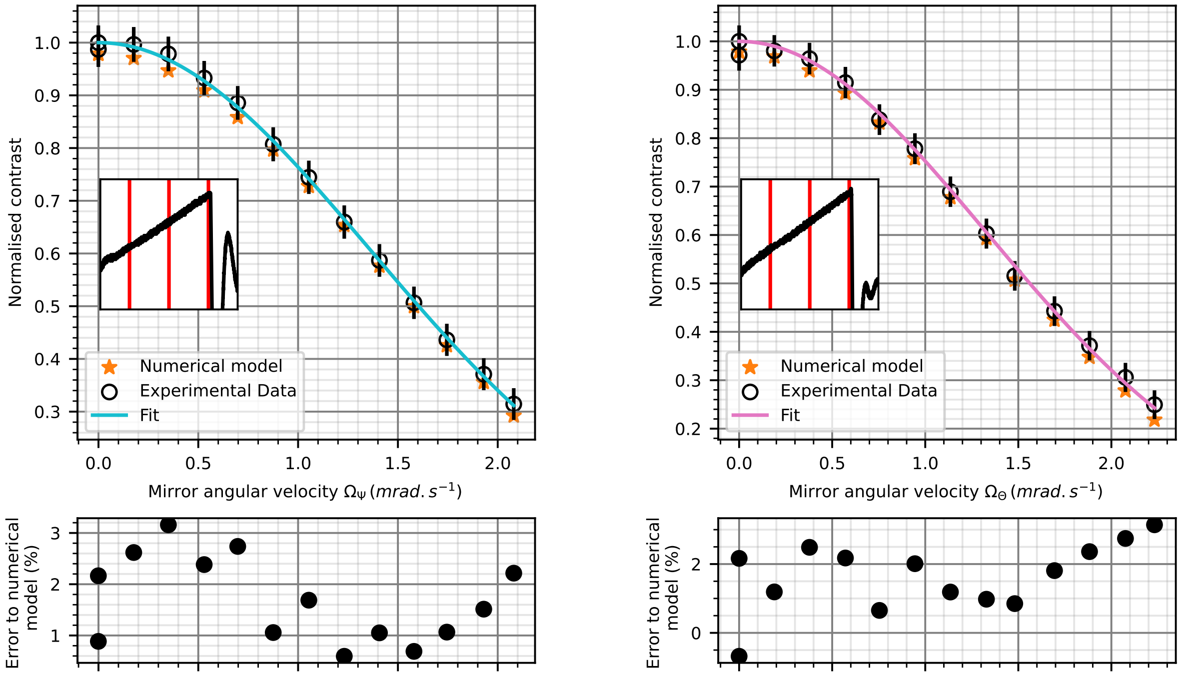

(a) Contrast loss due to a rotation around axis $\overrightarrow{z_M}$ (corresponding to the channel Ψ). The velocity distribution width along the axis $\overrightarrow{y_S}$ is measured with a fit with a value of $\sigma_{v_y} = 10.8 \pm 0.2\,\text{mm}\,\text{s}^{-1}$.

(b) Contrast loss due to a rotation around axis $\overrightarrow{y_M}$ (corresponding to the channel Θ). The velocity distribution width along the axis $\overrightarrow{z_S}$ is measured with a fit with a value of $\sigma_{v_z} = 11.1 \pm 0.2\,\text{mm}\,\text{s}^{-1}$

Figure 3.3: Impact of an angular ramp of the mirror on the normalised contrast and measurement of the atomic cloud velocity distribution. The angular movement is depicted in black in the insets. The three red lines represent the laser pulses of the interferometer.

Figure 3.3a shows the good agreement of the fit curve in light blue with the experimental data in black. The optimal fit corresponds to a deviation of the velocity distribution of $\sigma_{vy} = 10.8 \pm 0.2\,\text{mm}\,\text{s}^{-1}$ corresponding to a temperature of $1.22 \pm 0.05\,\mu\text{K}$. Equation 3.6 gives the corresponding formula to retrieve the temperature from the velocity distribution deviation. The numerical model was also computed and agrees with the experimental data with an error of less than 3% with the experimental data.

$$T = \frac{m\sigma_v^2}{k_B} \tag{3.6}$$

An angular ramp around the axis $\overrightarrow{y_M}$ was also performed to measure the atomic velocity distribution σ_{v_z} along the axis $\overrightarrow{z_S}$ (Equation 3.7). Figure 3.3b shows a good agreement between the fit curve, the numerical model and the experimental data. The optimal fit corresponds to a width of the velocity distribution of $\sigma_{v_z} = 11.1 \pm 0.2\,\mathrm{mm\,s^{-1}}$ corresponding to a temperature of $1.29 \pm 0.05\,\mu\mathrm{K}$. The fitting function of the experimental data in pink on Figure 3.3b is the following:

$$\frac{\bar{C}}{C_0} = \exp\left(-2k_{\mathrm{eff}}^2 T^4 \Omega_\Theta^2 \sigma_{v_z}^2 \right) \tag{3.7}$$

Sinusoidal angular movement at $\frac{1}{4T} \approx 5\,\mathrm{Hz}$

A second angular movement allows to cancel the angular acceleration detected by the interferometer. As the interferometer is sensitive to the mirror position only during the laser pulses, the movement between the pulses is not relevant to the interferometer. A sinusoidal angular movement at a frequency $\frac{1}{4T} \approx 5\,\mathrm{Hz}$ as depicted in the insets of Figure 3.4, presents a non-zero angular velocity and a null angular acceleration for the interferometer. The phase of the sinusoid movement is set at zero and is chosen to have a zero angular acceleration and a maximum angular velocity. This movement correspond to Equation 2.18 in Section 2.4.2. In this configuration, the contrast is only impacted by the Coriolis acceleration as there is no angular acceleration for the interferometer. As the sinusoid movement does not have any slope breaks (contrary to the ramp), the movement of the mirror is better controlled.

A sinusoidal angular movement was imposed around the axis $\overrightarrow{z_M}$ (channel Ψ of the EA) to measure the velocity distribution σ_{v_y} along the $\overrightarrow{y_S}$ axis. The amplitude of the sinusoidal movement A_Ψ was scanned and measured by the capacitive detection. The amplitude A_Ψ is extracted by a fit from the capacitive detection signal. The measured contrast was fitted with Equation 3.8 to access the deviation of the velocity distribution. Figure 3.4a shows a good agreement between the fit curve, the numerical model and the experimental data. The optimal fit corresponds to a deviation of the velocity distribution of $\sigma_{v_y} = 10.6 \pm 0.2\,\mathrm{mm\,s^{-1}}$ corresponding to a temperature of $1.18 \pm 0.05\,\mu\mathrm{K}$.

$$\frac{\bar{C}}{C_0} = \exp\left(-2k_{\mathrm{eff}}^2 T^2 A_\Psi^2 \sigma_{v_y}^2 \right) \tag{3.8}$$

The same procedure was performed for a rotation around the axis $\overrightarrow{y_M}$ (channel Θ of the EA) to measure the velocity distribution σ_{v_z} along the $\overrightarrow{z_S}$ axis. The amplitude of the sinusoidal movement A_Θ was scanned and the measured contrast was fitted with Equation 3.9. Figure 3.4b shows a good agreement between the fit curve, the numerical model and the experimental data. The optimal fit corresponds to a width of the velocity distribution of $\sigma_{vz} = 10.8 \pm 0.2\,\mathrm{mm\,s^{-1}}$ or a temperature of $1.22 \pm 0.05\,\mu\mathrm{K}$.

$$\frac{\bar{C}}{C_0} = \exp\left(-2k_{\mathrm{eff}}^2 T^2 A_\Theta^2 \sigma_{v_z}^2 \right) \tag{3.9}$$

The rotation of the mirror enables the measurement of the transverse temperature of the atomic cloud. Two angular movements were studied around two perpendicular rotation axes. The two velocity distribution measurements along the Y axis are in agreement at one standard deviation ($10.8 \pm 0.2\,\mathrm{mm\,s^{-1}}$ and $10.6 \pm 0.2\,\mathrm{mm\,s^{-1}}$). The two velocity distribution measurements along the Z axis are also in agreement but at two standard deviations ($11.1 \pm 0.2\,\mathrm{mm\,s^{-1}}$ and $10.8 \pm 0.2\,\mathrm{mm\,s^{-1}}$). The measured velocity distribution is slightly broader along the Z

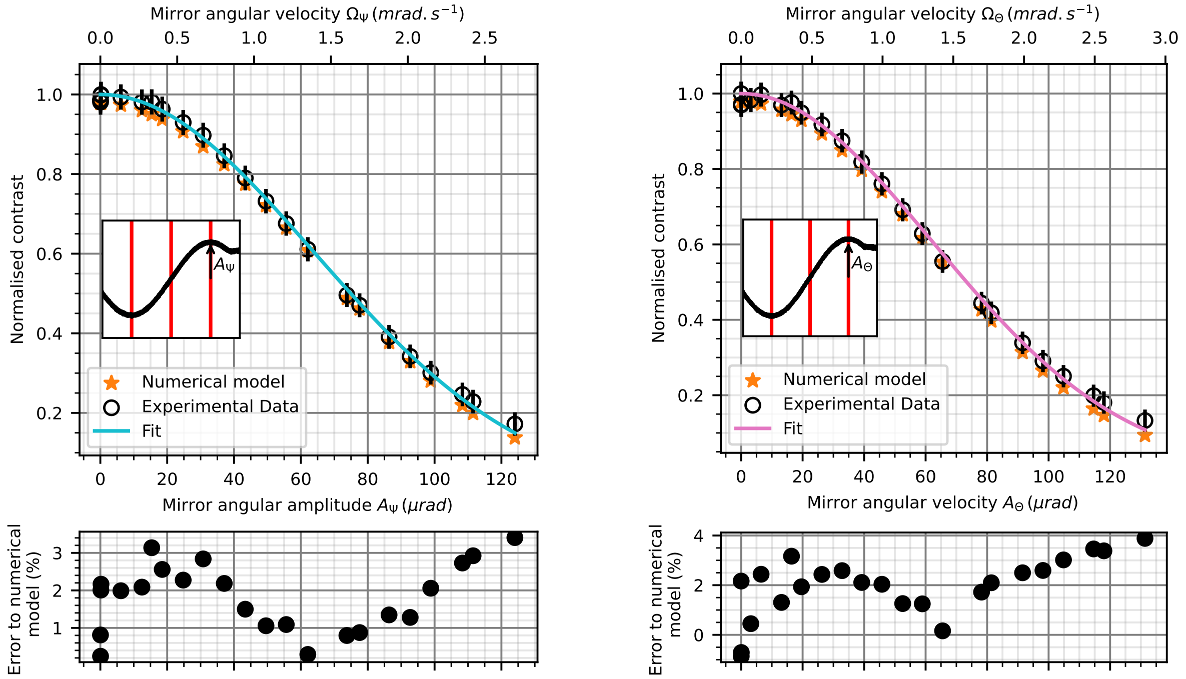

(a) Contrast loss due to a rotation around axis $\overrightarrow{z_M}$ (corresponding to the channel Ψ). The velocity distribution width along the axis $\overrightarrow{y_S}$ is measured with a fit with a value of $\sigma_{v_y} = 10.6 \pm 0.2\,\mathrm{mm\,s^{-1}}$

(b) Contrast loss due to a rotation around axis $\overrightarrow{y_M}$ (corresponding to the channel Θ). The velocity distribution width along the axis $\overrightarrow{z_S}$ is measured with a fit with a value of $\sigma_{v_z} = 10.8 \pm 0.2\,\mathrm{mm\,s^{-1}}$

Figure 3.4: Impact of a sinusoid angular movement at $\frac{1}{4T} \approx 5\,\mathrm{Hz}$ of the mirror on the normalised contrast and measurement of the atomic cloud velocity distribution. The angular movement is depicted in black in the insets. The three red lines represent the laser pulses of the interferometer.

axis than the Y axis: this will be discussed in Section 3.2.4. These temperature measurements performed thanks to the mirror rotation will be compared to measurements performed with other methods.

3.2.2 Raman spectroscopy

In order to compare the temperature measurement by mirror rotation to more standard methods, a temperature measurement by Raman spectroscopy was performed. This measurement uses the Doppler effect on the Raman transition which is sensitive to the vertical velocity (along the X axis) of the atoms. A scan of the laser frequency allows to retrieve the atomic cloud velocity distribution. Raman spectroscopy is commonly used to study the velocity distribution of atoms as in [124].

A Raman impulsion with an effective Rabi pulsation Ω_{eff} and a duration $\tau = \frac{\pi}{\Omega_{\text{eff}}}$ has a transition probability depending on the vertical velocity of the atom v_x [103]:

$$P_\pi(v_x) = \left(\frac{\pi}{2}\right)^2 \operatorname{sinc}^2\left(\frac{\pi\sqrt{1+\left(\frac{v_x k_{\text{eff}}}{\Omega_{\text{eff}}}\right)^2}}{2}\right) \tag{3.10}$$

A long pulse duration selects a narrow velocity class. The width of the selected velocity class Δv_x can be approximated as the width between the two first zeros of the cardinal sine of the transition probability: $\Delta v_x = \frac{\sqrt{3}\pi}{3k_{\text{eff}}\tau}$. For a pulse duration of $\tau = 250\,\mu\text{s}$, the selected velocity class is $\Delta v_x = 0.23\,\text{mm}\,\text{s}^{-1}$. This value can be considered as the Raman spectroscopy resolution. The scan of the frequency allows to evaluate the velocity distribution of the atomic cloud with a resolution 50 times lower than the distribution width ($\approx 10\,\text{mm}\,\text{s}^{-1}$).

To obtain the experimental data displayed on Figure 3.5, the Raman laser modulation frequency f was scanned from 6.8345 GHz to 6.8350 GHz with a pulse duration of $\tau_\pi = 250\,\mu\text{s}$. The atomic velocity $v_x = -\frac{2\pi}{k_{\text{eff}}}(f - f_0) + \frac{\hbar k_{\text{eff}}}{2m}$ can be deduced from the resonance condition (Equation 1.5) and computed thanks to the frequency of the transition at rest $f_0 = 2\pi G = 6.834\,682\,610\,904\,29\,\text{GHz}$ [107].

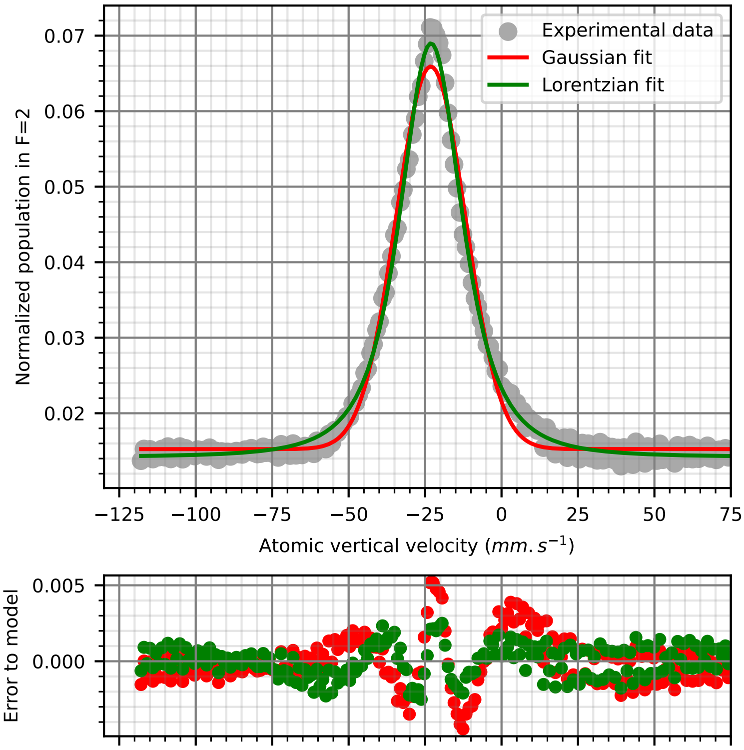

Figure 3.5: Vertical velocity distribution measurement by Raman spectroscopy. A Raman laser pulse is sent during the atoms free fall. Each experimental point corresponds to a different modulation frequency of the Raman laser.

Two different models were considered for the atomic velocity distribution: a Gaussian distribution which is a simple way to describe the velocity distribution and was used in the rotation models of Chapter 1 and a Lorentzian distribution of order b as used in [124] and predicted in [125].

Gaussian velocity distribution

The Gaussian distribution of Figure 3.5 was computed by fitting the experimental data with Equation 3.11 with a coefficient of determination of $R^2 = 0.987$. The deviation of the velocity distribution is $\sigma_{v_x} = 11.3 \pm 0.2\,\text{mm}\,\text{s}^{-1}$ corresponding to temperature of $1.34 \pm 0.05\,\mu\text{K}$. The mean initial velocity of the cloud could also be estimated at $v_{x_0} = -23.1 \pm 0.2\,\text{mm/s}$. Nevertheless, this value is actually the mean velocity at the start of the modulation frequency chirp. This chirp is applied to compensate the Doppler effect and starts around the end of the cooling step.

The value of the vertical mean velocity is more important than expected at the end of the cooling step. One could expect a mean velocity of the order of the mm s^{-1} instead of -23.1 mm/s. This could be explained by a delay between the end of the cooling stage and the start of the frequency chirp.

$$D_{\text{Gaussian}}(v_x) = y_0 + A\exp\left(-\frac{(v_x - v_{x_0})^2}{2\sigma_{v_x}^2}\right) \tag{3.11}$$

Lorentzian velocity distribution:

The Lorentzian distribution of Figure 3.5 was computed by fitting the experimental data with Equation 3.13 with a coefficient of determination of $R^2 = 0.995$. The optimal value of the parameter b is $b = 1.72 \pm 0.11$ which is different from [124] (b=2.50 ± 0.05). The parameter b is proportional to the typical light shift [128] and can be expressed as:

$$b \propto \frac{\hbar|\delta|s_0}{E_r} \tag{3.12}$$

with s_0 the saturation parameter of the molasses, δ the detuning and E_r the recoil energy. Thus, differences in the molasses parameters such as the laser intensity or the detuning would lead to a different value of b. The parameter $\Gamma = 17.0 \pm 0.7\,\mathrm{mm\,s^{-1}}$ is the width of the distribution at mid-height and cannot be compared directly to the Gaussian distribution. The width of the velocity distribution at $\frac{1}{\sqrt{e}}$ is $\sigma_{v_x} = 14.4 \pm 0.7\,\mathrm{mm\,s^{-1}}$ corresponding to a temperature of $2.2 \pm 0.8\,\mu$K.

$$D_{Lorentz}(v_x) = y_0 + \frac{A}{\left(1 + \frac{(v_x - v_{x_0})^2}{\Gamma^2}\right)^b} \tag{3.13}$$

On Figure 3.5, the Lorentzian distribution is closer to the experimental data than the Gaussian distribution as expected from [125]. The Lorentzian distribution is a better fit to the experimental data especially for the wings of the velocity distribution corresponding to the hottest atoms of the cloud.

This temperature measurement by Raman spectroscopy allows to check the measurement by rotation performed in 3.1.1. If the different measurements are of the same order of magnitude between ≈ 1 and $2\,\mu$K and in agreement with measurement performed previously in similar setup [98], the measurement by Raman spectroscopy gives a higher temperature than the measurement by rotation. This could be explained by the fact that the Raman spectroscopy is sensitive to the vertical velocity and the measurement by rotation to the transverse velocity. If the thermalisation of the cloud is not perfect, the transverse and vertical velocity distributions could be different due to asymmetry in the cooling setup caused for instance by the presence of a residual magnetic field during the molasses [129].

3.2.3 Asymetric interferometer

Another temperature measurement was performed by studying the contrast of a temporal asymmetric interferometer as described in [130]. The mirror laser pulse is shined earlier or later than the regular laser pulse (see Figure 3.6). The closure of the interferometer is imperfect inducing a contrast loss. This contrast now depends on the time asymmetry and on the vertical atomic velocity distribution.

The phase shift of the asymmetric interferometer can be calculated using 3.14 as ex-

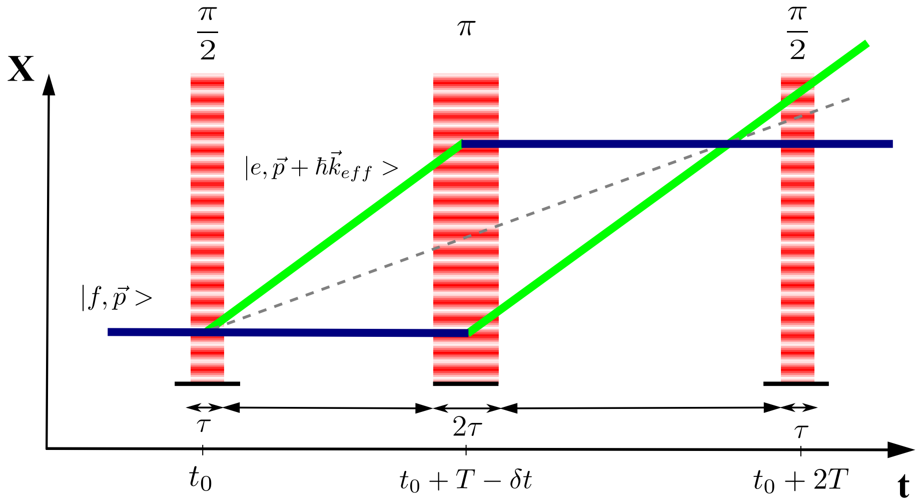

Figure 3.6: Space-time diagram of a temporal asymmetric interferometer. The mirror pulse is delayed from δt inducing an imperfect closure of the interferometer.

plained in Chapter 1 with t_0 the delay between the end of the cooling and the beginning of the interferometer, T the delay between two pulses of the interferometer and δt the temporal asymmetry.

$$\Delta\Phi = \varphi(t_0) - 2\varphi(t_0 + T - \delta t) + \varphi(t_0 + 2T) \tag{3.14}$$

The laser phase φ in the absence of rotation only depends on the vertical position of the atoms with respect to the mirror:

$$\varphi(t) = \vec{k}_{\text{eff}}(t).\vec{r}(t) = k_{\text{eff}}\left(a_{x_0}\frac{t^2}{2} + v_{x_0}t + x_{MA}\right)$$

The phase shift of the asymmetric interferometer can then be computed and will only depend on the vertical velocity and acceleration of the atom (Equation 3.15).

$$\overline{\Delta\Phi} = k_{\text{eff}}\left(2v_{x_0}\delta t + a_{x_0}T^2 + a_{x_0}\delta t(2t_0 - 2T + \delta t)\right) \tag{3.15}$$

The contrast of the asymmetric accelerometer can be deduced from the phase shift as presented in Chapter 1 under the approximation of a Gaussian velocity distribution. The contrast as a function of the temporal asymmetry δt depends only of the width of the vertical velocity distribution σ_{v_x} of the atomic cloud.

$$\frac{\overline{C}}{C_0} = \exp\left(-2k_{\text{eff}}^2\delta t^2\sigma_{v_x}^2\right) \tag{3.16}$$

The asymmetric interferometer was performed on the experimental setup with an interrogation time of $T = 46\,\text{ms}$ and a temporal asymmetry δt between -50 and 50 µs. The contrast was measured and fitted with Equation 3.16 as depicted on Figure 3.7. The optimal value of the width of the vertical velocity distribution is $\sigma_{v_x} = 8.8 \pm 0.2\,\text{mm}\,\text{s}^{-1}$ corresponding to a temperature of $T = 0.80 \pm 0.04\,\mu\text{K}$.

The temperature measured thanks to the asymmetric interferometer is the lowest measured temperature (0.8 µK) of the different measurements. This low temperature could be explained by the difference between the fit curve and the experimental data especially for low contrast (less than 10%). A possible improvement would be the use of a Lorentzian velocity distribution instead of Gaussian distribution in the contrast computation to better take into

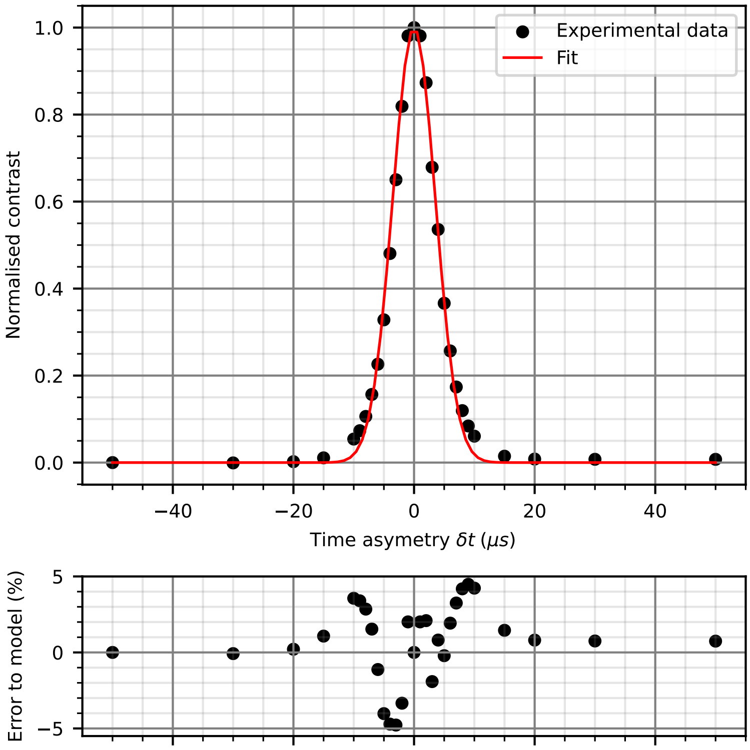

Figure 3.7: Contrast loss induced by a temporal asymmetry of the interferometer. The mirror pulse of the interferometer is delayed from δt inducing an imperfect closure and thus a contrast loss.

account the hotter atoms.

3.2.4 Conclusion about temperature measurements

In this Section, three different methods were used to measure the atomic cloud velocity width.

The first method is based on the contrast loss induced by the mirror rotation. The width of the velocity distribution (under the hypothesis of a Gaussian distribution) was measured along the two transverse axes thanks to the dominant Coriolis induced contrast loss. Two different mirror movements inducing only an angular velocities were used. The results of these measurements are the following:
along the $\overrightarrow{y_S}$ axis $\sigma_{vy} = 10.8 \pm 0.2\,\mathrm{mm\,s^{-1}}$ and $10.6 \pm 0.2\,\mathrm{mm\,s^{-1}}$
along the $\overrightarrow{z_S}$ axis $\sigma_{vz} = 11.1 \pm 0.2\,\mathrm{mm\,s^{-1}}$ and $10.8 \pm 0.2\,\mathrm{mm\,s^{-1}}$
The measurements along each axis agree but the measured temperature is slightly lower for the $\overrightarrow{y_S}$ axis than the temperature along the $\overrightarrow{z_S}$ axis.

The second implemented method uses Raman spectroscopy to measure the velocity distribution along the vertical axis. Under the hypothesis of a Gaussian velocity distribution, the width of the distribution is $\sigma_{v_x} = 11.3 \pm 0.2\,\mathrm{mm\,s^{-1}}$. This measurement is slightly higher than the measurement performed with the rotation method and is not fully in agreement with all the measurement performed with the rotation method.

The last method uses the contrast loss in a temporal asymmetric interferometer. This method measures the velocity distribution along the vertical axis at $\sigma_{v_x} = 8.8 \pm 0.2\,\mathrm{mm\,s^{-1}}$ for a Gaussian velocity distribution. This measurement is the lowest performed and shows some discrepancies the previous measurements.

While all the measurements are of the same order of magnitude $\approx 10\,\mathrm{mm\,s^{-1}}$, the observed differences could be due to several phenomena.
Firstly, the different methods are not sensitive to the same axis of the velocity distribution. If the cloud was not in thermodynamic equilibrium at the end of the cooling step, the velocity distribution could be different along each axis due to asymmetry in the cooling setup. Nevertheless, this hypothesis could not explain the difference between the results given by the Raman spectroscopy method and the asymmetric interferometer method as they are sensitive to the same axis.
Secondly, the velocity distribution of the atomic cloud is known to be closer to a Lorentzian distribution than a Gaussian distribution [125]. In the Raman spectroscopy results, the Gaussian distribution fails to fit properly the wings of the distribution. The contrast measurement of the asymmetric interferometer also displays some discrepancies with the model resulting of a Gaussian distribution.
Thirdly, all the atoms of the cloud might not take part in all the measurements. Some atoms might not be a part of the interferometer and others might not be detected by the detection system due to its spatial dependency. The spatial response of the detection system should be studied in detail as done in [124].

In the rest of this work, the values of the velocity distribution deviation along each axis are the following:
$\sigma_{v_x} = 11.3 \pm 0.2\,\mathrm{mm\,s^{-1}}$ (Raman spectroscopy)
$\sigma_{v_y} = 10.8 \pm 0.2\,\mathrm{mm\,s^{-1}}$ (Mirror rotation angular ramp)
$\sigma_{v_z} = 11.1 \pm 0.2\,\mathrm{mm\,s^{-1}}$ (Mirror rotation angular ramp)

3.3 Size of the cloud measurement

In this section, a method to measure the transverse size of the atomic cloud by rotating the mirror is presented. When the mirror is rotated with an important angular acceleration and no angular velocity, the contrast loss is only induced by the Angular acceleration depends on the position and velocity distributions of the cloud. Without an angular velocity, the contribution of the Coriolis and Centrifugal accelerations are null. The knowledge of the velocity distribution from Section 3.2.1 will be used to determine the size of the cloud. The used values for the width of the velocity distributions are $\sigma_{v_y} = 10.8 \pm 0.2\,\mathrm{mm\,s^{-1}}$ and $\sigma_{v_z} = 11.1 \pm 0.2\,\mathrm{mm\,s^{-1}}$ measured by rotating the mirror linearly. Concerning the position distribution, it is considered to be a Gaussian distribution.

The angular movement of the mirror was chosen such as its angular velocity is null and its angular acceleration important. A sinusoidal angular movement at $\frac{1}{2T} \approx 10\,\mathrm{Hz}$ depicted on Figure 3.8 has an important angular acceleration (up to $175\,\mathrm{mrad\,s^{-2}}$) and a small angular velocity (less than $4 \times 10^{-12}\,\mathrm{rad\,s^{-1}}$). This angular movement was depicted in Section 2.4.2 as Equation 2.19. The phase of the sinusoid is set at $\frac{\pi}{2}$ to cancel the angular velocity.

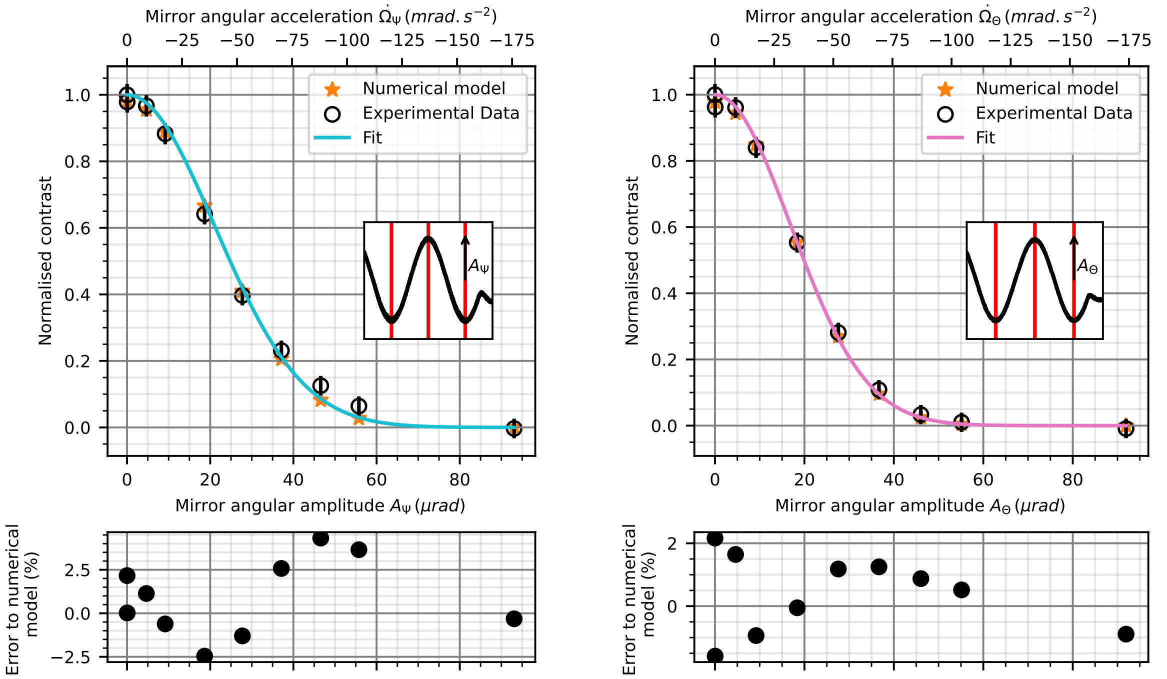

(a) Contrast loss due to a rotation around axis $\overrightarrow{z_M}$ (corresponding to the channel Ψ). The initial position distribution deviation along the axis $\overrightarrow{y_S}$ is measured with a fit with a value of $\sigma_{y_0} = 0.42 \pm 0.05\,\mathrm{mm}$

(b) Contrast loss due to a rotation around axis $\overrightarrow{y_M}$ (corresponding to the channel Ψ). The initial position distribution deviation along the axis $\overrightarrow{z_S}$ is measured with a fit with a value of $\sigma_{z_0} = 0.66 \pm 0.05\,\mathrm{mm}$

Figure 3.8: Impact of a sinusoid angular movement at $\frac{1}{2T} \approx 10\,\mathrm{Hz}$ of the mirror on the normalised contrast and measurement of the atomic cloud initial position distribution. The angular movement is depicted in black in the insets. The three red lines represent the laser pulses of the interferometer.

To measure the size of the cloud along the axis $\overrightarrow{y_S}$, the amplitude A_Ψ of the sinusoidal movement is scanned and the contrast of the interferometer measured. The normalised contrast is then fitted with Equation 3.17. Figure 3.8a shows a good agreement between the fit curve, the numerical model and the experimental data. The optimal fit corresponds to a width of the position distribution of $\sigma_{y_0} = 0.42 \pm 0.05\,\text{mm}$. This characterises the position distribution of the cloud immediately after the cooling stage.

$$\frac{\bar{C}}{C_0} = \exp\left(- 8k_{\text{eff}}^2 A_{\Psi}^2 \left(\sigma_{y_0}^2 + (t_0 + T)^2 \sigma_{v_y}^2 \right) \right) \tag{3.17}$$

The size of the cloud was also measured along the $\overrightarrow{z_S}$ axis by rotating the mirror along the channel Θ. The normalised contrast is then fitted with Equation 3.18. The Figure 3.8b shows a good agreement between the fit curve, the numerical model and the experimental data. The optimal fit corresponds to a width of the position distribution of $\sigma_{z_0} = 0.66 \pm 0.05\,\text{mm}$.

$$\frac{\bar{C}}{C_0} = \exp\left(- 8k_{\text{eff}}^2 A_{\Theta}^2 \left(\sigma_{z_0}^2 + (t_0 + T)^2 \sigma_{v_z}^2 \right) \right) \tag{3.18}$$

These measurements of the size of the cloud are in agreements with previous measurements performed in similar setup [2]: the width of the cloud was estimated at 500 µm. However, it is not possible to confirm these measurements on this experimental setup since there is no CCD camera installed inside the magnetic shield.

3.4 Mean kinetic parameters of the cloud

In this section, a method to measure the mean transverse initial positions and velocities of the atomic cloud is described. This method uses the impact of the mirror rotation on the interferometer phase shift. As the phase shift induced by the mirror rotation depends on the mean velocity and position of the cloud, the mean kinetic parameters of the cloud can be deduced for particular angular movements.

3.4.1 Mean velocity

The mean transverse velocity of the atomic cloud was measured through the impact of the Coriolis acceleration on the phase shift of the interferometer. The Coriolis induced phase shift only depends on the mean velocity of the atomic cloud. Nevertheless, the rotation has to be chosen such that the Coriolis acceleration is preponderant. The impact of the Angular acceleration can be limited by imposing a null angular acceleration. However, the Centrifugal acceleration cannot be cancelled. Since the Centrifugal induced phase shift only depends on the kinematic parameters of the cloud along the vertical axis $\overrightarrow{x_S}$ which are known through previous measurements, its contribution can be estimated. The acceleration of the atoms $a_{x_0} \approx 9.81\,\text{m}\,\text{s}^{-2}$ is the gravity acceleration in the lab. The initial vertical speed of the atoms $v_{x_0} = 29.0 \pm 0.2\,\text{mm/s}$ is measured by Raman spectroscopy (Section 3.2.2). The vertical distance between the cloud and the mirror $x_{MA} = 420\,\text{mm}$ can be measured mechanically. Moreover, the angular movements chosen are the same as the ones used in Section 3.2.1 to limit the angular acceleration of the mirror. The measured phase shifts presented below were corrected from the vertical acceleration of the mirror as explained in Chapter 2.

Angular ramp

The first angular movement used to perform the velocity measurement is an angular ramp (see Figure 3.9): the angular acceleration is null. The phase shift of the interferometer was measured as the angular velocity was scanned.

The mirror was rotated around the axis $\overrightarrow{z_M}$ (corresponding to channel Ψ) to determine the component of the initial velocity v_{y_0} along the axis $\overrightarrow{y_S}$. On Figure 3.9a, the phase shift shows a slope break for angular velocities Ω_Ψ higher than $1.3\,\mathrm{mrad\,s^{-1}}$. This phenomenon cannot be explained by the model of the rotating interferometer and will be investigated in Section 3.5.1. For angular velocities lower than $1.3\,\mathrm{mrad\,s^{-1}}$, the corrected phase shift was fitted by Equation 3.19 to determine the velocity and a value of $v_{y_0} = -1.3 \pm 0.3\,\mathrm{mm\,s^{-1}}$ was obtained. The experimental data is in good agreement with the fit curve and the numerical model for angular velocities below $1.3\,\mathrm{mrad\,s^{-1}}$.

$$\Delta\Phi = k_{\mathrm{eff}} T^2 (-2\Omega_\Psi v_{y_0} + 2\Omega_\Psi{}^2 (a_{x_0} (\frac{t_0^2}{2} + t_0 T + T^2) + v_{x_0}(t_0 + T) + x_{MA})) \tag{3.19}$$

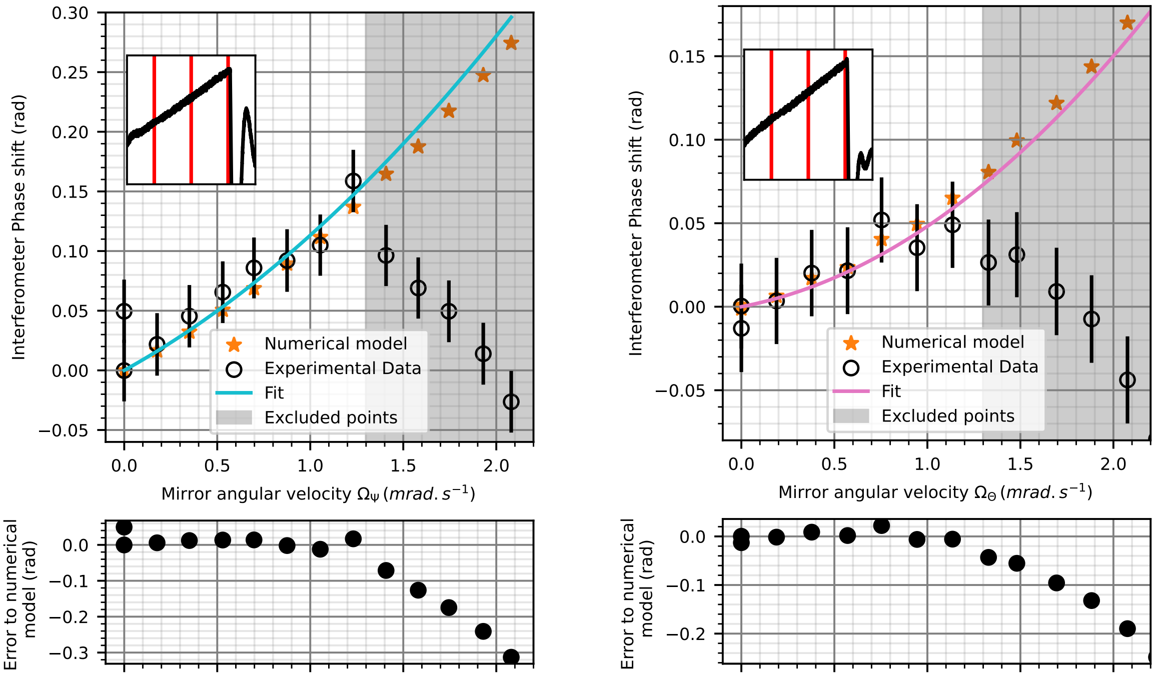

(a) Phase shift due to a rotation around axis $\overrightarrow{z_M}$ (corresponding to the channel Ψ). The initial velocity along the axis $\overrightarrow{y_S}$ is measured with a fit with a value of $v_{y_0} = -1.3 \pm 0.3\,\mathrm{mm\,s^{-1}}$

(b) Phase shift due to a rotation around axis $\overrightarrow{y_M}$ (corresponding to the channel Θ). The initial velocity along the axis $\overrightarrow{z_S}$ is measured with a fit with a value of $v_{z_0} = 0.3 \pm 0.3\,\mathrm{mm\,s^{-1}}$

Figure 3.9: Impact of an angular ramp of the mirror on the phase shift and measurement of the atomic cloud initial velocity. The angular movement is depicted in black in the insets. The three red lines represent the laser pulses of the interferometer.

The mirror was also rotated around the axis $\overrightarrow{y_M}$ (corresponding to channel Θ) to determine the component of the initial velocity v_{z_0} along the axis $\overrightarrow{z_S}$. On Figure 3.9b, the phase shift also displays a slope break for angular velocities Ω_Θ higher than $1.3\,\mathrm{rad\,s^{-1}}$. For angular velocities lower than $1.3\,\mathrm{rad\,s^{-1}}$, the corrected phase shift was fitted by Equation 3.20 to determine the velocity $v_{z_0} = 0.3 \pm 0.3\,\mathrm{mm\,s^{-1}}$. The experimental data is in good agreement with the fit curve and the numerical model for angular velocities below 1.3 $\mathrm{rad\,s^{-1}}$.

$$\Delta\Phi = k_{\mathrm{eff}} T^2 (2\Omega_\Theta v_{z0} + 2{\Omega_\Theta}^2 (a_{x_0}(\frac{t_0^2}{2} + t_0 T + T^2) + v_{x_0}(t_0 + T) + x_{MA})) \tag{3.20}$$

Sinusoidal angular movement at $\frac{1}{4T} \approx 5\,\mathrm{Hz}$

The second angular movement used to perform the velocity measurement is a sinusoidal movement at $\frac{1}{4T} \approx 5\,\mathrm{Hz}$ (see insets of Figure 3.10) with a phase of zero. This movement presents a null angular acceleration for the interferometer and a non-null angular velocity. In this configuration, the phase shift is only impacted by the Coriolis and Centrifugal accelerations. The contribution of the Angular acceleration is null. As for an angular ramp, the Centrifugal acceleration can be retrieved and the mean velocity of the cloud deduced from the Coriolis acceleration.

The mirror was rotated around $\overrightarrow{z_M}$ (channel Ψ) to determine the component of the initial velocity v_{y_0} along the axis $\overrightarrow{y_S}$. On Figure 3.10a, the phase shift also displays a slope break for angular amplitude A_Ψ higher than 70 µrad corresponding to an angular velocity of 1.5 $\mathrm{mrad\,s^{-1}}$. A similar error was observed for an angular ramp. For angular amplitude lower than 70 µrad, the corrected phase shift was fitted by Equation 3.21 to determine the velocity: $v_{y_0} = -1.1 \pm 0.2\,\mathrm{mm\,s^{-1}}$. The experimental data is in good agreement with the fit curve for angular velocities below 70 µrad. The numerical model start to display some difference from the experimental data as the velocity taken into account is the velocity determined by the angular ramp measurement at $-1.3 \pm 0.3\,\mathrm{mm\,s^{-1}}$.

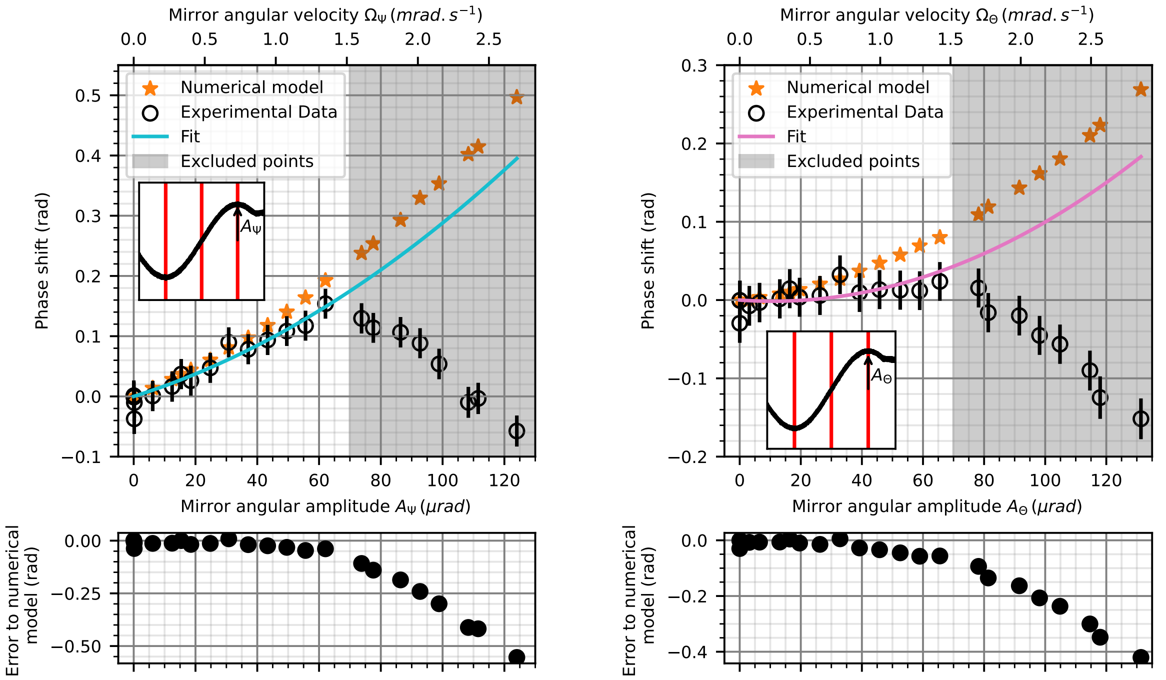

(a) Phase shift due to a rotation around axis $\overrightarrow{z_M}$ (corresponding to the channel Ψ). The initial velocity along the axis $\overrightarrow{y_S}$ is measured with a fit with a value of $v_{y_0} = -1.1 \pm 0.2\,\mathrm{mm\,s^{-1}}$

(b) Phase shift due to a rotation around axis $\overrightarrow{y_M}$ (corresponding to the channel Θ). The initial velocity along the axis $\overrightarrow{z_S}$ is measured with a fit with a value of $v_{z_0} = 0.2 \pm 0.2\,\mathrm{mm\,s^{-1}}$

Figure 3.10: Impact of a sinusoid angular movement at $\frac{1}{4T} \approx 5\,\mathrm{Hz}$ of the mirror on the phase shift and measurement of the atomic cloud initial velocity. The angular movement is depicted in black in the insets. The three red lines represent the laser pulses of the interferometer.

$$\Delta\Phi = k_{\text{eff}} T^2 \left(-2\frac{A_\Psi}{T} v_{y0} + 2\frac{A_\Psi^2}{T^2}\left(a_{x_0}\left(\frac{t_0^2}{2} + t_0 T + T^2\right) + v_{x_0}(t_0 + T) + x_{MA}\right)\right) \tag{3.21}$$

The mirror was also rotated around the axis $\overrightarrow{y_M}$ (channel Θ) to determine the component of the initial velocity v_{z0} along the axis $\overrightarrow{z_S}$. On Figure 3.10b, the phase shift also displays a slope break for angular amplitude A_Θ higher than 70 µrad corresponding to 1.5 mrad s^{-1}. For angular amplitude lower than 70 µrad, the corrected phase shift was fitted by Equation 3.22 to determine the velocity: $v_{z_0} = 0.2 \pm 0.2\,\text{mm}\,\text{s}^{-1}$. The experimental data is in good agreement with the fit curve for angular amplitude below 70 µrad. The numerical model displays some difference from the experimental data as the velocity taken into account is the velocity determined by the angular ramp measurement at 0.3 ± 0.3 mm.

$$\Delta\Phi = k_{\text{eff}} T^2 \left(2\frac{A_\Theta}{T} v_{z0} + 2\frac{A_\Theta^2}{T^2}\left(a_{x_0}\left(\frac{t_0^2}{2} + t_0 T + T^2\right) + v_{x_0}(t_0 + T) + x_{MA}\right)\right) \tag{3.22}$$

The rotation of the mirror allows the measurements of the initial velocity of the atomic cloud in two different ways. The two measurements are in agreements at one standard deviation for the velocity along the $\overrightarrow{y_S}$ axis ($-1.3 \pm 0.3\,\text{mm}\,\text{s}^{-1}$ and $-1.1 \pm 0.2\,\text{mm}\,\text{s}^{-1}$) and for the velocity along the $\overrightarrow{z_S}$ axis ($0.3 \pm 0.3\,\text{mm}\,\text{s}^{-1}and0.2 \pm 0.2\,\text{mm}\,\text{s}^{-1}$). The non-zero initial velocity of the cloud could originate from the cooling phase of the atoms. It can be due to imbalanced laser beams during the molasses stage [131]. The measured velocity is in agreement with the residual velocity in molasses cooled atoms in similar setup [98] estimated to be less than 2 mm s^{-1}.

3.4.2 Mean position

The transverse mean position of the atomic cloud with respect to the mirror centre of rotation was measured by rotating the mirror. This is possible as the phase shift induced by the Angular acceleration depends on the mean position and mean velocity of the cloud. The knowledge of the mean velocity from Section 3.4.1 will be used to determine the position of the cloud. The values for the mean velocity are $v_{y_0} = -1.3 \pm 0.3\,\text{mm}\,\text{s}^{-1}$ and $v_{z_0} = 0.3 \pm 0.3\,\text{mm}\,\text{s}^{-1}$ derived by the angular ramp measurements. The measured phase shifts presented below were corrected from the vertical acceleration of the mirror as explained in Chapter 2.

To determine the mean position of the cloud, the angular movement of the mirror was chosen such that the interferometer is only impacted by the Angular acceleration and is the same as the one used in Section 3.3. The sinusoidal angular movement at $\frac{1}{2T} \approx 10\,\text{Hz}$ depicted on Figure 3.11 has an important angular acceleration (up to 175 mrad s^{-2}) and a small angular velocity (less than 4×10^{-12} rad s^{-1}). The contributions of the Coriolis and Centrifugal accelerations are negligible.

To measure the position of the cloud along axis $\overrightarrow{y_M}$, the amplitude A_Ψ of the sinusoidal movement around $\overrightarrow{z_M}$ is scanned and the phase shift is then fitted with Equation 3.23.

$$\Delta\Phi = k_{\text{eff}} T^2 \left[\frac{4A_\Psi}{T^2}\Big((t_0 + T) v_{y_0} + y_{MA}\Big)\right] \tag{3.23}$$

Figure 3.11a shows a good agreement between the fit curve, the numerical model and the experimental data. The optimal fit corresponds to a position of $y_{MA} = 1.09 \pm 0.03\,\text{mm}$. This characterise the position of the cloud with respect to the centre of rotation of the mirror immediately after the cooling stage.

The position of the cloud along the axis $\overrightarrow{z_M}$ was also measured by scanning the angular

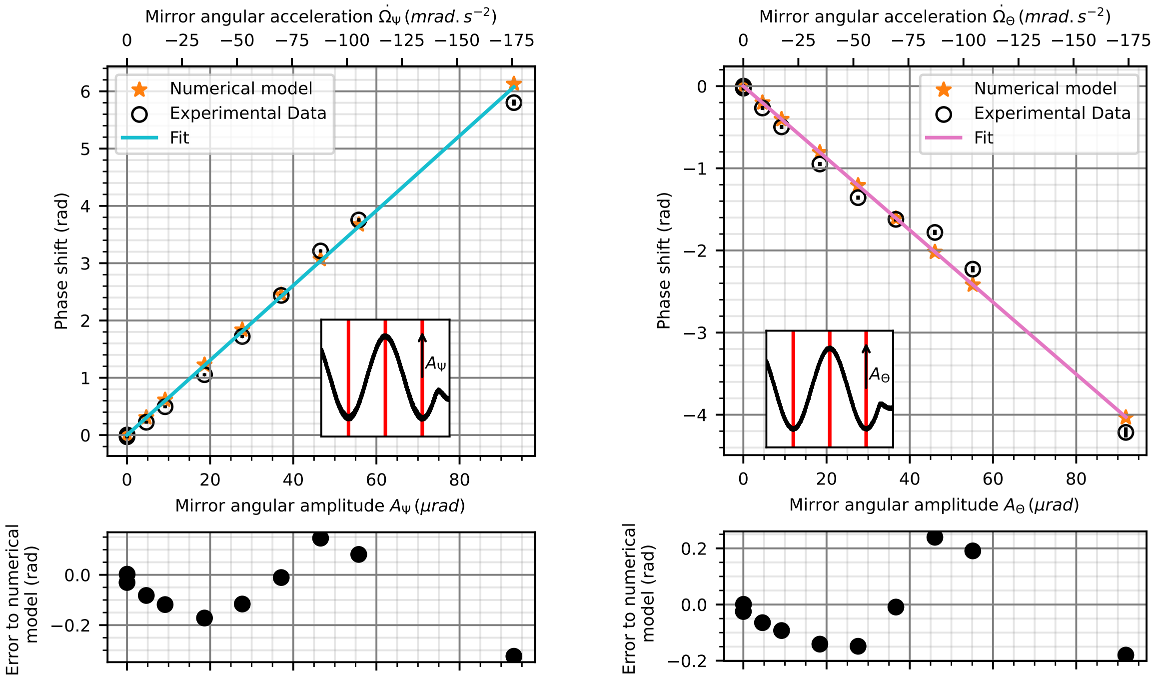

(a) Phase shift due to a rotation around axis $\overrightarrow{z_M}$ (corresponding to the channel Ψ). The initial position along the axis $\overrightarrow{y_S}$ is measured with a fit with a value of $y_{MA} = 1.09 \pm 0.03\,\text{mm}$

(b) Phase shift due to a rotation around axis $\overrightarrow{y_M}$ (corresponding to the channel Θ). The initial velocity along the axis $\overrightarrow{z_S}$ is measured with a fit with a value of $z_{MA} = 0.66 \pm 0.03\,\text{mm}$

Figure 3.11: Impact of a sinusoid angular movement at $\frac{1}{2T} \approx 10\,\text{Hz}$ of the mirror on the phase shift and measurement of the atomic cloud initial position. The angular movement is depicted in black in the insets. The three red lines represent the laser pulses of the interferometer.

amplitude A_Θ of the sinusoidal movement around $\overrightarrow{y_M}$ and measuring the phase shift of the interferometer. This phase shift is then fitted with Equation 3.24.

$$\Delta\Phi = k_{\text{eff}} T^2 \left[-\frac{4A_\Theta}{T^2} \Big((t_0 + T) v_{z_0} + z_{MA} \Big) \right] \tag{3.24}$$

Figure 3.11b shows a good agreement between the fit curve, the numerical model and the experimental data. The optimal fit corresponds to a position of $z_{MA} = 0.66 \pm 0.03\,\text{mm}$.

The initial position of the cloud measured by rotating the mirror are thus of the order of the millimetre and are coherent with what was observed during the alignment of the EA with the atomic setup.

3.5 Limitations of the EA proof-mass rotation

The EA used as an actuated mirror has many advantages such as the precise control of the proof-mass movement and the detection of its position. Nevertheless, several limitations linked to the EA were observed during this study.

3.5.1 Limitations of the reflection on the EA proof-mass

During the rotation study, an unexplained phase shift was observed in Section 3.1.1 and in Chapter 4. When the EA is rotated around the axes $\overrightarrow{y_M}$ or $\overrightarrow{z_M}$ with an angular velocity higher than $1.3\,\mathrm{mrad\,s^{-1}}$, a linear error to the model was observed up to $0.3\,\mathrm{rad}$ on the atomic interferometer phase shift. This effect was only observed when the mirror was rotated dynamically and not when its angle was constant. As this phenomenon was investigated, it appeared that this error is present whether the effective wavevector is downward or upward $\overrightarrow{k_{\mathrm{eff}}}$. Moreover the sign of this unexplained phase shift depends of the sign of $\overrightarrow{k_{\mathrm{eff}}}$.

Hypotheses

A first hypothesis is a variation of the measurement direction of the interferometer due to the rotation. The angle variation of the mirror is lower than $\theta_{max} = 100\,\mathrm{\mu rad}$ (Section 2.4.2). Such an angle would lead to a phase shift variation of $\Delta\Phi = -k_{\mathrm{eff}}T^2 g\theta_{max} \approx 3\,\mathrm{mrad}$. The variation of the measurement direction has an impact too weak on the phase shift to explain the observed error.

This unexpected phase shift could also be linked to the Raman laser wave front distortion due to the reflection on the EA proof-mass. As the angular velocity increases, the area of the wave front explored by the atoms increases and the effect on the phase shift of potential wave front aberrations also increases. The EA proof mass optical quality is expected to be better than $\frac{\lambda}{4}$ ($\lambda \approx 600\,\mathrm{nm}$) but it could be further characterised thanks to a wave front analyser in future studies. Nevertheless, to the current knowledge of the optical quality of the EA proof-mass and windows on the path of the Raman laser, the reflected laser wavefront is expected to have a curvature of $R \approx 100\,\mathrm{m}$. Such a curvature in the presence of a rotation would lead to a term $\delta\Phi = k_{\mathrm{eff}}T^2\left(\frac{2v_{y0}x_{MA}\Omega}{R}\right) \leq 1\,\mathrm{mrad}$ for $\Omega = 2\,\mathrm{mrad\,s^{-1}}$. The curvature of the wavefront could not explain the phase shift observed experimentally.

A last hypothesis would be the impact of the rotation during the detection step. During the experiments performed in this study, the mirror rotates when the detection laser is shined. Thus, reflected detection beam is rotated which could have an impact on the detected atoms.

Influence of the size of the reflected beam

To test the hypothesis of wave front distortion due to the EA proof-mass, the diameter of the collimated laser beam reflected on the proof mass was reduced by closing a diaphragm placed after the vacuum cell. By reducing the size of the laser beam reflected on the EA, the area of the proof mass used as a mirror was limited: the wave front explored by the atoms is also limited and the unexplained phase shift should decrease. The phase shift and contrast of the interferometer were measured for different laser diameter with an angular ramp of the mirror around the axis $\overrightarrow{z_M}$ (Figure 3.12). All the other measurements in Chapter 3 and 4 were performed with a diameter of 7 mm which is the size of the hole in the EA cage.

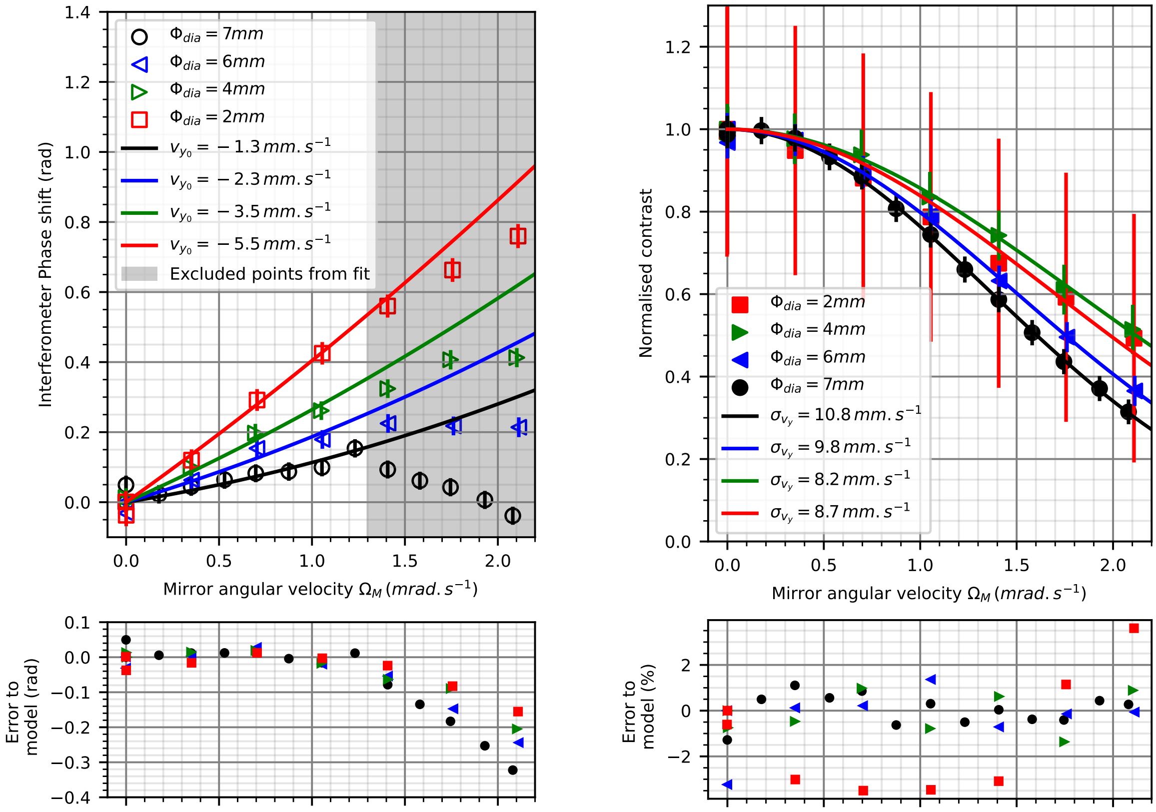

(a) Phase shift induced by an angular ramp around the axis $\overrightarrow{z_M}$ for different diameter of the reflected laser beam.

(b) Contrast loss induced by an angular ramp around the axis $\overrightarrow{z_M}$ for different diameter of the reflected laser beam.

Figure 3.12: Study of the reflection of the laser beam on the EA proof mass and its impact on the interferometer. The diameter of the laser reflected on the EA is reduced to limit the area of the proof-mass used as a mirror.

The effect of the beam size on the phase shift is important (Figure 3.12a). The phase shift increased as the diameter diminished. The error to the model decreased from -0.3 rad to -0.15 rad but the mean velocity of the atoms had to be adjusted. As the diameter decreased, a selection of the atoms participating in the interferometer is done resulting in a variation of the mean velocity. This result tends to confirm an effect linked to the wave front distortion of the reflected laser. For a small diaphragm, the atoms participating in the interferometer are colder and do not explore the wave front as much.

The effect of atomic selection seems to be confirmed by the contrast measured on Figure 3.12b. As the diameter decreases, the contrast in the absence of rotation decreased from 41% ($\phi_{dia} = 7$ mm) to 4% ($\phi_{dia} = 2$ mm) as the number of atoms participating in the interferometer diminished. It is also interesting to note that the contrast loss due to the rotation lessens when the beam diameter got smaller. The atomic selection reduced the width of the velocity distribution of the atoms participating in the interferometer from $\sigma_{vy} = 10.8\,\mathrm{mm\,s^{-1}}$ to $\sigma_{vy} = 8.7\,\mathrm{mm\,s^{-1}}$.

If this result supports the hypothesis of a wave front distortion of the reflected beam, further investigation will be required. For example, the wave front of the reflected laser could be measured with a wave front analyser.

3.5.2 Imperfections of the proof-mass control

During the experiments involving the rotation of the EA proof-mass, some limitations in the proof-mass control were noticed. First, the rotation of the proof-mass induces a vertical movement of the proof-mass. Secondly, the driven rotation along a given axis cause a residual rotation around its perpendicular axis. Measurements were carried out to study these residual movements. These two effects are taken into account in the data processing. The vertical acceleration of the proof-mass induced a phase shift which is subtracted in the experimental data of Chapter 3 and 4. The effect of the residual rotation on the perpendicular axis is taken into account in the numerical model.

Vertical acceleration of the EA proof mass

The vertical movement of the proof-mass with respect to the proof-mass rest position at the centre of the electrodes was studied thanks to the capacitive detection of the EA along the $\overrightarrow{x_S}$ axis. In this paragraph, the vertical movement for an angular ramp along the channel Ψ and Θ is presented and its impact on the interferometer characterised (Figure 3.13). The acceleration of the proof-mass is the relevant value as the interferometer is sensitive to the acceleration of the mirror. The impact of the proof-mass vertical movement can be computed as follows:

$$\Delta\Phi_{acc\,EA} = k_{\text{eff}} T^2 a_{x_{EA}} \tag{3.25}$$

with $a_{x_{EA}}$ the acceleration of the proof-mass with respect to the EA cage. As can be seen on Figure 3.13a, an angular ramp along the channel Ψ leads to an acceleration of the proof-mass reaching $-0.36\,\mu\mathrm{m\,s^{-1}}$. Respectively, for the channel Θ, the acceleration is up to $0.8\,\mu\mathrm{m\,s^{-1}}$. This difference could be explained by the design of the EA electrodes (see Figure 2.22a): three pairs of electrodes (X1±, X2± and X3±) contributes to the control of the vertical position. Among them, two "small" pairs (X2± and X3±) generate the rotation along Ψ while all pairs generate the rotation along Θ. This design could explain the difference of behaviour between the two channels leading to different couplings between inclination and piston.

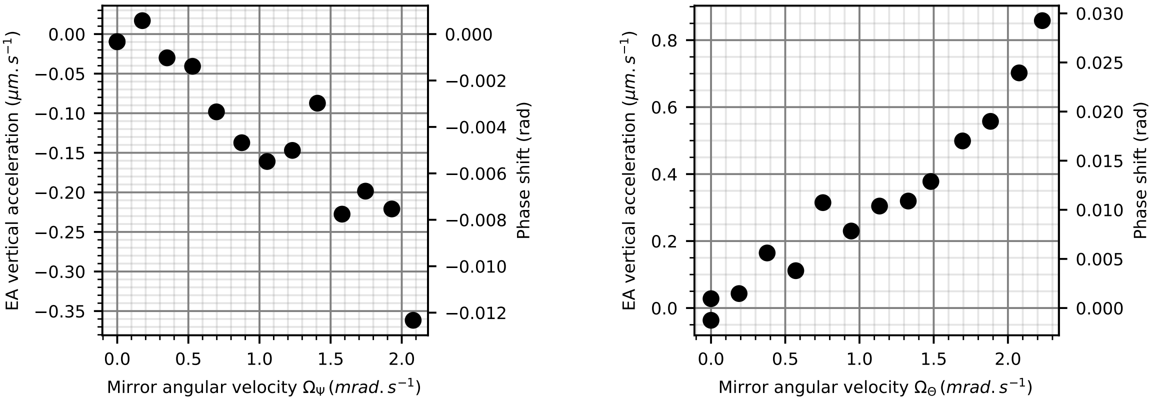

(a) EA vertical acceleration relevant for the interferometer for an angular ramp along the channel Ψ.

(b) EA vertical acceleration relevant for the interferometer for an angular ramp along the channel Θ.

Figure 3.13: Residual vertical acceleration of the EA proof-mass generated by an angular ramp. The acceleration and phase shift that should be measured by the interferometer are presented.

Residual rotation along the perpendicular axis of the EA proof mass

The residual rotation was studied thanks to the capacitive detection for an angular ramp along channel Ψ or Θ. For a driven angular ramp along Ψ, the residual rotation along Θ

is characterised by an angular velocity up to 29 µrad s^{-1} and an angular acceleration up to −19.8 µrad s^{-2} leading to a phase shift up to 180 µrad (Figure 3.14a). The phase shift induced by the residual rotation was computed using Equation 3.26 and the numerical model.

$$\Delta\Phi_{\mathrm{res}\,\Theta} = k_{\mathrm{eff}}T^2\Big[\,2\Omega_\Theta v_{z_0} + 2\Omega_\Theta^2\Big(a_{x_L}\big(\frac{t_0^2}{2} + t_0T + T^2\big) + (t_0+T)v_{x_0} + x_{AM}\Big) + \dot{\Omega}_\Theta\big((t_0+T)v_{z_0} + z_{AM}\big)\,\Big] \tag{3.26}$$

For a driven angular ramp along Θ, the residual rotation along Ψ is characterised by an angular velocity up to −1.1 µrad s^{-1} and an angular acceleration up to 8.7 µrad s^{-2} leading to a phase shift up to −400 µrad (Figure 3.14b). The phase shift induced by the residual rotation was computed using Equation 3.27 and the numerical model. If the residual rotation is smaller for a driven rotation along the Θ, the phase shift is more important due to the kinematic parameters of the atomic cloud.

$$\Delta\Phi_{\mathrm{res}\,\Psi} = k_{\mathrm{eff}}T^2\Big[\,-2\Omega_\Psi v_{y_0} + 2\Omega_\Psi^2\Big(a_{x_L}\big(\frac{t_0^2}{2} + t_0T + T^2\big) + (t_0+T)v_{x_0} + x_{AM}\Big) - \dot{\Omega}_\Psi\big((t_0+T)v_{y_0} + y_{AM}\big)\,\Big] \tag{3.27}$$

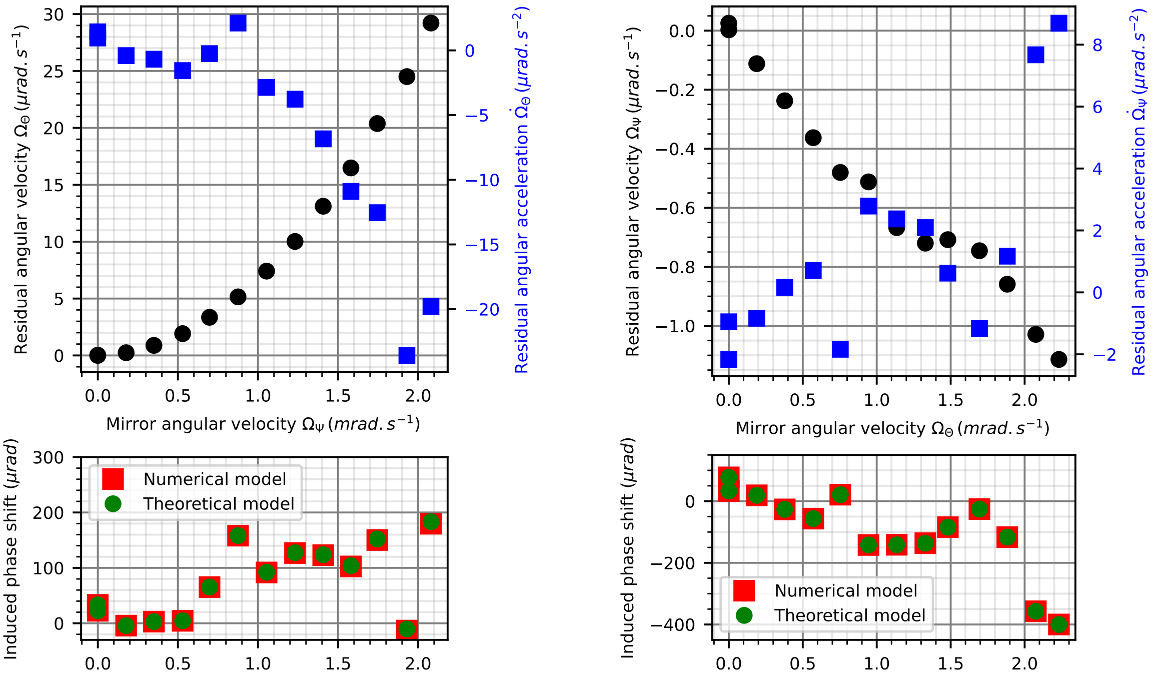

(a) Residual angular velocity and acceleration along channel Θ for a principal ramp rotation along the channel Ψ and the interferometer phase shift induced by the residual rotation.

(b) Residual angular velocity and acceleration along channel Ψ for a principal ramp rotation along the channel Θ and the interferometer phase shift induced by the residual rotation.

Figure 3.14: Characterisation of the residual rotation around the axis of the EA proof mass perpendicular to the principal linear rotation and its impact on the interferometer phase shift.

The behaviour is different between channel Θ and channel Ψ due to the electrodes disposition (see Chapter 2). If the mirror acceleration is bigger for a rotation along the channel Θ, the residual rotation is more important for driven rotations along Ψ. Those limitations could be reduced by modifying the electrodes design to improve the control of the proof mass. The pair of electrodes X1± could be for example divided in two pairs of electrodes.

The effects presented in this Section were considered in the data processing. The phase shift induced by the vertical acceleration of the mirror was corrected in all the experimental data presented. The residual rotation was taken into account in the numerical model but not in the theoretical model.

Conclusion

In this Chapter, the impact of the mirror angular velocity and angular acceleration were studied separately. The contrast loss and phase shift induced by the mirror rotation were compared to the theoretical and numerical models. The experimental data agree with the models except for the phase shift induced by important angular velocities.

The atomic cloud was also characterised through the rotation of the retro-reflection mirror. The mirror rotation method allows the measurement of the transverse kinematic parameters of the cloud such as the deviation of its velocity distribution ($\sigma_{vy} = 10.8 \pm 0.2\,\mathrm{mm\,s^{-1}}$ and $\sigma_{vz} = 11.1 \pm 0.2\,\mathrm{mm\,s^{-1}}$), its mean velocity ($v_{y_0} = -1.3 \pm 0.3\,\mathrm{mm\,s^{-1}}$ and $v_{z_0} = 0.3 \pm 0.3\,\mathrm{mm\,s^{-1}}$), its size ($\sigma_{y_0} = 0.42 \pm 0.05\,\mathrm{mm}$ and $\sigma_{z_0} = 0.66 \pm 0.05\,\mathrm{mm}$) and mean position ($y_{MA} = 1.09 \pm 0.03\,\mathrm{mm}$ and $z_{MA} = 0.66 \pm 0.03\,\mathrm{mm}$). The Raman spectroscopy provides an estimation of the vertical cloud parameters such as the width of the velocity distribution ($\sigma_{v_x} = 11.3 \pm 0.2\,\mathrm{mm\,s^{-1}}$) and its mean velocity ($v_{x_0} = 29.0 \pm 0.2\,\mathrm{mm/s}$). In this characterisation, the velocity and position distributions were considered as Gaussian distributions.

For important rotation, an unexplained phase shift appears probably linked with the laser reflection on the EA. It could be due to a deterioration of the laser wave front as it is reflected on the proof-mass. A characterisation of the reflected laser wave front could help understand this effect.

The imperfect motion control of the EA proof-mass was also studied and its impact on the interferometer phase shift estimated. If the residual motions effects on the phase shift can be computed, an increased number of electrodes could be considered in the future to reduce the residual motions.

CHAPTER 4

Characterisation of a rotating sensor and rotation compensation strategy

Outline of the current chapter

Introduction

In this Chapter are presented the experimental results of the rotation compensation. Moreover, the impact of the sole sensor rotation was also studied. The rotation compensation method was implemented on the experimental setup for sinusoidal angular movements due to experimental restrictions. Two different cases were studied by tuning the phase of the sinusoidal angular movement. In the first case, the interferometer is performed during the side of the sinusoidal angular oscillation: the angular velocity is maximised and an attempt is made to compensate its effects. In the second case, the interferometer is performed during the top of the sinusoidal angular oscillation: the angular acceleration is maximised and an attempt is made to compensate its effects.

To understand the different mechanisms at stake, several steps were carried out. Firstly, the consequences of the sensor rotation and the mirror rotation were studied independently. For this step, the sensor rotation and the mirror rotation were not performed at the same time and were opposite to anticipate the rotation compensation method. Secondly, the rotation compensation method was implemented by rotating the sensor and the mirror oppositely. The rotation of the mirror was adjusted manually to compensate as best as possible the sensor rotation. This step allows to test the principle of the rotation compensation method. Thirdly, an automated rotation compensation setup was implemented. The mirror rotation is driven directly by the sensor rotation through an action chain. All the experimental data were gathered for an interferometer with an interrogation time of 46 ms.

4.1 Preamble to the experimental results

Prior to the experimental results presentation, here is some information concerning the data processing of the experimental data below. Information on the data processing can also be found in 2.4.

4.1.1 Gyroscope signal

The sensor was rotated by driving the height of a piezo-electric actuator. To avoid exciting vibrations mode, the rotation excitation was sinusoidal with a 4 Hz frequency. The frequency of the rotation excitation is imposed by the 250 ms repetition rate of the experimental sequence. As the rotation and the experimental cycle have the same frequency, it is easier to synchronise the rotation with the interferometer. The gyroscope signal Ω_{gyro} was acquired during the interferometer as can be seen on Figure 4.1. This signal is fitted by a sinusoidal function $\Omega_S(t)$ at a 4 Hz frequency (Equation 4.1 and dark green curve on Figure 4.1).

$$\Omega_S^{\mathrm{fit}}(t) = \Omega_0 + A_S \omega \cos(\omega(t - t_0 - T) + \phi_S) \tag{4.1}$$

with Ω_0 an offset, A_S the angular amplitude, ω the frequency of the sinusoid, ϕ_S its phase, T is the interrogation time of the interferometer and t_0 the time of the first laser pulse. The knowledge of the amplitude A_S and phase ϕ_S enables the calculation of the angular position through integration given by Equation 4.2 in dotted blue on Figure 4.1.

$$\theta_S^{\mathrm{fit}}(t) = A_S \sin(\omega(t - t_0 - T) + \phi_S) \tag{4.2}$$

The angular position of the sensor is only relevant for the interferometer during the laser pulses (black crosses). The angular movement can be approximate by a second-degree polynomial expression (Equation 4.3 in dark blue).

$$\theta_S^{\mathrm{poly}}(t) = \theta_S^0 + \Omega_S.(t - t_0 - T) + \dot{\Omega}_S.\frac{(t - t_0 - T)^2}{2} \tag{4.3}$$

with θ_S^0 the angular position at the second laser pulse, Ω_S the angular velocity and $\dot{\Omega}_S$ the angular acceleration seen by the interferometer. This polynomial expression allows to compare the actual rotation movement with the theoretical angular movement given by Equation 1.46 in Chapter 1. The coefficients of the polynomial expression Ω_S and $\dot{\Omega}_S$ will be used to compute the theoretical model presented in Chapter 1 and to compared it to the experimental data. These coefficients can also be computed as:

$$\begin{aligned} \Omega_S &= \frac{\theta_S^{\mathrm{fit}}(t_0 + 2T) - \theta_S^{\mathrm{fit}}(t_0)}{2T} \\ \dot{\Omega}_S &= \frac{\theta_S^{\mathrm{fit}}(t_0) - 2\theta_S^{\mathrm{fit}}(t_0 + T) + \theta_S^{\mathrm{fit}}(t_0 + 2T)}{T^2} \end{aligned} \tag{4.4}$$

This treatment of the gyroscope signal considers the actual phase of the sinusoidal gyroscopic signal. In the case where the angular velocity is maximised, the phase ϕ_S of the angular movement target value is 0 at the second laser pulse. However, due to experimental limitations, this phase ranges from −0.06 rad to 0.11 rad. In the case of a maximised angular acceleration, the phase target value is $\frac{\pi}{2}$ but ranges experimentally from 1.63 rad to 1.73 rad. This phase is important as it increases the angular acceleration (respectively velocity) of the sensor when the angular velocity (respectively acceleration) is maximised.

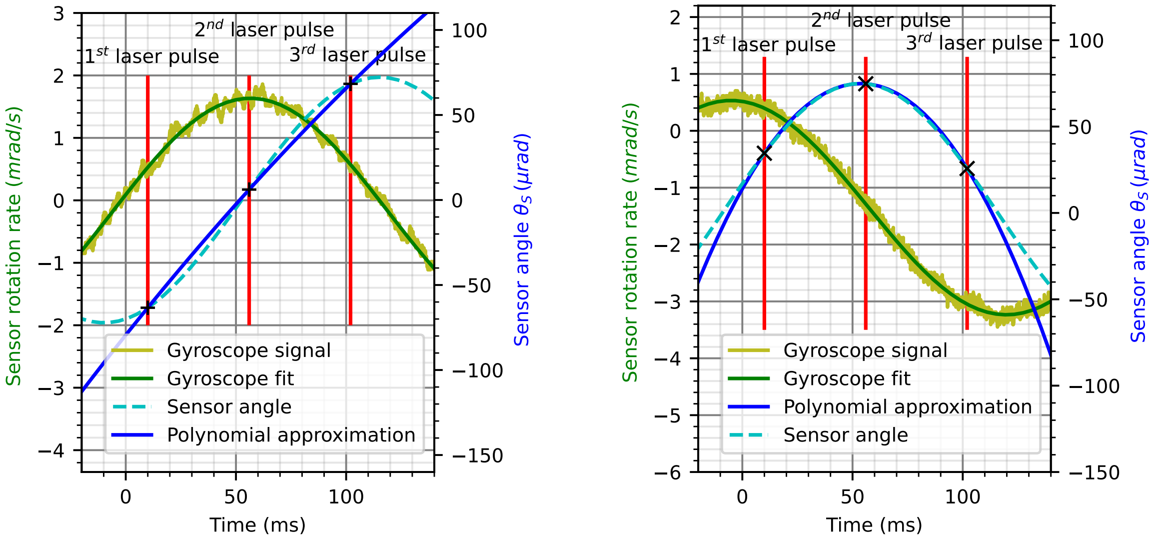

(a) Maximised angular velocity: the interferometer is performed during the side of the sinusoidal angular oscillation. This case corresponds to Equation 2.15.

(b) Maximised angular acceleration: the interferometer is performed during the top of the sinusoidal angular oscillation. This case corresponds to Equation 2.16.

Figure 4.1: Processing of the gyroscope signal (in light green). The signal is fitted by a sinusoid (in dark green), the angular position of the sensor is deduced by integration (dotted light blue line). As the sensor position impacts the interferometer only during the laser pulses (in red), its position at the three laser pulses (black cross) can be approximated by a second-degree polynomial (in dark blue). The angular velocity and acceleration are the coefficients of this polynomial.

4.1.2 EA signal

The mirror of the interferometer was rotated thanks to EA control setup by tuning the electrostatic forces applied to the proof-mass. The EA capacitive detection signal along the channel Ψ (corresponding to the angular position around the $\overrightarrow{z_M}$) was also acquired during the interferometer as can be seen on Figure 4.2. The data processing is very similar to the one applied to the gyroscope signal (Section 4.1.2). As the capacitive detection supplies directly the angular position of the mirror, its signal is fitted by a sinus at 4 Hz (Equation 4.5 in light blue on Figure 4.2).

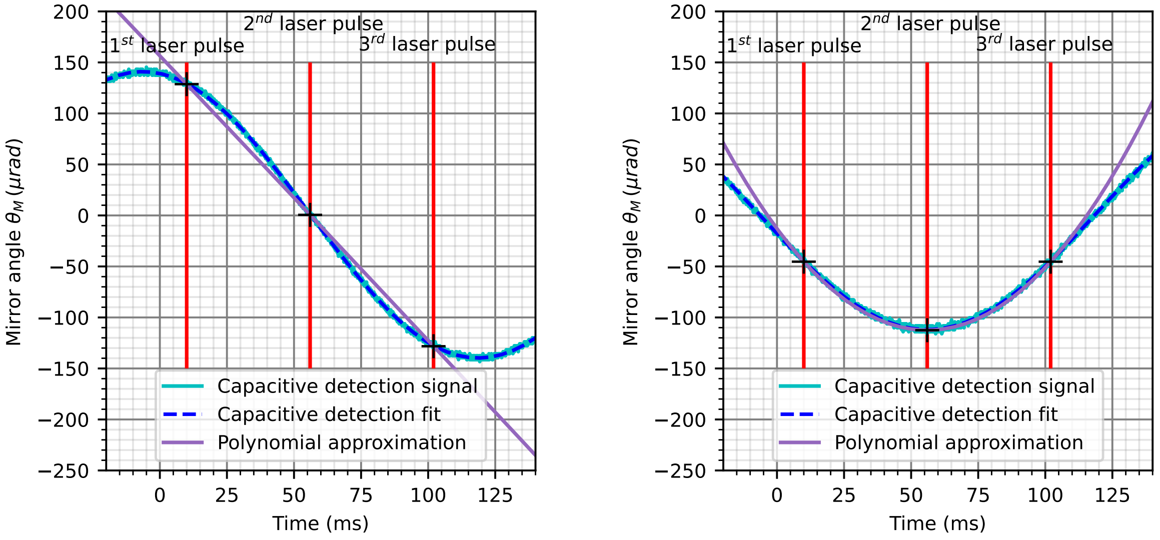

(a) Maximised angular velocity: the interferometer is performed during the side of the sinusoidal angular oscillation. This case corresponds to Equation 2.20.

(b) Maximised angular acceleration: the interferometer is performed during the top of the sinusoidal angular oscillation. This case corresponds to Equation 2.21.

Figure 4.2: Processing of the EA capacitive detection signal (in light blue). The signal is fitted by a sinusoid (in dark blue). As the sensor position impacts the interferometer only during the laser pulses (in red), its position at the three laser pulses (black cross) can be approximated by a second-degree polynomial (in purple). The angular velocity and acceleration are the coefficients of this polynomial.

$$\theta_M^{\text{fit}}(t) = \theta_{\text{offset}} + A_M \sin(\omega(t - t_0 - T) + \phi_M) \tag{4.5}$$

with θ_{offset} an offset, A_M the angular amplitude and ϕ_M the phase of the sinusoid. The angular position of the mirror is only relevant for the interferometer during the laser pulses (black crosses). The angular movement can then be approximated by a second-degree polynomial expression (Equation 4.6 in purple).

$$\theta_M^{\text{poly}}(t) = \theta_M^0 + \Omega_M.(t - t_0 - T) + \dot{\Omega}_M.\frac{(t - t_0 - T)^2}{2} \tag{4.6}$$

with θ_M^0 the angular position at the second laser pulse, Ω_M the angular velocity and $\dot{\Omega}_M$ the angular acceleration seen by the interferometer. This polynomial expression allows to compare the actual rotation movement with the theoretical angular movement described by 1.49 in Chapter 1. The coefficients of the polynomial expression Ω_M and $\dot{\Omega}_M$ will be used to compute the theoretical model and to compared it to the experimental data. These coefficients can also be computed as:

$$\begin{aligned} \Omega_M &= \frac{\theta_M^{\text{fit}}(t_0 + 2T) - \theta_M^{\text{fit}}(t_0)}{2T} \\ \dot{\Omega}_M &= \frac{\theta_M^{\text{fit}}(t_0) - 2\theta_M^{\text{fit}}(t_0 + T) + \theta_M^{\text{fit}}(t_0 + 2T)}{T^2} \end{aligned} \tag{4.7}$$

This treatment of the capacitive detection signal considers the actual phase of the sinusoidal capacitive signal. In the case of a maximised angular velocity, the phase of the angular movement target value is 0 at the second laser pulse. Experimentally this phase ranges from −6 mrad to 0.3 mrad. In the case of a maximised angular acceleration, the phase target value is $\frac{\pi}{2}$ and ranges experimentally from 1.56 rad to 1.57 rad. As the mirror is better controlled than the sensor, this uncontrolled phase is smaller leading to a smaller angular acceleration (respectively velocity) of the mirror when the angular velocity (respectively acceleration) is maximised.

4.1.3 Phase shift

The experimental phase shift was extracted from the interference fringes as described in Chapter 2. The phase shift of interest in this study is the rotation induced phase shift. It is calculated by subtracting the phase shift in the absence of rotation from the experimental phase shift. In the rest of this Chapter, only the phase shift induced by the angular movement is presented.

The angular motion of the sensor induces several side effects due to experimental imperfections impacting the phase shift. The two main side effects are the vertical movement of the EA proof-mass and the parasite rotation around the $\overrightarrow{y_S}$ axis of the sensor. Those effects are considered in the numerical model. Thus, the experimental data can be directly compared to the numerical model as can be seen in Figure 4.3. The phase shift is mostly induced by the side effects in this case where the sensor is rotated in order to maximised the angular velocity. During this experiment, the proof-mass acceleration with respect to its cage was up to $-37.2\,\mu\text{m}\,\text{s}^{-2}$ inducing a phase up to −1.27 rad. The phase shift induced by the EA vertical acceleration was computed using the capacitive detection signal for the vertical position.

The phase shift induced by the rotation around the $\overrightarrow{y_S}$ axis in orange in Figure 4.3 was computed using the gyroscope signal. In the case presented on Figure 4.3, the rotation around $\overrightarrow{y_S}$ is up to $0.13\,\text{mrad}\,\text{s}^{-1}$ and $-2.44\,\text{mrad}\,\text{s}^{-2}$ leading to a phase shift of −1.03 rad.

To compare the experimental data to the theoretical model presented in Chapter 1, the two side effects have to be corrected from the experimental data. The detail of the calculation of the side effects are presented in Section 2.4.4. In the rest of this Chapter, all the experimental data exposed are corrected from the side effects. The phase shift induced by the two side effects are also subtracted from the numerical model in order to compare the numerical model to the theoretical model and corrected experimental data.

To compute the theoretical and numerical models, the kinematic parameters of the atomic cloud have to be estimated. The transverse mean velocities v_{y_0} and v_{z_0} as well as the deviation of the transverse velocity distributions σ_{v_y} and σ_{v_z} were measured through the impact of the mirror rotation on the phase shift and contrast. The same method was used to estimate the mean transverse position of the cloud with respect to the mirror centre of rotation y_{MA} and z_{MA} and the deviation of the transverse position distribution σ_{y_0} and σ_{z_0}. The vertical mean velocity v_{x_0} and velocity distribution deviation σ_{v_x} were measured by Raman spectroscopy. The details of these measurements are given in Chapter 3. The vertical distances between the cloud and the

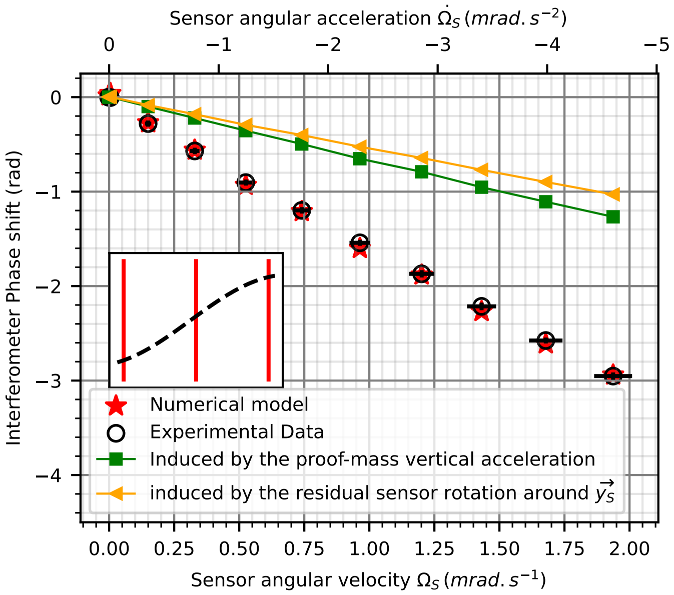

Figure 4.3: Uncorrected experimental phase shift induced by the sensor rotation around $\overrightarrow{z_S}$. The angular movement was chosen such as the angular velocity is maximised. In the inset, the angular position is represented in black and the laser pulses of the interferometer in red. the phase shift is mainly induced by the side effects: the proof-mass vertical acceleration and the sensor residual rotation around $\overrightarrow{y_S}$.

mirror and sensor centres of rotation x_{MA} and x_{OA} can be estimated thanks to the architecture of the experimental setup. On the contrary, the transverse distances between the cloud and the sensor centre of rotation are not known precisely and are then free parameters in the models presented in this Chapter. The values of the kinematic parameters are summed up in Table 2.2.

4.1.4 Contrast

The fringes amplitude A was extracted from the interference fringes as described in Chapter 2. The experimental contrast is calculated thanks to Equation 4.8 with C_{noise} the residual noise of the atomic proportion when the contrast is cancelled by an important rotation. Experimentally, the residual contrast noise was determined at $C_{noise} = 0.008$. The experimental contrast in the absence of rotation C_0 reaches 40% as can be seen on Figure 4.4.

$$C_{exp} = 2A - C_{ann} \tag{4.8}$$

To enable the comparison with the theoretical and numerical model, the experimental contrast was normalised with respect to the contrast in the absence of rotation.

$$C_{norm} = \frac{C_{exp}}{C_0} \tag{4.9}$$

4.2 Impact of angular velocity

In this section, the impact of the angular velocity on the interferometer is studied. The angular velocity is maximised and the angular acceleration minimised by implementing the interferometer during the linear part of the sinusoidal angular movement. However due to experimental limitations, the angular acceleration cannot be totally cancelled and still strongly

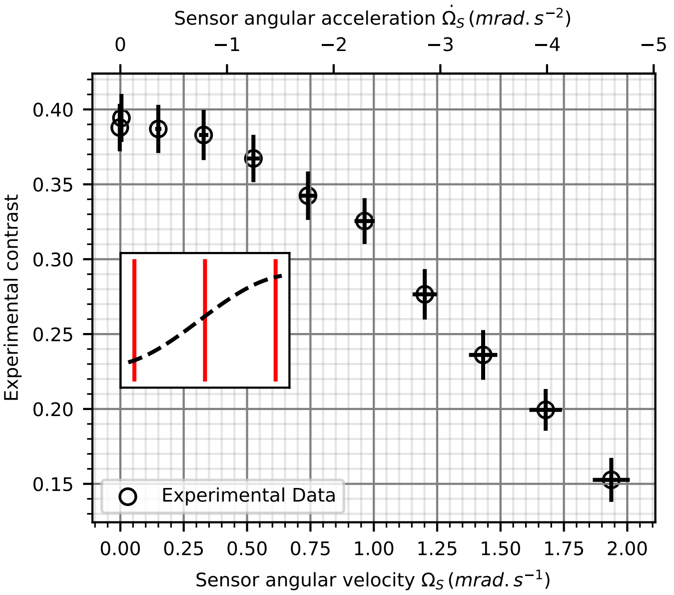

Figure 4.4: Experimental contrast loss induced by the sensor rotation around the axis $\overrightarrow{z_S}$. The angular movement was chosen such as the angular velocity is maximised. In the inset, the angular position is represented in black and the laser pulses of the interferometer in red.

impacts the interferometer. All the experimental data presented here have be gathered for an interrogation time of 46 ms.

4.2.1 Study of the sensor rotation

An experimental study of the impact of the sensor rotation on the interferometer was conducted by rotating the whole setup: the atomic sensor head, the EA sensor head and the vibration isolation platform. A study of the rotation impact on an interferometer was carry out in [42, 96] but for more important rotation velocities in the context of terrestrial onboard applications.

Contrast

The contrast loss was measured as a function of the angular velocity as can be seen on Figure 4.5b. For an angular velocity of 1 mrad s^{-1}, the measured contrast is 80% of the contrast in the absence of rotation: the sensor rotation generates a loss of contrast. Equation 4.10 is used to compute the theoretical model which agrees with the experimental data as well as the numerical model.

$$\frac{\overline{C}_S}{C_0} = \exp\left[-\frac{k_{\text{eff}}^2 T^4}{2}\left(\,\Omega_S^4\sigma_x^2 + \dot{\Omega}_S^2\sigma_y^2 + (t_0+T)^2\Omega_S^4\sigma_{v_x}^2 + ((t_0+T)\dot{\Omega}_S + 2\Omega_S)^2\sigma_{v_y}^2\,\right)\right] \tag{4.10}$$

The contrast loss is mainly due to the Coriolis acceleration linked with the cloud temperature as observed in [3] corresponding to the term $4\Omega_S^2\sigma_{v_y}^2$ in Equation 4.10. The contribution of the Coriolis acceleration to the contrast loss is represented in red on Figure 4.5b. If the Centrifugal acceleration doesn't contribute to the loss of contrast, the Angular acceleration plays a part in this phenomenon. The main term in the contrast loss formula can be approximated to $\frac{\overline{C}_S}{C_0} \approx \exp\left(-\frac{k_{\text{eff}}^2 T^4}{2}((t_0+T)\dot{\Omega}_S + 2\Omega_S)^2\sigma_{v_y}^2\right)$ when the Centrifugal acceleration contribution is neglected. Let's give some numbers: if $\Omega_S = 1.43\,\mathrm{mrad\,s^{-1}}$ and $\dot{\Omega}_S = -3.4\,\mathrm{mrad\,s^{-2}}$ (one experimental point on Figure 4.5b), the expected contrast loss is $\frac{\overline{C}_S}{C_0} \approx \exp\left(-\frac{k_{\mathrm{eff}}^2 T^4}{2}((t_0+T)\dot{\Omega}_S + 2\Omega_S)^2\sigma_{v_y}^2\right) = 60\%$. In the absence of angular acceleration $\dot{\Omega}_S = 0$, the expected contrast loss is $\frac{\overline{C}_S}{C_0} \approx \exp\left(-\frac{k_{\mathrm{eff}}^2 T^4}{2}(2\Omega_S)^2\sigma_{v_y}^2\right) = 56\%$. In this case, as the angular acceleration has an opposite sign to the angular velocity, the contrast is higher in the presence of an angular acceleration.

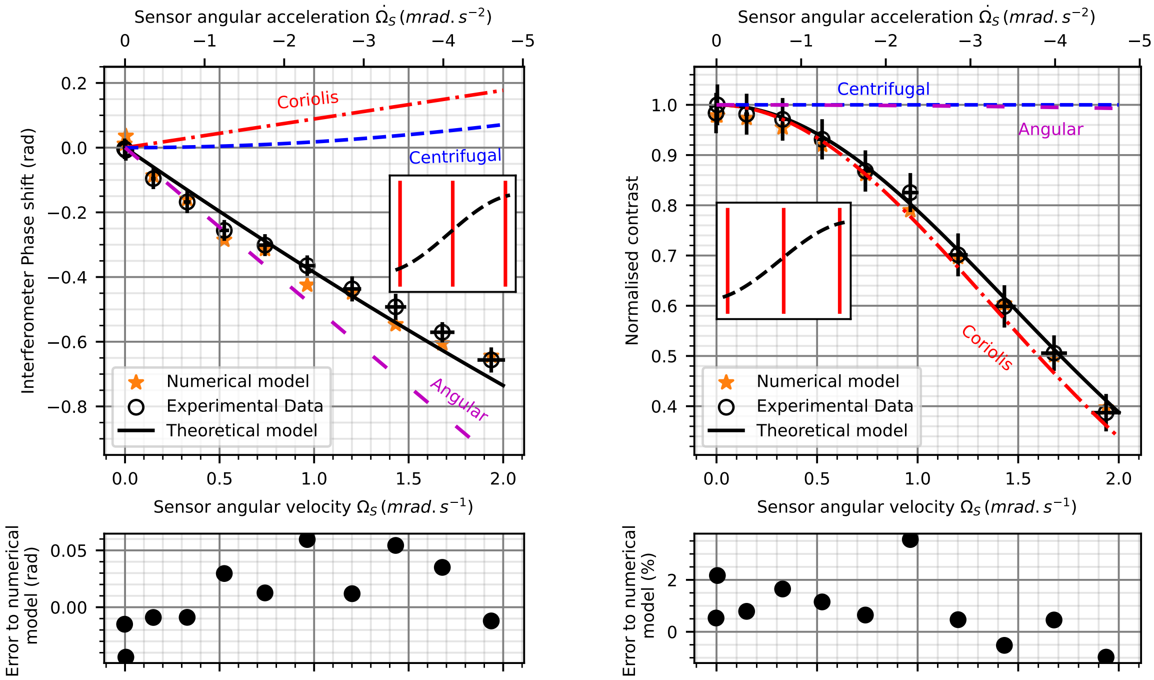

(a) Phase shift due to a sinusoidal angular movement around the axis $\overrightarrow{z_S}$.

(b) Contrast loss due to a sinusoidal angular movement around the axis $\overrightarrow{z_S}$.

Figure 4.5: Influence of the sensor angular velocity on the interferometer. The angular movement of the sensor is depicted in dotted black in the insets. The three red lines represent the laser pulses of the interferometer. The contributions of the inertial accelerations are represented as follows: Coriolis acceleration in red, Centrifugal acceleration in blue and Angular acceleration in purple. The interrogation time of the interferometer is 46 ms.

Phase shift

The phase shift induced by the rotation was also observed. As can be seen in Figure 4.5a, the phase shift is impacted by all the inertial accelerations. The theoretical model corresponds to Equation 4.11.

$$\overline{\Delta\Phi}_S = k_{\text{eff}}T^2[-a_{x_L} - 2\Omega_S v_{y_0} - \dot{\Omega}_S(v_{y_0}(t_0+T)+y_{OA}) + \Omega_S{}^2(a_{x_L}(\frac{t_0^2}{2}+t_0T+T^2)+v_{x_0}(t_0+T)+x_{OA})] \tag{4.11}$$

The different contributions of the inertial forces are represented in Figure 4.5a. The Coriolis contribution scaling as $\propto 2\Omega_S v_{y_0}$ is linear and due to residual transverse velocity at the end of the cooling stage. This residual transverse velocity could be due to unbalanced laser beam during the molasses stage [131]. The Centrifugal acceleration scaling as $\propto \Omega_S{}^2(a_{x_L}(\frac{t_0^2}{2}+t_0T+T^2)+v_{x_0}(t_0+T)+x_{OA})$ has a quadratic impact on the phase shift due to the vertical distance between the atomic cloud and the sensor centre of rotation. The Angular acceleration scaling as $\propto \dot{\Omega}_S(v_{y_0}(t_0+T)+y_{OA})$ has an impact on the interferometer phase shift due to the transverse distance between the atomic cloud and the centre of rotation. This distance in the horizontal plane is a free parameter chosen at $y_{OA} = -6\,\text{mm}$ and $z_{OA} = 12.4\,\text{mm}$ to fit the phase shift experimental data. The transverse velocity also contributes to the Angular acceleration.

The three inertial accelerations have contributions of similar magnitudes despite our efforts to minimise the angular acceleration. The apparition of the angular acceleration contribution can be explained by imperfections in the timing between the sensor angular movement and the interferometer laser pulses. Due to the vibration isolation platform, the sensor angular movement is difficult to control. The numerical model taking into account the imperfections in the sensor angular movement shows a better agreement with the experimental data than the theoretical model.

4.2.2 Study of the mirror rotation

After the study of the rotation of the whole sensor, the impact of the mirror angular velocity was studied on its own. This experiment allows to verify the theoretical predictions of Chapter 1 by rotating the EA proof-mass around the $\overrightarrow{z_M}$ axis. The rotation was chosen opposite to the sensor rotation studied in Subsection 4.2.1 to anticipate the rotation compensation study. Similar experiments rotating the retro-reflection mirror were conducted by [3, 95]. A difference was the use of a piezo-electrical mounted mirror instead of an EA proof-mass. In [3], the Coriolis acceleration impact on the contrast was studied. In [95], the impact of both Centrifugal and Coriolis accelerations on the phase shift was demonstrated on a gradiometer.

Contrast

The contrast was studied as a function of the mirror angular velocity as can be seen in Figure 4.6b. For an angular velocity of $1\,\text{mrad}\,\text{s}^{-1}$, the contrast loss is measured at 75% for an interrogation time of 46 ms. This contrast loss can be fully explained by the impact of the Coriolis acceleration (term in $4\Omega_M^2\sigma_{v_y}^2$ in Equation 4.12).

$$\frac{\overline{C}_M}{C_0} = \exp\left(-\frac{k_{\text{eff}}^2T^4}{2}\left(4\Omega_M^4\sigma_x^2 + \dot{\Omega}_M^2\sigma_y^2 + 4(t_0+T)^2\Omega_M^4\sigma_{v_x}^2 + ((t_0+T)\dot{\Omega}_M + 2\Omega_M)^2\sigma_{v_y}^2\right)\right) \tag{4.12}$$

The contrast is not impacted by the Angular acceleration as the angular acceleration of the mirror is small. The mirror angular acceleration is 10 times smaller than the angular acceleration of the sensor as the mirror rotation is easier to control. The timing of the sinusoidal movement is better controlled leading to a very small angular acceleration. So the contrast loss is only due to Coriolis acceleration: it is not compensated by the Angular acceleration leading to a more important contrast loss than in the sensor case (Section 4.2.1). The theoretical model based on Equation 4.12 is in good agreement with the numerical model.

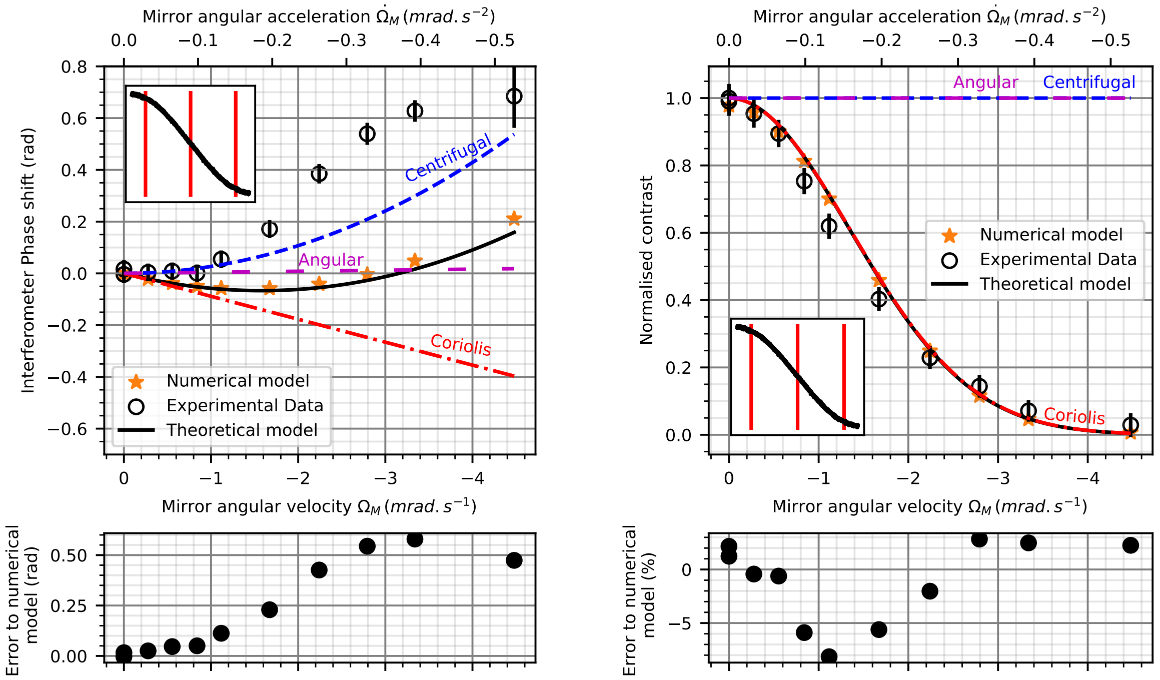

(a) Phase shift due to a sinusoidal angular movement around the axis $\overrightarrow{z_M}$.

(b) Contrast loss due to a sinusoidal angular movement around the axis $\overrightarrow{z_M}$.

Figure 4.6: Influence of the mirror angular velocity on the interferometer. The angular movement of the mirror is depicted in black in the insets. The three red lines represent the laser pulses of the interferometer. The contributions of the inertial accelerations are represented as follows: Coriolis acceleration in red, Centrifugal acceleration in blue and Angular acceleration in purple. The interrogation time of the interferometer is 46 ms.

Phase shift

The phase shift on Figure 4.6a is only affected by the Coriolis and Centrifugal accelerations and not by the Angular acceleration. This can be explained by the small angular acceleration of the mirror and by the shorter horizontal distance between the atomic cloud and the mirror centre of rotation: $y_{MA} = 1.09\,\text{mm}$ and $z_{MA} = 0.66\,\text{mm}$. These values were measured by rotating the mirror as presented in Chapter 3. However, the theoretical model (Equation 4.13) is not in agreement with the experimental data for angular velocity above 1 mrad s^{-1}.

$$\overline{\Delta\Phi}_M = k_{\text{eff}}T^2[-a_{x_L} - 2\Omega_M v_{y_0} - \dot{\Omega}_M((t_0+T)v_{y_0} + y_{MA}) + 2\Omega_M{}^2(a_{x_L}(\frac{t_0^2}{2} + t_0T + T^2) + (t_0+T)v_{x_0} + x_{MA})] \tag{4.13}$$

As the numerical model is close to the theoretical model, those discrepancies cannot be explained by imperfections in the mirror movement as they are taken into account by the numerical model. Such discrepancies were already observed in Section 4.1.1 and in Chapter 3. These unexpected phase shifts were investigated in Section 3.5.1.

4.2.3 Study of the rotation compensation method

A study of the rotation compensation method was implemented on the experimental setup. The sensor rotation was set to an angular velocity of $\Omega_S = 1.59\,\mathrm{mrad\,s^{-1}}$ and a sensor angular acceleration at $\dot{\Omega}_S = -3.5\,\mathrm{mrad\,s^{-2}}$. Then the mirror was rotated in the opposite way and the amplitude of the mirror rotation was scanned. According to Chapter 1, in this configuration, the Coriolis acceleration should be compensated for $\Omega_M = -\Omega_S$. The position of the sensor center of rotation moved slightly in comparison to Section 4.2.1 maybe due to variations of the center of mass position. In this paragraph, the horizontal distance is $y_{OA} = -5\,\mathrm{mm}$ and $z_{OA} = 12.4\,\mathrm{mm}$. Closely related experiments were implemented in [3, 91] to compensate the Earth rotation, in [96] to extend the increase the measurement range of a gyroscope and in [42] to operate an onboard accelerometer in dynamical environments.

Contrast

The contrast was studied as a function of the mirror angular velocity: the results are presented in Figure 4.6b. For angular velocities below Ω_S, the sensor rotation is under compensated and for angular velocities over Ω_S, the sensor rotation is over compensated. When $\Omega_M = -\Omega_S$, the angular velocity is compensated and the contrast should reach a maximum. The contrast recovery achieved during this experiment is up to 99%. This can be explained by the compensation of the Coriolis acceleration scaling as $2(\Omega_M + \Omega_S))^2\sigma_{v_y}^2$ in the contrast Equation 4.14.

$$\begin{aligned}\frac{\overline{C}_{M+S}}{C_0} = \exp\Bigg(&- \frac{k_{\mathrm{eff}}^2 T^4}{2} \big(\, (2\Omega_M^2 + \Omega_S^2 + 2\Omega_M\Omega_S)^2\sigma_x^2 + (\dot{\Omega}_S + \dot{\Omega}_M)^2\sigma_y^2 \\ &+ ((t_0 + T)(2\Omega_M^2 + \Omega_S^2 + 2\Omega_M\Omega_S))^2\sigma_{v_x}^2 + ((t_0 + T)(\dot{\Omega}_S + \dot{\Omega}_M) + 2(\Omega_M + \Omega_S))^2\sigma_{v_y}^2 \, \big) \Bigg)\end{aligned} \tag{4.14}$$

Nevertheless, the maximum of contrast is not achieved exactly for $\Omega_M = -\Omega_S$. The theoretical model is shifted from the contrast loss due to Coriolis acceleration in red: $\frac{\overline{C}}{C_0} = \exp\left(-\frac{k_{\mathrm{eff}}^2 T^4}{2} \left(\, 4(\Omega_M + \Omega_S)^2\sigma_{v_y}^2 \, \right)\right)$. This can be explained by a phenomenon similar to the one explained in 4.2.1. In this experiment, the sensor angular acceleration is not compensated: $\dot{\Omega}_S \neq -\dot{\Omega}_M \approx 0$. Thus, the sensor angular acceleration creates an Angular acceleration compensating the Coriolis acceleration in the following term $((t_0 + T)\dot{\Omega}_S + 2(\Omega_M + \Omega_S))^2\sigma_{v_y}^2$ leading to a shifted contrast recovery. In this experimental setup, the Centrifugal acceleration does not lead to a loss of contrast as its impact is too small.

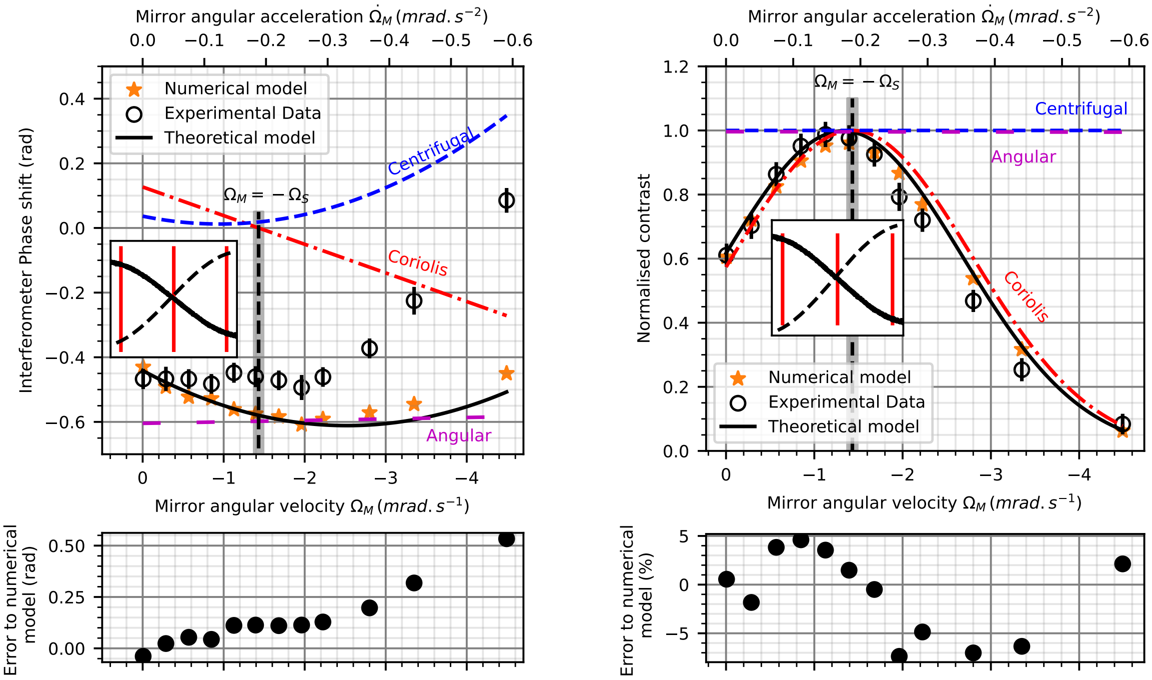

(a) Phase shift due to the compensation of a sinusoidal angular movement around the axis $\overrightarrow{z_S}$.

(b) Contrast due to the compensation of a sinusoidal angular movement around the axis $\overrightarrow{z_S}$.

Figure 4.7: Influence on the interferometer of the compensation of the sensor angular velocity ($\Omega_S = 1.6\,\mathrm{mrad\,s^{-1}}$ and $\dot{\Omega}_S = -3.5\,\mathrm{mrad\,s^{-2}}$). The angular movement of the sensor is depicted in dotted black in the insets and the movement of the mirror in continuous black. The three red lines represent the laser pulses of the interferometer. The contributions of the inertial accelerations are represented as follows: Coriolis acceleration in red, Centrifugal acceleration in blue and Angular acceleration in purple. The interrogation time of the interferometer is 46 ms. The grey area corresponds to the uncertainty on Ω_S.

Phase shift

The phase shift of the interferometer was also measured during this experiment. As shown in Figure 4.7a and as expected in Equation 4.15, the phase shift is never compensated.

$$\begin{aligned}\overline{\Delta\Phi}_{M+S} = {} & k_{\text{eff}}T^2[-a_{x_L} - 2(\Omega_M+\Omega_S)v_{y_0} - (\dot{\Omega}_S+\dot{\Omega}_M)((t_0+T)v_{y_0}+y_{OA}) - \dot{\Omega}_M y_{MO})] \\ & + (2\Omega_M^2+\Omega_S^2+2\Omega_M\Omega_S)(a_{x_L}(\frac{t_0^2}{2}+t_0T+T^2)+(t_0+T)v_{x_0}+x_{OA})+2\Omega_M^2 x_{MO}]\end{aligned} \tag{4.15}$$

If the Coriolis acceleration is perfectly compensated, the Centrifugal acceleration is only reduced when the angular velocity is compensated $\Omega_M = -\Omega_S$. Although, the principal contribution to the phase shift is due to the Angular acceleration induced by the sensor rotation. The phase shift created by the sensor angular acceleration is not compensated by the mirror angular acceleration as its is much smaller. The experimental data is not in agreement with the theoretical model and the numerical model with an error up to 0.4 rad. The cause of those discrepancies could be the same as the ones observed in 4.2.2.

This study of the compensation of the sensor angular velocity showed promising results on the contrast recovery. Nevertheless, due to experimental limitation, it was not possible to study the sole effect of the sensor angular velocity. To reach the limit of the compensation of the angular velocity, the sensor rotation should be better controlled to avoid any angular acceleration. Moreover, the unexpected phase shift which appears when the mirror rotates, should be further investigated.

4.2.4 First step toward an automatic rotation compensation scheme

In order to study a setup closer to a field-operated sensor, an automatic rotation method was implemented in which the mirror rotation is driven by the measurement of the sensor rotation. The action chain on the mirror angular position is depicted on Figure 4.8. The sensor rotation along the $\overrightarrow{z_S}$ axis is measured by the gyroscope, integrated with a passive low-pass filter to obtain a voltage proportional to the angular position of the sensor. The passive low-pass filter is made of a resistor of 1 MΩ and a capacitance of 1 µF so the filter cut-off frequency is $f_c = 150\,\mathrm{mHz}$. The voltage is then amplified by a first amplifier with a gain $G_0 = 200$ and by a second amplifier with a variable gain G_V between 0 and 8. Finally, the voltage is used as the mirror angular position setpoint for the angle Ψ of the EA proof-mass.

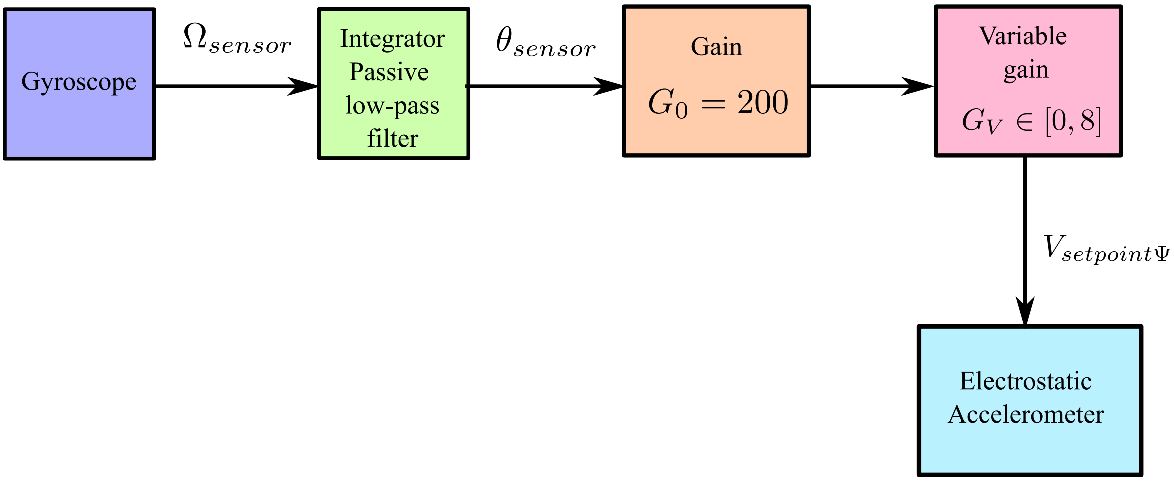

Figure 4.8: Automatic rotation compensation action chain. The gyroscope signal is integrated and amplified by a passive low-pass filter to obtain an angular setpoint for the electrostatic accelerometer.

The automatic setup was tested by applying a given rotation on the sensor and scanning the gain G_V of the action chain. This corresponds to a scan of the mirror rotation amplitude. The sensor angular velocity is set to $\Omega_S = 1.3\,\mathrm{mrad\,s^{-1}}$ and the angular acceleration to $\dot{\Omega}_S = 2.4\,\mathrm{mrad\,s^{-2}}$. The position of the sensor centre of rotation moved slightly during this experiment in comparison to Section 4.2.1 and 4.2.3 maybe due to variations in the sensor centre of mass position. In this paragraph, the horizontal distance between the cloud and the sensor centre of rotation is estimated to be equal to $y_{OA} = -5\,\mathrm{mm}$ and $z_{OA} = 2\,\mathrm{mm}$.

Contrast

The contrast recovery obtained with the automated setup is up to 90% as can be seen on Figure 4.9b and is impacted by both Coriolis and Angular accelerations. During this experiment, the mirror angular acceleration was quite important (up to $65\,\mathrm{mrad\,s^{-2}}$) which is one order of magnitude more important than the sensor angular acceleration. This can be explained by the delay in the mirror response due to the integration of the gyroscope signal. Thus, the angular movement of the mirror is not exactly opposite to the angular movement of the sensor and have an important angular acceleration. When $\Omega_M = -\Omega_S$, the Coriolis acceleration is compensated but the important Angular acceleration deteriorates the contrast recovery as $\dot{\Omega}_M \neq -\dot{\Omega}_S$. This phenomenon also explains why the theoretical model (Equation 4.14) does not reach a maximum for $\Omega_M = -\Omega_S$.

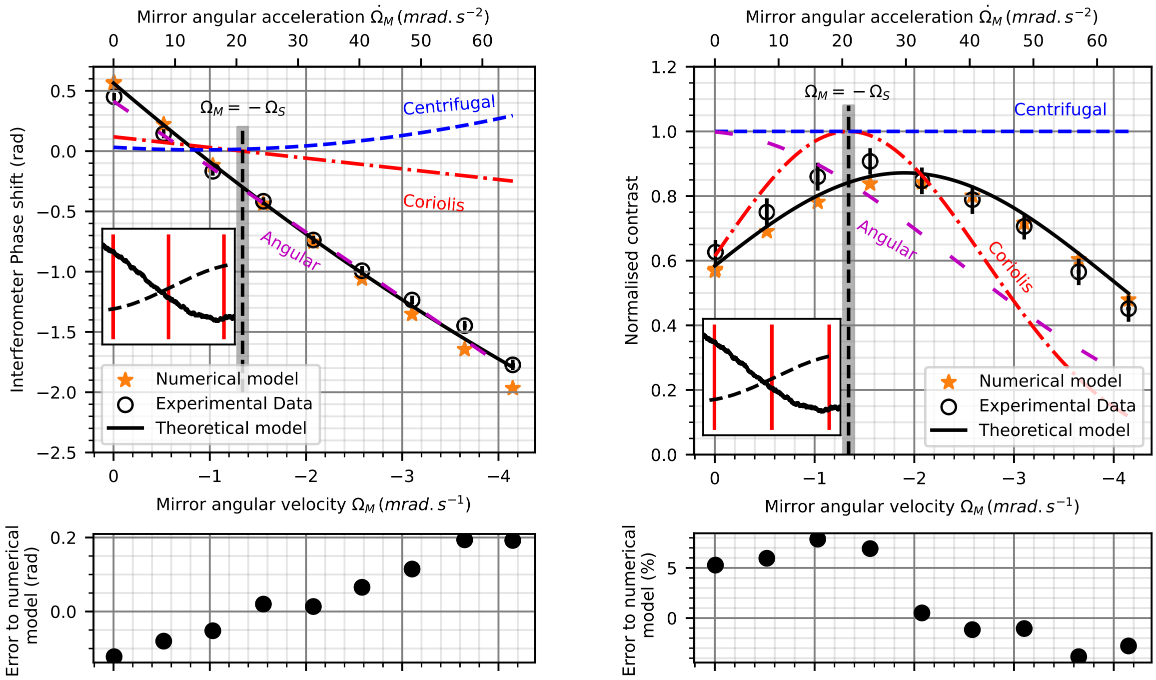

(a) Phase shift due to the automatic compensation of a sinusoidal angular movement around the axis $\overrightarrow{z_S}$.

(b) Contrast due to the automatic compensation of a sinusoidal angular movement around the axis $\overrightarrow{z_S}$.

Figure 4.9: Influence on the interferometer of the automatic compensation of the sensor angular velocity ($\Omega_S = 1.3\,\mathrm{mrad\,s^{-1}}$ and $\dot{\Omega}_S = 2.4\,\mathrm{mrad\,s^{-2}}$). The angular movement of the sensor is depicted in dotted black in the insets and the movement of the mirror in continuous black. The three red lines represent the laser pulses of the interferometer. The contributions of the inertial accelerations are represented as follows: Coriolis acceleration in red, Centrifugal acceleration in blue and Angular acceleration in purple. The interrogation time of the interferometer is 46 ms. The grey area corresponds to the uncertainty on Ω_S.

Phase shift

During this experiment, the phase shift is dominated by the Angular acceleration due to the sensor angular acceleration and the mirror angular acceleration (Figure 4.9a). If the Coriolis acceleration is compensated for $\Omega_M = -\Omega_S$, the Angular acceleration and the Centrifugal acceleration are not. The theoretical model on Figure 4.9a is based upon Equation 4.15.

The automatic compensation setup demonstrated an important contrast recovery but could be improved with a more rapid action chain. This would limit the delay in the retroaction on the mirror leading to a more important contrast recovery and a smaller residual phase shift. Moreover, in this study, the angular movement only had only one frequency. A more complete study could characterise the frequency response of the automatic compensation: the frequency response of the integrator and of the EA control of the proof-mass could be studied. Lastly, in this study, the gain of the action chain was scanned in order to find the maximum of contrast. In an operating sensor, the gain would have to be fixed and chosen beforehand.

4.3 Impact of angular acceleration

As demonstrated in the previous Section 4.2, an uncompensated angular acceleration can have a detrimental effect on the interferometer. In this section, the effect of a controlled angular acceleration is studied and an attempt to compensate it is made. The angular acceleration is maximised and the angular velocity minimised by implementing the interferometer during the top of the sinusoidal angular movement. In other terms, the sinusoidal angular movement phase is $\frac{\pi}{2}$ with respect to the second interferometric pulse. Due to experimental limitations, the angular velocity is non-zero and can still impact the interferometer.

4.3.1 Study of the sensor rotation

The whole sensor head was rotated in order to impose an angular acceleration up to $55\,\mathrm{mrad\,s^{-2}}$ during the atomic accelerometer. This distance in the horizontal plane between the sensor centre of rotation and the centre of the atomic cloud is a free parameter with a value of $y_{OA} = -5.1\,\mathrm{mm}$ and $z_{OA} = 12.4\,\mathrm{mm}$ to fit the phase shift experimental data.

Contrast

As shown by Figure 4.10b, the contrast loss is mainly induced by the Angular acceleration. For an angular acceleration of $\dot{\Omega}_S = 50\,\mathrm{mrad\,s^{-2}}$, the contrast is only 30% of the contrast in the absence of rotation. This preponderant term is the contribution of the Angular acceleration and scales as $((t_0+T)\dot{\Omega}_S)^2\sigma_{v_y}^2 + \dot{\Omega}_S^2\sigma_y^2$ in Equation 4.10: the temperature and the size of the cloud both play a role in the contrast loss. The Coriolis and Centrifugal accelerations do not contribute significantly to the contrast loss in this case. If the theoretical and numerical models agree, they do not perfectly explain the experimental data and an error of roughly 10% remains between the experimental data and the numerical model. This difference could be explained by a variation of the cloud temperature or a variation of the cloud size. A velocity dispersion of $\sigma_{v_y} = 14\,\mathrm{mm\,s^{-1}}$ instead of $\sigma_{v_y} = 11\,\mathrm{mm\,s^{-1}}$ would explain the experimental data. A position dispersion of $\sigma_y = 680\,\mathrm{\mu m}$ instead of $\sigma_y = 400\,\mathrm{\mu m}$ would also explain the contrast loss.

Phase shift

The phase shift is also mainly impacted by the Angular acceleration in this configuration as can be seen on Figure 4.10a. The phase shift generated by the rotation is up to 11 rad and is reproduced by the numerical and theoretical models. This phase shift scales as $-\dot{\Omega}_S(v_{y_0}(t_0+T)+y_{OA})$ and depends from the initial cloud velocity but also from the transverse misalignment between the cloud and the sensor centre of rotation y_{OA}. The theoretical model is based upon Equation 4.11.

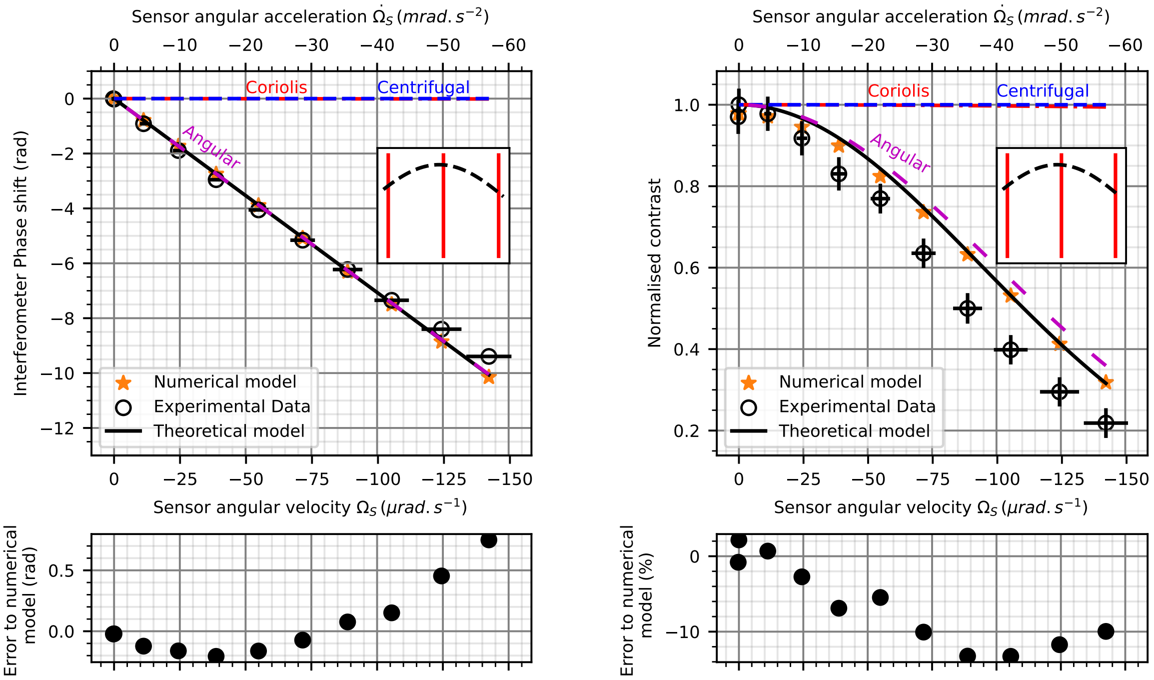

(a) Phase shift due to a sinusoidal angular movement around the axis $\overrightarrow{z_S}$.

(b) Contrast due to a sinusoidal angular movement around the axis $\overrightarrow{z_S}$.

Figure 4.10: Influence of the sensor angular acceleration on the interferometer. The angular movement of the sensor is depicted in dotted black in the insets. The three red lines represent the laser pulses of the interferometer. The contributions of the inertial accelerations are represented as follows: Coriolis acceleration in red, Centrifugal acceleration in blue and Angular acceleration in purple. The interrogation time of the interferometer is 46 ms.

4.3.2 Study of the mirror rotation

The impact of the mirror angular acceleration was also studied in a configuration maximising its impact. The angular movement of the mirror was chosen to anticipate the compensation of the sensor rotation. As the mirror rotation is better controlled than the sensor rotation, the residual angular velocity is reduced to a few mrad s^{-1} and the angular acceleration applied is up to 125 mrad s^{-2}.

Contrast

The loss of contrast on Figure 4.11b is mainly due to the Angular acceleration linked to the velocity and position distribution of the cloud. The Angular acceleration contribution in Equation 4.12 scales also as $((t_0+T)\dot{\Omega}_M)^2\sigma_{v_y}^2+\dot{\Omega}_M^2\sigma_y^2$. For an angular acceleration of $\dot{\Omega}_M = 50\,\mathrm{mrad\,s^{-2}}$, the normalised contrast has a value of 45% which is less than the measured value in the sensor case.

Phase shift

The phase shift is also affected by the Angular acceleration which scales as $-\dot{\Omega}_M((t_0+T)v_{y_0}+y_{MA})$ in Equation 4.13. This Angular acceleration induced phase shift depends on the initial velocity of the cloud which is similar to the sensor rotation case. However, this phase shift depends on the transverse distance between the atomic cloud and the mirror centre of rotation y_{MA} and not of the transverse distance between the atomic cloud and the sensor centre

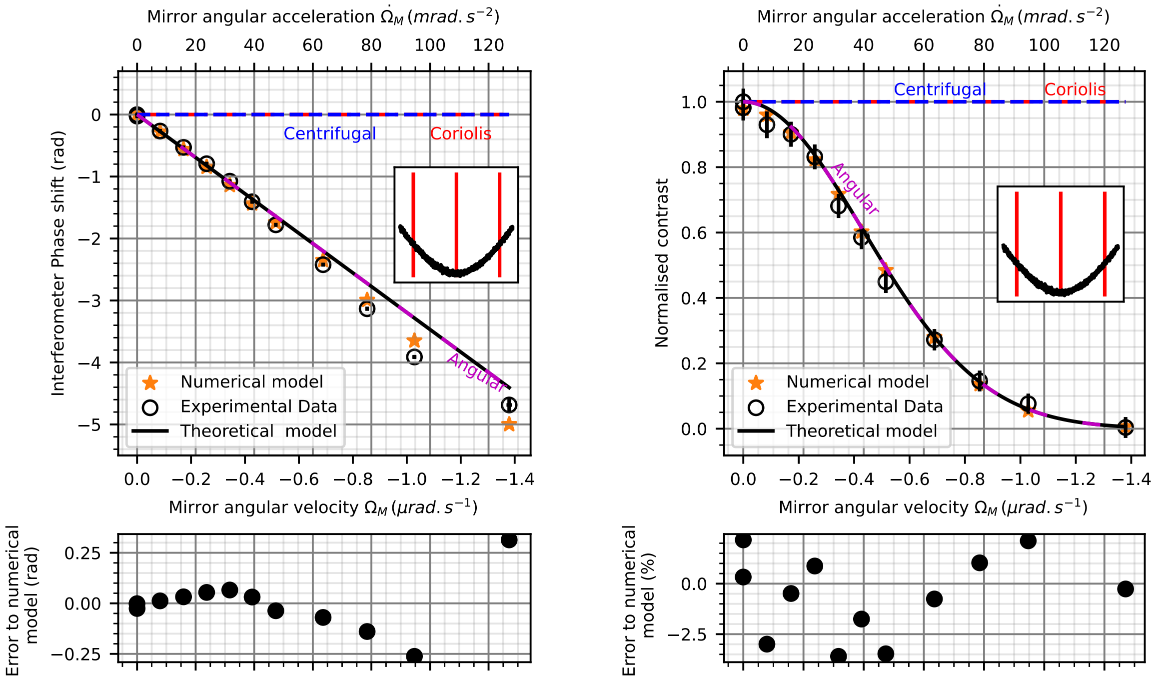

(a) Phase shift due to a sinusoidal angular movement around the axis $\overrightarrow{z_M}$.

(b) Contrast due to a sinusoidal angular movement around the axis $\overrightarrow{z_M}$.

Figure 4.11: Influence of the mirror angular acceleration on the interferometer. The angular movement of the sensor is depicted in black in the insets. The three red lines represent the laser pulses of the interferometer. The contributions of the inertial accelerations are represented as follows: Coriolis acceleration in red, Centrifugal acceleration in blue and Angular acceleration in purple. The interrogation time of the interferometer is 46 ms.

of rotation y_{OA}. In the case of the mirror, the phase shift is up to −4.7 rad which is smaller than the phase shift in the sensor case. This can be explained by the smaller distance in the mirror case ($y_{MA} = 1.09$ mm) than in the sensor case ($y_{OA} = -5.1$ mm). The theoretical model is based upon Equation 4.13 and gives different results compared to the numerical model. This could be explained by the higher order terms not taken into account in the theoretical model such as $k_{\text{eff}} T^2 [\frac{\dot{\Omega}_M^2}{2}(a_{x_L} \frac{t_0^2}{2} T^2 + t_0 T v_{x_0} + T^2 x_{MA})]$ due to the important magnitude of $\dot{\Omega}_M$.

4.3.3 Study of the rotation compensation method

A study of the rotation compensation method was implemented on the experimental setup in an attempt to compensate the angular acceleration of the sensor. The sensor rotation was set at a sensor angular acceleration of $\dot{\Omega}_S = -43\,\text{mrad}\,\text{s}^{-2}$ and an angular velocity of $\Omega_S = -204\,\mu\text{rad}\,\text{s}^{-1}$. Then the mirror was rotated in the opposite way and the amplitude of the mirror rotation was scanned. According to Chapter 1, in this configuration, the Angular acceleration should be partly compensated when $\dot{\Omega}_M = -\dot{\Omega}_S$. The position of the sensor centre of rotation moved slightly in comparison to Section 4.2 maybe due to variations in the centre of mass position. In this paragraph, the transverse distance between the sensor centre of rotation and the cloud is $y_{OA} = -5$ mm and $z_{OA} = 12.4$ mm.

Contrast

The contrast was recovered up to 92% (Figure 4.12b) as the term $(\dot{\Omega}_S + \dot{\Omega}_M)^2 \sigma_y^2 + ((t_0 +$

$T)(\dot{\Omega}_S+\dot{\Omega})^2\sigma_{v_y}^2$ is cancelled. Nevertheless, the contrast recovery is not perfect and the theoretical and numerical model do not explain this imperfect contrast recovery. Moreover, the maximum of contrast is not achieved for $\dot{\Omega}_M = -\dot{\Omega}_S$. The theoretical model optimal contrast is shifted from the point $\dot{\Omega}_M = -\dot{\Omega}_S$ due to Coriolis acceleration. This can be explained by a phenomenon similar to the one explained in 4.2.1: the sensor angular velocity creates a Coriolis acceleration compensating the Angular acceleration as $((t_0+T)(\dot{\Omega}_S+\dot{\Omega}_M)+2\Omega_S)^2\sigma_{v_y}^2$. The mirror angular velocity is very small and can be neglected $\Omega_M \approx 0$.

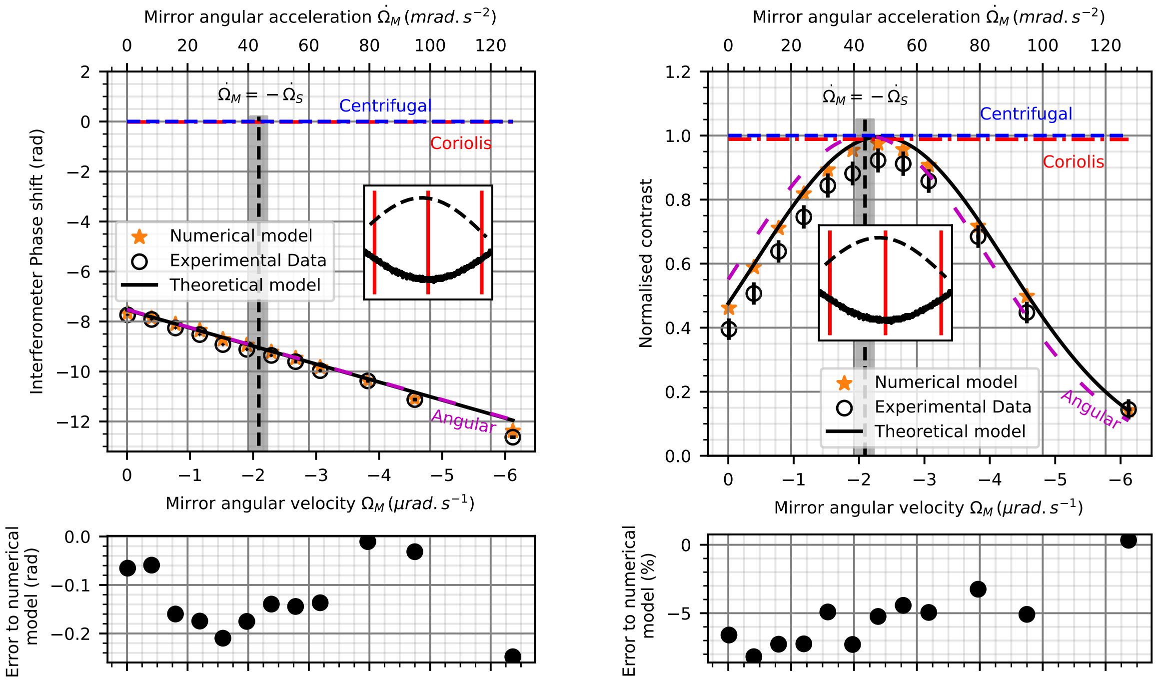

(a) Phase shift due to the compensation of a sinusoidal angular movement around the axis $\overrightarrow{z_S}$.

(b) Contrast due to the compensation of a sinusoidal angular movement around the axis $\overrightarrow{z_S}$.

Figure 4.12: Influence on the interferometer of the compensation of the sensor angular acceleration ($\Omega_S = -204\,\mu\text{rad}\,\text{s}^{-1}$ and $\dot{\Omega}_S = -43\,\text{mrad}\,\text{s}^{-2}$) The angular movement of the sensor is depicted in dotted black in the insets and the movement of the mirror in continuous black. The three red lines represent the laser pulses of the interferometer. The contributions of the inertial accelerations are represented as follows: Coriolis acceleration in red, Centrifugal acceleration in blue and Angular acceleration in purple. The interrogation time of the interferometer is 46 ms. The grey area corresponds to the uncertainty on $\dot{\Omega}_S$.

Phase shift

The phase shift due to the Angular acceleration is not compensated by the mirror rotation but is increased as can be seen on Figure 4.12a. This can be explained by the term $-(\dot{\Omega}_S+\dot{\Omega}_M)((t_0+T)v_{y_0}+y_{OA})-\dot{\Omega}_M y_{MO})$ in Equation 4.15. If the term in v_{y_0} cancels when $\dot{\Omega}_M = -\dot{\Omega}_S$, the term depending of the distance between the sensor centre of rotation and the mirror centre of rotation does not: the centres of rotation of the mirror and the sensor do not coincide.

This study demonstrated that the compensation of the Angular acceleration allows to recover the contrast of the interferometer. However, the compensation cannot cancel the Angular acceleration contribution to the phase shift if centres of rotation of the sensor and mirror do not coincide. If the centres coincide $O \equiv M$, then the Angular induced phase shift becomes

$-(\dot{\Omega}_S + \dot{\Omega}_M)((t_0 + T)v_{y_0} + y_{OA}) - \dot{\Omega}_M y_{MO}) = -(\dot{\Omega}_S + \dot{\Omega}_M)((t_0 + T)v_{y_0} + y_{OA})$. This term can be cancelled if $\dot{\Omega}_M = -\dot{\Omega}_S$.

4.3.4 First step toward an automatic rotation compensation scheme

The automated setup was also used to compensate the angular acceleration of the sensor. The action chain is the same as the one described in Section 4.2.4. The sensor angular acceleration was set to $\dot{\Omega}_S = -43\,\mathrm{mrad\,s^{-2}}$ and the angular velocity to $\Omega_S = -247\,\mathrm{\mu rad\,s^{-1}}$. The gain G_V was scanned to vary the mirror rotation amplitude. In this paragraph, the horizontal distance between the sensor centre of rotation and the cloud is $y_{OA} = -5\,\mathrm{mm}$ and $z_{OA} = 15\,\mathrm{mm}$.

Contrast

The contrast recovery was up to 94% as can be seen on Figure 4.13b. If the Angular acceleration is compensated for $\dot{\Omega}_M = -\dot{\Omega}_S$, a Coriolis acceleration appears with the mirror compensation leading to a position shift of the optimal contrast recovery: the maximum of contrast is not for $\dot{\Omega}_M = -\dot{\Omega}_S$. This effect is due to the delay in the mirror rotation with respect to the sensor rotation. The mirror rotation induces an angular velocity in addition the expected angular acceleration. This phenomenon could be reduced with a more rapid integration of the gyroscope signal.

Phase shift

The automatic compensation generates an increased phase shift as can be seen on Figure 4.13a: the mirror rotation does not cancel the phase shift. The main contribution to the phase shift is the Angular acceleration. The phase shift visible on Figure 4.13a can mainly be explained by the term $-(\dot{\Omega}_S + \dot{\Omega}_M)((t_0 + T)v_{y_0} + y_{OA}) - \dot{\Omega}_M y_{MO})$ in Equation 4.15.

The automatic compensation of the sensor angular acceleration enabled an important contrast recovery but failed to cancel the Angular acceleration contribution to the phase shift. The phase shift cannot be compensated for the same reasons as in Section 4.3.3: the centres of rotation of the sensor and mirror have to coincide for the phase shift to be compensated.

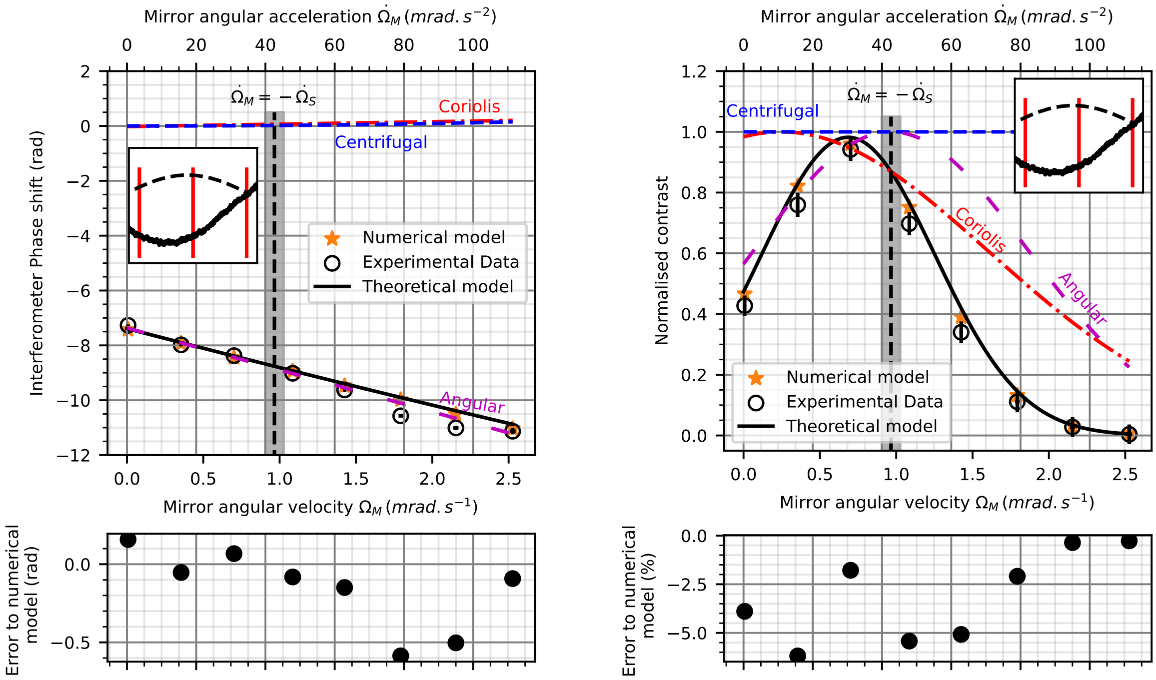

(a) Phase shift due to the automatic compensation of a sinusoidal angular movement around the axis $\overrightarrow{z_S}$.

(b) Contrast due to the automatic compensation of a sinusoidal angular movement around the axis $\overrightarrow{z_S}$.

Figure 4.13: Influence on the interferometer of the automatic compensation of the sensor angular acceleration ($\Omega_S = -247\,\mu\text{rad}\,\text{s}^{-1}$ and $\dot{\Omega}_S = -43\,\text{mrad}\,\text{s}^{-2}$). The angular movement of the sensor is depicted in dotted black in the insets and the movement of the mirror in continuous black. The three red lines represent the laser pulses of the interferometer. The contributions of the inertial accelerations are represented as follows: Coriolis acceleration in red, Centrifugal acceleration in blue and Angular acceleration in purple. The interrogation time of the interferometer is 46 ms. The grey area corresponds to the uncertainty on $\dot{\Omega}_S$.

4.4 Advantages and limitations of the rotation compensation method

During this work, a rotation compensation method using the proof-mass of an EA as an actuated mirror was tested experimentally. The experimental results collected were presented in the previous Sections.

Contrast

Some promising results were obtained concerning the contrast recovery with the rotation compensation. Experimentally, the compensation of the Coriolis acceleration led to a contrast recovery up to 99%. The compensation of the Angular acceleration was also demonstrated with a contrast recovery up to 92%. An automated compensation demonstrated a contrast recovery of more than 90%, enough to perform measurements in dynamical environments. The theoretical model and numerical model allow to explain the experimental results with an error below 10% for the numerical model. With the exception of Section 4.3.1 in which the models are further from the experimental data with an error up to 14%. If the contrast loss due to the Angular and Coriolis accelerations can be suppressed, the contrast loss due to the Centrifugal acceleration cannot be compensated. Nevertheless, the Centrifugal acceleration is not a source of contrast loss in this experiment. The compensation is easier for the contrast as the recovery does not have to be perfect to perform a measurement and the position of the centres of rotation is not relevant.

Phase shift

If the results concerning the contrast are interesting and well explained, the phase shift results are less satisfactory. As expected, the phase shift cannot be compensated as well as the contrast: only the Coriolis induced phase shift can be suppressed. Moreover, very important phase shifts up to 10 rad were observed for a compensated rotation in Section 4.3.3. The important residual phase shift is mainly due to the Angular acceleration and can be explained by the positions of the rotation centres of the sensor and the mirror. If the rotation centres coincided, this phase shift could be suppressed. Nevertheless, the Centrifugal induced phase shift would never be suppressed. The phase shift is also more difficult to explain as it is very sensitive and affected by several effects. Still, the developed theoretical and numerical models fail to explain the experimental phase shift. The numerical model taking into account side effects still displays discrepancy from -0.8 rad to 0.9 rad to the experimental data. To be able to correct the rotation induced phase shift, this discrepancy has to be explained and reduced as it would limit the performances of the sensor. This discrepancy could be partially explained by defects in the EA cage such as wave front distortion. Thus, an improved design could help reduce this discrepancy.

Conclusion

In this Chapter, the experimental results of the rotation compensation method were presented. Firstly, the impact of the sensor rotation was measured. Secondly, the impact of the mirror rotation was studied. Thirdly, the rotation compensation method was tested by rotating the mirror and the sensor. Lastly, an automated rotation compensation action chain was implemented. All the experiments were conducted in two cases: one maximising the angular velocity and the other maximising the angular acceleration.

To explain the experimental data collected, two models were employed: the theoretical model based on the calculations of Chapter 1 and the numerical model considering a more realistic movement of the sensor and mirror. If the contrast is in good agreement with the models, the phase shift is more difficult to explain.

The rotation compensation method displays a contrast recovery exceeding 90% but fails to cancel the rotation induced phase shift. If the Coriolis induced phase shift is easily compensated, the Angular induced phase shift is only cancelled if the mirror and sensor centres of rotation coincide while the Centrifugal induced phase can never be cancelled.

An automatic rotation compensation setup was implemented: the rotation rate is measured with a gyroscope integrated and amplified to provide an angular setpoint to the mirror. The results of this automatic compensation enlighten the importance of the frequency response of the action chain of the mirror. The bandwidth of the system acting on the mirror (integration, amplification and actuation) should be consider and would strongly depend on the interferometer interrogation time.

CHAPTER 5

Atomic accelerometer in a spatial environment

Outline of the current chapter

Introduction

The rotation compensation method was implemented experimentally on a lab prototype as described in the previous chapters but one could wonder what performances this instrument would have in space. In this Chapter, a literal model of a space atomic accelerometer is used to compute the impact of the rotation on the accelerometer uncertainty. The calculation presented in this Chapter is restricted to the effect of the satellite rotation and the rotation compensation method: no other effects are taken into account.

This study takes place in the context of gravimetry missions such as GRACE, GRACE-FO and the future missions GRACE-C and NGGM which use the knowledge of the distance between two satellites in orbit to measure the Earth gravity field. For that reason, the satellite considered is based upon the requirements for one of the two satellites of the NGGM mission. The boarded accelerometer retrieves the non-gravitational forces undergone by the satellite such as the drag due to residual atmosphere or the radiative pressure. The considered atomic instrument presents some similarities with the lab prototype presented in the previous chapters: a 87 Rubidium Mach-Zehnder interferometer. However, as this interferometer operates in a micro-gravity environment, several atomic transitions are allowed and the double diffraction phenomenon has to be dealt with. Lastly, different potential atomic sources with different temperature will be examined.

5.1 Description of the hybrid instrument

Here is a description of the considered atomic/electrostatic accelerometer boarded on a satellite. This potential instrument is close to the one described in [30] and to the lab prototype presented in the previous Chapters. The peculiarity of this design is the reflection of the interferometer laser on the EA proof-mass. This configuration allows in principle the compensation of the satellite rotation with the EA proof-mass. EA are already boarded on gravimetry satellites and offer a real-time control and measurement of the EA proof-mass position.

5.1.1 The atomic accelerometer

Let's consider a Mach-Zehnder atomic interferometer close to the one described in Chapters 1 and 2. This interferometer uses two-photons Raman transitions to put a 87 Rubidium atom in a superposition of state between its two arms. The Raman laser is once again reflected on the EA proof-mass acting as an actuated mirror. The distance between the mirror and the atomic cloud is smaller for this space instrument ($\approx 10\,\mathrm{cm}$) as the satellite is a micro-gravity environment. Another remarkable difference between the lab prototype described previously and the potential space interferometer is the double diffraction scheme implemented on the space interferometer [132–134]. An orbiting satellite is a micro-gravity environment: the atom acceleration relative to the satellite is close to zero. This impacts the interferometer as the important acceleration of the atoms falling in the Earth gravity field allows to select one of the possible Raman transitions. In the lab, the effective wave vector $\overrightarrow{k_{\mathrm{eff}}}$ can be chosen upward or downward by tuning the laser frequency. This choice is not possible in micro-gravity: the two transitions are allowed for the same laser frequency (Figure 5.1): the atom momentum can gain a momentum $+\hbar\overrightarrow{k_{\mathrm{eff}}}$ or loses $-\hbar\overrightarrow{k_{\mathrm{eff}}}$.

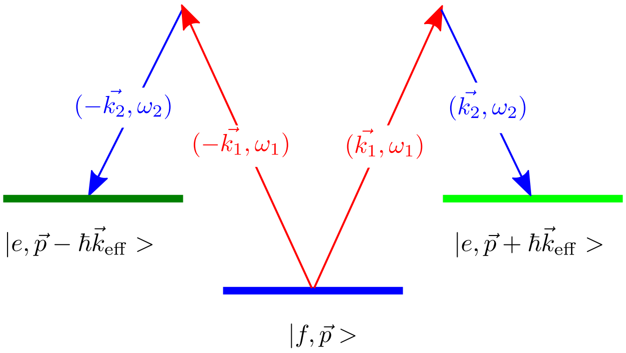

Figure 5.1: Double diffraction transitions and involved atomic levels. $\left|f, \overrightarrow{p}\right\rangle$ is the input state of the interferometer and $\left|e, \overrightarrow{p} + \hbar\overrightarrow{k_{\text{eff}}}\right\rangle$ and $\left|e, \overrightarrow{p} - \hbar\overrightarrow{k_{\text{eff}}}\right\rangle$ the diffracted states during the interferometer. In micro-gravity, both transitions are possible for the same laser frequency.

In a double diffraction interferometer, the two possible Raman transitions happen at each laser pulse. Hence, in the interferometer, the atom is in a state superposition between $\left|e, \overrightarrow{p} + \hbar\overrightarrow{k_{\text{eff}}}\right\rangle$ and $\left|e, \overrightarrow{p} - \hbar\overrightarrow{k_{\text{eff}}}\right\rangle$ (Figure 5.2). In a simple diffraction interferometer, the atom is in the states $\left|f, \overrightarrow{p}\right\rangle$ and $\left|e, \overrightarrow{p} + \hbar\overrightarrow{k_{\text{eff}}}\right\rangle$. The space time area of the double diffraction interferometer is multiplied by two in comparison to the simple diffraction interferometer. Thus, the phase shift of the double diffraction interferometer is also multiplied by two, increasing the sensitivity.

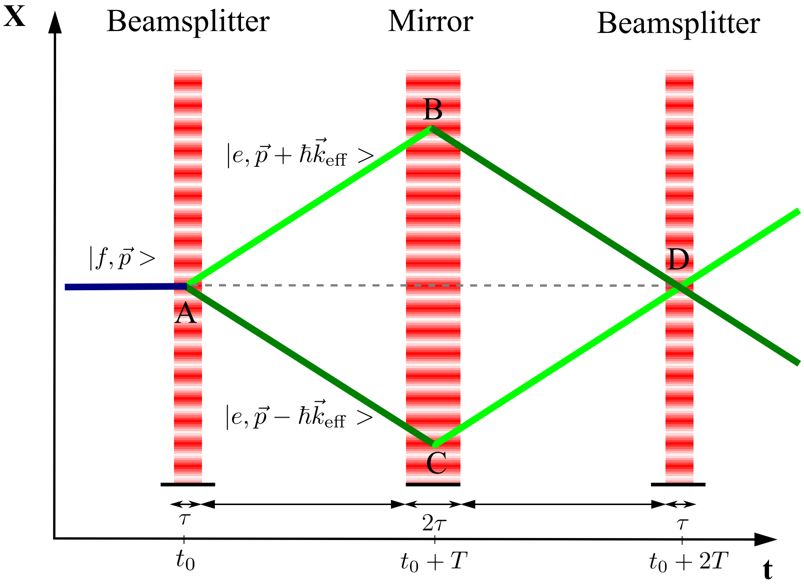

Figure 5.2: Space-time diagram of a double diffraction Mach-Zehnder interferometer with a direction of measurement along the X axis. The three long red rectangles represent the laser pulses $\frac{\pi}{2} - \pi - \frac{\pi}{2}$ driving the atomic transitions between the ground state $\left|f, \overrightarrow{p}\right\rangle$, the excited states $\left|e, \overrightarrow{p} + \hbar\overrightarrow{k_{\text{eff}}}\right\rangle$ and $\left|e, \overrightarrow{p} - \hbar\overrightarrow{k_{\text{eff}}}\right\rangle$. The atoms free fall for a time t_0 before the beginning of the interferometer. The first and third laser pulses put the atoms in a superposition of states while the second pulse redirects the atomic cloud.

In this Chapter, the performances of the interferometer will be explored for three different atomic sources. Each source has different velocity and position characteristics which impact the contrast and phase shift of the rotating interferometer. The easiest source to build is a molasses source obtained from a typical MOT-based experimental setup. With a more complex instrument allowing an evaporative cooling step, a Bose-Einstein Condensate (BEC) can be obtained: the velocity and position distributions are narrowed. The stability of the initial velocity and position of the source is also improved. An even colder source can be achieved by adding a Delta-Kick Cooling (DKC) step: the velocity distribution gets narrower but the position distribution broadens. The velocity and position stabilities are unchanged by the DKC step.

Molasses atomic source

The first atomic source considered is a molasses source close to the one of the lab prototype. This source supplies an important number of atoms in a short time and is the less demanding in time and electrical power. However, molasses have a relatively broad velocity and position distributions and poor velocity and position stabilities. The velocity (respectively position) stability is the variation of the initial velocity (resp. position) of the atomic cloud shot-to-shot. The typical kinetic parameters of the molasses source are summed up in Table 5.1.

Velocity stability	δv	$2\,\mathrm{mm\,s^{-1}}$
Position stability	δr	$200\,\mathrm{\mu m}$
Velocity dispersion	σ_v	$10\,\mathrm{mm\,s^{-1}}$ ($1\,\mathrm{\mu K}$)
Position dispersion	σ_r	$500\,\mathrm{\mu m}$
Number of atoms	N_{tot}	10^6

Table 5.1: Atomic cloud parameters for a molasses source [2, 98, 135].

BEC-like source

The second source is a BEC-like source which comprises less atoms than the molasses source. If the addition of an evaporative cooling step requires more time and power, the BEC-like source is smaller and have a narrower velocity distribution. Its initial velocity and position are also more stable. The typical kinetic parameters of the BEC-like source considered are summed up in Table 5.2.

Velocity stability	δv	$100\,\mathrm{\mu m\,s^{-1}}$
Position stability	δr	$10\,\mathrm{\mu m}$
Velocity dispersion	σ_v	$2\,\mathrm{mm\,s^{-1}}$ ($40\,\mathrm{nK}$)
Position dispersion	σ_r	$5\,\mathrm{\mu m}$
Number of atoms	N_{tot}	10^5

Table 5.2: Atomic cloud parameters for a BEC-like source [76, 136, 137].

Delta-Kick Cooled (DKC) source

A last source is an even colder one: a BEC-like source is cooled after its preparation with a Delta-Kick Cooling method. This source has very narrow velocity distribution but its position distribution is enlarged. The DKC source velocity and position stabilities are similar to the BEC-like source.

Velocity stability	δv	$100\,\mu\mathrm{m\,s^{-1}}$
Position stability	δr	$10\,\mu\mathrm{m}$
Velocity dispersion	σ_v	$100\,\mu\mathrm{m\,s^{-1}}$ (100 pK)
Position dispersion	σ_r	$50\,\mu\mathrm{m}$
Number of atoms	N_{tot}	10^5

Table 5.3: Atomic cloud parameters for a Delta-Kick Cooled source [76,136–138].

5.1.2 The electrostatic accelerometer

The atomic interferometer is hybridised with an electrostatic accelerometer to keep the advantages of both instruments [30]. In this work, the EA operates as an actuated mirror. Let's consider an EA with a cubic proof mass similar to the MicroStar accelerometer described in [113]. This design of EA is considered for future gravimetry missions such as NGGM and for the design of a hybrid instrument.

Let's assume that the EA was designed with an adequate angular freedom and the appropriate control law to compensate the satellite rotation: $\theta_{EA}^{max} \geq 2T\Omega_{max}$ with θ_{EA}^{max} the total angular range accessible to the EA proof-mass, Ω_{max} the maximal angular velocity of the satellite and T the interrogation time of the interferometer. When implementing the rotation compensation method, the EA capacitive detection will be important to measure the angular velocity and angular acceleration of the mirror. These values can be used to correct the interferometer measurement from the rotation induced bias. In terms of uncertainty, the uncertainty of the mirror angular velocity and acceleration will impact the uncertainty of the acceleration measured by the interferometer.

The EA capacitive detection noise limits the angular position detection of the proof-mass. This noise will be assumed to be a white noise of standard deviation $10\,\mathrm{nradHz^{-1/2}}$ [139]. Thus the uncertainty at 1σ of the angular capacitive detection will be considered as $\delta\theta \approx 10\,\mathrm{nrad}$ for an integration of the EA signal of the order of the second. Nevertheless, this value of the uncertainty of the EA angular position is a first approximation and has to be confirmed. The angular position of the mirror only impacts the interferometer during the three laser pulses: $\theta_M(t_0)$, $\theta_M(t_0+T)$ and $\theta_M(t_0+2T)$. The mean angular velocity Ω_M^i and the mean angular acceleration $\dot{\Omega}_M^i$ seen by the interferometer along each axis $i = x, y, z$, can be deduced from these angular positions and the associated uncertainty is the following:

$$\Omega_M^i = \frac{\theta_M(t_0+2T) - \theta_M(t_0)}{2T} \quad \Rightarrow \quad \delta\Omega_M^i = \frac{\delta\theta}{T} \tag{5.1}$$

$$\dot{\Omega}_M^i = \frac{\theta_M(t_0+2T) - 2\theta_M(t_0+T) - \theta_M(t_0)}{2T^2} \quad \Rightarrow \quad \delta\dot{\Omega}_M^i = \frac{2\delta\theta}{T^2} \tag{5.2}$$

Let's consider that the control law of the EA is limited by the capacitive detection. Thus, the only uncertainty is due to the capacitive detection and the mean angular velocities and accelerations are equal to the set point given to the control law. The rotation of the satellite is expected to be mainly around the Z axis due to the satellite rotation around the Earth (see Figure 5.3). That is why, the angular velocity and acceleration of the mirror with respect to the satellite around the axis Z (Ω_z^M and $\dot{\Omega}_z^M$) are null in the absence of rotation compensation and opposite to the satellite angular velocity and acceleration ($-\Omega_S^z$ and $-\dot{\Omega}_S^z$) when the rotation compensation is implemented. As shown in Table 5.4, the mean value of the angular velocities and accelerations around the axis X and Y (Ω_M^x,Ω_M^y,$\dot{\Omega}_M^x$ and $\dot{\Omega}_M^y$) are expected to be null. The rotation is not compensated for these axes in the case considered here.

Measurement	Mean value	Uncertainty
Ω_M^x	0	$\frac{\delta\theta}{T}$ (1σ)
Ω_M^y	0	$\frac{\delta\theta}{T}$ (1σ)
Ω_M^z	0 or $-\Omega_S^z$	$\frac{\delta\theta}{T}$ (1σ)
$\dot{\Omega}_M^x$	0	$\frac{2\delta\theta}{T^2}$ (1σ)
$\dot{\Omega}_M^y$	0	$\frac{2\delta\theta}{T^2}$ (1σ)
$\dot{\Omega}_M^z$	0 or $-\dot{\Omega}_S^z$	$\frac{2\delta\theta}{T^2}$ (1σ)

Table 5.4: EA capacitive detection measurements and the associated uncertainties.

5.2 Satellite environment

The satellite environment has an important impact on the accelerometer performances either in terms of accelerations, rotations or satellite design (positions of the different elements). Let's study the case of a Nadir pointing satellite similar to one of the satellites of the NGGM mission. As shown by Figure 5.3, the potential atomic accelerometer would measure along the X axis which is tangential to the orbit of the satellite.

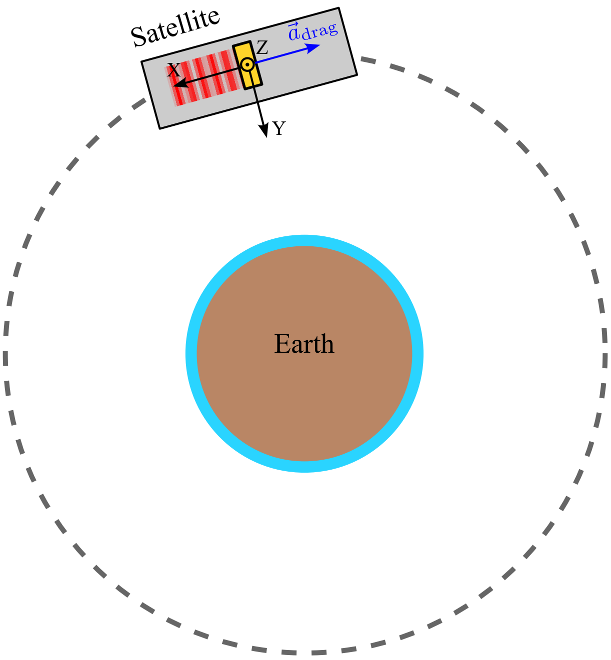

Figure 5.3: Diagram of a Nadir pointing satellite orbiting around the Earth. The EA proof-mass is at the centre of mass of the satellite. $\{X, Y, Z\}$ is the satellite frame.

The acceleration measured by the accelerometer is mostly a drag acceleration due to the residual atmosphere: $a_S^x \vec{u_x} = \vec{a}_{drag}$. No uncertainty associated to this acceleration is considered. The accelerations along Y and Z are not considered in this work. The Earth gravity gradient is also neglected as it would lead to an acceleration of $\approx 3 \times 10^{-8}\,\mathrm{m\,s^{-2}}$ [139] during the interferometer which is much smaller than the drag acceleration $\approx 1 \times 10^{-6}\,\mathrm{m\,s^{-2}}$ [18]. The EA proof-mass M is at the centre of mass O of the satellite with an uncertainty on the position of 200 µm (3σ). The distance between the proof-mass M and the atomic cloud A along the X axis is 10 cm with an uncertainty of 200 µm (3σ). The uncertainty on distances between elements has a value of 200 µm (3σ) which corresponds to a position uncertainty of 100 µm (3σ) on each elements.

The gyroscope of the potential satellite is an ASTRIX200 gyroscope (Airbus) [140] already boarded on several space missions. This gyroscope presents a white noise with a standard deviation lower than $\sigma_{gyro} = 3 \times 10^{-8}\,\text{rad/sHz}^{-1/2}$ (1σ). This white noise will be considered the limiting factor on the gyroscope measurement. The atomic interferometer is sensitive to rotation with a frequency up to $\frac{1}{T}$. Thus, the gyroscope noise will be integrated in the interferometer bandwidth to obtain the uncertainty on the gyroscope measurement.

$$\delta\Omega^2 = \int_0^{1/T} \sigma_{gyro}^2 d\nu = \frac{\sigma_{gyro}^2}{T} \tag{5.3}$$

The error on the angular velocity around each axis (i=x,y or z) integrated during the interferometer is then:

$$\delta\Omega_S^i = \frac{\sigma_{gyro}}{\sqrt{T}} \tag{5.4}$$

The angular acceleration is also measured by the ASTRIX200 gyroscope and the associated uncertainty is:

$$\delta\dot{\Omega}_S^i = \frac{\Omega_S^{i(2)} - \Omega_S^{i(1)}}{T} = \frac{2\sigma_{gyro}}{T\sqrt{T}} \tag{5.5}$$

with $\Omega_S^{i(1)}$ the mean angular velocity between the first and second pulse and $\Omega_S^{i(2)}$ the mean angular velocity between the second and third pulse.

The architecture of the considered mission places the interferometer mirror at the centre of mass of the satellite $O \equiv M$. This architecture is close to current gravimetry mission architecture. The EA (acting as a mirror) is at the CoM to provide an accurate measurement of the non-gravitational forces applied on the satellite. The atomic instrument considered here is only used to correct the EA drift: its measurement is less crucial to the mission. Table 5.5 is a summary of the satellite environmental data and their associated uncertainties. The acceleration and rotation data are detailed above. The satellite centre of mass O, the EA proof-mass M and the atomic cloud A are perfectly aligned along the axis X with an uncertainty of $200\,\mu\text{m}(3\sigma)$. The considered distance between the atomic cloud and the mirror is 10 cm. As the sensor operates in a microgravity environment, the free fall distance does not have to be as important as on Earth.

Measurement	Maximal value	Uncertainty
a_S^x	$-1\times10^{-6}\,\mathrm{m\,s^{-2}}$	0
x_{MO}	0	$200\,\mu\mathrm{m}$ (3σ)
y_{MO}	0	$200\,\mu\mathrm{m}$ (3σ)
z_{MO}	0	$200\,\mu\mathrm{m}$ (3σ)
x_{AM}	10 cm	$200\,\mu\mathrm{m}$ (3σ)
y_{AM}	0	$200\,\mu\mathrm{m}$ (3σ)
z_{AM}	0	$200\,\mu\mathrm{m}$ (3σ)
Ω_S^x	$10^{-4}\,\mathrm{rad\,s^{-1}}$	$\frac{\sigma_{gyro}}{\sqrt{T}}$ (1σ)
Ω_S^y	$10^{-4}\,\mathrm{rad\,s^{-1}}$	$\frac{\sigma_{gyro}}{\sqrt{T}}$ (1σ)
Ω_S^z	$1.2\,\mathrm{mrad\,s^{-1}}$	$\frac{\sigma_{gyro}}{\sqrt{T}}$ (1σ)
$\dot{\Omega}_S^x$	$10^{-6}\,\mathrm{rad\,s^{-2}}$	$\frac{2\sigma_{gyro}}{T\sqrt{T}}$ (1σ)
$\dot{\Omega}_S^y$	$10^{-6}\,\mathrm{rad\,s^{-2}}$	$\frac{2\sigma_{gyro}}{T\sqrt{T}}$ (1σ)
$\dot{\Omega}_S^z$	$10^{-6}\,\mathrm{rad\,s^{-2}}$	$\frac{2\sigma_{gyro}}{T\sqrt{T}}$ (1σ)

Table 5.5: Satellite environmental context: positions of the satellite elements, satellite acceleration and rotation parameters and the associated uncertainties.

5.3 Expected performances in space with rotation compensation

In this Section, is presented a calculation of the expected performances in space of a hybrid accelerometer implementing the rotation compensation method. The considered instrument is the one described in the Sections 5.1.1 and 5.1.2. The chosen approach consists in a theoretical approach close to the model of Chapter 1. From the literal equations of contrast and phase shift, an uncertainty associated to the acceleration measurement is computed.

5.3.1 Theoretical model of the instrument

The first step to evaluate the phase shift uncertainty associated to the rotation compensation method, is the calculation of the phase shift and contrast of the space instrument. The calculation is the same as the one presented in Chapter 1 but for a double diffraction interferometer. The satellite only rotation considered is around the Z axis i.e. the axis perpendicular to the measurement direction. The mirror rotation is also around the Z axis.

Phase shift

The phase shift of the double diffraction Mach-Zehnder interferometer can be expressed as the sum of the laser phase φ at the pulse instants along each path. The letters refer to Figure 5.2.

$$\Delta\Phi = 2\varphi_A - 2\varphi_B - 2\varphi_C + 2\varphi_D \tag{5.6}$$

As the recoil velocity is neglected, $\varphi_B = \varphi_C$ and the phase shift expression becomes:

$$\Delta\Phi = 2\varphi(t_0) - 4\varphi(t_0+T) + 2\varphi(t_0+2T) \tag{5.7}$$

The phase accumulated along the two arms of the interferometer is multiplied by two in comparison to the "simple" Mach-Zehnder interferometer: each arm experiences a state modification at the first and second pulses. For example, at $t = t_0$, the state of both arms changes. The upper arm state goes from the state $\left|f, \overrightarrow{p}\right\rangle$ to $\left|e, \overrightarrow{p} + \hbar\overrightarrow{k_{\text{eff}}}\right\rangle$ while the lower arm changes from $\left|f, \overrightarrow{p}\right\rangle$ to $\left|e, \overrightarrow{p} - \hbar\overrightarrow{k_{\text{eff}}}\right\rangle$. The phase $\pm\varphi(t_0)$ is gained for each arm. The double diffraction interferometer phase shift is then computed as a function of the rotation and cloud parameters. As the only rotation considered is around the Z axis, the notations will be simplified as $\Omega_M = \Omega_M^z$, $\dot{\Omega}_M = \dot{\Omega}_M^z$, $\Omega_S = \Omega_S^z$ and $\dot{\Omega}_S = \dot{\Omega}_S^z$.

$$\begin{aligned}\Delta\Phi_{M+S} = 2k_{eff}T^2\Bigg[& -a_S^x + (2\Omega_M^2 + \Omega_S^2 + 2\Omega_M\Omega_S)(a_S^x(\frac{t_0^2}{2} + t_0T + T^2) + (t_0+T)v_{x0} + x_{OA}) + 2\Omega_M^2 x_{MO} \\ & - 2(\Omega_M + \Omega_S)v_{y0} - (\dot{\Omega}_S + \dot{\Omega}_M)((t_0+T)v_{y0} + y_{OA}) - \dot{\Omega}_M y_{MO})\Bigg]\end{aligned} \tag{5.8}$$

with Ω_M and Ω_S the mean angular velocities of the mirror and of the satellite around the Z axis, $\dot{\Omega}_M$ and $\dot{\Omega}_S$ the mean angular accelerations of the mirror and of the satellite around the same axis, v_{x0} and v_{y0} the cloud velocity right after the cooling step, x_{OA} and y_{OA} the distance between the satellite centre of mass O and the centre of the atomic cloud A and x_{MO} and y_{MO} the distance between the mirror and the satellite centre of mass. Equation 5.8 is exactly the same only multiplied by two as the result obtained for a simple rotating Mach-Zehnder interferometer in Chapter 1.

When the rotation is compensated, $\Omega_M = -\Omega_S$ and $\dot{\Omega}_M = -\dot{\Omega}_S$, Equation 5.8 is simplified and becomes:

$$\Delta\Phi_{M=S} = 2k_{eff}T^2\Bigg[-a_S^x + \dot{\Omega}_S y_{MO} + \Omega_S^2(a_S^x(\frac{t_0^2}{2} + t_0T + T^2) + (t_0+T)v_{x_0} + x_{OA} + 2x_{MO})\Bigg] \tag{5.9}$$

Contrast

The contrast loss due to the rotation is computed using Equation 5.8 and the method presented in Chapter 1:

$$\begin{aligned}\frac{\overline{C}_{M+S}}{C_0} = \exp\Bigg(& -2k_{\text{eff}}^2T^4(\,(2\Omega_M^2 + \Omega_S^2 + 2\Omega_M\Omega_S)^2\sigma_x^2 + (\dot{\Omega}_S + \dot{\Omega}_M)^2\sigma_y^2 \\ & + ((t_0+T)(2\Omega_M^2 + \Omega_S^2 + 2\Omega_M\Omega_S))^2\sigma_{v_x}^2 + ((t_0+T)(\dot{\Omega}_S + \dot{\Omega}_M) + 2(\Omega_M + \Omega_S))^2\sigma_{v_y}^2\,)\Bigg)\end{aligned} \tag{5.10}$$

with C_0 the contrast in the absence of rotation, σ_x and σ_y the standard deviation of the Gaussian position distribution of the atomic cloud and σ_{v_x} and σ_{v_y} the standard deviation of the Gaussian velocity distribution. When the rotation is compensated, the contrast loss expression is simplified:

$$\frac{\overline{C}_{M=S}}{C_0} = \exp\Bigg(-2k_{\text{eff}}^2T^4(\,\Omega_S^4\sigma_x^2 + (t_0+T)^2\Omega_S^4\sigma_{v_x}^2\,)\Bigg) \tag{5.11}$$

Uncertainty

The implementation of the rotation compensation method and the correction of the rotation generated phase shift bias induce an uncertainty on the acceleration measurement. This uncertainty can be computed using Equation 5.8. The method of the total exact differential was chosen to extract the uncertainty from Equation 5.8. This method gives an upper bound to the uncertainty and takes into account the null parameter values. Most of the values in Equation 5.8 are null and an uncertainty around zero is given by this method. This total exact differential method considers the uncertainty in this case. As an example, let's consider a function f of two variables a and b defined as:

$$f(a,b) = a.b \tag{5.12}$$

The function f can be differentiated as:

$$\begin{aligned} f + \delta f &= f(a+\delta a, b+\delta b) \\ &= (a+\delta a)(b+\delta b) \\ &= a.b + \delta a.b + \delta b.a + \delta a.\delta b \end{aligned} \tag{5.13}$$

Thus, the uncertainty of f can be expressed as a function of a, b and their uncertainty δa and δb:

$$\delta f = \delta a.b + \delta b.a + \delta a.\delta b \tag{5.14}$$

This method is applied on Equation 5.8 to compute the rotation related uncertainty. To simplify the expression, the following notations are introduced:

$$\begin{aligned} A &= 2\Omega_M^2 + \Omega_S^2 + 2\Omega_M\Omega_S \\ \delta A &= 4\delta\Omega_M\Omega_M + 2\delta\Omega_S\Omega_S + 2\Omega_M\delta\Omega_S + 2\delta\Omega_M\Omega_S + 2\delta\Omega_M\delta\Omega_S \end{aligned} \tag{5.15}$$

The uncertainty of the rotation induced phase shift is summed up in Table 5.6.

Acceleration	Bias ($\mathrm{m\,s^{-2}}$)	Uncertainty ($\mathrm{m\,s^{-2}}$)
Coriolis	$-2(\Omega_M+\Omega_S)v_{y0}$	$2(\delta\Omega_M+\delta\Omega_S)\lvert v_{y0}\rvert + 2\lvert(\Omega_M+\Omega_S)\rvert\delta v_{y0} + 2(\delta\Omega_M+\delta\Omega_S)\delta v_{y0}$
Centrifugal	$(2\Omega_M^2+\Omega_S^2+2\Omega_M\Omega_S)(a_S^x(\frac{t_0^2}{2}+t_0T+T^2)+(t_0+T)v_{x0}+x_{OA})+2\Omega_M^2x_{MO}$	$2\Omega_M^2\delta x_{MO} + 4\delta\Omega_M\lvert\Omega_M x_{MO}\rvert + 4\delta\Omega_M\lvert\Omega_M\rvert\delta x_{MO} + \delta A\lvert(t_0+T)v_{x0}+x_{OA})\rvert + \lvert A\rvert((t_0+T)\delta v_{x0}+\delta x_{OA})) + \delta A((t_0+T)\delta v_{x0}+\delta x_{OA})) + \delta A a_S^x(\frac{t_0^2}{2}+t_0T+T^2)$
Angular	$-(\dot{\Omega}_S+\dot{\Omega}_M)((t_0+T)v_{y0}+y_{OA}) - \dot{\Omega}_M y_{MO}$	$\delta\dot{\Omega}_M\lvert y_{MO}\rvert + \lvert\dot{\Omega}_M\rvert\delta y_{MO} + \delta\dot{\Omega}_M\delta y_{MO} + (\delta\dot{\Omega}_S+\delta\dot{\Omega}_M)\lvert((t_0+T)v_{y0}+y_{OA})\rvert + \lvert(\dot{\Omega}_S+\dot{\Omega}_M)\rvert((t_0+T)\delta v_{y0}+\delta y_{OA}) + (\delta\dot{\Omega}_S+\delta\dot{\Omega}_M)((t_0+T)\delta v_{y0}+\delta y_{OA})$

Table 5.6: Rotation induced bias and uncertainty on the acceleration measurement.

Quantum projection noise

The quantum projection noise is the fundamental limit of the acceleration measurement. This noise comes from the quantum fluctuations of the atomic population measurement at the end of the interferometer [21]. It is interesting to compare the quantum projection noise to the uncertainty associated with the rotation compensation to determine which one limits the measurement. Moreover, the quantum noise depends on the interferometer contrast so the quantum noise conveys the contrast recovery to a certain extent. The quantum projection noise can be characterised by the standard deviation σ_P of the probability fluctuations assuming a normal law [103].

$$\sigma_P = \sqrt{\frac{P(1-P)}{N_{tot}}} \tag{5.16}$$

with P the probability of one state of the two levels system and N_{tot} the total number of atoms. The uncertainty on the phase shift measurement is then:

$$\begin{aligned} \sigma_{\Delta\Phi} &= \left|\frac{\mathrm{d}\Delta\Phi}{\mathrm{d}P}\right|\sigma_P \\ &= \frac{2}{C|\sin(\Delta\Phi)|}\sigma_P \end{aligned} \tag{5.17}$$

Thus, the quantum projection noise on the acceleration measurement is the following as $P = P_0 - \frac{C}{2}\cos(\Delta\Phi)$.

$$\sigma_a = \frac{1}{k_{eff}T^2}\frac{2}{C|\sin(\Delta\Phi)|}\sigma_P \tag{5.18}$$

The interferometer was considered operating at mid-fringe (the maximum of sensitivity) so $P = 0.5$ and $\sin(\Delta\Phi) = 0.5$. The noise on the acceleration measurement can be simplified as:

$$\sigma_a = \frac{2}{k_{eff}T^2C\sqrt{N_{tot}}} \tag{5.19}$$

In the following Sections, the only source of contrast loss considered will be the rotation. In Equation 5.10, the contrast in the absence of rotation will be considered equal to one: $C_0 = 1$. This is not a realistic hypothesis as many phenomena can reduce the interferometer contrast. Nevertheless, the displayed quantum noise is the minimal quantum noise achievable when implementing the rotation compensation method.

5.3.2 Expected contrast recovery

The main goal of the rotation compensation method is to increase the contrast of a rotating interferometer. In the absence of rotation compensation, the satellite rotation lowers drastically the contrast and prevents the use of long interrogation times. In this Section, the foreseen contrast recovery was computed for different atomic sources.

In the absence of rotation compensation, the estimated contrast loss of the hybrid instrument considering a molasses source (Table 5.1) is displayed on Figure 5.4a. The contrast loss was computed using Equation 5.10. The contrast decreases rapidly as the interrogation time increases: interrogations times longer than a hundred of µs are unattainable. If the contrast loss is due to all inertial accelerations (Coriolis, Angular and Centrifugal accelerations), the main source of contrast loss is the Coriolis acceleration as the Coriolis acceleration varies across the velocity distribution of the atomic cloud. To a lesser extent, the Centrifugal and Angular accelerations contribute to the contrast loss. Their two contributions depend on both the position and velocity distribution and have a similar amplitude in this case. To conclude, for a molasses source, in the absence of rotation compensation, the contrast is limited by the width of the atomic velocity distribution. For the BEC source and DKC source, the velocity distributions are narrower. Nevertheless, the contrast is still limited by the width of the velocity distribution. To obtain a higher contrast either the width of the velocity distribution has to be reduced or the Coriolis acceleration has to be compensated.

With the rotation compensation technique, the contrast is fully recovered for interrogation times inferior to 500 ms for a molasses source as shown by Figure 5.4b. When $\Omega_M = -\Omega_S$ and $\dot{\Omega}_S = -\dot{\Omega}_M$, the contributions of the Coriolis and Angular accelerations to the contrast loss cancel. The contrast is now limited by the Centrifugal acceleration and both the position and velocity distributions of the cloud. It is noticeable that the Centrifugal contribution to the

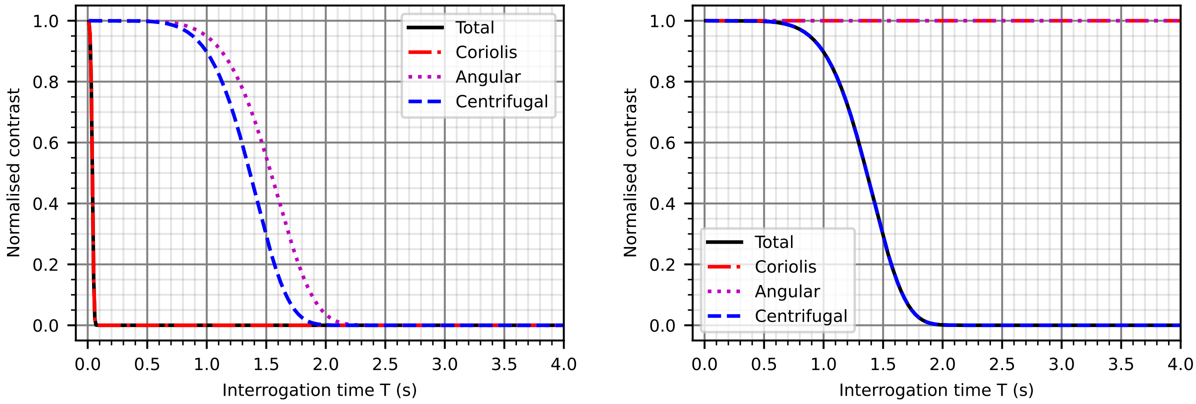

(a) Contrast loss in the absence of rotation compensation: $\Omega_M = 0$ and $\dot{\Omega}_M = 0$

(b) Contrast recovery with the rotation compensation: $\Omega_M = -\Omega_S$ and $\dot{\Omega}_M = -\dot{\Omega}_S$

Figure 5.4: Impact of the inertial accelerations on the contrast loss for a molasses source. Rotation and atomic cloud parameters can be found in Tables 5.5 and 5.1.

contrast loss is unchanged by the rotation compensation (Equation 5.11). In Equation 5.10, the term $(2\Omega_M^2 + \Omega_S^2 + 2\Omega_M\Omega_S)$ characterises the contribution of the Centrifugal acceleration. In the absence of compensation $\Omega_M = 0$, this term equals $(2\Omega_M^2 + \Omega_S^2 + 2\Omega_M\Omega_S) = \Omega_S^2$. When compensating, $\Omega_M = -\Omega_S$ this term also becomes $(2\Omega_M^2 + \Omega_S^2 + 2\Omega_M\Omega_S) = \Omega_S^2$. The Centrifugal contribution stays the same with or without the rotation compensation.

As the velocity and position distributions of the cloud limits the contrast recovery, it makes sense to find ways to reduce their width. This can be achieved by cooling further the atomic cloud. For example, a BEC-like source (Table 5.2) can be obtained after a stage of evaporative cooling. Such a source has smaller velocity and position dispersions. Furthermore, a DKC source (Table 5.3) can be considered with the addition of another step to the cooling procedure. If this last source has a very narrow velocity distribution, its position distribution is wider than the one of the BEC source.

Let's study the contrast recovery for these three potential sources. Without rotation compensation, the maximum interrogation time achievable never exceeds 1 s even for the colder DKC source (Figure 5.5a). With the rotation compensation, the maximum interrogation time achievable increases significantly. With an acceptable contrast loss of 80%, the molasses source grants an interrogation time up to 1 s while the BEC source grants a 2 s interrogation time (Figure 5.5b). The best result is achieved with the DKC with an interrogation time up to 5 s.

The rotation compensation seems to be efficient to recover the contrast onboard a satellite enabling the acceleration measurement for long interrogation times. The contrast recovery is limited by the Centrifugal acceleration term (Equation 5.11). More precisely, the term depending on the velocity distribution width has the greater contribution: $(t_0 + T)^2\Omega_S^4\sigma_{v_x}^2$. Besides, the rotation compensation method impacts not only the contrast but also the phase shift of the interferometer. This rotation induced bias has to be corrected from the acceleration measurement leading to a rotation induced uncertainty.

5.3.3 Phase shift bias and uncertainty due to rotation

The satellite rotation has an effect on both the contrast and phase shift of the interferometer. The rotation creates a bias on the phase shift which has to be removed to measure the

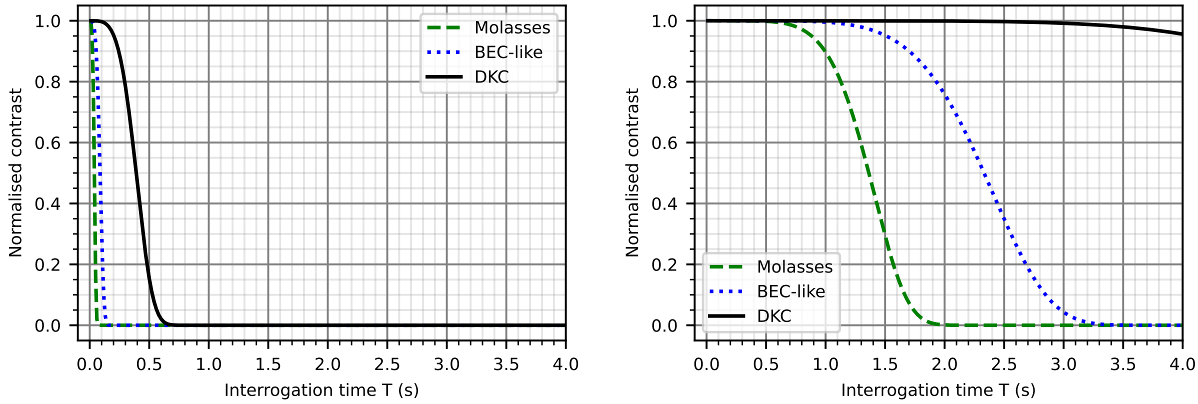

(a) Contrast in the absence of rotation compensation.

(b) Contrast with rotation compensation.

Figure 5.5: Rotation compensation method influence on the contrast considering different atomic sources (molasses, BEC and DKC atomic sources).

acceleration even when using the rotation compensation. In this Section, the rotation induced bias and the associated uncertainty are studied through Equation 5.8 and Table 5.6. Ultimately, the acceleration measurement precision is limited by the quantum projection noise. Besides, the quantum noise on the acceleration measurement depends of the interferometer contrast as expressed in Equation 5.19. Thus, the rotation induced contrast loss will influence the quantum noise. A comparison between the quantum noise and the rotation related uncertainty is presented in this Section to examine the trade-off between the contrast recovery thanks to the rotation compensation and the uncertainty generated by the rotation. This calculation is done for the three potential atomic sources. Be careful to note that the only source of contrast loss taken into account is the rotation.

Molasses source

For a molasses source, the contrast decreases very quickly without the compensation preventing any measurement. This is reflected by the quantum noise without compensation (in cyan on Figure 5.6b) which increases very quickly. The rotation induced uncertainty (in dark blue) is due to the satellite rotation and comes mostly from the Coriolis acceleration. With the compensation, interrogation times of the order of 1 s seem achievable as the contrast recovery exceeds 80%. The rotation induced uncertainty decreases by two orders of magnitude as some terms in Table 5.6 are cancelled by the compensation. For example the term $|(\Omega_M + \Omega_S)|\delta v_{y0}$ cancels. The quantum noise is also reduced thanks to the contrast recovery (Figure 5.6a). To conclude, the performance remains limited by the contrast loss for interrogation times lower than 2 s. In this interval, the uncertainty is limited by the rotation, more precisely by the Centrifugal acceleration and its term depending on the cloud velocity $(2\Omega_M^2 + \Omega_S^2 + 2\Omega_M\Omega_S)(t_0 + T)v_{x0}$. For an interrogation time of 1 s the uncertainty induced by rotation has a value of $4.0 \times 10^{-9}\,\mathrm{m\,s^{-2}}$. The acceleration bias has an almost constant value of $-1.44 \times 10^{-7}\,\mathrm{m\,s^{-2}}$ in the interrogation time interval. The main contribution to the bias is the following term of the Centrifugal acceleration: $\Omega_S^2 x_{OA} = -1.44 \times 10^{-7}\,\mathrm{m\,s^{-2}}$.

BEC-like source

The BEC-like source has narrower velocity and position distributions as well as more stable velocity and position at the end of the cooling stage. Even if the velocity distribution is narrower, the contrast drops drastically for interrogation times longer than a hundred of µs

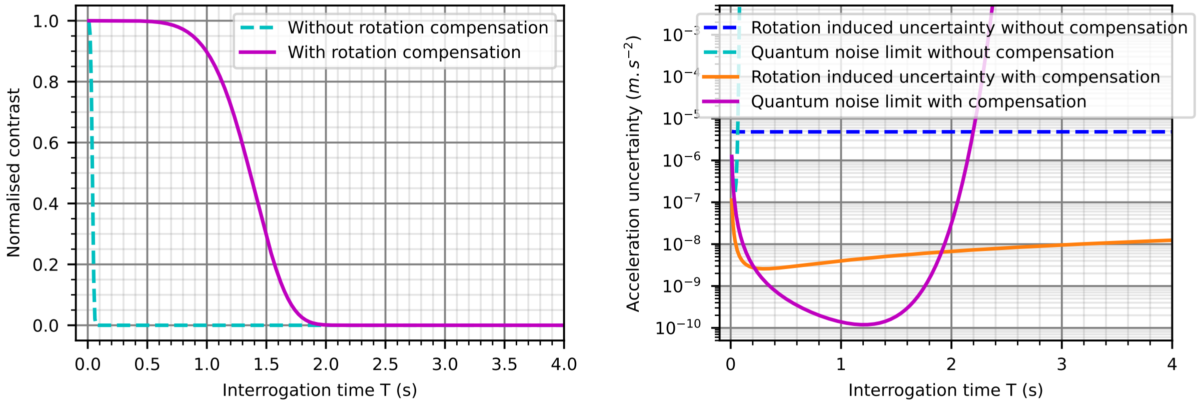

(a) Rotation induced contrast loss.

(b) Uncertainty associated with the acceleration.

Figure 5.6: Expected performances for a rotating interferometer with a molasses source.

in the absence of rotation compensation (Figure 5.7a). With the rotation compensation, the contrast recovery is more important than for a molasses source allowing interrogation times up to 2 s with a 80% contrast recovery. The quantum noise stays below the rotation induced uncertainty for interrogation times between 0.8 and 3 s (Figure 5.7b). Thanks to the better position and velocity stabilities of the BEC-like source, the rotation uncertainties with and without rotation compensation are one order of magnitude smaller than the molasses uncertainties. For a BEC-like source, an interrogation time of 1 s would lead to a rotation induced uncertainty of $6.6 \times 10^{-10}\,\mathrm{m\,s^{-2}}$. For short interrogation times, the rotation uncertainty is limited by the measurement of the satellite and mirror rotation. Where for long interrogation times, the rotation uncertainty starts to increase due to the cloud trajectory. Some uncertainty terms depend on T such as the Centrifugal and Angular accelerations. These terms lead to an interrogation time dependant uncertainty due to terms like $\dot{\Omega}_M((t_0+T)\delta v_{y0}+\delta y_{OA})$. The bias is exactly the same as for a molasses source: the bias only depends on the distance between the atomic cloud and the satellite centre of mass.

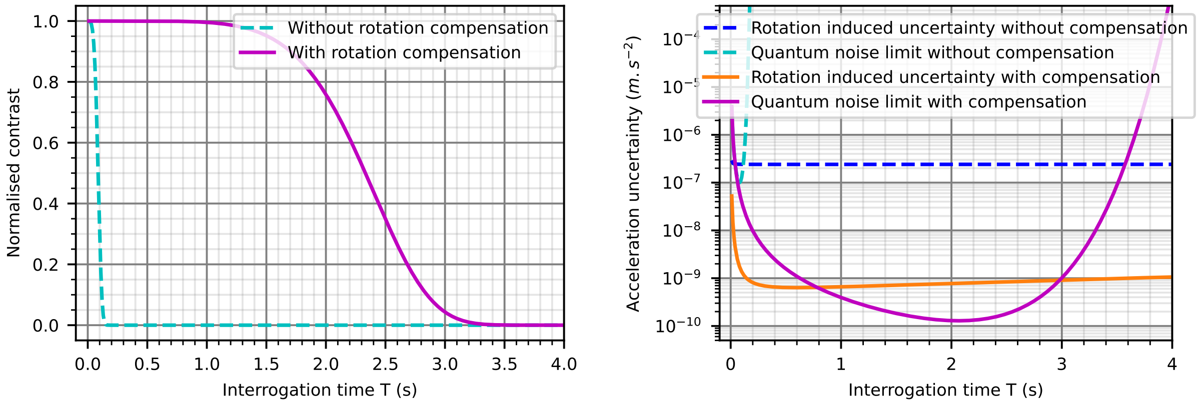

(a) Rotation induced contrast loss.

(b) Uncertainty associated with the acceleration.

Figure 5.7: Expected performances for a rotating interferometer with a BEC-like source.

Delta kick cooled source

Despite, the very narrow velocity distribution of the DKC source, the contrast decays rapidly in the absence of rotation compensation (Figure 5.8a). With the compensation, the contrast recovery is the more important of the three considered atomic sources with a 80%

recovery for up to 5 s. The rotation uncertainty with and without rotation is the same as the ones of the BEC-like source as the two sources have the same velocity and position stabilities (Figure 5.8b). However, the span where the quantum noise is below the rotation uncertainty is larger (between 0.5 and 9 s). The rotation induced uncertainty for an interrogation time of 1 s is exactly the same as the BEC-like source (6.6×10^{-10} m s^{-2}) as the rotation induced uncertainty depends of the source stability. The phase bias is still equal to -1.44×10^{-7} m s^{-2} as for the two other sources.

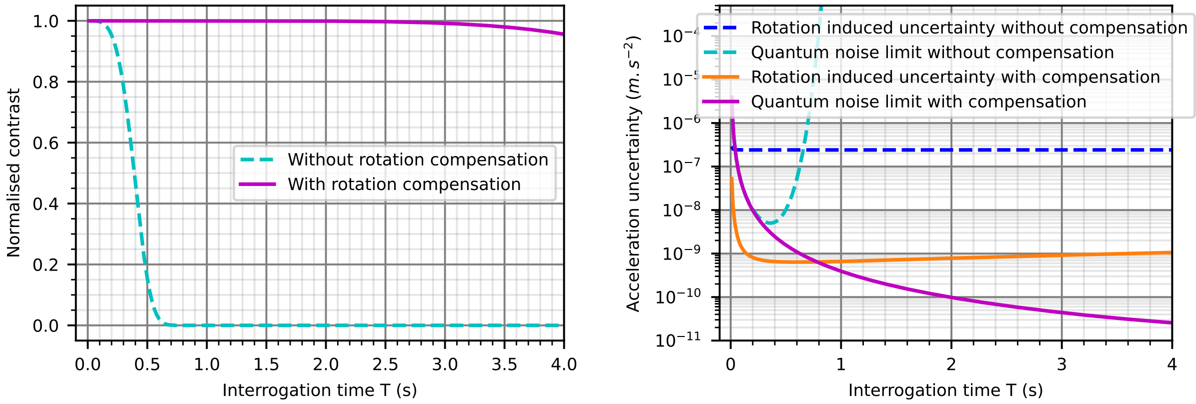

(a) Rotation induced contrast loss. (b) Uncertainty associated with the acceleration.

Figure 5.8: Expected performances for a rotating interferometer with a delta-kicked cooled source.

Table 5.7 sums up the results for an interrogation time of 1 s for the three sources highlighting the similar performances of the BEC-like and DKC sources. If upgrading from a molasses source to a BEC source improves the uncertainty by one order a magnitude, further cooling does not improve the performances. The DKC source allows longer interrogation times but without a decrease in the rotation uncertainty.

Source	Acceleration bias (m s^{-2})	Uncertainty induced by rotation (m s^{-2})	Quantum noise (m s^{-2})
Molasses	-1.4×10^{-7}	4.0×10^{-9}	1.4×10^{-10}
BEC-like	-1.4×10^{-7}	6.6×10^{-10}	3.9×10^{-10}
DKC	-1.4×10^{-7}	6.6×10^{-10}	3.9×10^{-10}

Table 5.7: Expected performances for an interrogation time of $T = 1$ s with the implementation of rotation compensation for the three atomic sources.

Limiting parameter

The previous study showed that the rotation limits the performances of the instrument. One can wonder what is the greatest contribution to the rotation induced uncertainty. Let's consider a rotation compensated interferometer with a BEC-like source. The rotation induced uncertainty main contribution is the Centrifugal acceleration. On Figure 5.9, the contributions of the different inertial acceleration were drawn. For an interrogation time of 1 s, the Coriolis and Angular contributions are below 1×10^{-10} m s^{-2} while the Centrifugal contribution explains most of the uncertainty on the acceleration. More precisely, the uncertainty is partly due to the velocity stability of the cloud. This term is $A(t_0 + T)\delta v_{x_0}$ and is represented in green on Figure 5.9. The term depending on the position of the cloud, mirror and CoM of the satellite also contributes greatly. This term is $2\Omega_M^2 \delta x_{MO} + A(\delta x_{AM} + \delta x_{MO})$ and is represented in orange. The other terms of the Centrifugal acceleration uncertainty presented in Table 5.6 are below $1 \times 10^{-11}\,\mathrm{m\,s^{-2}}$.

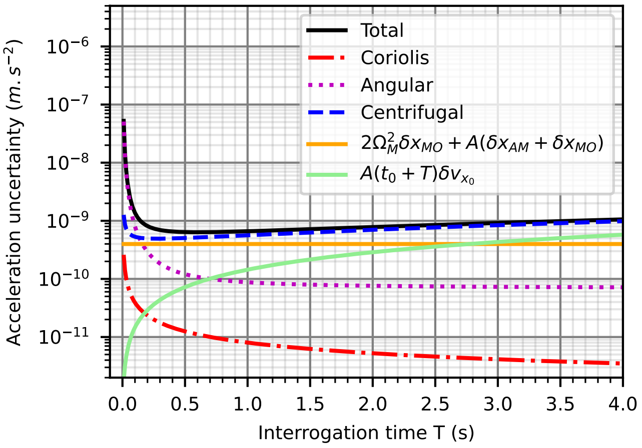

Figure 5.9: Contributions to the rotation induced uncertainty for a BEC-like source with rotation compensation.

To conclude, a BEC source with an interrogation time around 1 s would give an optimal result under our hypotheses. A colder source would allow to reach longer interrogation times but this would not improve the sensor performances. There is no need for longer interrogation times as the rotation uncertainty increases with the interrogation time due to rotation terms depending of the interrogation time. Under the hypotheses of this study, the rotation induced uncertainty is limited by the knowledge of the position of the different elements (cloud, mirror and CoM) and by the stability of the cloud velocity. To improve the uncertainty, either the uncertainty associated with these parameters have to be decreased or the Centrifugal acceleration has to be compensated. Nevertheless, the scope of this study is limited as no other sources of contrast loss and uncertainty were considered.

Conclusion

In this Chapter, a potential space atomic accelerometer was studied to assess the efficiency of the rotation compensation method onboard a satellite. More precisely, the satellite considered is similar to a gravimetry satellite such as a satellite of the NGGM mission. Three different atomic sources with different velocity and position distributions were studied.

In this context, the rotation compensation method could allow to recover the contrast for interrogation times of several seconds. Thanks to the compensation, the rotation induced uncertainty and the quantum noise of the acceleration measurement were significantly reduced. A performance of the order of $7 \times 10^{-10}\,\mathrm{m\,s^{-2}}$ seems achievable for a BEC-like source with an interrogation time of 1 s. The limiting parameter is the rotation related uncertainty and more precisely the Centrifugal acceleration. A BEC-like source is cold enough to reach this limit. In this model, further cooling does not improve the performances of the atomic accelerometer. Moreover longer interrogation times would not reduce the rotation uncertainty as it increases with the interrogation time.

Conclusion and future prospects

The work presented in this PhD manuscript contributes to the research effort dedicated to assess the possibility to use cold atom sensors in space. This work is the continuation of the development of the hybrid instrument presented in [30]. In this previous work, the potential of the hybrid instrument was demonstrated and the atomic accelerometer was able to correct the long-term drift of the electrostatic accelerometer.

Here, the presented work has been devoted to the problem of the negative impact of the rotation on the hybrid instrument. The hybrid instrument is an original setup with unique features to study the rotation impacts but also to limit those impacts. The rotation issue is indeed a limitation for future space atomic sensors and more globally for terrestrial onboard sensors.

Conclusion

The cross-talk between acceleration and rotation is an issue for any accelerometer. Nevertheless, this cross-talk is reduced for accelerometers with an immobile proof-mass (for example electrostatic accelerometers) as the Coriolis acceleration is null. For accelerometers with a free proof-mass, all the inertial accelerations contributes to the cross-talk. Atom interferometry based sensors belong to the second category. Moreover, for these sensors, rotation leads not only to the apparition of inertial accelerations but also to deterioration of the sensitivity due to a loss of contrast of the interferometer. This work aimed at studying and mitigating the effect of rotation on the hybrid setup in the range of rotation encountered on a satellite dedicated to gravimetry missions.

Before this work, a method to limit the impact of rotation on atomic interferometers have already been implemented. This method consists in rotating the retro-reflection mirror of the laser interrogating the atoms. When the mirror rotation is opposite to the whole sensor rotation, the direction of measurement is constant during the interferometer. This method was successfully implemented to limit the impact of the Earth rotation on cold atom interferometers [3, 90, 91] allowing to improve the contrast and to limit the rotation induced bias. As the Earth rotation has a low angular velocity of $70\,\mu\mathrm{rad\,s^{-1}}$, the principal inertial acceleration impacting atomic interferometer is the Coriolis acceleration which also happens to be corrected in theory by the compensation method. This method was also tested to correct higher angular velocities encountered in onboard applications [42, 96]. If the contrast recovery seems promising, the rotation induced bias needs to be modelled carefully as both Centrifugal and Coriolis accelerations have to be considered. Moreover, if the carrier has an angular acceleration, the

Angular acceleration impact on the sensor could be significant and has to be considered. The rotation compensation method is also considered for future space instruments onboard satellites [27–30, 95] . In space applications, the considered angular velocity is around 1 mrad s^{-1} which is more important than the Earth angular velocity but lower than angular velocities encountered in marine or airborne applications. Usually, the implementation of the rotation compensation requires a tip-tilt mount to rotate the mirror.

In this work, an original implementation of the rotation compensation is presented using an electrostatic accelerometer as an actuated mirror instead of a tip-tilt mount. An beneficial feature of this experimental setup is the real time measurement of the mirror angular position thanks to the EA capacitive detection.

This feature advantageously enabled a thorough study of the impact of the mirror rotation on the interferometer. Contrasts and phase shifts were measured for angular velocities of a few mrad s^{-1}. As the EA can be rotated with a non-linear movement, the impact of angular accelerations of the order of 100 mrad s^{-2} on the interferometer was also analysed. The loss of contrast due to the Angular acceleration was thus highlighted. These measurements were confronted to theoretical predictions and brought information on the kinematic parameters of the atomic cloud such as its position, velocity, size and velocity distribution. Moreover, the theoretical model predicted a variation of the effective wave vector magnitude in addition to a change in the measurement direction. The magnitude variation is similar to a variation of the laser frequency creating a position dependant phase shift. This effect leads to a pseudo Centrifugal acceleration in addition to the Centrifugal acceleration due to the variation of measurement direction.

The impact of the rotation of the whole sensor was also studied thanks to piezo actuators. The rotation of the sensor was more difficult to control and monitor than the mirror rotation and the effects of the angular velocity and the angular acceleration could not be studied separately. The experimental contrast loss and phase shift in the presence of rotation were confronted to the theoretical model. When the sensor rotates, the direction of measurement varies but not the magnitude of the effective wave vector: the impact of the inertial accelerations on the cold atom sensor measurement is the same as on any accelerometer using a free proof-mass. Nevertheless, the atomic sensor also exhibits a loss of contrast due to the rotation. The contrast loss due to the Coriolis acceleration but also due to the Angular acceleration were observed and for some configurations these two contributions counterbalanced each other leading to a smaller contrast loss.

The rotation compensation method was finally implemented by rotating the sensor and the mirror at the same time. The compensation of the Coriolis acceleration was demonstrated as the contrast was recovered up to 99% when the Coriolis acceleration was the main source of contrast loss. The experiment was performed for an angular velocity of the order of the mrad s^{-1}. The compensation of the Angular acceleration was also demonstrated with a contrast recovery up to 92% for an angular velocity around 40 mrad s^{-2}. When the rotation is compensated, the only contribution to the contrast loss should be the pseudo Centrifugal term induced by the variation of the effective wave vector magnitude. Nevertheless, this contribution is negligible for the lab prototype and should only be observed for longer interrogation times. The rotation induced phase shift was also measured and confronted to the theoretical prediction with an error below 0.5 rad. The prediction of the rotation induced phase shift is challenging due to its strong dependence on the kinematic parameters of the atomic cloud. An important contribution of an uncompensated Angular acceleration was identified: this term is the greatest contribution to the experimental data and limits their analysis. On a theoretical point of view, the Coriolis acceleration is cancelled by the rotation compensation. The Angular acceleration can be suppressed only if the sensor and mirror centres of rotation are aligned transversally to the measurement direction. The Centrifugal acceleration cannot be fully compensated and a term resulting in the distance between the sensor O and mirror M centres of rotation arises: $\Omega_S^2 x_{MO}$. This term results in the mirror (i.e. the measurement reference) rotation in the satellite or laboratory frame. Moreover, the mirror rotation induces a variation of the effective wave vector magnitude leading to a term in $\Omega_S^2(a_{x_L}(\frac{t^2}{2} + t_0 T + T^2) + (t_0 + T)v_{x_0} + x_{MA})$.

A prevision of a space cold atom accelerometer performances was also provided. The case of a Nadir pointing satellite belonging to a gravimetry mission similar to NGGM is examined with the mirror placed at the satellite centre of rotation. In the simple considered case, the uncertainty due to rotation effects is expected to be of the order of 7×10^{-10} m s^{-2} for an interrogation time around 1 s. When the rotation is compensated, the term contributing the most to the uncertainty is the Centrifugal acceleration. More precisely, the uncertainty on the positions of the cloud and the mirror and sensor centres of rotation as well as the uncertainty on the cloud velocity limit the total uncertainty on the acceleration measurement. Thus, to improve the sensor exactitude, either the Centrifugal acceleration has to be corrected or the knowledge of the cloud velocity and the positions of the different elements improved. This result is a preliminary result as it does not consider any effects other than the satellite rotation and its compensation. Other phenomena could limit the achievable uncertainty such as wave front aberrations or detection limits.

This work paves the way to satellite-boarded cold atom accelerometer with an experimental test of an original implementation of the rotation compensation method. Nevertheless, several points could be addressed to further improve the performances and design of the accelerometer.

Prospects

The rotation compensation method with an electrostatic actuated mirror showed interesting results, the work presented here could be pursued by addressing several limitations enlightened in this work and adding possible improvements to the current experiment.

Toward a rotation-proof cold atom accelerometer

This work on the hybrid experiment using an EA as an actuated mirror displayed promising results. The hybrid prototype is a first step toward a space rotation-proof cold atom accelerometer. To further improve the prototype, several points could be considered.

The EA as an actuated mirror

The use of the EA has the advantage to provide a continuous measurement of the mirror position along the six degrees of freedom easing the calculation of the rotation induced bias. Nevertheless, it is still a challenge to predict reliably the rotation induced bias in order to correct the acceleration measurement from this bias. Firstly, the wave front aberrations induced by the EA proof mass could affect the bias and their measurement could help improve the accelerometer uncertainty. Secondly, some cross-talk was noticed between the different degrees of freedom of the EA proof-mass. The precision of the mirror rotation also has to be considered in the bias calculation. To improve the EA proof-mass control, a different design could be consider involving a cubic proof-mass with an increased number of electrodes. Such a design could reduce the cross-talk between the degrees of freedom.

Rotation compensation

The analysis of the experimental results of the rotation compensation was limited by an uncontrolled angular acceleration of the sensor. A new prototype could be tested in better controlled conditions to reach the theoretical limit of the rotation compensation method in the lab. If the ground performances cannot be extrapolated in space, they contribute to the model validation. Then, the space performances can be anticipated thanks to the validated model.
Ultimately, for a perfectly compensated rotation, only the Centrifugal acceleration should lead to a loss of contrast. The measurement bias would also be affected by the Centrifugal acceleration but a contribution due to the Angular acceleration can be present if the mirror and sensor centres of rotation do not coincide. The residual contribution of the Centrifugal acceleration can be explained by the distance between the sensor centre of rotation O and the mirror centre of rotation M leading to a term in $\Omega_S^2 x_{MO}$. This term could be suppressed by placing the mirror at the centre of rotation of the sensor. Another residual term is also present due to the magnitude variation of the effective wave vector: $\Omega_S^2(a_{x_L}(\frac{t_0^2}{2}+t_0T+T^2)+(t_0+T)v_{x_0}+x_{MA})$. A driven variation of the one-photon Raman detuning Δ during the interferometer would increase the magnitude of the effective wave vector thus suppressing this term. The magnitude variation of the effective wave vector due to the mirror is $\overrightarrow{\Delta k_{\text{eff}}^{rot}} = k_{\text{eff}}\frac{\theta_S^2}{2}\overrightarrow{x_M}$. Thus, to compensate this variation the detuning Δ should be scanned quadratically as $\Delta = \Delta_0(1-\beta t^2)$ during the interferometer. Such a variation of Δ would lead to a quadratic variation of the wave vector compensating the rotation effect.
Lastly, in an operating instrument, the rotation compensation should be automated. First, the sensor rotation would be measured by a gyroscope. Then, the gyroscope signal has to be integrated to give an angular setpoint to the EA proof-mass control. The integration step has to be fast enough to limit the time delay between the sensor rotation and the mirror rotation. The requirement on the speed of the integration process depends on the interrogation time: a long interrogation reduces the need to a fast integration. In this work, only the impact of a sinusoidal rotation at 4 Hz was studied. A more complete study should consider a broader range of rotation frequency. The frequency response of the gyroscope signal integration setup and of the EA actuation system could also be studied.

Atomic source

The choice of the atomic source is crucial for a cold atom sensor and becomes even more important when attempting to measure in the presence of rotation. The velocity and position distributions have to be narrow to limit the contrast loss due to rotation. Moreover, the measurement bias induced by the rotation depends on the initial velocity and position of the cloud. Thus, these parameters have to be stable to limit the sensor uncertainty. A Bose-Einstein Condensate source presents interesting characteristics: narrow velocity and position distributions as well as stable initial kinematic parameters. For these reasons, a BEC is a source considered for space cold atom sensors [27, 28, 34]. Nevertheless, the implementation of a BEC source makes the sensor architecture more complex. The mass and electrical consumption of the instrument are increased.

Design of a space cold atom accelerometer

Once the cold atom accelerometer is ready to operate in space, its design have to take into account the space mission environment. Considering the case of gravimetry missions, previous satellites boarded electrostatic accelerometers. These accelerometers still display unrivalled short-term sensitivity in microgravity and would probably not be replaced totally by cold atom sensors in a close future. Future studies would have to determine the best articulation of the EA and atomic accelerometer.

As demonstrated in [30], the combination of the electrostatic and atomic sensors is a promising approach to correct the drift of the EA with the atomic accelerometer. Nevertheless, one could ask if the hybridisation and the rotation compensation could be performed at the same time. The use of the EA as an actuated mirror could deteriorate its performances as an accelerometer. This problem could be solved by boarding two EA instead of one. The first EA dedicated to acceleration measurement and calibrated by the atomic accelerometer. The other only used as an actuated mirror to correct the satellite rotation. Moreover, the second EA can also be a backup instrument for the first EA. This solution would require to find an architecture allowing the first EA used as an accelerometer to be close to the atomic sensor. To avoid adding errors when correcting the EA drift, both accelerometers have to measure the same quantity. Thus, their points of measurement have to be close to each other.
As demonstrated in this work, the distance between the sensor centre of rotation and the mirror centre of rotation is an important parameter for the rotation compensated atomic accelerometer. In the case of a satellite boarded sensor, the relevant distance is the distance between the satellite centre-of-mass (CoM) and the mirror centre of rotation. This fact raises the importance of the cold atom accelerometer location inside the satellite.

To conclude, the path is still long before considering a future gravimetry mission boarding atomic accelerometers. Different concepts and instrument architectures have to be validated and the implemented technologies need to mature. Nevertheless, the pathfinder mission CARIOQA should demonstrate the potential of technologies of major interest for future gravimetry mission boarding atomic accelerometers.

APPENDIX A

Scientific communications

Publications in scientific journals

N. Zahzam, B.Christophe, V.Lebat, E. Hardy, P. Huynh, **N. Marquet**, C. Blanchard, Y. Bidel, A. Besson, P. Abrykosov, T. Gruber, R. Pail, I. Daras and O. Carraz
"Hybrid Electrostatic-Atomic Accelerometer for Future Space Gravity Missions"
Remote Sensing, 2021,14 3273, `https://doi.org/10.3390/rs141432730`

N. Marquet, N. Zahzam and A. Godard
"Impact of rotation on an atomic interferometer and compensation strategy"
To be submitted to *Physical Review A*

International conferences

Frontiers of Matter Wave Optics School and Conference 2022
Trieste, Italy, September 2022
A Hybrid Cold Atom Interferometer for Space Geodesy Missions
Poster

Young Atom Opticians Conference 2023
Barcelona, Spain, June 2023
A Hybrid Cold Atom Interferometer for Inertial Measurements
Oral presentation

26ème Congrès Général de la Société Française de Physique
Paris, France, July 2023
A Hybrid Cold Atom Interferometer for Space Geodesy Missions
Best Poster Prize

28th International Conference on Atomic Physics
London, United-Kingdom, July 2024
A Hybrid Cold Atom Interferometer for Space Gravimetry Missions
Poster

Congrès de la Société Française d'Optique
Rouen, France, July 2024
Développement d'un accéléromètre à froids dans le contexte des missions spatiales de gravimétrie
Oral presentation

National conferences

Journée des Doctorants de l'ONERA 2022
Palaiseau, France, January 2022
Développement d'un gravimètre à atomes froids hybride multi-espèces
Oral presentation

Journée des Doctorants de l'ONERA 2023
Palaiseau, France, February 2023
Développement d'un accéléromètre à atomes froids hybride multi-espèces
Oral presentation

Ecole Doctorale Ondes et Matières Days 2023
Orsay, France, Frebruary 2023
Hybrid multi-species cold atom interferometry for inertial measurements
Oral presentation

Quantum-Saclay Day 2023
Orsay, France, October 2023
A Hybrid Cold Atom Interferometer for Space Geodesy Missions
Poster

Rencontres des Jeunes Physiciens
Paris, France, November 2023
A Hybrid Cold Atom Interferometer for Space Geodesy Missions
Oral presentation

Journée des Doctorants de l'ONERA 2024
Palaiseau, France, February 2024
A Hybrid Cold Atom Accelerometer for Space Geodesy Missions
Oral presentation

remote sensing

Article

Hybrid Electrostatic–Atomic Accelerometer for Future Space Gravity Missions

Nassim Zahzam [1,*], Bruno Christophe [1], Vincent Lebat [1], Emilie Hardy [1], Phuong-Anh Huynh [1], Noémie Marquet [1], Cédric Blanchard [1], Yannick Bidel [1], Alexandre Bresson [1], Petro Abrykosov [2], Thomas Gruber [2], Roland Pail [2], Ilias Daras [3] and Olivier Carraz [4]

[1] DPHY, ONERA, Université Paris-Saclay, Chemin de la Hunière-BP80100, F-91123 Palaiseau, France; bruno.christophe@onera.fr (B.C.); vincent.lebat@onera.fr (V.L.); emilie.hardy@onera.fr (E.H.); phuong-anh.huynh@onera.fr (P.-A.H.); noemie.marquet@onera.fr (N.M.); cedric.blanchard@onera.fr (C.B.); yannick.bidel@onera.fr (Y.B.); alexandre.bresson@onera.fr (A.B.)

[2] Lehrstuhl für Astronomische und Physikalische Geodäsie, Technische Universität München, Arcisstraße 21, 80333 München, Germany; petro.abrykosov@tum.de (P.A.); thomas.gruber@tum.de (T.G.); roland.pail@tum.de (R.P.)

[3] European Space Agency, Keplerlaan 1, P.O. Box 299, 2200 AG Noordwijk, The Netherlands; ilias.daras@esa.int

[4] RHEA for ESA–European Space Agency, Keplerlaan 1, P.O. Box 299, 2200 AG Noordwijk, The Netherlands; olivier.carraz@esa.int

* Correspondence: nassim.zahzam@onera.fr

Abstract: Long-term observation of Earth's temporal gravity field with enhanced temporal and spatial resolution is a major objective for future satellite gravity missions. Improving the performance of the accelerometers present in such missions is one of the main paths to explore. In this context, we propose to study an original concept of a hybrid accelerometer associating a state-of-the-art electrostatic accelerometer (EA) and a promising quantum sensor based on cold atom interferometry. To assess the performance potential of such an instrument, numerical simulations were performed to determine its impact in terms of gravity field retrieval. Taking advantage of the long-term stability of the cold atom interferometer (CAI), it is shown that the reduced drift of the hybrid sensor could lead to improved gravity field retrieval. Nevertheless, this gain vanishes once temporal variations of the gravity field and related aliasing effects are taken into account. Improved de-aliasing models or some specific satellite constellations are then required to maximize the impact of the accelerometer performance gain. To evaluate the achievable acceleration performance in-orbit, a numerical simulator of the hybrid accelerometer was developed and preliminary results are given. The instrument simulator was in part validated by reproducing the performance achieved with a hybrid lab prototype operating on the ground. The problem of satellite rotation impact on the CAI was also investigated both with instrument performance simulations and experimental demonstrations. It is shown that the proposed configuration, where the EA's proof-mass acts as the reference mirror for the CAI, seems a promising approach to allow the mitigation of satellite rotation. To evaluate the feasibility of such an instrument for space applications, a preliminary design is elaborated along with a preliminary error, mass, volume, and electrical power consumption budget.

Keywords: cold atom interferometer; electrostatic accelerometer; hybrid accelerometer; gravity mission; quantum space gravity; satellite geodesy

check for updates

Citation: Zahzam, N.; Christophe, B.; Lebat, V.; Hardy, E.; Huynh, P.-A.; Marquet, N.; Blanchard, C.; Bidel, Y.; Bresson, A.; Abrykosov, P.; et al. Hybrid Electrostatic–Atomic Accelerometer for Future Space Gravity Missions. *Remote Sens.* **2021**, *14*, 3273. https://doi.org/10.3390/rs14143273

Academic Editors: Luca Massotti and David N. Wiese

Received: 20 May 2022
Accepted: 1 July 2022
Published: 7 July 2022

1. Introduction

1.1. General Context of Space Gravity Missions and Emergence of Cold Atom Interferometry

Sustained observations from dedicated satellite gravity missions (e.g., GOCE, GRACE, and GRACE-FO) are key to monitoring the Earth system's dynamic processes related to mass transport and in understanding their coupling mechanisms. Satellite gravimetry is a

List of Tables

List of Figures

Bibliography

[1] Y. Bidel, N. Zahzam, C. Blanchard, A. Bonnin, M. Cadoret, A. Bresson, D. Rouxel, and M. F. Lequentrec-Lalancette, "Absolute marine gravimetry with matter-wave interferometry," *Nature Communications*, vol. 9, p. 627, Feb. 2018.

[2] Y. Bidel, N. Zahzam, A. Bresson, C. Blanchard, M. Cadoret, A. V. Olesen, and R. Forsberg, "Absolute airborne gravimetry with a cold atom sensor," *Journal of Geodesy*, vol. 94, p. 20, Jan. 2020.

[3] S.-Y. Lan, P.-C. Kuan, B. Estey, P. Haslinger, and H. Müller, "Influence of the Coriolis Force in Atom Interferometry," *Physical Review Letters*, vol. 108, p. 090402, Feb. 2012.

[4] C. Reigber, P. Schwintzer, and H. Lühr, "The CHAMP geopotential mission," *Bollettino di Geofisica Teorica ed Applicata*.

[5] R. Floberghagen, M. Fehringer, D. Lamarre, D. Muzi, B. Frommknecht, C. Steiger, J. Piñeiro, and A. da Costa, "Mission design, operation and exploitation of the gravity field and steady-state ocean circulation explorer mission," *Journal of Geodesy*, vol. 85, pp. 749–758, Nov. 2011.

[6] EO and ESA, "GOCE (Gravity field and steady-state Ocean Circulation Explorer)." Available at https://www.eoportal.org/satellite-missions/goce#mission-status.

[7] B. D. Tapley, M. M. Watkins, F. Flechtner, C. Reigber, S. Bettadpur, M. Rodell, I. Sasgen, J. S. Famiglietti, F. W. Landerer, D. P. Chambers, J. T. Reager, A. S. Gardner, H. Save, E. R. Ivins, S. C. Swenson, C. Boening, C. Dahle, D. N. Wiese, H. Dobslaw, M. E. Tamisiea, and I. Velicogna, "Contributions of GRACE to understanding climate change," *Nature Climate Change*, vol. 9, pp. 358–369, May 2019.

[8] V. Humphrey, M. Rodell, and A. Eicker, "Using Satellite-Based Terrestrial Water Storage Data: A Review," *Surveys in Geophysics*, vol. 44, pp. 1489–1517, Oct. 2023.

[9] B. R. Scanlon, S. Fakhreddine, A. Rateb, I. de Graaf, J. Famiglietti, T. Gleeson, R. Q. Grafton, E. Jobbagy, S. Kebede, S. R. Kolusu, L. F. Konikow, D. Long, M. Mekonnen, H. M. Schmied, A. Mukherjee, A. MacDonald, R. C. Reedy, M. Shamsudduha, C. T. Simmons, A. Sun, R. G. Taylor, K. G. Villholth, C. J. Vörösmarty, and C. Zheng, "Global water resources and the role of groundwater in a resilient water future," *Nature Reviews Earth & Environment*, vol. 4, pp. 87–101, Feb. 2023.

[10] M. Mandea, V. Dehant, and A. Cazenave, "GRACE Gravity Data for Understanding the Deep Earth's Interior," *Remote Sensing*, vol. 12, p. 4186, Jan. 2020.

[11] H. Lecomte, S. Rosat, M. Mandea, and M. Dumberry, "Gravitational Constraints on the Earth's Inner Core Differential Rotation," *Geophysical Research Letters*, vol. 50, no. 23, 2023.

[12] EO and ESA, "CHAMP (Challenging Minisatellite Payload)," 2012. Available at \href{https://www.eoportal.org/satellite-missions/champ#blackjack-gps-flight-receiver}.

[13] R. Rummel, W. Yi, and C. Stummer, "GOCE gravitational gradiometry," *Journal of Geodesy*, vol. 85, pp. 777–790, Nov. 2011.

[14] B. D. Tapley, S. Bettadpur, M. Watkins, and C. Reigber, "The gravity recovery and climate experiment: Mission overview and early results," *Geophysical Research Letters*, vol. 31, no. 9, 2004.

[15] B. S. Sheard, G. Heinzel, K. Danzmann, D. A. Shaddock, W. M. Klipstein, and W. M. Folkner, "Intersatellite laser ranging instrument for the GRACE follow-on mission," *Journal of Geodesy*, vol. 86, pp. 1083–1095, Dec. 2012.

[16] "GRACE-FO," 2024. JET Propulsion Laboratory, Available at https://gracefo.jpl.nasa.gov/.

[17] A. F. Purkhauser, C. Siemes, and R. Pail, "Consistent quantification of the impact of key mission design parameters on the performance of next-generation gravity missions," *Geophysical Journal International*, vol. 221, pp. 1190–1210, May 2020.

[18] L. Massotti, C. Siemes, G. March, R. Haagmans, and P. Silvestrin, "Next Generation Gravity Mission Elements of the Mass Change and Geoscience International Constellation: From Orbit Selection to Instrument and Mission Design," *Remote Sensing*, vol. 13, p. 3935, Jan. 2021.

[19] I. Daras, *Gravity field processing towards future LL-SST satellite missions.* PhD thesis, Technische Universität München, 2016.

[20] J. Kitching, S. Knappe, and E. A. Donley, "Atomic Sensors – A Review," *IEEE Sensors Journal*, vol. 11, pp. 1749–1758, Sept. 2011.

[21] W. M. Itano, J. C. Bergquist, J. J. Bollinger, J. M. Gilligan, D. J. Heinzen, F. L. Moore, M. G. Raizen, and D. J. Wineland, "Quantum projection noise: Population fluctuations in two-level systems," *Physical Review A*, vol. 47, pp. 3554–3570, May 1993.

[22] D. J. Wineland, J. J. Bollinger, W. M. Itano, and D. J. Heinzen, "Squeezed atomic states and projection noise in spectroscopy," *Physical Review A*, vol. 50, pp. 67–88, July 1994.

[23] Edmund, "Edmund Optics website: Building a Mach-Zehnder Interferometer." Edmund Optics, Available at https://www.edmundoptics.fr/knowledge-center/application-notes/optomechanics/building-a-mach-zehnder-interferometer/.

[24] A. Peters, K. Y. Chung, and S. Chu, "High-precision gravity measurements using atom interferometry," *Metrologia*, vol. 38, p. 25, Feb. 2001.

[25] O. Carraz, C. Siemes, L. Massotti, R. Haagmans, and P. Silvestrin, "A Spaceborne Gravity Gradiometer Concept Based on Cold Atom Interferometers for Measuring Earth's Gravity Field," *Microgravity Science and Technology*, vol. 26, pp. 139–145, Oct. 2014.

[26] K. Douch, H. Wu, C. Schubert, J. Müller, and F. Pereira dos Santos, "Simulation-based evaluation of a cold atom interferometry gradiometer concept for gravity field recovery," *Advances in Space Research*, vol. 61, pp. 1307–1323, Mar. 2018.

[27] A. Trimeche, B. Battelier, D. Becker, A. Bertoldi, P. Bouyer, C. Braxmaier, E. Charron, R. Corgier, M. Cornelius, K. Douch, N. Gaaloul, S. Herrmann, J. Müller, E. Rasel, C. Schubert, H. Wu, and F. P. d. Santos, “Concept study and preliminary design of a cold atom interferometer for space gravity gradiometry,” *Classical and Quantum Gravity*, vol. 36, p. 215004, Oct. 2019.

[28] F. Migliaccio, M. Reguzzoni, K. Batsukh, G. M. Tino, G. Rosi, F. Sorrentino, C. Braitenberg, T. Pivetta, D. F. Barbolla, and S. Zoffoli, “MOCASS: A Satellite Mission Concept Using Cold Atom Interferometry for Measuring the Earth Gravity Field,” *Surveys in Geophysics*, vol. 40, pp. 1029–1053, Sept. 2019.

[29] A. HosseiniArani, M. Schilling, Q. Beaufils, A. Knabe, B. Tennstedt, A. Kupriyanov, S. Schön, F. Pereira dos Santos, and J. Müller, “Advances in Atom Interferometry and their Impacts on the Performance of Quantum Accelerometers On-board Future Satellite Gravity Missions,” *Advances in Space Research*, vol. 74, pp. 3186–3200, Oct. 2024.

[30] N. Zahzam, B. Christophe, V. Lebat, E. Hardy, P.-A. Huynh, N. Marquet, C. Blanchard, Y. Bidel, A. Bresson, P. Abrykosov, T. Gruber, R. Pail, I. Daras, and O. Carraz, “Hybrid Electrostatic–Atomic Accelerometer for Future Space Gravity Missions,” *Remote Sensing*, vol. 14, p. 3273, Jan. 2022.

[31] P. Touboul, S. Metris, O. Le Traon, A. Bresson, N. Zahzam, B. Christophe, and M. Rodrigues, “Gravitation and Geodesy with Inertial Sensors, from Ground to Space,” *AerospaceLab Journal*, vol. Issue 12, p. 16, 2016.

[32] D. C. Aveline, J. R. Williams, E. R. Elliott, C. Dutenhoffer, J. R. Kellogg, J. M. Kohel, N. E. Lay, K. Oudrhiri, R. F. Shotwell, N. Yu, and R. J. Thompson, “Observation of Bose–Einstein condensates in an Earth-orbiting research lab,” *Nature*, vol. 582, pp. 193–197, June 2020.

[33] S.-w. Chiow, J. Williams, and N. Yu, “Laser-ranging long-baseline differential atom interferometers for space,” *Physical Review A*, vol. 92, p. 063613, Dec. 2015.

[34] T. Lévèque, C. Fallet, M. Mandea, R. Biancale, J. M. Lemoine, S. Tardivel, S. Delavault, A. Piquereau, S. Bourgogne, F. Pereira Dos Santos, B. Battelier, and P. Bouyer, “Gravity field mapping using laser-coupled quantum accelerometers in space,” *Journal of Geodesy*, vol. 95, p. 15, Jan. 2021.

[35] P. Abrykosov, R. Pail, T. Gruber, N. Zahzam, A. Bresson, E. Hardy, B. Christophe, Y. Bidel, O. Carraz, and C. Siemes, “Impact of a novel hybrid accelerometer on satellite gravimetry performance,” *Advances in Space Research*, vol. 63, pp. 3235–3248, May 2019.

[36] H. Müntinga, H. Ahlers, M. Krutzik, A. Wenzlawski, S. Arnold, D. Becker, K. Bongs, H. Dittus, H. Duncker, N. Gaaloul, C. Gherasim, E. Giese, C. Grzeschik, T. W. Hänsch, O. Hellmig, W. Herr, S. Herrmann, E. Kajari, S. Kleinert, C. Lämmerzahl, W. Lewoczko-Adamczyk, J. Malcolm, N. Meyer, R. Nolte, A. Peters, M. Popp, J. Reichel, A. Roura, J. Rudolph, M. Schiemangk, M. Schneider, S. T. Seidel, K. Sengstock, V. Tamma, T. Valenzuela, A. Vogel, R. Walser, T. Wendrich, P. Windpassinger, W. Zeller, T. van Zoest, W. Ertmer, W. P. Schleich, and E. M. Rasel, “Interferometry with Bose-Einstein Condensates in Microgravity,” *Physical Review Letters*, vol. 110, p. 093602, Feb. 2013.

[37] D. Becker, M. D. Lachmann, S. T. Seidel, H. Ahlers, A. N. Dinkelaker, J. Grosse, O. Hellmig, H. Müntinga, V. Schkolnik, T. Wendrich, A. Wenzlawski, B. Weps, R. Corgier, T. Franz, N. Gaaloul, W. Herr, D. Lüdtke, M. Popp, S. Amri, H. Duncker, M. Erbe, A. Kohfeldt, A. Kubelka-Lange, C. Braxmaier, E. Charron, W. Ertmer, M. Krutzik, C. Lämmerzahl, A. Peters, W. P. Schleich, K. Sengstock, R. Walser, A. Wicht, P. Windpassinger, and E. M.

Rasel, "Space-borne Bose-Einstein condensation for precision interferometry," *Nature*, vol. 562, pp. 391–395, Oct. 2018.

[38] L. Liu, D.-S. Lü, W.-B. Chen, T. Li, Q.-Z. Qu, B. Wang, L. Li, W. Ren, Z.-R. Dong, J.-B. Zhao, W.-B. Xia, X. Zhao, J.-W. Ji, M.-F. Ye, Y.-G. Sun, Y.-Y. Yao, D. Song, Z.-G. Liang, S.-J. Hu, D.-H. Yu, X. Hou, W. Shi, H.-G. Zang, J.-F. Xiang, X.-K. Peng, and Y.-Z. Wang, "In-orbit operation of an atomic clock based on laser-cooled 87Rb atoms," *Nature Communications*, vol. 9, p. 2760, July 2018.

[39] M. Planck, "Ueber das Gesetz der Energieverteilung im Normalspectrum," *Annalen der Physik*, vol. 309, no. 3, pp. 553–563, 1901.

[40] A. Einstein, "Zur Elektrodynamik bewegter Körper," *Annalen der Physik*, vol. 322, no. 10, pp. 891–921, 1905.

[41] A. Einstein, "Zur Quantentheorie der Strahlung," *Physikalische Zeitschrift*, 1917.

[42] Q. d'Armagnac de Castanet, C. Des Cognets, R. Arguel, S. Templier, V. Jarlaud, V. Ménoret, B. Desruelle, P. Bouyer, and B. Battelier, "Atom interferometry at arbitrary orientations and rotation rates," *Nature Communications*, vol. 15, p. 6406, July 2024.

[43] I. Estermann and O. Stern, "Beugung von Molekularstrahlen," *Zeitschrift für Physik*, vol. 61, pp. 95–125, Jan. 1930.

[44] H. V. Halban and P. Preiswerk, "Preuve expérimentale de la diffraction des neutrons," *Contre Rendu des séances de l'Académie des sciences*, 1936.

[45] D. P. Mitchell and P. N. Powers, "Bragg Reflection of Slow Neutrons," *Physical Review*, vol. 50, pp. 486–487, Sept. 1936.

[46] L. Marton, "Electron Interferometer," *Physical Review*, vol. 85, pp. 1057–1058, Mar. 1952.

[47] H. Maier-Leibnitz and T. Springer, "The use of neutron optical devices on beam-hole experiments on beam-hole experiments," *Journal of Nuclear Energy. Parts A/B. Reactor Science and Technology*, vol. 17, pp. 217–225, July 1963.

[48] N. F. Ramsey, "A Molecular Beam Resonance Method with Separated Oscillating Fields," *Physical Review*, vol. 78, pp. 695–699, June 1950.

[49] H. Rauch, W. Treimer, and U. Bonse, "Test of a single crystal neutron interferometer," *Physics Letters A*, vol. 47, pp. 369–371, Apr. 1974.

[50] R. Colella, A. W. Overhauser, and S. A. Werner, "Observation of Gravitationally Induced Quantum Interference," *Physical Review Letters*, vol. 34, pp. 1472–1474, June 1975.

[51] O. Carnal and J. Mlynek, "Young's double-slit experiment with atoms: A simple atom interferometer," *Physical Review Letters*, vol. 66, pp. 2689–2692, May 1991.

[52] D. W. Keith, C. R. Ekstrom, Q. A. Turchette, and D. E. Pritchard, "An interferometer for atoms," *Physical Review Letters*, vol. 66, pp. 2693–2696, May 1991.

[53] F. Riehle, T. Kisters, A. Witte, J. Helmcke, and C. J. Bordé, "Optical Ramsey spectroscopy in a rotating frame: Sagnac effect in a matter-wave interferometer," *Physical Review Letters*, vol. 67, pp. 177–180, July 1991.

[54] M. Kasevich and S. Chu, "Atomic interferometry using stimulated Raman transitions," *Physical Review Letters*, vol. 67, pp. 181–184, July 1991. Publisher: American Physical Society.

[55] C. Bordé, "Atomic interferometry with internal state labelling," *Physics Letters A*, vol. 140, pp. 10–12, Sept. 1989.

[56] X.-Z. Li, L. Marks, J. Maciejewski, L. Fehrenbacher, J. Zabinski, and J. O'Neill, "Stable quasicrystalline phase in Al-Cu-Fe-Cr coating materials," *Metallurgical and Materials Transactions A*, vol. 33, pp. 675–679, Jan. 2002.

[57] C. Curceanu, J. Marton, and E. Milotti, "Mini-Proceedings ECT*: Speakable in quantum mechanics: atomic, nuclear and subnuclear physics tests," Dec. 2011.

[58] M. Kasevich and S. Chu, "Measurement of the gravitational acceleration of an atom with a light-pulse atom interferometer," *Applied Physics B*, vol. 54, pp. 321–332, May 1992.

[59] A. Aspect, E. Arimondo, R. Kaiser, N. Vansteenkiste, and C. Cohen-Tannoudji, "Laser Cooling below the One-Photon Recoil Energy by Velocity-Selective Coherent Population Trapping," *Physical Review Letters*, vol. 61, pp. 826–829, Aug. 1988.

[60] J. Dalibard and C. Cohen-Tannoudji, "Laser cooling below the Doppler limit by polarization gradients: simple theoretical models," *Journal of the Optical Society of America B*, vol. 6, p. 2023, Nov. 1989.

[61] A. L. Migdall, J. V. Prodan, W. D. Phillips, T. H. Bergeman, and H. J. Metcalf, "First Observation of Magnetically Trapped Neutral Atoms," *Physical Review Letters*, vol. 54, pp. 2596–2599, June 1985.

[62] W. D. Phillips and H. Metcalf, "Laser Deceleration of an Atomic Beam," *Physical Review Letters*, vol. 48, pp. 596–599, Mar. 1982.

[63] S. Chu, L. Hollberg, J. E. Bjorkholm, A. Cable, and A. Ashkin, "Three-dimensional viscous confinement and cooling of atoms by resonance radiation pressure," *Physical Review Letters*, vol. 55, pp. 48–51, July 1985.

[64] P. D. Lett, R. N. Watts, C. I. Westbrook, W. D. Phillips, P. L. Gould, and H. J. Metcalf, "Observation of Atoms Laser Cooled below the Doppler Limit," *Physical Review Letters*, vol. 61, pp. 169–172, July 1988.

[65] T. M. Niebauer, G. S. Sasagawa, J. E. Faller, R. Hilt, and F. Klopping, "A new generation of absolute gravimeters," *Metrologia*, vol. 32, p. 159, Jan. 1995.

[66] J. M. McGuirk, G. T. Foster, J. B. Fixler, M. J. Snadden, and M. A. Kasevich, "Sensitive absolute-gravity gradiometry using atom interferometry," *Physical Review A*, vol. 65, p. 033608, Feb. 2002.

[67] A. Gauguet, B. Canuel, T. Lévèque, W. Chaibi, and A. Landragin, "Characterization and limits of a cold-atom Sagnac interferometer," *Physical Review A*, vol. 80, p. 063604, Dec. 2009.

[68] L. Morel, Z. Yao, P. Cladé, and S. Guellati-Khélifa, "Determination of the fine-structure constant with an accuracy of 81 parts per trillion," *Nature*, vol. 588, pp. 61–65, Dec. 2020.

[69] R. H. Parker, C. Yu, W. Zhong, B. Estey, and H. Müller, "Measurement of the fine-structure constant as a test of the Standard Model," *Science*, vol. 360, pp. 191–195, Apr. 2018.

[70] M. Fattori, G. Lamporesi, T. Petelski, J. Stuhler, and G. M. Tino, "Towards an atom interferometric determination of the Newtonian gravitational constant," *Physics Letters A*, vol. 318, pp. 184–191, Nov. 2003.

[71] P. Asenbaum, C. Overstreet, M. Kim, J. Curti, and M. A. Kasevich, "Atom-Interferometric Test of the Equivalence Principle at the 10 -12 Level," *Physical Review Letters*, vol. 125, p. 191101, Nov. 2020.

[72] A. Sugarbaker, S. M. Dickerson, J. M. Hogan, D. M. S. Johnson, and M. A. Kasevich, "Enhanced Atom Interferometer Readout through the Application of Phase Shear," *Physical Review Letters*, vol. 111, p. 113002, Sept. 2013.

[73] M. Schilling, E. Wodey, L. Timmen, D. Tell, K. H. Zipfel, D. Schlippert, C. Schubert, E. M. Rasel, and J. Muller, "Gravity field modelling for the Hannover 10 m atom interferometer," *Journal of Geodesy*, vol. 94, p. 122, Nov. 2020.

[74] A. Peters, K. Y. Chung, and S. Chu, "Measurement of gravitational acceleration by dropping atoms," *Nature*, vol. 400, pp. 849–852, Aug. 1999.

[75] Z.-K. Hu, B.-L. Sun, X.-C. Duan, M.-K. Zhou, L.-L. Chen, S. Zhan, Q.-Z. Zhang, and J. Luo, "Demonstration of an ultrahigh-sensitivity atom-interferometry absolute gravimeter," *Physical Review A*, vol. 88, p. 043610, Oct. 2013. Publisher: American Physical Society.

[76] R. Karcher, A. Imanaliev, S. Merlet, and F. P. D. Santos, "Improving the accuracy of atom interferometers with ultracold sources," *New Journal of Physics*, vol. 20, p. 113041, Nov. 2018.

[77] P. A. Altin, M. T. Johnsson, V. Negnevitsky, G. R. Dennis, R. P. Anderson, J. E. Debs, S. S. Szigeti, K. S. Hardman, S. Bennetts, G. D. McDonald, L. D. Turner, J. D. Close, and N. P. Robins, "Precision atomic gravimeter based on Bragg diffraction," *New Journal of Physics*, vol. 15, p. 023009, Feb. 2013.

[78] P. Gillot, O. Francis, A. Landragin, F. P. D. Santos, and S. Merlet, "Stability comparison of two absolute gravimeters: optical versus atomic interferometers," *Metrologia*, vol. 51, p. L15, June 2014.

[79] L. Antoni-Micollier, D. Carbone, V. Ménoret, J. Lautier-Gaud, T. King, F. Greco, A. Messina, D. Contrafatto, and B. Desruelle, "Detecting Volcano-Related Underground Mass Changes With a Quantum Gravimeter," *Geophysical Research Letters*, vol. 49, no. 13, p. e2022GL097814, 2022.

[80] V. Ménoret, P. Vermeulen, N. Le Moigne, S. Bonvalot, P. Bouyer, A. Landragin, and B. Desruelle, "Gravity measurements below 10-9 g with a transportable absolute quantum gravimeter," *Scientific Reports*, vol. 8, p. 12300, Aug. 2018. Publisher: Nature Publishing Group.

[81] S. Merlet, P. Gillot, T. Farah, Q. Bodart, J. Le Gouet, P. Cheinet, C. Guerlin, A. Louchet-Chauvet, N. Malossi, A. Kopaev, O. Francis, G. D'Agostino, M. Diament, G. Geneves, A. Clairon, A. Landragin, and F. Pereira Dos Santos, "Détermination de l'accélération de la pesanteur pour la balance du watt du LNE," *Revue française de métrologie*, pp. 11–27, Jan. 2015.

[82] S.-K. Wang, Y. Zhao, W. Zhuang, T.-C. Li, S.-Q. Wu, J.-Y. Feng, and C.-J. Li, "Shift evaluation of the atomic gravimeter NIM-AGRb-1 and its comparison with FG5X," *Metrologia*, vol. 55, p. 360, Apr. 2018.

[83] X. Wu, Z. Pagel, B. S. Malek, T. H. Nguyen, F. Zi, D. S. Scheirer, and H. Müller, "Gravity surveys using a mobile atom interferometer," *Science Advances*, vol. 5, Sept. 2019.

[84] C. Freier, M. Hauth, V. Schkolnik, B. Leykauf, M. Schilling, H. Wziontek, H.-G. Scherneck, J. Müller, and A. Peters, "Mobile quantum gravity sensor with unprecedented stability," *Journal of Physics: Conference Series*, vol. 723, p. 012050, June 2016.

[85] Exail, "A free-fall absolute gravimeter based on laser-cooled atoms." Available at https://www.ixblue.com/wp-content/uploads/2021/12/brochure-4volets-quantumgravimeter-v3-web.pdf.

[86] Y.-Y. Xu, J.-F. Cui, K. Qi, L.-L. Chen, X.-B. Deng, Q. Luo, H. Zhang, Y.-J. Tan, C.-G. Shao, M.-K. Zhou, X.-C. Duan, and Z.-K. Hu, "Evaluation of the transportable atom gravimeter HUST-QG," *Metrologia*, vol. 59, p. 055001, Aug. 2022.

[87] Y. Bidel, N. Zahzam, A. Bresson, C. Blanchard, A. Bonnin, J. Bernard, M. Cadoret, T. E. Jensen, R. Forsberg, C. Salaun, S. Lucas, M. F. Lequentrec-Lalancette, D. Rouxel, G. Gabalda, L. Seoane, D. T. Vu, S. Bruinsma, and S. Bonvalot, "Airborne Absolute Gravimetry With a Quantum Sensor, Comparison With Classical Technologies," *Journal of Geophysical Research: Solid Earth*, vol. 128, no. 4, 2023.

[88] B. Wu, C. Zhang, K. Wang, B. Cheng, D. Zhu, R. Li, X. Wang, Q. Lin, Z. Qiao, and Y. Zhou, "Marine Absolute Gravity Field Surveys Based on Cold Atomic Gravimeter," *IEEE Sensors Journal*, vol. 23, Oct. 2023.

[89] R. Geiger, V. Ménoret, G. Stern, N. Zahzam, P. Cheinet, B. Battelier, A. Villing, F. Moron, M. Lours, Y. Bidel, A. Bresson, A. Landragin, and P. Bouyer, "Detecting inertial effects with airborne matter-wave interferometry," *Nature Communications*, vol. 2, p. 474, Sept. 2011.

[90] M. Hauth, C. Freier, V. Schkolnik, A. Senger, M. Schmidt, and A. Peters, "First gravity measurements using the mobile atom interferometer GAIN," *Applied Physics B*, vol. 113, pp. 49–55, Oct. 2013.

[91] W.-T. Duan, C. He, S.-T. Yan, Y.-H. Ji, L. Zhou, X. Chen, J. Wang, and M.-S. Zhan, "Suppression of Coriolis error in weak equivalence principle test using ^{85} Rb– ^{87} Rb dual-species atom interferometer*," *Chinese Physics B*, vol. 29, p. 070305, Aug. 2020.

[92] S. M. Dickerson, J. M. Hogan, A. Sugarbaker, D. M. S. Johnson, and M. A. Kasevich, "Multiaxis Inertial Sensing with Long-Time Point Source Atom Interferometry," *Physical Review Letters*, vol. 111, p. 083001, Aug. 2013.

[93] J. Glick, Z. Chen, T. Deshpande, Y. Wang, and T. Kovachy, "Coriolis force compensation and laser beam delivery for 100-m baseline atom interferometry," *AVS Quantum Science*, vol. 6, p. 014402, Jan. 2024.

[94] A. Louchet-Chauvet, T. Farah, Q. Bodart, A. Clairon, A. Landragin, S. Merlet, and F. P. D. Santos, "The influence of transverse motion within an atomic gravimeter," *New Journal of Physics*, vol. 13, p. 065025, June 2011.

[95] Q. Beaufils, J. Lefebve, J. G. Baptista, R. Piccon, V. Cambier, L. A. Sidorenkov, C. Fallet, T. Lévèque, S. Merlet, and F. Pereira Dos Santos, "Rotation related systematic effects in a cold atom interferometer onboard a Nadir pointing satellite," *npj Microgravity*, vol. 9, pp. 1–6, July 2023.

[96] Y. Zhao, X. Yue, F. Chen, and C. Huang, "Extension of the rotation-rate measurement range with no sensitivity loss in a cold-atom gyroscope," *Physical Review A*, vol. 104, p. 013312, July 2021.

[97] T. Sato, N. Nishimura, N. Kaku, S. Otabe, T. Kawasaki, T. Hosoya, and M. Kozuma, "Closed-loop measurement in atom interferometer gyroscope with velocity-dependent phase dispersion compensation," *arXiv.org*, July 2024.

[98] Y. Bidel, O. Carraz, R. Charrière, M. Cadoret, N. Zahzam, and A. Bresson, "Compact cold atom gravimeter for field applications," *Applied Physics Letters*, vol. 102, p. 144107, Apr. 2013.

[99] C. Diboune, *Développement d'un capteur inertiel à atomes froids 87Rb/85Rb/133Cs*. PhD thesis, Université Paris Sud, May 2019.

[100] C. Cohen-Tannoudji, B. Diu, and F. Laloë, *Mécanique Quantique - Tome 1 - Nouvelle édition révisée*. edp sciences CNRS Editions, 2018.

[101] C. Cohen-Tannoudji, "Cours de physique atomique et moléculaire: Interférométrie atomique, année scolaire 1992-1993," 1993. Collège de France.

[102] D. M. Giltner, R. W. McGowan, and S. A. Lee, "Atom Interferometer Based on Bragg Scattering from Standing Light Waves," *Physical Review Letters*, vol. 75, pp. 2638–2641, Oct. 1995.

[103] P. Cheinet, *Conception et réalisation d'un gravimètre à atomes froids*. These de doctorat, Paris 6, Jan. 2006.

[104] C. Cohen-Tannoudji, B. Diu, and F. Laloë, *Mécanique Quantique - Tome 2 - Nouvelle édition révisée*. edp sciences CNRS Editions, 2018.

[105] A. Gauguet, T. E. Mehlstäubler, T. Lévèque, J. Le Gouët, W. Chaibi, B. Canuel, A. Clairon, F. P. Dos Santos, and A. Landragin, "Off-resonant Raman transition impact in an atom interferometer," *Physical Review A*, vol. 78, p. 043615, Oct. 2008.

[106] A. Gauguet, *Gyromètre à atomes froids : étude de la stabilité limite et des effets systématiques liés aux séparatrices lasers*. These de doctorat, Paris 6, Jan. 2008.

[107] D. A. Steck, "Rubidium 87 D Line Data," 2001. Available at https://steck.us/alkalidata/rubidium87numbers.1.6.pdf.

[108] F. Lienhart, *Etude d'un gravimètre à atomes froids embarquable*. These de doctorat, Observatoire de Paris, Jan. 2007.

[109] K. Bongs, R. Launay, and M. Kasevich, "High-order inertial phase shifts for time-domain atom interferometers," *Applied Physics B*, vol. 84, pp. 599–602, Sept. 2006.

[110] J. Bernard, *Développement d'une centrale inertielle hybride à atomes froids*. These de doctorat, Paris, HESAM, Dec. 2022.

[111] A. Bonnin, *Interférométrie Simultanée avec Deux Espèces Atomiques 87Rb/85Rb et Applications aux Mesures Inertielles*. These de doctorat, Université Paris-Saclay, Nov. 2015.

[112] J. Hogan, D. M. S. Johnson, and M. Kasevich, "Light-pulse atom interferometry," *Proceedings of the International Summer School of Physics "Enrico Fermi" on Atom Optics and Space Physics (Varenna)*, July 2007.

[113] B. Christophe, D. Boulanger, B. Foulon, P. A. Huynh, V. Lebat, F. Liorzou, and E. Perrot, "A new generation of ultra-sensitive electrostatic accelerometers for GRACE Follow-on and towards the next generation gravity missions," *Acta Astronautica*, vol. 117, pp. 1–7, Dec. 2015.

[114] "Specifications BM-4 Bench Top Vibration Isolation Platform," 2023. MinusK Technology, Available at https://www.minusk.com.

[115] PI, "Specifications P-212, P-216 PICA Power Piezo Stack Actuators," 2008. Physik Instruments (PI), Available at https://www.pi-usa.us/fileadmin/user_upload/pi_us/files/product_datasheets/P212_P216_Piezo_Stack_Actuator.pdf.

[116] Innalabs, "Specifications Innalabs Two Axis Gyroscope," 2015. Available at https://www.innalabs.com/u-series-gyroscope.

[117] E. L. Raab, M. Prentiss, A. Cable, S. Chu, and D. E. Pritchard, "Trapping of Neutral Sodium Atoms with Radiation Pressure," *Physical Review Letters*, vol. 59, pp. 2631–2634, Dec. 1987.

[118] D. Allan, "Time and Frequency (Time-Domain) Characterization, Estimation, and Prediction of Precision Clocks and Oscillators," *IEEE Transactions on Ultrasonics, Ferroelectrics, and Frequency Control*, vol. 34, pp. 647–654, Nov. 1987.

[119] E. J. Harrison, M. A. Meldrum, and Z. Milburn, "Development of a Miniature Electrostatic Accelerometer /MESA/ for low g applications Summary report," Apr. 1965. Available at https://www.semanticscholar.org/paper/Development-of-a-Miniature-Electrostatic-MESA-for-g-Harrison-Meldrum/db59839f57a510678e1f9b1f08e10b59561faafb.

[120] J. Beaussier, A.-M. Mainguy, A. Olivero, and R. Rolland, "In orbit performance of the Cactus accelerometer (D5B spacecraft)," *Acta Astronautica*, vol. 4, pp. 1085–1102, Sept. 1977.

[121] F. Liorzou, P. Touboul, M. Rodrigues, G. Métris, Y. André, J. Bergé, D. Boulanger, S. Bremer, R. Chhun, B. Christophe, P. Danto, B. Foulon, D. Hagedorn, E. Hardy, P.-A. Huynh, C. Lämmerzahl, V. Lebat, M. List, F. Löffler, B. Rievers, A. Robert, and H. Selig, "MICROSCOPE instrument description and validation," *Classical and Quantum Gravity*, vol. 39, p. 204002, Sept. 2022.

[122] Z. Wang, Y. Li, J. Lei, Z. Wang, D. Xi, J. Min, Y. Wei, S. Yang, and Z. Luo, "Design and experimental verification of the working mode of an electrostatic suspension accelerometer," *AIP Advances*, vol. 13, p. 095014, Sept. 2023.

[123] R. Chen, *Étude du bruit des accéléromètres électrostatiques ultrasensibles de la mission GOCE*. phdthesis, Université Pierre et Marie Curie - Paris VI, Feb. 2017.

[124] T. Farah, P. Gillot, B. Cheng, A. Landragin, S. Merlet, and F. Pereira Dos Santos, "Effective velocity distribution in an atom gravimeter: Effect of the convolution with the response of the detection," *Physical Review A*, vol. 90, p. 023606, Aug. 2014.

[125] Y. Castin, J. Dalibard, and C. Cohen-Tannoudji, "Light Induced Kinetic Effects on Atoms, Ions and Molecules," *ETS Editrice, Pisa*, p. 5, 1991.

[126] J. Jersblad, H. Ellmann, K. Støchkel, A. Kastberg, L. Sanchez-Palencia, and R. Kaiser, "Non-Gaussian velocity distributions in optical lattices," *Physical Review A*, vol. 69, p. 013410, Jan. 2004.

[127] Y. Sortais, S. Bize, C. Nicolas, A. Clairon, C. Salomon, and C. Williams, "Cold Collision Frequency Shifts in a 87Rb Atomic Fountain," *Physical Review Letters*, vol. 85, pp. 3117–3120, Oct. 2000.

[128] T. W. Hodapp, C. Gerz, C. Furtlehner, C. I. Westbrook, W. D. Phillips, and J. Dalibard, “Three-dimensional spatial diffusion in optical molasses,” *Applied Physics B Laser and Optics*, vol. 60, no. 2-3, pp. 135–143, 1995.

[129] M. Walhout, J. Dalibard, S. L. Rolston, and W. D. Phillips, “Optical molasses in a longitudinal magnetic field,” *JOSA B*, vol. 9, pp. 1997–2007, Nov. 1992.

[130] M. Carey, J. Saywell, D. Elcock, M. Belal, and T. Freegarde, “Velocimetry of cold atoms by matter-wave interferometry,” *Physical Review A*, vol. 99, p. 023631, Feb. 2019.

[131] J. Werner and H. Wallis, “Laser cooling by sigma +- sigma - circularly polarized beams of unequal intensities,” *Journal of Physics B: Atomic, Molecular and Optical Physics*, vol. 26, p. 3063, Sept. 1993.

[132] T. Lévèque, A. Gauguet, F. Michaud, F. Pereira Dos Santos, and A. Landragin, “Enhancing the Area of a Raman Atom Interferometer Using a Versatile Double-Diffraction Technique,” *Physical Review Letters*, vol. 103, p. 080405, Aug. 2009.

[133] N. Malossi, Q. Bodart, S. Merlet, T. Lévèque, A. Landragin, and F. P. D. Santos, “Double diffraction in an atomic gravimeter,” *Physical Review A*, vol. 81, p. 013617, Jan. 2010. Publisher: American Physical Society.

[134] L. Zhou, S. Long, B. Tang, X. Chen, F. Gao, W. Peng, W. Duan, J. Zhong, Z. Xiong, J. Wang, Y. Zhang, and M. Zhan, “Test of Equivalence Principle at $1{0}^{\ensuremath{-}8}$ Level by a Dual-Species Double-Diffraction Raman Atom Interferometer,” *Physical Review Letters*, vol. 115, p. 013004, July 2015.

[135] A. Trimeche, M. Langlois, S. Merlet, and F. Pereira Dos Santos, “Active Control of Laser Wavefronts in Atom Interferometers,” *Physical Review Applied*, vol. 7, p. 034016, Mar. 2017.

[136] T. Hensel, S. Loriani, C. Schubert, F. Fitzek, S. Abend, H. Ahlers, J.-N. Siemß, K. Hammerer, E. M. Rasel, and N. Gaaloul, “Inertial sensing with quantum gases: a comparative performance study of condensed versus thermal sources for atom interferometry,” *The European Physical Journal D*, vol. 75, p. 108, Mar. 2021.

[137] H. Albers, R. Corgier, A. Herbst, A. Rajagopalan, C. Schubert, C. Vogt, M. Woltmann, C. Lämmerzahl, S. Herrmann, E. Charron, W. Ertmer, E. M. Rasel, N. Gaaloul, and D. Schlippert, “All-optical matter-wave lens using time-averaged potentials,” *Communications Physics*, vol. 5, pp. 1–7, Mar. 2022.

[138] C. Deppner, W. Herr, M. Cornelius, P. Stromberger, T. Sternke, C. Grzeschik, A. Grote, J. Rudolph, S. Herrmann, M. Krutzik, A. Wenzlawski, R. Corgier, E. Charron, D. Guéry-Odelin, N. Gaaloul, C. Lämmerzahl, A. Peters, P. Windpassinger, and E. M. Rasel, “Collective-Mode Enhanced Matter-Wave Optics,” *Physical Review Letters*, vol. 127, p. 100401, Aug. 2021.

[139] ONERA and TUM, “Final Report of the ESA study "Hybrid Atom Electrostatic System Follow-On for Satellite Geodesy",” tech. rep., 2021.

[140] AIRBUS, “Specifications Gyroscope ASTRIX 200,” 2022. Available at https://www.airbus.com/sites/g/files/jlcbta136/files/2022-02/ScE-AVIONICS-ASTRIX200v3_2022.pdf.